Topics in Organometallic Chemistry 70

Philippe Kalck *Editor*

Modes of Cooperative Effects in Dinuclear Complexes

Springer

70
Topics in Organometallic Chemistry

Aims and Scope

The series *Topics in Organometallic Chemistry* presents critical overviews of research results in organometallic chemistry. As our understanding of organometallic structure, properties and mechanisms increases, new ways are opened for the design of organometallic compounds and reactions tailored to the needs of such diverse areas as organic synthesis, medical research, biology and materials science. Thus the scope of coverage includes a broad range of topics of pure and applied organometallic chemistry, where new breakthroughs are being achieved that are of significance to a larger scientific audience.

The individual volumes of *Topics in Organometallic Chemistry* are thematic. Review articles are generally invited by the volume editors. All chapters from Topics in Organometallic Chemistry are published Online First with an individual DOI. In references, *Topics in Organometallic Chemistry* is abbreviated as Top Organomet Chem and cited as a journal.

Philippe Kalck
Editor

Modes of Cooperative Effects in Dinuclear Complexes

With contributions by

T. P. Brewster · C. Elleouet · Z. Freixa · N. Guihéry · P. Kalck · R. Malcolm Charles III · T. Mallah · L. Maron · R. Maurice · F. Y. Pétillon · P. Schollhammer · P. W. N. M. van Leeuwen

Springer

Editor
Philippe Kalck
Equipe C 'Catalyse et Chimie Fine'
Laboratoire de Chimie de
Coordination du CNRS
Toulouse, France

ISSN 1436-6002 ISSN 1616-8534 (electronic)
Topics in Organometallic Chemistry
ISBN 978-3-031-32249-5 ISBN 978-3-031-32250-1 (eBook)
https://doi.org/10.1007/978-3-031-32250-1

This Springer imprint is published by the registered company Springer Nature Switzerland AG
The registered company address is: Gewerbestrasse 11, 6330 Cham, Switzerland

Preface

The activation of small molecules generally occurs more efficiently on dinuclear frameworks than on mononuclear species, especially in the context of catalysis in which it is necessary to combine high reactivity, chemoselectivity, regioselectivity, and long-lived activity. More than 85% of the products elaborated in the chemical industry are using a catalyst. Numerous compounds or intermediates for the efficient production of derivatives of petrochemicals, intermediates, and fine chemicals such as pharmaceuticals use catalysis. At the present time, alternative feedstocks, such as biomass and renewables, to crude oil and natural gas, are being investigated, and selective catalysis is more and more necessary. Moreover, a broad effort aims at using abundant metals to obtain large performances, including their efficient recycling. Particularly important is the use of iron, cobalt, and nickel compounds.

Transition metal complexes, which contain appropriate ligands to adjust their electronic and steric effects, when coordinated to a metal center, have been synthesized to have the coordination sphere with the flexibility to obtain the various steps of the catalytic cycle and to obtain powerful performances [1]. Moreover, the reactivity can be tuned by the introduction of two metals in a close vicinity in order to exalt their catalytic activity. Various homo- and hetero-dinuclear complexes have been shown to maintain a higher catalytic activity than the mononuclear counterparts, their dinuclear framework being preserved along the full catalytic cycle [2]. Selectivity [3] and cooperative effects [4] have recently been reviewed. Moreover, bio-inspired chemistry has allowed the synthesis of thiolato-bridged homo- (Fe, Co, Mn, or Cu) and hetero-dinuclear complexes that are active in oxygen reduction or hydrogen evolution reactions [5].

The present volume is dedicated to the available concepts that govern the modes of cooperative effects in dinuclear complexes. Much work is still necessary to anticipate how to build the right catalytic cycle that is efficient for all steps occurring along the transformation of the substrates into the expected product(s). In situ spectroscopic characterization and kinetic studies as well as theoretical calculations allow ascertaining that the catalytic cycle involves dinuclear species in all steps.

The first contribution from Zoraida Freixa, Piet van Leeuwen, and Philippe Kalck, entitled "Reactivity on one metal center exalted by the second one" analyzes the three elementary steps of oxidative addition, migratory insertion, and reductive elimination in light of the cooperative effect induced by the second metal center exalting the reactivity of the first one. The nature of the bridging ligands holding together both metals and their electronic and steric properties governs the cooperative effect. There are various ways by which one metal can influence the reactivity of the second neighboring metal, both in stoichiometric and catalytic reactions. For instance, in the following example, not only the oxidative addition of H_2 occurs on one metal center, but also one hydride stays in a bridging position along intermediate steps to increase the communication before the last reductive elimination step.

The second chapter entitled "Chemical Transformations in Heterobimetallic Complexes Facilitated by the Second Coordination Sphere" is from R. Malcolm Charles III and Timothy P. Brewster.

Complexes in which the second metal center is close to the first one and resides in its second coordination sphere could enable bond activation processes, due to the synergistic activity with the first metal, a situation that could be not available when the complexes are monometallic. The spatial proximity between the two metal centers as well as the electronic global response can allow for modification and tuning of reactivity, so that switchable catalytic systems (redox-switchable and cation-responsive systems) can be developed. For instance, the ferrocene-aluminum complex in its reduced state $[Fe\text{-}Al]^{red}$ catalyzes the ring-opening polymerization of 1,3-trimethylene carbonate, β-butyrolactone, whereas the oxidized form $[Fe\text{-}Al]^{ox}$ is inactive.

The third chapter "Role of a Redox-Active Ligand Close to a Dinuclear Activating Framework" by Catherine Elleouet, François Y. Pétillon, and Philippe Schollhammer is dedicated to the development of bio-inspired di-iron and di-nickel complexes, and similar species, containing a redox-active ligand in their coordination sphere.

The structural characterization of the active sites of [FeFe]- and [NiFe]-hydrogenases and the search for understanding how they are operating have stimulated the development of novel bio-inspired di-iron (and nickel-iron) compounds with a redox ligand in the coordination sphere of the bimetallic site. It is possible to obtain a well-adjusted electronic balance between the dinuclear framework and the redox ligand, allowing a catalytic activity.

For instance, the complex $[Fe_2(CO)_3(\kappa^1\text{-Fc}')(\kappa^2\text{-dppv})(\mu\text{-adt}^{Bn})]$ (Fc′ = $[Fe(\eta^5\text{-}C_5Me_5)\{\eta^5\text{-}C_5Me_4(CH_2PEt_2)\}]$ and $adt^{Bn} = (SCH_2)_2NCH_2C_6H_5$) is a rare example in which arises an intramolecular electron transfer between the di-iron center and a ferrocenyl-phosphine. Here, the electroactive Fc′ ligand in the coordination sphere of the azadithiolato di-iron complex operates as an electron reservoir, allowing bidirectional H^+/H_2 catalysis. The oxidation of this dinuclear complex by $[H(OEt_2)_2](BAr^F{}_4)$ leads to the dicationic species in which the $\{Fe^{II}Fe^{I}\}$ core exhibits an inverted conformation while the iron atom of the Fc′ ligand is in the oxidation state III. The coordination of H_2 to the dicationic species induces an intramolecular

electron transfer from the di-iron platform to the oxidized ferrocenyl group and leads to the heterolytic cleavage of H_2.

In the fourth chapter, Laurent Maron and Philippe Kalck analyze the "Dinuclear reactivity between the two metal centers." In addition to complexes where only the substrate is coordinated to the two metal centers in a bridging position or bridging ligands maintain the two metal centers in close vicinity, but have no significant role as redox systems, sophisticated ligands, having multi-coordination sites, can be synthesized to maintain the right distance between the two metal centers, with sometimes some structural flexibility. In the $1e^-$-$1e^-$activation of the substrate on the two metals, these centers present somewhat the same oxidation state, whereas along the various catalytic activation steps the redox characteristics of these ligands play a pro-active role. Most of the time these ligands contain nitrogen coordination centers and unsaturated systems, and their reactivity is more deeply understood, due to mechanistic and DFT theoretical studies. For the redox-active ligands, it is possible to obtain active catalytic systems involving metals from the first line, particularly nickel, iron, and cobalt.

Interestingly, as an example, the dicopper(I) complex, containing the diimine-1,8-naphthyridine expanded pincer ligand, reacts with dioxygen and KOH at 60°C in toluene to generate the (μ-η^2:η^2-peroxo)dicopper(II) active species, that coordinates the alcohol, and catalyzes the formation of an aldehyde which reacts with primary amines to prepare imines.

In the fifth and last chapter, Rémi Maurice, Talal Mallah, and Nathalie Guihéry present a theoretical study entitled "Magnetism in Binuclear Compounds: Theoretical Insights."

This contribution is devoted to theoretical calculations for determining the electronic structure of binuclear complexes, including isotropic and anisotropic interactions both in the strong and in the weak exchange coupling limits. Use of the theory of effective Hamiltonians is performed to extract the magnetic anisotropy terms in various regimes and in particular, those for which the giant spin approximation holds. While only a second rank symmetric tensor is necessary to describe the zero-field splitting in centrosymmetric compounds with a single electron on each metal ion, a 4-rank tensor is necessary to describe the anisotropic exchange in the case of two unpaired electrons per metal ion.

This volume would be helpful to academic and industrial researchers who are involved in the field of highly efficient syntheses in organic chemistry in order to use performant catalysts in the context of the sustainable development for using novel substrates and more abundant metals than noble metals that opened the way to the present highly performing catalysis.

As Editor of this volume, I have the pleasure to thank all the contributors for their enthusiastic participation in this synthetic view of bimetallic catalysis. I would like also to offer my warm thanks to the Springer team for their continuous support, their patience, and their efficiency.

Toulouse, France Philippe Kalck

References

1. Cornils B, Hermann WA, Beller M, Paciello R (2018) Applied homogeneous catalysis with organometallic compounds: a comprehensive handbook in four volumes, 3rd edn. Wiley-VCH Verlag GmbH & Co. KGaA
2. Kalck P (2016) Homo- and heterobimetallic complexes in catalysis. Top Organomet Chem 59
3. Mankad NP (2016) Selectivity effects in bimetallic catalysis. Chem Eur J 22:5822–5829
4. Maity R, Birenheide BS, Breher F, Sarkar B (2021) Cooperative effects in multimetallic complexes applied in catalysis. ChemCatChem 13:2337–2370
5. Gennari M, Duboc C (2020) Bio-inspired, multifunctional metal−thiolate motif: From electron transfer to sulfur reactivity and small-molecule activation. Acc Chem Res 53:2753–2761

Contents

Top Organomet Chem (2023) 70: 1–66
https://doi.org/10.1007/3418_2022_80

Published online: 30 January 2023

Dinuclear Reactivity of One Metal Exalted by the Second One

Zoraida Freixa, Piet W. N. M. van Leeuwen, and Philippe Kalck

Contents

Z. Freixa
Department of Applied Chemistry, Faculty of Chemistry, University of the Basque Country (UPV/EHU), San Sebastián, Spain

IKERBASQUE, Basque Foundation for Science, Bilbao, Spain
e-mail: zoraida_freixa@ehu.eus

P. W. N. M. van Leeuwen
Emeritus Chair Holder IDEX Chaire d'Attractivité de l'Université Fédérale Toulouse Midi-Pyrénées, Laboratoire de Physique et Chimie de Nano-Objets, INSA, Toulouse, France
e-mail: vanleeuw@insa-toulouse.fr

P. Kalck (✉)
Laboratoire de Chimie de Coordination du CNRS, Equipe C "Catalyse et Chimie Fine," composante de l'Ecole Nationale Supérieure des Ingénieurs en Arts Chimiques et Technologiques – INP Toulouse, Toulouse, Cedex 4, France
e-mail: philippe.kalck@ensiacet.fr

Abstract This chapter is devoted to the coordination sphere of the two metals of a dinuclear framework for which the reactivity of one metal center is exalted by the second one. Kinetic studies and theoretical calculations are efficient tools nowadays to ascertain that along the catalytic cycle, bimetallic species are operating in the various steps converting the substrate. Bimetallic coordination complexes are described, in which the nature of the bridging ligand plays an essential role, as their mutual steric and electronic influences are determined by the distance and orientation of the two metal centers. By many ways, one metal can influence the reactivity of a neighboring metal both in stoichiometric and catalytic reactions. The three elementary steps of oxidative addition, migratory insertion, and reductive elimination are analyzed in the light of the cooperative effect induced by the second metal center exalting the reactivity. The electronic effects played by the ligands of the coordination sphere appear essential, but in some examples, steric effects add a supplementary influence, which may result in an increased selectivity. The tug-in effect of one metal on the other one, especially in heterodinuclear species, can allow tuning the reactivity through an appropriate adjustment of the distance between the two metal centers and a Lewis acid functionality. These concepts can be extended to dinuclear species bonded to a surface. Of course, much progress is still necessary to anticipate the right way to design the multidentate ligands, which scaffold a dinuclear entity for a given stoichiometric or catalytic reaction.

Keywords Cooperative effect · Dinuclear complexes · Electronic and steric effects of the coordination sphere · Migratory insertion · Oxidative addition · Reactivity of a single metal center · Reductive elimination · Synergistic effect

1 Introduction

In coordination chemistry, the elementary reactions occurring either in stoichiometric reactions or in catalysis involve most of the time mononuclear complexes. Reactions involving dinuclear species have also been known since long ago. In the context of this book, essentially dedicated to the concepts which govern the cooperative effect in dinuclear complexes, this chapter is focused on the enhanced reactivity that occurs for a two-electron elementary step. Such reactions can operate on one metal center, the reactivity of which being influenced by the second metal center, either through electronic effects or due to the steric hindrance of its

coordination sphere. Keeping steric effects aside, we will mainly focus on the reactivity of the first metal center in reactions in which a two-electron process occurs, i.e. oxidative addition, migratory insertion, and reductive elimination. As we will see, electronic effects mainly influence reactivity, while steric effects play a major role in determining the selectivity of the reaction. When possible, comparison with mononuclear species will be made to show that the cooperative effect initiates the reactivity or significantly increases it. Recent theoretical calculations help us to specify how the synergy occurs between the two metal centers. On several occasions, further reactivity on the second metal center can be established. These calculations and kinetic studies sometimes allow us to show that the reactivity occurs on a monometallic species and that the bimetallic complexes present at the beginning and the end of the reaction should be considered as sleeping species. Even though it is difficult to give all the rules to build the appropriate coordination sphere around a bimetallic complex, to choose the nature of the two metals, and to obtain the expected reactivity, some salient features emerge from the present analysis. Several reviews that touch upon the present theme have been published recently [1–7].

2 Mechanisms in Which Only One Metal Center Undergoes Oxidative Addition Reaction

2.1 Two Electrons Oxidative Addition on One Metal Center

2.1.1 Direct 2 Electrons Oxidative Addition on M'

Recent DFT calculations performed on the oxidative addition of iodomethane on a dinuclear platinum(II) complex show clearly that the first CH_3I reaction is faster than the second one [8].

This process involves an S_N2 attack of an electron-rich platinum metal center to the methyl group of CH_3I with an energy barrier of 30.0 kJ mol^{-1} (Schemes 1 and 2). The cleavage of the Me-I bond in the transition state followed by the coordination of the methyl ligand to platinum(IV) provides the first cationic intermediate. Coordination of the I^- ligand gives rise to the Pt(IV)-Pt(II) complex; it reacts in a second step more slowly with a second molecule of CH_3I, with an energy barrier of 31.9 kJ mol^{-1} mainly because an electronic effect occurs from Pt(II) to Pt

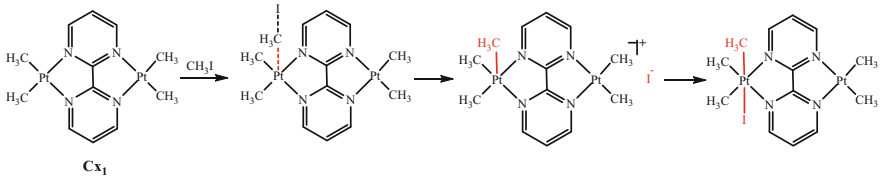

Scheme 1 Oxidative addition of CH_3I on a single platinum metal atom through an S_N2 mechanism

Scheme 2 First S_N2 oxidative addition with attack of one Pt(II) center of the $[Pt_2(\mu\text{-}\mathbf{L_1})Me_4]$ $\mathbf{Cx_1}$ complex to the carbon atom of CH_3I [9]

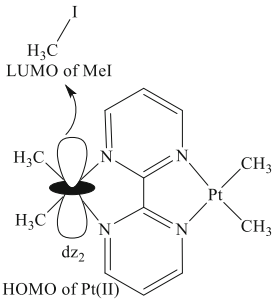

Fig. 1 Proposed initiation of the second oxidative addition

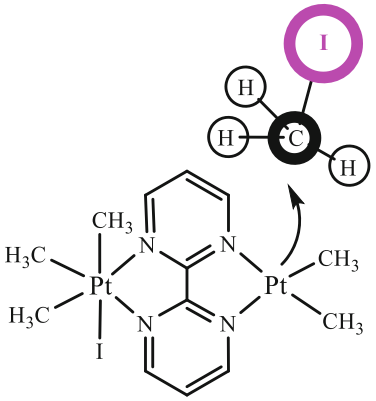

(IV) through the bridging 2,2′-bipyrimidine ligand $\mathbf{L_1}$, reducing the nucleophilicity of the Pt(II) center. The free energy barrier to form the Pt(IV)-Pt(IV) complex from the Pt(IV)-Pt(II) intermediate is $\Delta G^{\ddagger} = 75.1$ kJ mol^{-1}, whereas that for the first oxidative addition is 74.5 kJ mol^{-1} consistent with the first kinetic measurements performed in acetone at 25°C providing a k_2 second-order rate constant of 9.7 L mol^{-1} s^{-1} for the first step and 1.4 for the second one, so that the Pt(II)-Pt(II) $\mathbf{Cx_1}$ complex reacts with CH_3I about 7 times as fast as the Pt(IV)-Pt(II) intermediate, as initially observed [9]. The DFT calculations show clearly that the two HOMO highest occupied molecular orbitals in the starting complex are mainly located on the two Pt(II) centers, whereas the LUMO lowest unoccupied molecular orbital is essentially localized on the $\mathbf{L_1}$ bridging ligand. In the Pt(II)-Pt(IV) intermediate the LUMO is still centered on the $\mathbf{L_1}$ ligand, but the dz^2 orbital of the Pt(II) center is the main component of the HOMO-1, the two HOMOs being located on the iodide ligand of the Pt(IV) center (Fig. 1) [8]. Thus, the second S_N2 type oxidative addition reaction proceeds through the removal of electron density from the HOMO of the Pt(II) center into the LUMO of CH_3I to form the Pt(IV) complex.

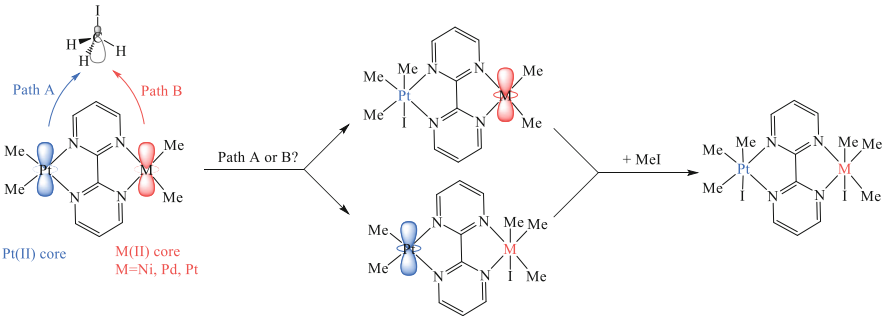

Scheme 3 Oxidative addition of MeI to heterobimetallic complexes $\mathbf{C_{x1}}$, [15]

These DFT calculations are consistent with the kinetic measurements and observations made on platinum dimers bridged by diimine ligands [9], bis (diphenylphosphino)ferrocene [10, 11], two phosphorus atoms of bis (2-(diphenylphosphino)ethyl)phenylphosphine [12], bis(diphenylphosphino)-acetylene [13], or even a rollover bipyridine [14]. For the diimine ligands the authors concluded that steric effects should also be included [2].

In a subsequent DFT study, Hosseini et al. replaced one of the Pt atoms in the bypim complexes $\mathbf{C_{x1}}$ by Ni or Pd (Scheme 3) [15]. It was found that in the Pt(II)-Ni (II) as well as in the Pd(II) analogs ($\mathbf{C_{x1}}$,) the first oxidative addition takes place at the Pt center and thus of the three Group 14 metals Pt(II) is the most nucleophilic one in the bypim complexes. The order of reactivity for the first step, addition to Pt, is Ni > Pd > Pt, while for the second CH_3I addition the order is reversed.

Interestingly, in a complex containing the two bis(diphenylphosphino)methane and phthalazine bridging ligands, one Pt(II) atom is coordinated by two methyl ligands, whereas the second one is part of platina(II)cyclopentane ring providing to it a higher electron density and inducing the first oxidative addition reaction [16]. In the second oxidative addition process cationic diplatinum(IV) forms with one iodide in bridging position.

The oxidative addition of methyl halides to the dinuclear $[Rh_2(\mu\text{-}Cl)_2(CO)_2(PR_3)_2]$ $\mathbf{Cx_2}$ complexes occurs on the two metal centers and results in the formation of the $[Rh_2(CH_3)_2X_2(\mu\text{-}Cl)_2(CO)_2(PR_3)_2]$ $\mathbf{Cx_3}$ complexes. For CH_3I, a further migratory insertion of the methyl group occurs giving rise to the bis-acetyl $[Rh_2(C(O)CH_3)_2I_2(\mu\text{-}Cl)_2(solv)_2(PR_3)_2]$ $\mathbf{Cx_4}$ complexes in equilibrium with the previous ones. Under a CO atmosphere the $[Rh_2(COCH_3)_2I_2(\mu\text{-}Cl)_2(CO)_2(PR_3)_2]$ $\mathbf{Cx_5}$ complexes are formed, which can eliminate acetyl chloride by a reductive elimination process (Scheme 4) [17–19].

On the contrary, the addition of one equivalent of CH_3Br or CH_3I to the μ-thiolato Rh(I) dinuclear $[Rh_2(\mu\text{-}StBu)_2(CO)_2(PMe_2Ph)_2]$ $\mathbf{Cx_6}$ complex leads to the Rh(I)-Rh (III) $[(PMe_2Ph)(COCH_3)(I)Rh(\mu\text{-}StBu)_2Rh(CO)(PMe_2Ph)]$ $\mathbf{Cx_7}$ complex in which only one metal center has reacted (Scheme 5) [19, 20]

The addition of a second equivalent of reactant leads to complex mixtures of products. However, reacting powder of $\mathbf{Cx_6}$ with vapor of CH_3Br led to the Rh(III)-

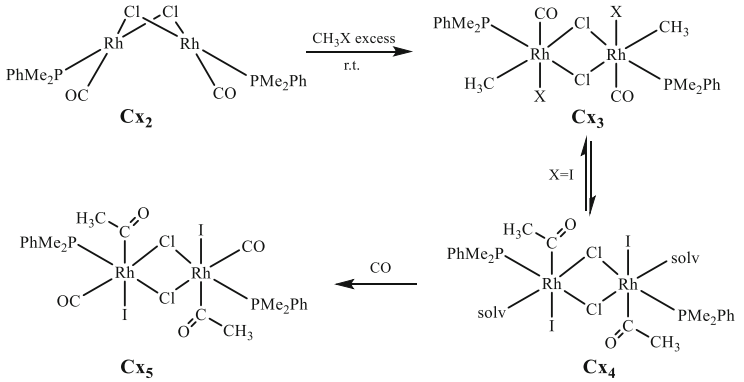

Scheme 4 Oxidative addition of CH_3Cl, CH_3Br, and CH_3I on $\mathbf{Cx_2}$ (for CH_3Br, Cl, and Br atoms statistically occupy the terminal and bridging positions) [17–19]

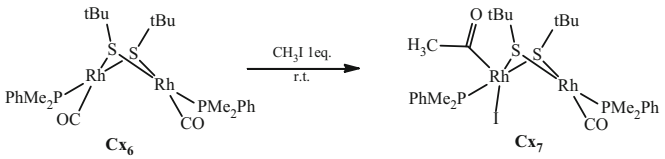

Scheme 5 Oxidative addition of CH_3I on one rhodium center of $\mathbf{Cx_6}$ providing the Rh(III)-Rh(I) $\mathbf{Cx_7}$ complex

Rh(III) complex having one acetyl ligand on one metal center and a methyl group on the other one [20]. Direct metal–metal interaction should be weak since in the Rh(I)-Rh(I) $\mathbf{Cx_6}$ complex, the distance between the two rhodium centers is 3.061(1) Å [21] and in the Rh(I)-Rh(III) acetyl $\mathbf{Cx_7}$ complex of 3.110(1) Å [20]. Presumably the $Rh_2(\mu\text{-StBu})_2$ core is electron rich, since the methyl group is sufficiently nucleophilic to attack the CO ligand; on the remaining Rh(I) center, the increase of 25 cm^{-1} in the ν_{CO} stretching frequency is consistent with a significant decrease in the electron density.

In a similar way, the $[Rh_2(\mu\text{-}1,8\text{-}(NH)_2napht)(CO)_2(PR_3)_2]$ $\mathbf{Cx_8}$ complexes that contain the flexible $\mathbf{L_2}$ 1,8-diamidonaphthalene bridging ligand, and tris(isopropyl)-, triphenyl-, or tris(*p*-tolyl)phosphine, react at room temperature with one equivalent of CH_3I to give the Rh(I)-Rh(III) acetyl $\mathbf{Cx_9}$ complexes of general formula $[(PR_3)(COCH_3)(I)Rh(\mu\text{-}\mathbf{L_2})Rh(CO)(PR_3)]$, with the ν_{CO} stretching frequency having a roughly 25 cm^{-1} higher value than the average of the two terminal CO infrared bands in $\mathbf{Cx_8}$ [22]. These complexes do not undergo the oxidative addition of a second molecule of CH_3I on the Rh(I) center under ambient conditions. Reaction of a 10-fold excess at 70°C results in the decomposition of the $P(i\text{Pr})_3$ and PPh_3 complexes, but allows to obtain in modest yield the Rh(III)-Rh(III) $[(PR_3)(COCH_3)(I)Rh(\mu\text{-}\ \mathbf{L_2})Rh(I)(COCH_3)(CO)(PR_3)]$ $\mathbf{Cx_{10}}$ complex for R = *p*-tolyl (Scheme 6).

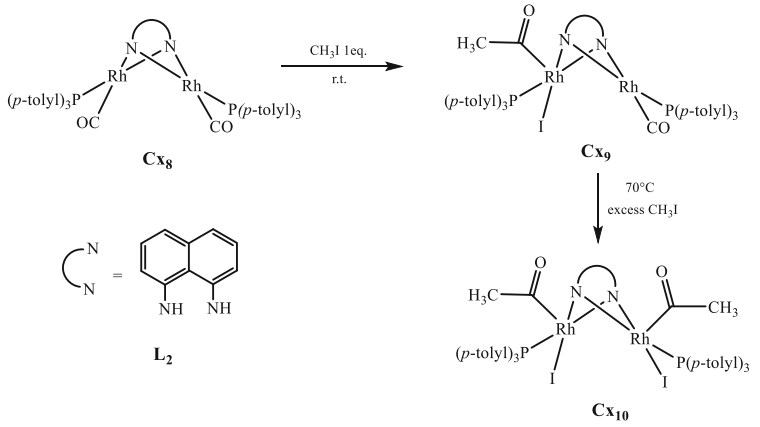

Scheme 6 Reaction at room temperature of complex $\mathbf{Cx_8}$ (R = *p*-tolyl) with 1 equivalent of CH_3I and then at 70°C with a 10-fold excess

Presumably, there is a competition between the migratory insertion of the methyl group and a second oxidative addition on the second metal center according to the electron density on the Rh(I) center of the Rh(I)-Rh(III) species and also the steric hindrance of the ligands. Using diphosphine ligands that present the property to exclusively coordinate the metal in the two *trans*-positions, it has been shown that, contrary to the mononuclear complex, the di(μ-chloro)dirhodium(I) dinuclear complex containing the *trans*-spanning diphosphine ligand SPANphos $\mathbf{L_3}$ is able to activate CH_3I (Scheme 7) [23].

Various diphosphine ligands, of which three representative examples are shown on Scheme 7, have been designed and synthesized to provide exclusively bimetallic complexes. Their addition to $[Rh_2(\mu\text{-}Cl)_2(CO)_4]$ in a P/Rh ratio of 1/1 leads to the *syn* dimers [24]. In highly diluted conditions (MeOH/MeI/H_2O/Rh = 9,670/1,000/6,820/2 mol), in order to avoid any medium effect on the activity caused by phosphine quaternization, these complexes show a high activity in the low CO pressure methanol carbonylation, since the turnover frequencies can reach 980 h^{-1} and the turnover number 1470 for a reaction performed at 150°C, 22 bar of CO (at 22°C) and for 1.5 h with the two ligands built on the benzofurobenzo-furan-based backbone and dibenzodioxocin skeletons [24]. With the SPANphos $\mathbf{L_3}$ ligand, the performances are slightly more modest since the TOF is 592 h^{-1} and the TON 888 cycles.

DFT theoretical calculations show that the activation barrier for the reaction of CH_3I with the model $[Rh_2(\mu\text{-}Cl)_2(CO)_2(PMe_3)_2]$ complex is 5.5 kcal mol^{-1} or 5.9 for $[Rh_2(\mu\text{-}Cl)_2(CO)_2(PH_3)_2]$, whereas it is 6.8 for the mononuclear *trans*-[RhI(CO)$(PH_3)_2$] complex (Fig. 2). The approach of CH_3I to one Rh center of the dinuclear species adopts an S_N2-like transition state [25].

Reaction of the 2-([2-(diphenylphosphino)benzoyl]phenylamino)ethyl-2-(diphenylphosphino)benzoate diphosphine ligand $\mathbf{L_4}$ (ligand represented in

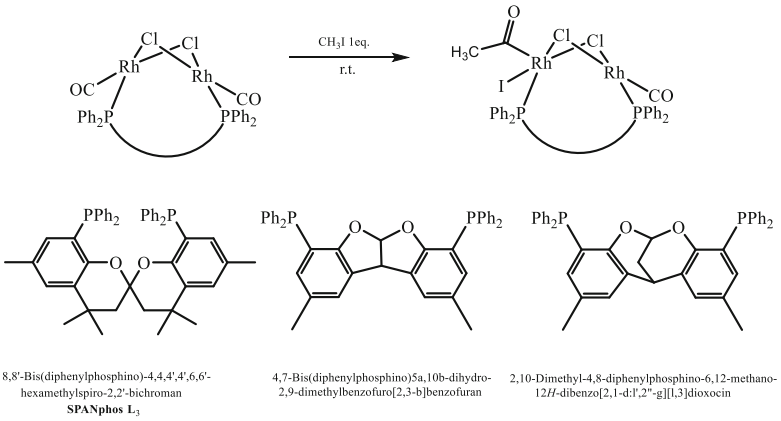

$$CH_3OH + CO \xrightarrow[1.5\ h]{32\ bar,\ 150°C} CH_3COOH$$

TOF (h^{-1}) =	592	980	979
Turnover number	888	1470	1468

Scheme 7 Reaction of CH_3I on one Rh metal center in a dinuclear complex bridged by a diphosphine ligand and reactivity of three ligands in the carbonylation of methanol

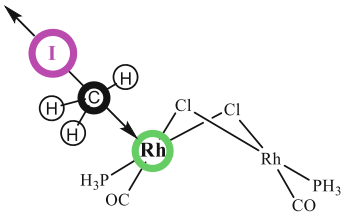

Fig. 2 Approach of CH_3I in the axial position of the square-planar "$Rh(Cl)_2(CO)(PH_3)$" entity

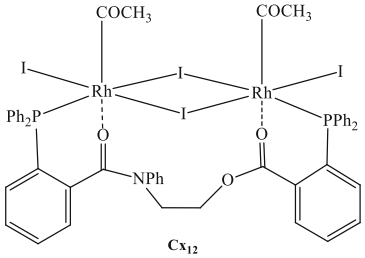

Scheme 8 Coordination of the $Ph_2PC_6H_4C(O)NPh(CH_2)_2OC(O)C_6H_4PPh_2$ **L4** diphosphine ligand to the dinuclear bis (acetyl)rhodium(III) complex, in an octahedral geometry; only the *syn*-**Cx12** isomer is represented

Scheme 8), with $[Rh_2(\mu\text{-}Cl)_2(CO)_4]$ in a P/Rh ratio of 2/1 leads to the mononuclear *trans*-[RhCl(CO)diphos] **Cx11** complex which is highly active in the methanol carbonylation into acetic acid since a TON of 803 is obtained in 15 min at 170°C and 22 bar [26]. Along the recycling of the catalyst, Thomas and Süß-Fink detected the dinuclear complexes *syn*- and *anti*-**Cx12** in the solution, and the X-ray crystal

structures show clearly an octahedral coordination geometry consistent with the interaction of the two oxygen atoms of the amino alcohol spacers with the rhodium centers, so that these dinuclear species are considered as the resting states of the mononuclear active species [26, 27]. Diphosphine ligands built on rigid spacers generate exclusively mononuclear entities with TON values close to 800, providing an indirect confirmation that the dinuclear complex remains outside the catalytic cycle, the cooperative effect between the metal centers playing no peculiar role in the CH_3I activation [28, 29].

2.1.2 Oxidative Addition on One Metal Center Followed by Migration to the Second Metal Center

The *racemic*-Et,Ph-P4 tetraphosphine **L_5** ligand coordinates two rhodium metal centers to produce the $[Rh_2(nbd)_2(rac\text{-}\mathbf{L_5})](BF_4)_2$ **Cx_{13}** dicationic complex, which is an active and regioselective bimetallic hydroformylation catalyst providing a high initial turnover of 20 min^{-1} and a high 28/1 linear/branched aldehyde regioselectivity [30]. The analogous complex containing the *meso*-**L_5** ligand is 22 times slower and provides more internal alkenes and alkanes. The CH_2 bridge between the P_2 and P_3 phosphorus atoms is essential for the cooperative effect exerted by one Rh metal center onto the second one, since when the bridge is a *p*-xylyldiyl or a 1,3-propanediyl group the catalytic activity is very low (Scheme 9).

The $[Rh_2(nbd)_2(rac\text{-}\mathbf{L_5})](BF_4)_2$ **Cx_{13}** precursor is transformed under 20 bar of CO pressure into $[Rh_2(CO)_4(rac\text{-}\mathbf{L_5})](BF_4)_2$ **Cx_{14}** (Scheme 10), which reacts with dihydrogen on one metal center to form the mixed Rh(I)-Rh(III) dicationic $[Rh(CO)_3(\mu\text{-}rac\text{-}\mathbf{L_5})Rh(H)_2(CO)]^{2+}$ **Cx_{15}** species, with a reorganization of the coordination sphere occurring into a new framework **Cx_{16}** with two phosphorus atoms moving from bridging into terminal positions and having one hydride/one CO or two hydride ligands in the bridging positions (shown in Scheme 10). Substitution of one terminal CO ligand with the alkene (**Cx_{17}**), followed by the migratory C=C double bond insertion into the $Rh_2(\mu\text{-}H)$ hydride (**Cx_{18}**), and then the migratory CO insertion, leads to the proposed acyl intermediate $[Rh(C(O)CH_2CH_2R)CO(\mu\text{-}H)(\mu\text{-}CO)(\mu\text{-}rac\text{-}\mathbf{L_5})Rh(CO)_2]^{2+}$ **Cx_{19}**. Reductive elimination of the aldehyde, using the

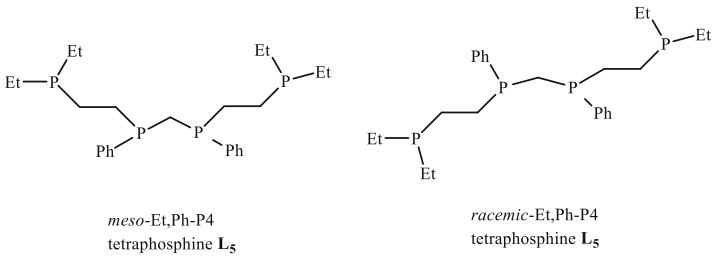

Scheme 9 The two diastereomeric binucleating tetraphosphine *meso*- and *racemic*-**L_5** ligands, $[(Et_2P_1CH_2CH_2)P_2(C_6H_5)CH_2P_3(C_6H_5)(CH_2CH_2P_4Et_2)]$

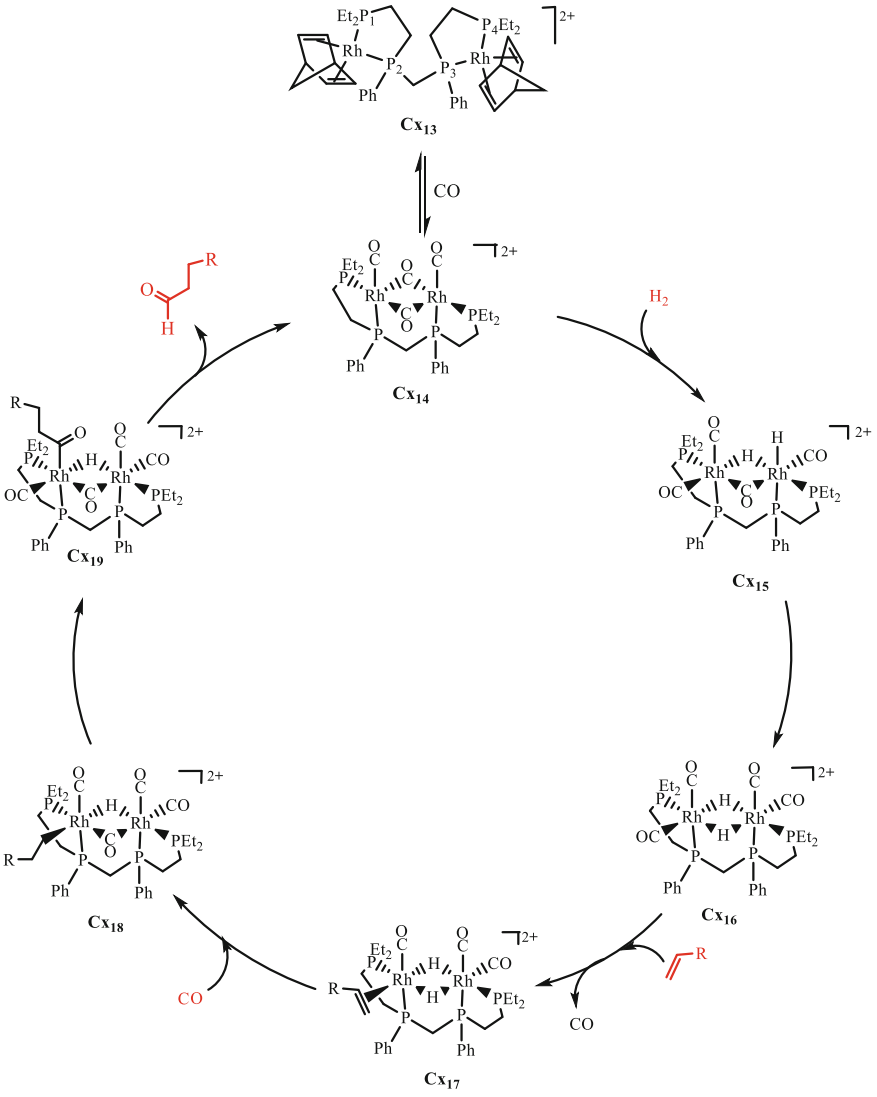

Scheme 10 Proposed intermediates for hydroformylation of the RCH=CH_2 alkene starting from the tetracarbonyl precursor **Cx$_{14}$**

bridging hydride and the acyl group from the Rh(III) metal center, restores the active $[Rh(CO)(\mu\text{-}rac\text{-}\mathbf{L_5})(\mu\text{-}CO)_2Rh(CO)]^{2+}$ Rh(I)-Rh(I) species **Cx$_{14}$**, which reacts with H_2 to form **Cx$_{15}$** (Scheme 10).

Interestingly, addition of 30% water to the acetone solvent results in an increase of the initial TOF from 20 to 73 min^{-1} and a higher heptanal l/b selectivity moving from 25/1 to 33/1 with only 2% by-products [30, 31]. The dicationic dihydride

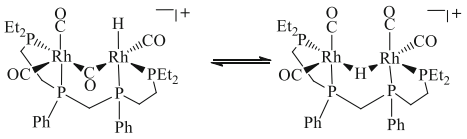

Scheme 11 Monocationic $[Rh_2(H)(CO)_4(\mu\text{-}rac\text{-}\mathbf{L_5})]^+$ $\mathbf{Cx_{20}}$ complexes with the Rh(I)(μ-CO)Rh(I) and Rh(I)(μ-H)Rh(I) isomers

catalyst deprotonates easily to generate a new monocationic monohydride dirhodium $[Rh(CO)_3(\mu\text{-}rac\text{-}\mathbf{L_5})Rh(H)(CO)]^+$ $\mathbf{Cx_{20}}$ species, which is still more active than the dicationic species $\mathbf{Cx_{14}}$. DFT analyses show two bimetallic complexes that possess either one CO or one hydride bridge, with the second complex being only 1.8 kcal higher in energy, and that significant electron density is present between the two metallic centers (Scheme 11).

Based on DFT calculations the bimetallic hydroformylation mechanism starts from the Rh(I)(μ-H)Rh(I) dinuclear $\mathbf{Cx_{20}}$ complex with substitution of a CO terminal ligand with the alkene followed by the hydride migration to give an alkyl complex and then an acyl complex on which the oxidative addition of H_2 provides a Rh(I)-Rh(III) intermediate. The reductive elimination of the aldehyde from the two acyl and hydride ligands requires a 21.6 kcal mol^{-1} activation energy and is the rate-determining step. It restores the active species with a terminal hydride ligand, which rapidly evolves to the Rh(I)(μ-H)Rh(I) dinuclear $\mathbf{Cx_{20}}$ complex (Scheme 11) [30, 31].

Nkajima, Tanase, et al. introduced tetraphosphine *meso*-$\mathbf{L_6}$ containing bridges different from those of Stanley's ligands $\mathbf{L_5}$ and the chemistry developed for Rh(I) is also different (Scheme 12). Complexes of several metals were studied, but here we are only concerned with those changing oxidation state, such as Rh(I). Reaction of $\mathbf{L_6}$ with $[Rh_2(\mu\text{-}Cl)_2(COD)_2]$ resulted in complex $\mathbf{Cx_{21}}$ that was found to reversibly react with dioxygen on one metal center [32]. The Rh−Rh distances (2.68 Å) in complexes of structure $\mathbf{Cx_{21}}$ suggest the presence of a bonding interaction between the two rhodium centers, which was confirmed as a Rh → Rh dative bond by DFT calculations [33]. Complex $\mathbf{Cx_{21}}$ underwent oxidative addition of one molecule of HCl, which took place at one of the Rh centers; the ratio of products $\mathbf{Cx_{22}}$ and $\mathbf{Cx_{23}}$ depends on the precise nature of the ligand and the bridging ligand. Both complexes are Rh(I)-Rh(III) complexes which can be further oxidized in the presence of air for which no exact mechanism was established.

The dirhodium complex $\mathbf{Cx_{24}}$, containing the sulfonamido-phosphoramidite ligand $\mathbf{L_7}$, is a hydrogenation catalyst as was reported by Reek et al. According to DFT calculations, the reaction takes place with the dimeric catalyst [34]. The Rh–Rh distance is 3.24 Å, and it was described as a weak metal–metal interaction. The catalyst hydrogenates methyl-2-acetamidoacrylate with a high rate and very high enantioselectivities (99% ee). The mechanism is presented in Scheme 13 for the hydrogenation of ethene. The active species is $\mathbf{Cx_{24}}$, which after dissociation of a weakly bound sulfonate group forms a complex with dihydrogen, $\mathbf{Cx_{25}}$. According to DFT calculations, the most stable complex after oxidative addition is the dihydride $\mathbf{Cx_{26}}$, with one terminal and one bridging hydride. The Rh–Rh distance

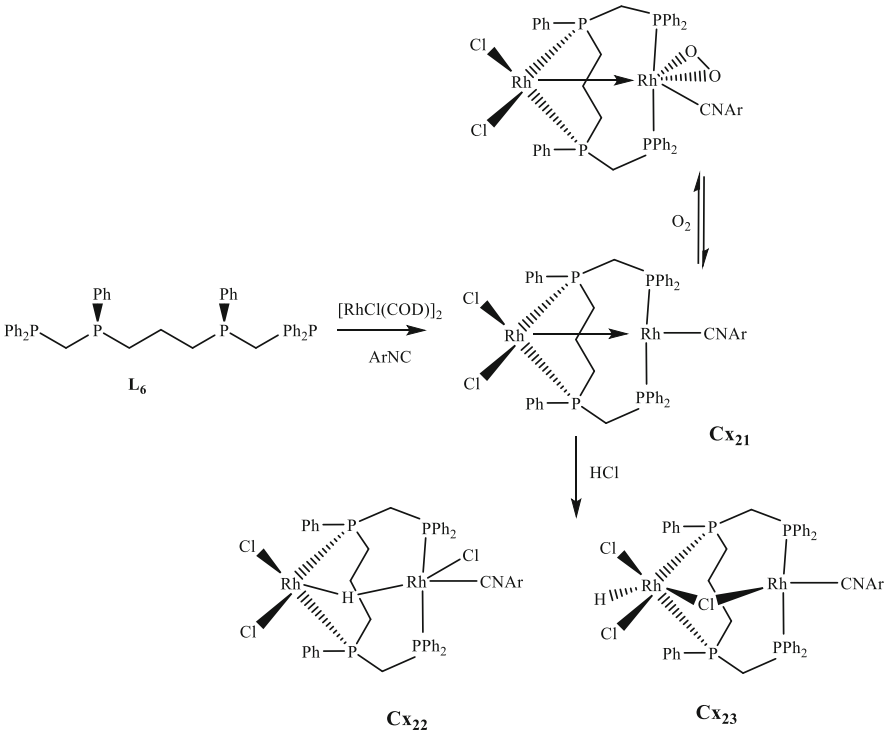

Scheme 12 Rh(I)-Rh(III) complexes of ligand $\mathbf{L_6}$ (Ar = xylyl)

is now slightly shorter at 3.16 Å, and the complex is best described as Rh(III)–Rh (I) with a dative bond between the two metals. The decoordination of the sulfonate leaves a vacancy for ethene coordination ($\mathbf{Cx_{27}}$) and the reaction is completed in the usual way, migratory insertion ($\mathbf{Cx_{28}}$) and reductive elimination from $\mathbf{Cx_{29}}$ to give again $\mathbf{Cx_{24}}$. In agreement with the experimental kinetic data the barriers for the steps were of the same order of magnitude. Recent NMR and DFT calculations show that the $Rh_2(\mathbf{L_7})_2$ framework of the norbornadiene precursor of $\mathbf{Cx_{24}}$ involves a strong N-Rh bond ($J^{103}Rh\text{-}^{15}N = 30$ Hz) in addition to the strong P-Rh bond ($J^{103}Rh\text{-}^{31}P = 261$ Hz) [35].

Early-late Transition Metal complexes have a long history in heterobimetallic complexes and catalysis, in particular for Zr, Rh, and sulfur ligands, but the mutual influence is usually weak [36]. We will make an exception for the reaction of the early–late heterobimetallic compound $[Cp^{tt}_2Zr(\mu_3\text{-}S)_2(\mu\text{-dppm})(Rh(CO))_2]$ ($\mathbf{Cx_{30}}$ in Scheme 14) [37]. Reaction with MeI affords the unusual oxidative addition product $[Cp^{tt}_2Zr(\mu_3\text{-}S)_2Rh_2(\mu\text{-CO})(\mu\text{-dppm})(I)(COCH_3)]$ ($\mathbf{Cx_{31}}$), showing the presence of a bridging carbonyl and a terminal acetyl ligand, in which notably the reactive centers are two Rh atoms and Zr is just part of the bridging ligand. The optimized structure

Scheme 13 Bimetallic Rh hydrogenation catalyst with the dirhodium complex **Cx$_{24}$**, containing the sulfonamido-phosphoramidite ligand **L$_7$**

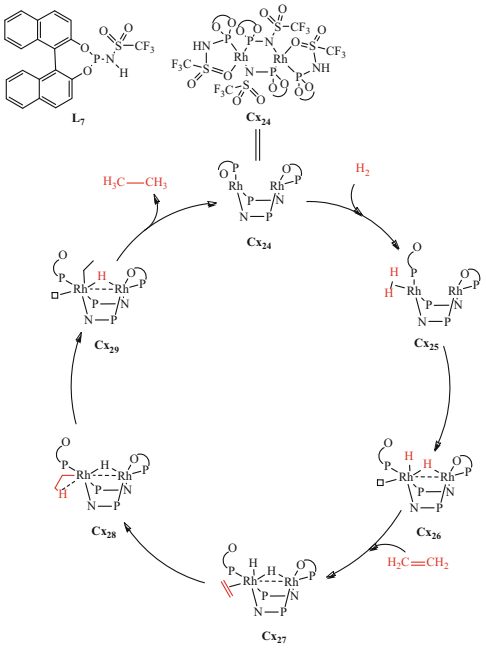

Scheme 14 Oxidative addition of MeI to the trinuclear ZrRh$_2$ complex **Cx$_{30}$** [37]

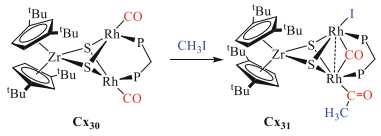

Scheme 15 The mechanism of imine hydrogenation by iridium dimers **Cx$_{32}$**

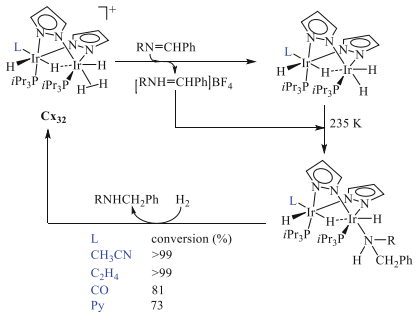

of **Cx$_{31}$** by DFT calculations is further substantiated by the spectroscopic data of the ^{13}CO-labeled complex.

Sola, Oro et al. reported on the bimetallic iridium complexes **Cx$_{32}$** bridged by pyrazolyl and hydride ligands which are active in the hydrogenation of alkenes, alkynes [38], and imines [39]. One metal center participates in the hydrogenation of imines and instead of an oxidative addition of H_2, a heterolytic transfer of a proton

and a hydride takes place, but the ligand on the second metal strongly influences the rate of reaction (Scheme 15).

2.1.3 Sequential Double Oxidative Addition

With organic *gem*-dichloro $CHRCl_2$ compounds, the oxidative addition reaction on the $[(COD)Rh((\mu\text{-}Pz)_2Rh(CNtBu)_2]$ **Cx$_{33}$** complex, in which the two Rh(I) metal centers are bridged by two pyrazolyl ligands and are coordinated to tBuNC isonitriles **L$_8$** and COD ligands, results in consecutive oxidative additions [40]. The reaction of $CHCl_2(CO_2Me)$ with the **Cx$_{33}$** complex results in one C–Cl oxidative addition on the more electron-rich metal center that contains the **L$_8$** ligands providing the Rh(I)-Rh(III) complex **Cx$_{34}$** (Scheme 16) which has been isolated and fully characterized. For R = CO_2Me the reaction stops here and no oxidative addition takes place at the Rh(COD) second center. However, further addition of **L$_8$** ligands that replace COD leads to reaction of the second C–Cl bond [41]. Due to the proximity of the C atom to the electron-rich Rh(I) center the second oxidative addition occurs and complex **Cx$_{34}$** produces immediately the Rh(III)-Rh(III) complex **Cx$_{35}$** containing the $CH(CO_2Me)$ bridge.

Complex **Cx$_{33}$** reacts with a monochloro alkyl substrate RCH_2Cl (R = Ph, $CH{=}CH_2$, CO_2Me) at the more nucleophilic rhodium atom bearing the two isocyanide ligands and leads to the $[(COD)Rh^{(I)}(\mu\text{-}Pz)_2Rh^{(III)}(Cl)(CH_2R)(CNtBu)_2]$ **Cx$_{36}$** complex for which the two conformers have the CH_2R group in *endo* and *exo* position, which interconvert at room temperature in benzene, whereas in $CDCl_3$ only the *endo* species is detected by NMR [42]. The reaction follows an S_N2 pathway, and provided it is performed in strict darkness, alkyl bromides lead to similar mixed-valence complexes. As for **Cx$_{34}$**, addition of two tBuNC ligands to **Cx$_{36}$** induces substitution of the cyclooctadiene ligand and the formation of a more nucleophilic $Rh^{(I)}$ center. In a similar S_N2 type reaction this metal center reacts with a second RCH_2Cl molecule so that the cationic $[(CNtBu)_2(CH_2R)$

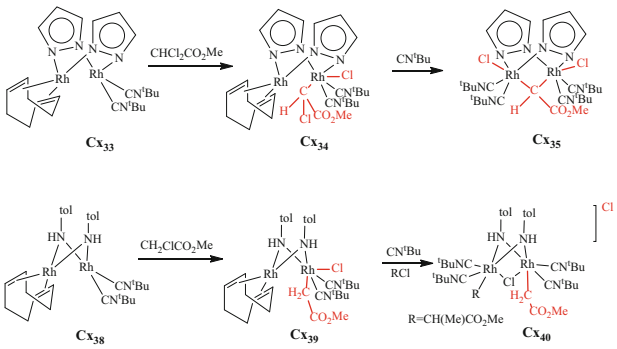

Scheme 16 Oxidative addition of $CHCl_2(CO_2Me)$ on a single metal center in the first step and activation for a second oxidative addition by isonitrile substitution of the cyclooctadiene [41]

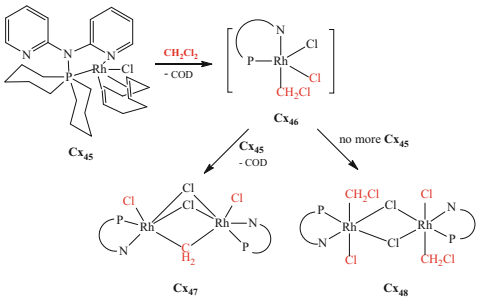

Scheme 17 Mechanism for the reactivity of CH_2Cl_2 with the $[Rh_2(\mu\text{-}Cl)_2(C_8H_{12})_2]$/**L9** system

$Rh^{(III)}(\mu\text{-}Pz)_2Rh^{(III)}(\mu\text{-}Cl)(CH_2R)(CNtBu)_2]^+[Cl]^-$ **Cx37** is formed with the first chloro ligand becoming in the bridging position due to the proximity of the two metal centers. Using a similar strategy, the complex [(COD)Rh(μ-NH(*p*-tolyl))$_2$Rh(CNtBu)$_2$] (**Cx38**) was reacted by Oro et al. [43] with $CH_2Cl(CO_2Me)$ to lead to the mixed-valence $[(COD)Rh^{(I)}(\mu\text{-}NH(p\text{-}tolyl))_2Rh^{(III)}(Cl)(CH_2CO_2Me)(CNtBu)_2]$ **Cx39** complex. After addition of two molar equivalents of tBuNC, and reaction with the chiral (−)-(*S*)-$ClCH(CH_3)(CO_2Me)$ alkyl chloride, the ionic $[(CNtBu)_2(\eta^1\text{-}CH_2CO_2Me)Rh^{(III)}(\mu\text{-}NH\{p\text{-tolyl}\})_2(\mu\text{-}Cl)Rh^{(III)}\{(R)\text{-}CH(CH_3)(CO_2Me)\}(CNtBu)_2]^+[Cl]^-$ **Cx40** is isolated (Scheme 16). The inversion of the configuration at the chiral carbon is consistent with an S_N2 type reaction for the second step.

When considering diphosphine complexes of the type $[Rh_2(\mu\text{-}Cl)_2(diphos)_2]$, the direct addition of two diphosphine ligands to the $[Rh_2(\mu\text{-}Cl)_2(diene)_2]$ complex under the catalytic conditions is not a reliable methodology. Indeed, as [(diene)Rh(μ-Cl)$_2$Rh(diphos)] and [Rh(diene)(diphosphine)]$^+$, [Rh(diphosphine)$_2$]$^+$ and [RhCl(diene)(diphosphine)] species could also be formed, depending on the ligand and reaction conditions, which hamper the direct interpretation of the observed activities as being due to the dimeric nature of the catalyst [44]. When the carbon-halogen bond is easy to cleave, the direct double oxidative addition on the two metal centers occurs as for the reaction of CH_2I_2 with $[Ir_2(\mu\text{-}tBuS)_2(CO)_2L_2]$ (L = CO, $P(OMe)_3$, PPh_3, PPh_2Me, and PMe_3) producing easily the $[Ir_2I_2(\mu\text{-}CH_2)(\mu\text{-}tBuS)_2(CO)_2L_2]$ **Cx41** Ir(III)-Ir(III) complexes [45]. When the two metal centers possess a high electron density, the CH_2Cl_2 double oxidative addition occurs to produce the $[Rh_2Cl_2(\mu\text{-}Cl)_2(\mu\text{-}CH_2)(diphosphine)_2]$ **Cx42** complexes [46, 47]. However, it is necessary to be very careful interpreting the double oxidative addition as resulting from a cooperative effect between the two metal centers. Indeed, when PEt_3 is added to $[Rh_2(\mu\text{-}Cl)_2(C_8H_{14})_4]$ the mononuclear $[RhCl(PEt_3)_3]$ complex is rapidly formed and reacts with the starting dinuclear cyclooctene complex to provide the expected $[Rh_2(\mu\text{-}Cl)_2(PEt_3)_4]$ **Cx43** complex in THF [48]. Furthermore, $[RhCl(PEt_3)_3]$ reacts slowly with CH_2Cl_2 at room temperature to provide the $[Rh_2Cl_2(\mu\text{-}Cl)_2(\mu\text{-}CH_2)(PEt_3)_4]$ **Cx44** complex. Reaction of the **L9** PN ligands (2-pyridyl)$_2$NPR$_2$ (Scheme 17), which contain the bulky isopropyl, tert-butyl, or cyclohexyl R substituents, with the cyclooctadiene $[Rh_2(\mu\text{-}Cl)_2(C_8H_{12})_2]$ precursor affords the mononuclear pentacoordinated [RhCl(PN)(COD)] complex **Cx45** [49]. This intermediate reacts in CH_2Cl_2 to give by loss of cyclooctadiene and oxidative addition the very reactive

Rh(III) **Cx$_{46}$** [$RhCl_2(CH_2Cl)(P\tilde{N})$] species, which immediately reacts with **Cx$_{45}$** to form the methylene-bridged dinuclear [$Rh_2Cl_2(\mu\text{-}Cl)_2(\mu\text{-}CH_2)(P\tilde{N})_2$] **Cx$_{47}$** complex (Scheme 17). At the end of the reaction, when all the **Cx$_{45}$** has been consumed, **Cx$_{46}$** dimerizes into the [$Rh_2Cl_2(\mu\text{-}Cl)_2(CH_2Cl)_2(P\tilde{N})_2$] **Cx$_{48}$** complex.

Analyzing the reactivity of the [$Rh_2(\mu\text{-}Cl)_2(diphos)_2$] complexes containing the **L$_{10}$** 1,2-bis(diphenylphosphino)ethane and **L$_{11}$** 1,3-bis(diphenylphosphino)propane ligands and the mixed species [(**L$_{10}$**)Rh(μ-Cl)$_2$Rh(**L$_{11}$**)], the kinetics of the reaction, and NMR spectroscopic evidences allowed Mannu, Heller et al. to propose that the intermediate is the highly reactive 14-electron [RhCl(diphos)] mononuclear species [50].

2.2 *Preliminary Coordination of a Part of the Substrate onto the Other Metal Center*

In many cases, the initial coordination of a C=C double bond on the M center providing a π-interaction assists the oxidative addition on M'.

For instance, the dinickel ($^{i\text{-}Pr}$NDI)$Ni_2(C_6H_6)$ **Cx$_{49}$** complex reacts with vinylcyclopropane with coordination of the C=C double bond and the approach of the C-C bond of the cyclopropane moiety on the second nickel center. The two nickel atoms, at a distance of 2.496(1)Å, are maintained in close proximity by the introduction of the **L$_{12}$** binucleating tetranitrogen containing ($^{i\text{-}Pr}$NDI) ligand, 1,1′--(1,8-Naphthyridine-2,7-diyl)bis(N-(2,6-diisopropylphenyl)ethan-1-imine [51]. The oxidative addition is barrierless after this approach and, with regard to the precursor, is exothermic by 17.2 kcal mol^{-1}, producing a dinickel metallacycle. The reductive elimination gives rise to cyclopentene [52]. The second nickel metal center allows the precoordination of the alkene as well as the stabilization of the allyl moiety (Scheme 18).

The same catalytic rearrangement occurs for 1-phenyl- and 1-hexyl-2-vinylcyclopropane leading to 3-phenyl- and 3-hexylcyclopentene with 93 and 92% yields, respectively. Similarly, catalytic rearrangement of cyclopropanes bearing heteroatom-containing substituents occurs on the **Cx$_{49}$** dinuclear entity, providing with high yields 1-(*N*-phenylimine)but-2-ene from *N*-phenylcyclopropylimine, crotonaldehyde from cyclopropylcarboxaldehyde, and 5-phenylpent-3-one from

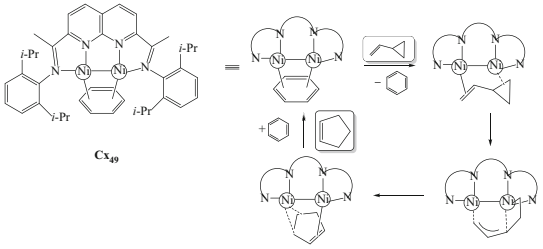

Scheme 18 Rearrangement of vinylcyclopropane into cyclopentene on a dinickel (I) framework, complex **Cx$_{49}$**

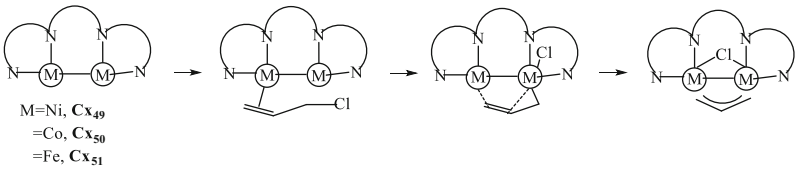

Scheme 19 Precoordination of the allylic C=C bond, and C–Cl oxidative addition on the second metal center of **Cx$_{49}$**, **Cx$_{50}$,** and **Cx$_{51}$**

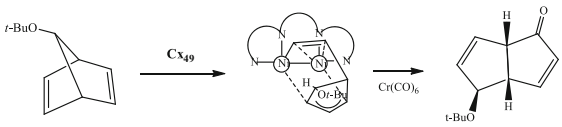

Scheme 20 Diastereoselective rearrangement of 7-substituted norbornadiene under a CO atmosphere, through **Cx$_{49}$**

1-phenylethylcyclopropan-1-ol [52]. Synthesis of the diamagnetic **Cx$_{50}$** [$Co_2(C_6H_6)$(**L$_{12}$**)] and paramagnetic **Cx$_{51}$** [$Fe_2(C_6H_6)$(**L$_{12}$**)] complexes has been performed by reacting Na_2[**L$_{12}$**] with $CoCl_2$ or $FeCl_2$ to produce the [M_2Cl_3(**L$_{12}$**)] complexes followed by their reduction with KC_8 [53]. The three **Cx$_{49}$**, **Cx$_{50}$**, and **Cx$_{51}$** dinuclear complexes react with allyl chloride, with a preliminary coordination of the C=C double bond on one metal center, which acts as an electron source and stabilizes the incoming substrate. The oxidative addition then occurs on the second metal center with an activation barrier of 4.1, 2.7, and 0.4 kcal mol^{-1} for Ni_2, Co_2, and Fe_2, respectively, generating the two M-allyl and M-Cl bonds. Then the two C_3H_5 and Cl ligands move into bridging positions (Scheme 19).

Through an analogous process, complex **Cx$_{49}$** can activate norbornadiene by coordination of a C=C double bond and a C-C oxidative addition. Further reaction with CO in such a way that the **L$_{12}$** ligand is not displaced, for instance by introducing small amounts of $Cr(CO)_6$ to provide CO, results in the formation of the [3.3.3] product. Starting with a substituent in the 7-position of norbornadiene produces a single diastereoisomer (Scheme 20) [54].

Complex **Cx$_{49}$** was used by Uyeda et al. for the addition of vinylidenes to alkenes to give methylenecyclopropanes via a catalytic reductive methylene cyclopropanation reaction of alkenes, utilizing 1,1-dichloroalkenes as vinylidene precursors [55]. The reaction proceeds via Ni_2(vinylidenoid) intermediates generated by C–Cl oxidative addition (Scheme 21).

Meyer and co-workers reported on various reactions of dinickel complexes with structure **Cx$_{52}$** based on a trianion pyrazolate-bis(β-diketiminato) ligand holding two $Ni^{(II)}H$ fragments together. The complex easily eliminates H_2 with the formation of a highly reactive $Ni^{(I)}$ dimer that reacts with various substrates in an asymmetric manner at the two metal centers or it undergoes intramolecular C–H oxidative addition involving the two metal centers. The latter is reversible, thus still allowing

Scheme 21 Methylene cyclopropanation with $\mathbf{Cx_{49}}$

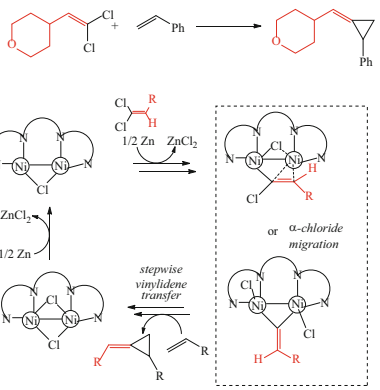

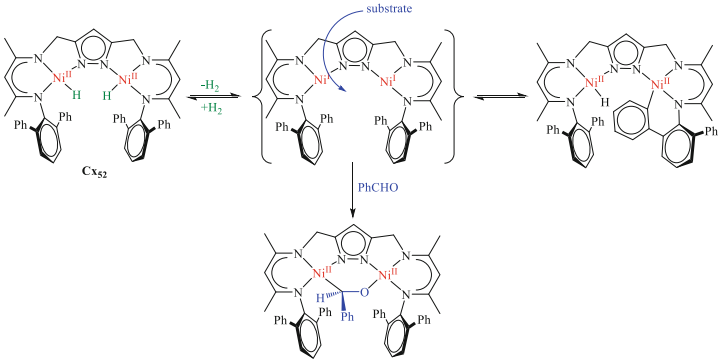

Scheme 22 Formation and reaction of $\mathbf{Cx_{52}}$

reaction with an intermolecular substrate. Scheme 22 shows benzaldehyde as a simple substrate oxidatively adding to the two $Ni^{(I)}$ ions [56].

3 Migratory Insertion on a Single Metal Center

3.1 Bimetallic Alkene Polymerization

3.1.1 Ti-Ti complexes

Bimetallic complexes have emerged as powerful polymerization catalysts, and metal–metal cooperative effects have been shown to affect polymer microstructure, as for instance shown for the enantioselective polymerization of propylene oxide in which the absolute stereochemistry of the binaphthol linker between two cobalt metal centers is crucial [57]. Significantly, bimetallic "constrained geometry catalysts" exhibit high activities and significant cooperative effects, affording

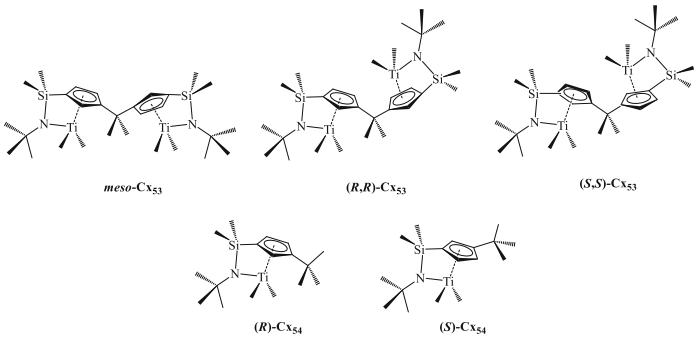

Scheme 23 $Ti(NMe_2)_2$ active centers for which the (μ-CMe_2-3,3′){(η^5-cyclopentadienyl)[1-Me_2Si(^{t}BuN] ligand bridges the two titanium centers **Cx$_{53}$**, or the [(3-*t*-Bu-C_5H_3)$SiMe_2$N-*t*-Bu] ligand completes the coordination sphere of the monometallic **Cx$_{54}$** ligand

macromolecular products with enhanced M_n and copolymerization properties [58–60]. In an approach reminiscent of that of Stanley in bimetallic Rh-catalyzed hydroformylation [30], Marks and co-workers studied the polymerization characteristics of the *rac* and *meso* dimeric compounds of the constraint geometry catalysts (CGC) *rac*-(μ-CMe_2-3,3′)((η^5-cyclopentadienyl)[1-Me_2Si(^{t}BuN][$Ti(NMe_2)_2$])$_2$ *rac*-**Cx$_{53}$** (either *rac*-(*R*,*R*) or *rac*-(*S*,*S*)) and *meso*-(μ-CMe_2-3,3′)((η^5-cyclopentadienyl)[1-Me_2Si(^{t}BuN][$Ti(NMe_2)_2$])$_2$ *meso*-**Cx$_{53}$** (Scheme 23) [61]. The two diastereomers of the complex diamido intermediates could be separated by crystallization, which were then converted to the methyl analogs by treatment with $AlMe_3$. Upon heating *rac*-**Cx$_{53}$** and *meso*-**Cx$_{53}$** release two molecules of methane and a doubly bridged methylene complex was obtained. Homopolymerization and copolymerization of ethene, propene, 1-octene, and styrene were performed in toluene at 25°C. The monometallic catalyst [(3-*t*-Bu-C_5H_3)$SiMe_2$N-*t*-Bu]$TiMe_2$ **Cx$_{54}$** (either (*R*) or (*S*)) was used as a control. It was demonstrated that *rac*-**Cx$_{53}$** and *meso*-**Cx$_{53}$** remain structurally intact during polymerization, consistent with the observed diastereoselectivity effects. On activation with 1 equivalent of $[Ph_3C][B(C_6F_5)_4]$ per Ti metal center, *rac*-**Cx$_{53}$** is far more active for ethylene homopolymerizations than *meso*-**Cx$_{53}$**. In contrast, the monometallic analog produces significantly more polymer than either of the binuclear catalysts. The relative activities were mono/*rac*/*meso* = 50:12:1. The same trend was found for propene and 1-octene. The second metal in these instances slows the catalysis. For ethene-styrene copolymerization the activity increased in the order *rac, meso*, and mono. Styrene incorporation for the three catalysts was, respectively, 63, 100, and 30%, i.e. *meso*-**Cx$_{53}$** give homopolymerization of styrene in the presence of ethene. Thus, there is a clear effect of both the neighboring metal centers and the configuration of the two metals.

In Scheme 24 it is shown that the second metal helps to direct the substituent of the alkene in order to obtain stereoselectivity. **Cx$_{54}$** gives lower tacticity as it lacks the bulky directing group, reminiscent of other mononuclear polymerization catalysts that also require a bulky group to direct the alkene and/or the polymer chain. In Table 1 only one set of examples is reproduced.

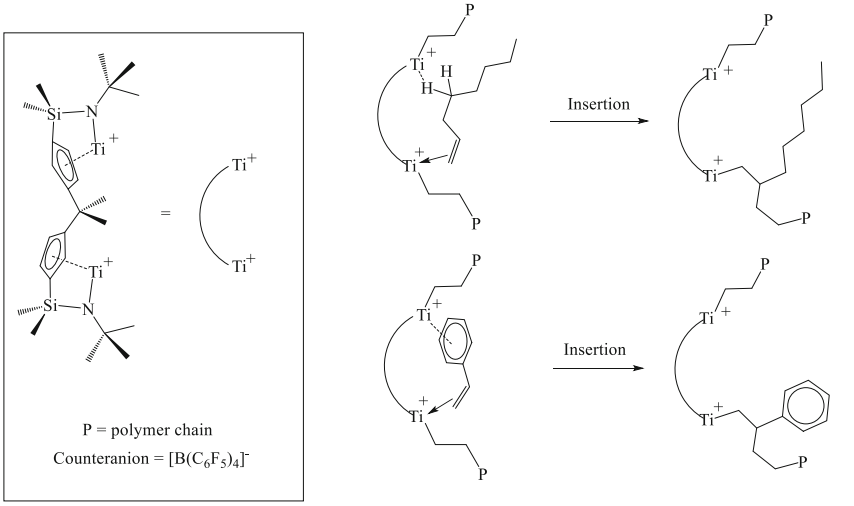

Scheme 24 A plausible mechanism for the influence of the second metal on the 1-octene and styrene polymerization

Table 1 1-Octene homopolymerization data[a] for catalysts **Cx$_{54}$**, *rac*-**Cx$_{53}$**, and *meso*-**Cx$_{53}$**

Entry	Cat.	Polymer (g)	Activity[b]	mmmm (%)[c]	M_n[d] (kg mol^{-1})	D[d]
1	**Cx$_{54}$**	1.43	5.95	36.2	14.2	1.9
2	*rac*-**Cx$_{53}$**	0.03	0.125	40.8	70.4	1.8
3	*meso*-**Cx$_{53}$**	0.02	0.083	91.7	26.1	1.1

[a] Polymerization conditions: [cat.] = 10 μmol of **Cx$_{54}$**, 5 μmol of *rac*-**Cx$_{53}$**, 5 μmol of *meso*-**Cx$_{53}$**; activator ratio of $B(C_6F_5)_3$ to Ti 1.2; 5.60 g of 1-octene for 24 h in 20 mL of toluene, at 25°C
[b] In units of kg of polymer (mol of Ti)$^{-1}$ h^{-1} atm^{-1}
[c] By ^{13}C NMR
[d] GPC vs polystyrene in units of kg mol^{-1}

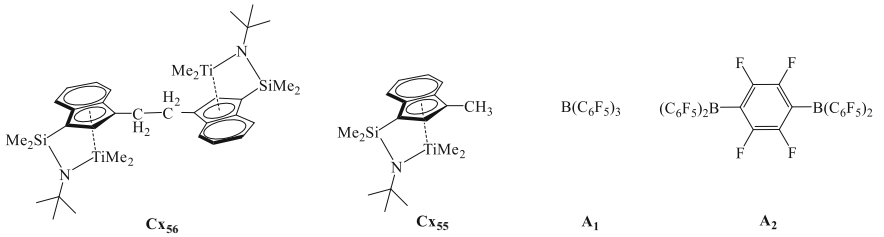

Scheme 25 Complexes **C$_{55}$** [1-Me_2Si(3-ethylindenyl)(*t*-BuN)]$TiMe_2$, **C$_{56}$** (μ-CH_2CH_2-3,3′)[1-(Me_2SiNH-*t*-Bu)indene][$TiMe_2$]$_2$ and activators **A$_1$** and **A$_2$**

Table 2 Styrene homopolymerization results[a]

Entry	Cat. + cocat.	Yield (g)	Act[b] ($\times 10^4$)	Tg[c] (°C)	Mw[d] ($\times 10^4$)	Mw/Mn[d]
1	$\mathbf{C_{55}}$ + $\mathbf{A_1}$	0.08	0.27	104.6	1.96	1.86
2	$\mathbf{C_{56}}$ + $\mathbf{A_1}$	3.13	10.43	96.4	1.04	1.55
3	$\mathbf{C_{55}}$ + $\mathbf{A_2}$	0.06	0.20	100.5	1.21	1.69
4	$\mathbf{C_{56}}$ + $\mathbf{A_2}$	3.36	11.20	89.2	0.80	1.47

[a] [Ti] = 10 μmol + [A] = 10 μmol, 5 mL of styrene +25 mL of toluene at 20°C, 3 h
[b] Units: g polymer/(mol Ti × h)
[c] DSC
[d] GPC relative to polystyrene standards

Scheme 26 Deactivation of complex $\mathbf{Cx_{55}}$ via intramolecular arene coordination, whereas the phenyl group coordinates the second titanium center in $\mathbf{Cx_{56}}$

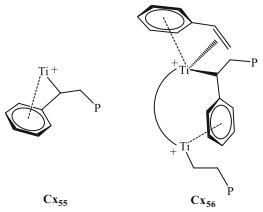

The mono $\mathbf{Cx_{55}}$ and bimetallic catalysts $\mathbf{Cx_{56}}$ in which the cyclopentadienyl moiety has been replaced with an indenyl entity (Scheme 25) were investigated with the monometallic and bimetallic activators $B(C_6F_5)_3$ $\mathbf{A_1}$ and 1,4-$C_6F_4[B(C_6F_5)_2]_2$ $\mathbf{A_2}$ [62]. Thus, four combinations of mono and bimetallics were evaluated in the polymerization and copolymerization of ethene and 1-octene. It was found that the catalyst derived from bimetallic $\mathbf{Cx_{56}}$ and bifunctional cocatalyst $\mathbf{A_2}$ enchains >11 times more 1-octene than that derived from mononuclear $\mathbf{Cx_{55}}$ complex and $\mathbf{A_1}$, while $\mathbf{Cx_{55}}$ + $\mathbf{A_2}$ and $\mathbf{Cx_{56}}$ + $\mathbf{A_1}$ each incorporate >2 times more (toluene, 24°C, 1 bar ethene, 0.64 M 1-octene). Molecular weights were similar at 150,000 and $\mathbf{Cx_{55}}$ is twice as fast as $\mathbf{Cx_{56}}$. The increased selectivity for highly encumbered comonomer enchainment was also observed for a zirconium complex analogue, and assigned to a cooperative comonomer capture/binding/delivery by the proximate cationic metal centers as shown above in Scheme 24 [63].

Monometallic and bimetallic CGC complexes $\mathbf{Cx_{55}}$ and $\mathbf{Cx_{56}}$ were used in the homopolymerization of styrene and in the copolymerization of styrene and ethene by Marks et al. [64] The results are shown in Table 2. Surprisingly, the bimetallic catalysts (entries 2, 4) are 40–50 times more active than the mononuclear ones (entries 1, 3), independent of the mono- or bimetallic character of the boron cocatalyst.

The explanation of the authors is illustrated in Scheme 26. In the monometallic catalyst the arene group of the last inserted styrene molecule blocks the open site of titanium ($\mathbf{Cx_{55}}$), while in the bimetallic catalyst the arene group coordinates to the other metal and the open site can be used for the coordination of the new styrene molecule ($\mathbf{Cx_{56}}$).

Scheme 27 Dinuclear titanium or zirconium complexes **Cx$_{57}$** containing the bisphenoxyimine bridging ligand

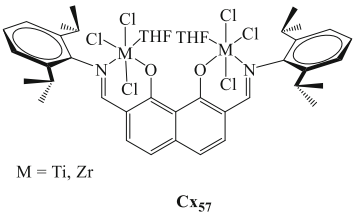

Cx$_{57}$

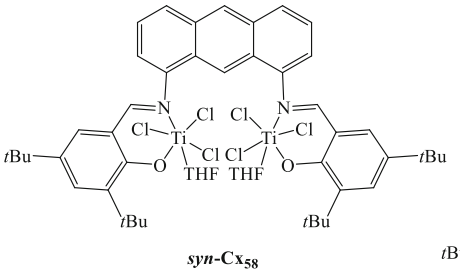

***syn*-Cx$_{58}$**

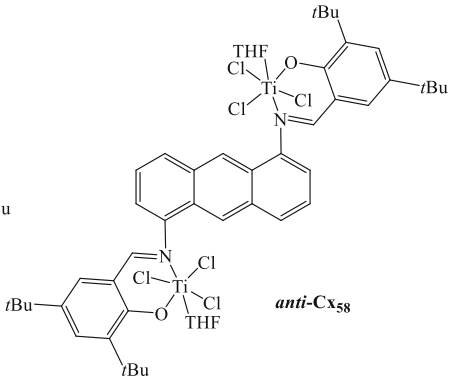

***anti*-Cx$_{58}$**

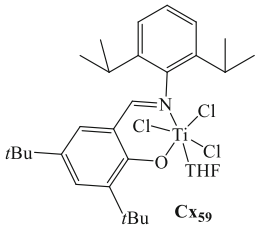

Cx$_{59}$

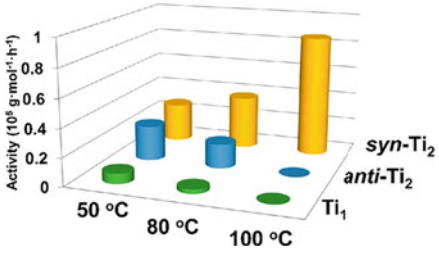

Scheme 28 Compounds **syn-Cx$_{58}$**, **anti-Cx$_{58}$** and monometallic **Cx$_{59}$** and comparison of their activity in ethylene homopolymerization at different reaction temperatures [67]

Bimetallic phenoxyiminato polymerization catalysts (FI) **Cx$_{57}$** were reported by Salata and Marks (Scheme 27) [65]. The monometallic catalysts were widely studied by Fujita [66]. As usual, the chlorides were activated by the addition of methylaluminoxane (MAO). The bimetallic catalysts are more active than the monometallic analogs and, more interestingly, they show higher incorporation of higher alkenes, either made in situ or added as 1-octene in a copolymerization. This was explained by the proximity of a second catalytic center that can tug in a higher alkene and transfer it to the nearby growing chain.

Liu, Li, and co-workers discovered a bimetallic Ti complex containing anthracene as the bridge that showed a very large rate effect, viz. **Cx$_{58}$**, in the MAO induced polymerization of ethane (Scheme 28). They studied the three complexes shown in Scheme 28, the Ti complexes connected in *syn* fashion and *anti* fashion to

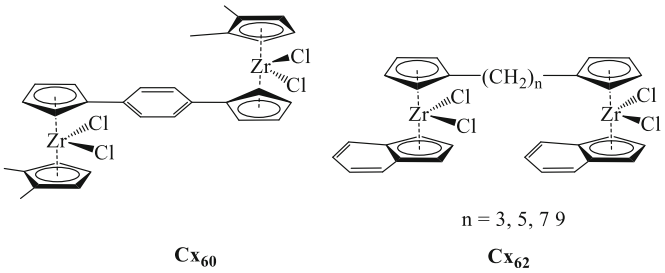

$\mathbf{Cx_{60}}$ $\mathbf{Cx_{62}}$

Scheme 29 Dinuclear polymethylene zirconocene complexes $\mathbf{Cx_{60}}$ and $\mathbf{Cx_{62}}$

anthracene, and the monometallic analog $\mathbf{Cx_{59}}$. As in the examples above, the effect is astounding; there is no explanation at hand, other than that the proximity of one metal center greatly activates the other one [67].

While proximity of the two catalyst centers has often been shown to be advantageous, Marks, Lohr, and co-workers found that a "too close" distance may cause decomposition of the catalyst and one loses the advantage of the bimetallic nature. Thus, the effects are subtle and careful performance studies should be conducted [68]. There is also an example of dizirconium, vide infra, Scheme 31.

3.1.2 Zr-Zr Complexes

The interest in bis-cyclopentadienyl-zirconium as alkene polymerization catalysts dates back to the early 1990s; for example, in one of the first publications on this topic, Mülhaupt and co-workers found that bimetallic cyclopentadienyl-zirconium catalysts $\mathbf{Cx_{60}}$, activated by MAO, gave lower activity in propene polymerization when the two cyclopentadienyl entities were connected by an aromatic ring, presumably because the reduced electron density at the second zirconium site induces a higher rate for the β-hydride elimination at the first metal center [69]. Lee et al. reported on bimetallic cyclopentadienyl-zirconium catalysts with several siloxane linkers $\mathbf{Cx_{61}}$ and noted that in ethene polymerization they gave higher molecular weight polymers than the monometallic homologs [70]. Noh et al. reported on dinuclear cyclopentadienyl-indenyl zirconium catalysts connected by alkyl chains of various lengths $\mathbf{Cx_{62}}$ [71]. The rate of ethene polymerization in the presence of MMAO at 40°C more than doubled in the range $n = 3$–9. All catalysts were faster than the mononuclear ones (Scheme 29).

Marks and co-workers developed monometallic $\mathbf{Cx_{63}}$ and bimetallic $\mathbf{Cx_{64}}$ constrained geometry catalysts (CGC) complexes using, respectively, diboron $\mathbf{A_3}$ and monoboron $\mathbf{A_4}$ anions as activators (Scheme 30) [72].

Typically zirconium CGC complexes produce rather low M_w materials in the polymerization of ethene or copolymerization with 1-hexene. In ethene homopolymerization $\mathbf{Cx_{64}}$ ($n = 1$) produces a 70 times higher Mw than $\mathbf{Cx_{64}}$ ($n = 2$) and with respect to mononuclear $\mathbf{Cx_{63}}$ the Mw increase was 130-fold. For

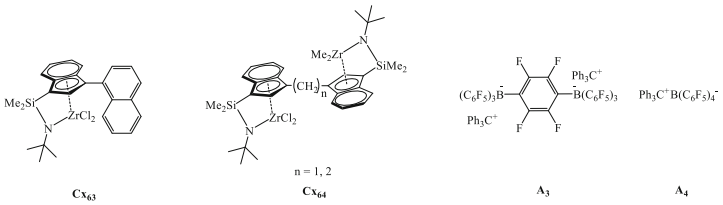

Scheme 30 Monometallic $\mathbf{Cx_{63}}$ and bimetallic $\mathbf{Cx_{64}}$ catalysts and diboron $\mathbf{A_3}$ and monoboron $\mathbf{A_4}$ anions as activators

Scheme 31 Catalysts $\mathbf{Cx_{65}}$ and $\mathbf{Cx_{66}}$ (MAO activated) used in copolymerization of ethene (5 bar) and 10-undecen-1-ol (80°C)

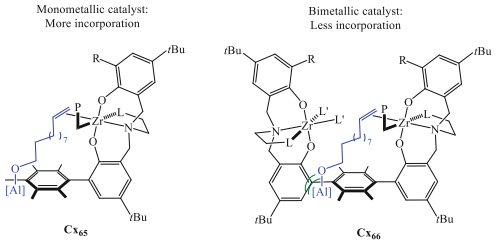

chloride-MAO based $\mathbf{Cx_{64}}$ systems, the increase was 600-fold of the $\mathbf{Cx_{63}}$ system. Comparison of various catalysts showed that the effect was not merely steric. Agostic interactions of the proximate metal with the growing chains or comonomer were suggested to be the cause of the phenomena observed.

Bimetallic polymerization catalysts do not as a rule outperform the mononuclear analogs and especially in copolymerization of ethane and a higher alkene (or functionalized alkene) the mononuclear catalysts are the ones giving the fastest catalyst and the highest incorporation of the comonomer as is shown by the examples in the report by Akhtar, Agapie, and co-workers [73]. They studied, i.e., the copolymerization of ethene and 10-undecen-1-ol (protected by TIBA, Al^iBu_3) with catalysts $\mathbf{Cx_{65}}$ mono and $\mathbf{Cx_{66}}$ di activated by MAO (Scheme 31). The bimetallic catalyst gave less incorporation of the comonomer and lower rates and apparently, a tug-in effect or local higher concentration in the dinuclear catalyst was dominated, they presumed, by steric effects slowing the polymerization of the more bulky comonomer.

3.1.3 Ti-Cr Complexes

Linear low-density polyethylene (LLDPE) is a PE in which certain amounts of 1-hexene or 1-octene have been incorporated in order to obtain the desired properties for the packaging market. Homogeneous catalyst systems offer the opportunity to make the comonomer in situ at a desired rate with a different metal catalyst compatible with the polymerization catalyst. The first example dates from the 1980s with a $MgCl_2$-supported Ti catalyst and a homogeneous Ti(alkoxide)

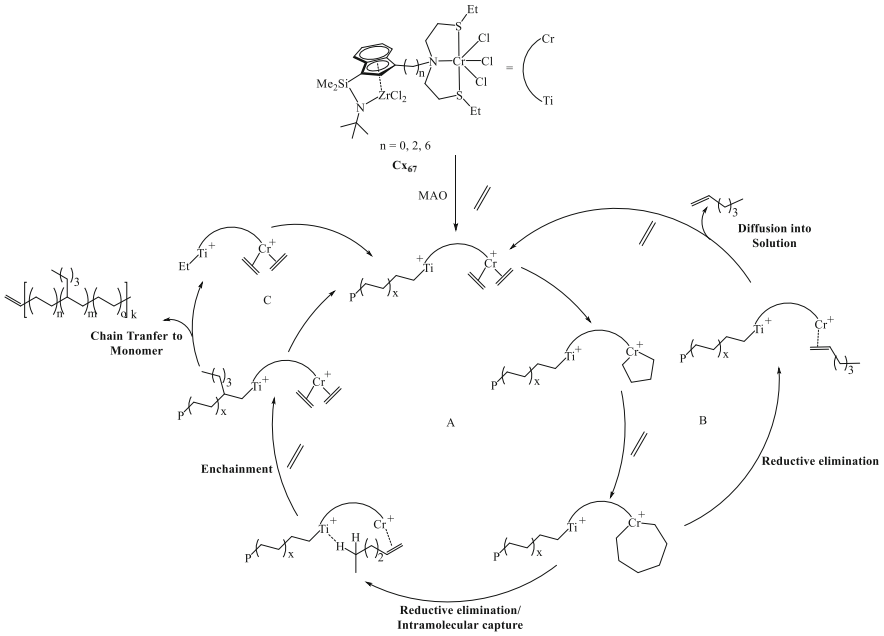

Scheme 32 Ethylene polymerization catalyzed by the Constrained Geometry [Ti-Cr] **Cx$_{67}$** catalysts (η^5-indenyl)[1-Me_2Si(N-^{t}Bu)$TiCl_2$]-3-C_nH_{2n}-[N,N-bis(2-ethylthio)ethyl)-amine]$CrCl_3$, $n = 0$, 2, 6

precursor that produces 1-butene as the comonomer [74]. In this tandem system the oligomerization catalyst based on Ti can only produce 1-butene relatively pure, but higher alkenes will be produced as Schulz–Flory mixtures. Cr-based catalysts, however, can give selectively 1-hexene or 1-octene/1-hexene mixtures, depending on the ligand system used. These catalysts operate via a metallocyclic mechanism and can thus produce 1-hexene in high selectivity. Large cooperative effects in heterobimetallic titanium-chromium **Cx$_{67}$** catalysts for ethylene polymerization/copolymerization were discovered by Delferro, Marks et al. (Scheme 32) [75].

The tandem mixture of two free catalysts, Dow's Constrained Geometry Catalyst and one of Sasol's first chromium catalysts [76], gave the fastest polymerization but the lowest incorporation of 1-hexene of the four systems presented here. Catalyst **Cx$_{67}$** ($n = 0$) is a less active catalyst for ethene polymerization but with the highest degree of branching, i.e. incorporation of 1-hexene. This was explained by the proximity of the two active centers. Competition experiments with added 1-pentene at 1.0 M gave only 10% propyl side chains of the total butyl + propyl side chains and thus the locally generated 1-hexene is strongly preferred by the bimetallic catalyst. The effective molar concentration of 1-hexene at the Ti catalyst center is as high as 8.6 M (pure 1-hexene is 8 M!!). The authors proposed that 1-hexene still π-bonded to Cr will bind to Ti via agostic interactions and by this way hexene is transferred from Cr to Ti with high efficiency. These numbers also mean

Table 3 Ethylene polymerization data for selected catalysts[a]

Catalyst	PE (g)	Activity[b] (PE)	Oligomers[c] (g)	Activity[d] oligomers	ρ_{br}[e]	M_w[f] (kg mol^{-1})	M_n[f] (kg mol^{-1})
CGCEtTi + SNSCr	3.200	480.0	0.204	30.6	6.4	26	11.4
Ti-C_0-CrSNS	0.820	123.0	0.491	73.7	25.8	593	237
Ti-C_2-CrSNS	0.184	27.6	0.075	11.3	18.2	461	184
Ti-C_6-CrSNS	0.134	20.1	0.066	9.9	6.8	319	127

[a] [Catalyst] = 10 μmol of CGCEtTi; 10 μmol of SNSCr; Ti-C_0-CrSNS, Ti-C_2-CrSNS, and Ti-C_6-CrSNS, MAO/catalyst =500, 50 mL toluene, 5 min, 80°C, constant 8 atm ethylene
[b] kg (PE)·mol^{-1} (catalyst)·h^{-1} atm^{-1}
[c] By GC-TOF, mesitylene internal standard
[d] kg (oligomers)·mol^{-1} (catalyst)·h^{-1} atm^{-1}
[e] Branch density (branches per 1,000 C atoms) as determined by ^{13}C NMR analysis
[f] By GPC

that most of the 1-hexene that escapes from the active centers does not return to Ti from the solvent to undergo incorporation. The bimetallic system **Cx$_{67}$** ($n = 0$) also gave the highest MWs and thus chain transfer is drastically reduced with respect to the mixture of monometallic catalysts. Since M_n is independent of ethene pressure the chain transfer mechanism involves β-hydride transfer (BHT) from the chain to ethene. Thus, the ethene adduct is crucial for the mechanism. The proximity of the Cr center causes a higher positive charge on Ti($n = 0$) (+0.487) than on Ti($n = 2$) (+0.432) and the Ti–C distances to the C-atoms adjacent to Cr are also larger in **Cx$_{67}$** ($n = 0$). The proximity of the positively charged Cr atom accelerates the insertion of ethene and slows chain transfer according to DFT calculations. For $n = 2$ and $n = 6$ both rate and branching were lower as is to be expected. The authors concluded that polymerization and DFT computational results show that Ti···Cr spatial proximity markedly influences chain transfer rates and selectivity for comonomer enchainment and that such proximity effects are relatively insensitive to conversion, but cocatalyst, solvent, and ligand framework strongly influence these effects (Table 3).

Whether slower β-hydrogen transfer (BHT) is due to an electronic effect finds no support in other data. Kamigaito et al. reported that CGC catalysts $C_5Me_4SiMe_2NRTiX_2$ equipped with electron-withdrawing R groups produce low average molecular weights in propylene polymerization [77]. Ehm and co-workers reported in a recent DFT study on CGC catalysts that the barriers for BHT chain termination are hardly influenced by electronic tuning, while the barriers for chain propagation show large dependences. Steric hindrance typically raises BHT barriers, which could be operative in the Marks–Delferro systems. Decreasing the electrophilicity of the metal center in CGC systems leads to higher MWs according to Ehm et al. [78]

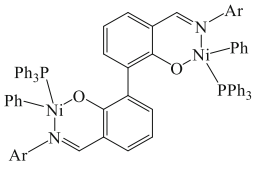

Cx$_{68}$

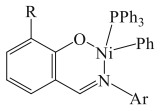

R = H, Ph, 9-phenanthrenyl, 9-anthrancenyl, Ar=2,6-*i*Pr$_2$C$_6$H$_3$

Cx$_{69}$

Scheme 33 Structure of the neutral **Cx$_{68}$** bis-nickel complex based on the 3,3′-bisalicylaldimine ligand and the corresponding mononuclear **Cx$_{69}$** complexes

3.1.4 Ni-Ni Complexes

Nickel catalysts, including binuclear ones, were reviewed by Pan, Li, and co-workers in 2015 [79]. While in monometallic catalysts phenoxy/carboxy-phosphine ligands are most often used, the majority of the bimetallic catalyst work was done with the use of phenoxy-imine ligands, borrowed from the monometallic Grubbs catalyst [80]. The P–O ligands are analogues of the SHOP ethene oligomerization catalyst. An early example of a bis(phenoxy-imine) ligand involves biphenol-based **Cx$_{68}$** (Scheme 33) [81].

The synthesis is straightforward from 2,2′-biphenol by introducing formyl groups in *ortho* position to the hydroxyl group and reacting it with 2,6-diisopropylaniline and then the sodium salt with 2 equivalents of *trans*-[NiCl(Ph)(PPh$_3$)$_2$]. The neutral and stable precursor complex contains triphenylphosphine ligands. Unlike the monometallic catalysts **Cx$_{69}$**, bimetallic **Cx$_{68}$** showed high activity without phosphine scavenger; for the former, [Ni(COD)$_2$] was needed to remove triphenylphosphine from the nickel site. Thus, **Cx$_{68}$** gave a rate of 4.55×10^5 g of PE/((mol of Ni)·h) without scavenger, while **Cx$_{69}$-Ph** gave 1.0×10^5 g of PE/((mol of Ni) h) with scavenger. The explanation given is that one catalyst moiety functions as the bulky substituent for the other catalyst, so that the rate of chain propagation is faster than the rate of chain transfer.

Agapie and co-workers utilized terphenyl scaffolds for bimetallic and monometallic polymerization catalysts. Dinickel complexes **Cx$_{70}$** with phenoxy and imine donor ligands were synthesized [82]. Full substitution of the central arene blocks rotation around the aryl−aryl bond, which yielded the formation of atropisomers of which the *syn*- and *anti*-forms could be isolated. Complexes **Cx$_{70}$** gave ethene polymerization in the presence of amines, in this instance the neutral ligands completing the tetra-coordination of the metal. The amines are inhibitors of the polymerization. This inhibiting effect of the amines is up to 270 times lower for the *syn*-isomer than the *anti*-isomer with tripropylamine. Comparisons with mononuclear systems indicate that the proximity of the metal centers in the *syn*-isomer leads to the observed inhibitory effect on the deactivation of the catalysts for steric reasons. In the more active isomer, one metal amine complex inhibits coordination

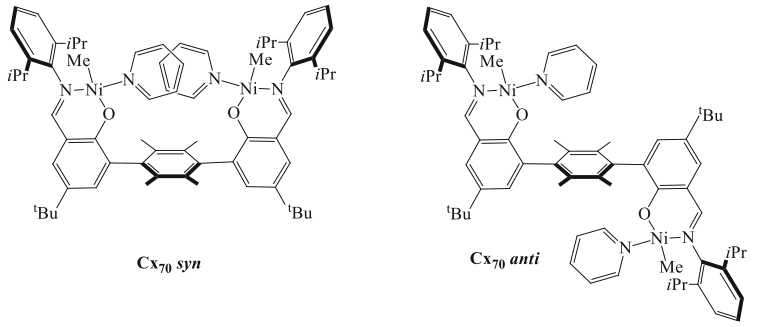

Scheme 34 Dinickel complexes **Cx$_{70}$** coordinated by a terphenyl scaffold containing phenoxy and imine ligands with the two *syn* and *anti* atropisomers

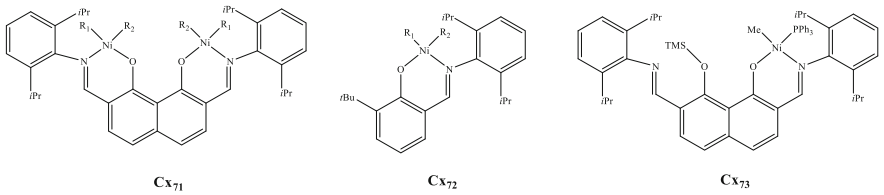

Scheme 35 Dinuclear **Cx$_{71}$** and mononuclear **Cx$_{72}$**, and **Cx$_{73}$** complexes for ethene and ethene-co-norbornene polymerization

of an amine to the second metal, which remains thus active (Schemes 34, 35, 36, and 37).

The results were corroborated in a subsequent publication for the PMe_3 precursor complexes of the para and meta terphenyl backbones [83]. The cocatalyst [Ni $(COD)_2$] was used, which abstracts the phosphine from the complex and thus allows a comparison of amine bases added of various sizes. The active species produced from the *syn*-**Cx$_{70}$** complex in which the pyridine or the phosphine ligands are removed exhibit activity for copolymerization of ethene and aminoalkenes and the inhibitory coordination of the amines at both Ni centers is disfavored because of steric repulsions [83]. Several bridged anilines have been reported as convenient linkers for the synthesis of bimetallic nickel catalysts containing phenoxy-imine ligands and the polymerization results were much in line with the examples shown here [84–89].

The distance between the two metals in the Agapie systems is relatively long and several complexes were designed in which the distance is shorter. Marks et al. had already used a naphthalene backbone which brings the two centers closer to one another [90]. The binuclear catalysts **Cx$_{71}$** show twice as high catalytic activities and double the amount of methyl branching compared to mononuclear **Cx$_{72}$** (Table 4). The higher activities were ascribed to the proximity of the two metal centers that

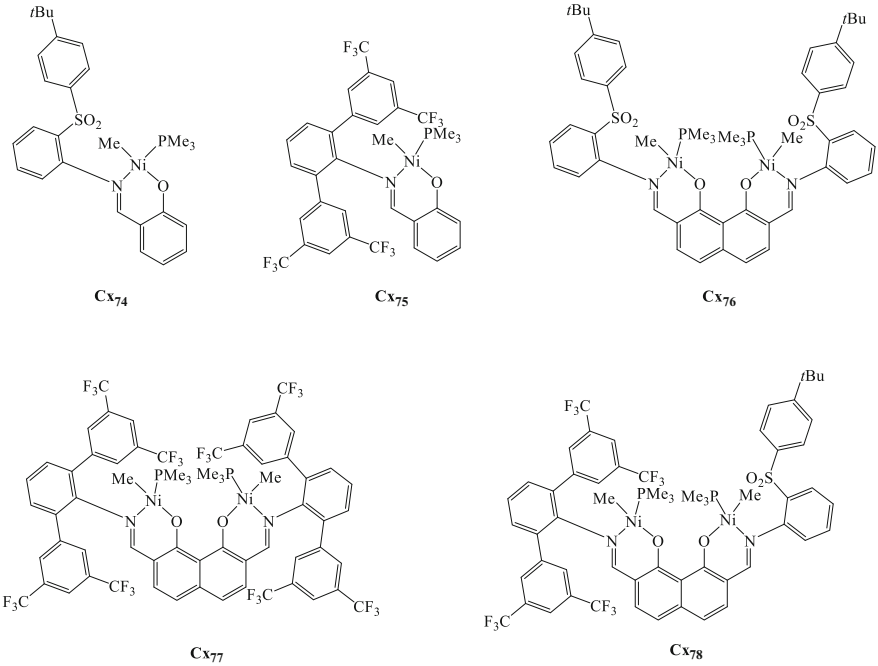

Scheme 36 Mononuclear **Cx$_{74}$** and **Cx$_{75}$** complexes and dinuclear **Cx$_{76}$**, **Cx$_{77}$** phenoxyiminato nickel complexes and the **Cx$_{78}$** dinickel complex with the unsymmetrical ligand for the polymerization of ethylene

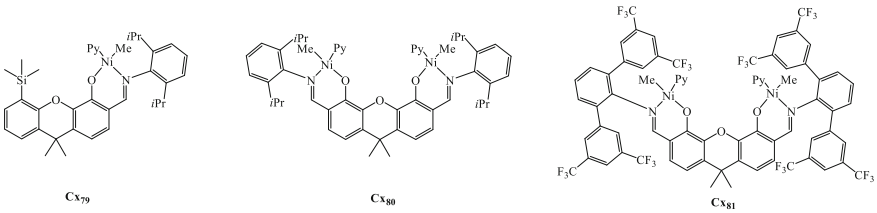

Scheme 37 Mononuclear **Cx$_{79}$** and dinuclear **Cx$_{80}$** and **Cx$_{81}$** nickel complexes based on the 9,9-dimethylxanthene framework

might facilitate dissociation of the first phosphine to create a vacant site needed for polymerization. Ethene/NBE copolymerization was also investigated.

Bimetallics **Cx$_{71}$** show higher activities and produce copolymers with more methyl branches (38 vs 11 methyl branches per 1,000 carbon atoms) than monometallic **Cx$_{72}$**. There is no explanation yet why bimetallic catalysts produce more methyl branching, without further chain-walk to longer side chains. The copolymerization of ethene and norbornene was studied as well. The molar percentage of NBE in the copolymers obtained by the bimetallic complexes (in the range from 9 to

Table 4 Polymerization results of complexes **Cx$_{71}$**, **Cx$_{72}$**, and **Cx$_{73}$**

Complex	R^1	R^2	Activity (10^3 g/mol Ni·h)	M_w[b] ($\times 10^3$)	M_w/M_n	Me[c] branches	Nor incorp.
Cx$_{71}$	Me	PMe_3	49.7	10.3	2.6	80	
Cx$_{71}$	PPh_3	1-naphthyl	51.3	10.1	2.6	93	
Cx$_{72}$	1-naphthyl	PMe_3	25.2	11.7	2.5	52	
Cx$_{72}$	1-naphthyl	PPh_3	25.9	10.5	2.5	54	
Cx$_{73}$			23.1	11.2	2.6	40	
Cx$_{71}$[b]	Me	PMe_3	9.1	66.4	5.2	34	9
Cx$_{71}$[b]	PPh_3	1-naphthyl	8.4	65.8	4.5	38	11
Cx$_{72}$[b]	1-naphthyl	PMe_3	2.1	63.2	2.3	9	3
Cx$_{72}$[b]	1-naphthyl	PPh_3	2.1	64.0	2.1	11	3

[a] Ethylene polymerization conditions [90]: toluene, 25 mL; catalyst, 10 μmol; 2 equiv of [Ni(COD)$_2$] cocatalyst/Ni; 25°C; 40 min; ethene, 0.7 MPa
[b] Copolymerization conditions: catalyst, 20 μmol; 90 min; 225 equiv. of norbornene
[c] Total Me/1,000 C, by ^{1}H NMR

11 mol%) is much higher than that by the monometallic counterparts (3 mol%). The modest incorporation lowers the rate of polymerization and methyl branching considerably with respect to the homopolymerization, while the molecular weight goes up five-fold for both mono and bimetallic catalysts.

In a subsequent publication Marks, Delferro et al. exploited the unsymmetric substitution at the two imine donor atoms on the bimetallic naphthalene catalyst **Cx$_{78}$** one group being a bulky electron-withdrawing terphenyl, the other one a less bulky diphenyl sulfone [91]

For these catalysts the usual effect of the bulk of the second metal is absent (Table 5), cf. entries 1 and 3, and 2 and 4. Probably the cocatalysts [Ni(COD)$_2$] or B(C_6F_5)$_3$ scavenge efficiently PMe_3 and the "shielding" effect is superfluous. The bulky terphenyl EWGs yield much faster catalysts than the sulfone substituted ones (entries 1 vs 2, and 3 vs 4). This was ascribed to interference of the sulfone group with the metal site. Interestingly, the fluoromethyl terphenyl catalysts give highly linear PE with only methyl branching (entries 2 and 4), but the sulfone catalysts gave more and longer branches. A mixture of the two monometallic catalysts exhibits independent behavior of the two catalysts and a bimodal M_w distribution. The mixed ligand catalyst **Cx$_{78}$** (entry 6) gave the most interesting result as the rate is almost the same as that of the symmetric CF_3-terphenyl catalyst (entry 4), but with a branching content and a narrow M_w distribution resembling that of the sulfone catalysts. It was proposed that, as in the Ti/Cr system described above, an efficient incorporation of the alkenes produced by the CF_3-terphenyl metal into the sulfone metal takes place. The reverse mechanism is less likely as the CF_3-terphenyl catalysts do not

Table 5 Ethylene polymerization data for catalysts **Cx$_{74}$**, **Cx$_{75}$**, **Cx$_{76}$**, **Cx$_{77}$**, **Cx$_{74}$ + Cx$_{75}$**, and **Cx$_{78}$**[a]

Entry	Catalyst	PE (g)	Act.[b]	TOF[c] (h^{-1})	ρ_{br}[d]	% Branch type[e]			M_w[f]	M_w/M_n (kg/mol)	T_m[g]
						Me	Hex+	Other			
1	**Cx$_{74}$**	0.40	60	1,488	140	45	19	36	5	1.6	
2	**Cx$_{75}$**	2.23	335	81,888	7	100	0	0	92	3.0	119.0
3	**Cx$_{76}$**	0.07	5	110	105	38	27	35	4.5	1.7	
4	**Cx$_{77}$**	0.32	24	2,000	40	100	0	0	25	2.4	115.8
5	**Cx$_{74}$ + Cx$_{75}$**	1.83	273	9,607	39	79	8	13	56	6.4	103.4, 114.1
6	**Cx$_{78}$**	0.27	20	2,289	69	58	16	26	24	1.7	121.6

[a] Polymerization in 25 mL toluene with 10 μmol catalyst at constant 8.0 atm ethylene pressure using 2 equiv. Ni(COD)2/Ni as phosphine scavenger/cocatalyst at 25°C, time 5 min

[b] Units: kg PE $[Ni]^{-1}$ atm^{-1} h^{-1}

[c] Ethylene turnover frequency (TOF) calculated from the polymer mass

[d] Branch density (branches/1,000 C atoms) determined by ^{1}H NMR

[e] Analysis by ^{13}C NMR

[f] GPC vs polystyrene standards

[g] Melting temperature determined by DSC

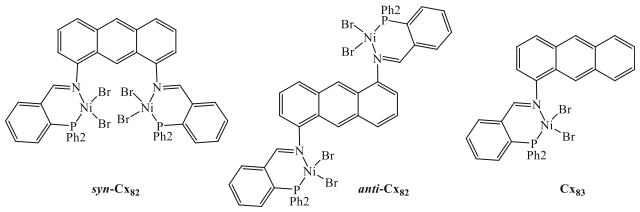

Scheme 38 Phosphino-iminate nickel complexes as studied by Lui et al. [94]

copolymerize 1-pentene, the authors say, but note that the high local concentration may overcome this feature of relative rates. Such highly branched PE polymers have important properties for certain applications.

Mononuclear neutral nickel catalyst **Cx$_{79}$** and binuclear complexes **Cx$_{80}$** and **Cx$_{81}$** based on rigid 9,9-dimethylxanthene frameworks featuring short Ni–Ni distances and pyridine as the neutral ligand were synthesized and applied in ethylene (co)polymerization by Li and co-workers [92]. Binuclear catalyst **Cx$_{80}$** is twice as active in ethylene polymerization as the corresponding mononuclear **Cx$_{79}$** complex. The product is a high molecular weight polymer, 15 times higher than that of **Cx$_{79}$**, with a bimodal molecular weight distribution. Catalyst **Cx$_{80}$** is remarkably thermally robust and still active at 93°C. The polymer microstructure produced by **Cx$_{79}$** reveals a hyperbranched structure with a variety of branch types, while **Cx$_{80}$** product features methyl branches primarily. Catalyst **Cx$_{81}$** shows rates similar to **Cx$_{80}$**, but the M_ws are reduced by a factor of 3–7. In the presence of comonomer 1,5-hexadiene, 1,7-octadiene, and methyl 10-undecenoate, mononuclear **Cx$_{79}$** suffers from either low catalytic activity or poor incorporation efficiency, as for the Marks/Delferro catalysts described above, while binuclear catalyst **Cx$_{80}$** effectively enchained these comonomers into the polymer chain, giving copolymer with unique microstructures. Notably, **Cx$_{80}$** incorporates 1,5-hexadiene as cyclopentane rings. As in the cases cites above, the second metal aids by coordination of the diene its insertion in the growing chain on the other metal. Since temperatures, neutral ligand (Py and PMe_3, respectively), and cocatalyst (none and $[Ni(COD)_2]$) are different for this system and those in Table 5, one cannot make a meaningful comparison

In addition to the FI-based nickel complexes above, Liu, Li, and co-workers also studied dinuclear versions of the phosphino-iminate nickel complexes (the mononuclear ones are known from the work by, *i.e.*, Braunstein) [93]. Liu et al. studied dinickel catalysts with P–N ligands connected by the anthracene backbone and the corresponding mononuclear one, reminiscent of their dititanium complexes, as shown in Scheme 38 [94]. Nickel phosphino-iminates are known as ethene dimerization catalysts. In the presence of $EtAlCl_2$, *syn*-Ni dimer **Cx$_{82}$** showed a remarkably high activity for ethene dimerization (>90%) (up to 9.10×10^6 g/((mol of Ni)·h), which is approximately 1.5- and 3.3-fold higher, respectively, than those of *anti*-Ni dimer or of mononuclear Ni, **Cx$_{83}$**. The dimeric species are also active isomerization catalysts and the yield mainly consists of 2-butene (70–80%). After

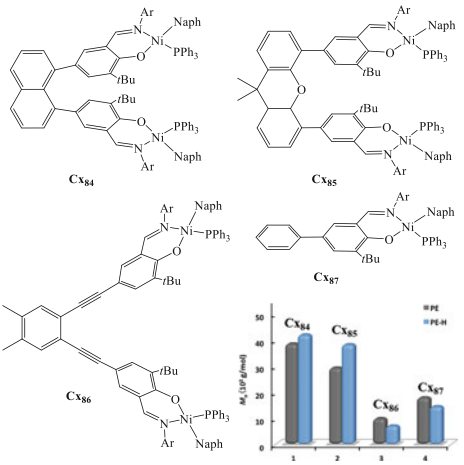

Scheme 39 Comparison of molecular weight of polyethylene and ethylene/1-hexene copolymer for complexes **Cx$_{84}$**–**Cx$_{87}$** (B$(C_6F_5)_3$ activator, toluene, ethene =6.5 bar, 25°C) [95]. Ask permission

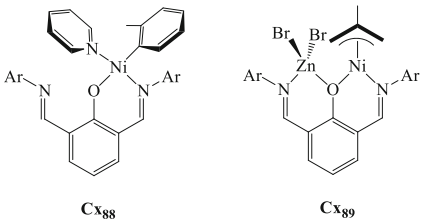

Scheme 40 Monometallic **Cx$_{88}$** and [Ni-Zn] bimetallic **Cx$_{89}$** complexes based on the 2,6-bis-((2,6-diisopropylphenyl) imino)methyl phenoxide

optimization, 94% selectivity of 2-butene in the C4 fraction was achieved using dinuclear *syn*-Ni. No detailed explanation was given for the "proximity" effect.

Related series of ethene (co)polymerization by binuclear nickel phenoxyiminato catalysts with cofacial orientation were reported by Ma and co-workers [95]. Complexes **Cx$_{84}$**–**Cx$_{86}$** proved once more that proximity of the two metal centers influenced the polymerization characteristics, i.e. proximity enhanced the rate of polymerization and the Mw, see Scheme 39.

3.1.5 Ni-Zn Complexes

Tonks and co-workers studied the effect of a neighboring Zn salt on the ethylene polymerization activity of complexes **Cx$_{88}$** and **Cx$_{89}$** [96]. An excess of $ZnBr_2$ was needed and the activation was difficult to control. In several reactions, bimodal M_w distributions were obtained indicating the presence of more than one active species. One conclusion could be drawn, namely that the presence of nearby Zn leads to a faster β-hydride elimination and the M_w obtained with **Cx$_{89}$** is much lower than that with **Cx$_{88}$**. This was corroborated through DFT calculations. Catalyst **Cx$_{89}$** is much slower than **Cx$_{88}$** and even more slower than a standard Grubbs catalyst such as

Scheme 41 In situ generated Ni-Zn catalyst **Cx$_{90}$** for ethylene polymerization

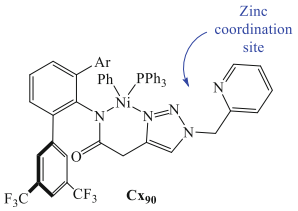

(6-tBu-salicyl(2,6-diisopropylphenyl)aldiminato)Ni(o-tolyl)(py), also included in this study (Scheme 40).

As was shown by Xiao and Do, the in situ formation of heterobimetallic complexes cannot left at chance. In their studies nickel complex **Cx$_{90}$** showed a perfect behavior in a fast ethene polymerization, but addition of zinc chloride to the complex, designed for this purpose, provided polymers with multimodal distributions (Scheme 41). It was shown that the formation of mixed adducts was the cause of this phenomenon [97].

3.2 Alkyne Activation

The trimerization of alkynes by [$Co_2(CO)_8$] was already described in the 1960s by Hubel and Hoogzand [98] and mechanistic aspects were recently reviewed by Powers and Uyeda [99]. The metal–metal bond stays intact during the process. The well-known Pauson–Khand reaction [100], cyclization of alkyne, alkene, and CO to give cyclopentenones, occurs on the same catalyst precursor [$Co_2(CO)_8$] while the Co–Co bond is also retained during the process, although only the first adduct of Co_2 and the alkyne has been identified [101]. Initially the reaction was stoichiometric in [$Co_2(CO)_8$]. Here we focus on more recent examples of bimetallic catalysts.

Bimetallic nickel complexes **Cx$_{49}$** catalyze the trimerization of alkynes as shown in Scheme 42 [102]. The 1,2,4-substituted benzene derivative is the main product. Monometallic nickel complexes such as [Ni(bpy)(COD)] produce cyclooctatetraene derivatives.

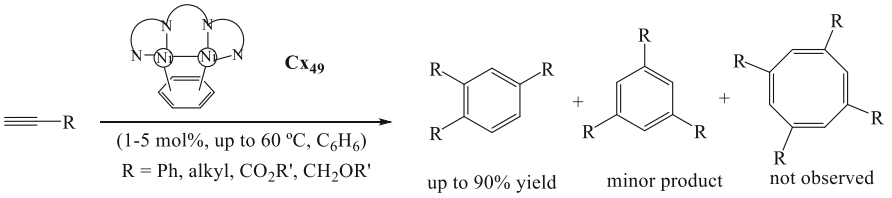

Scheme 42 Trimerization of alkynes catalyzed by the dinickel complex **Cx$_{49}$**

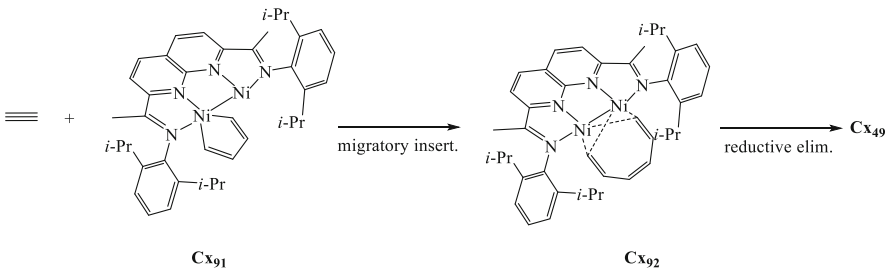

Scheme 43 Cyclotrimerization pathways with a migratory insertion of acetylene on **Cx$_{91}$** to generate the dimetallacyclooctatriene **Cx$_{92}$** with the Ni-vinyl bonds in a *cis* configuration

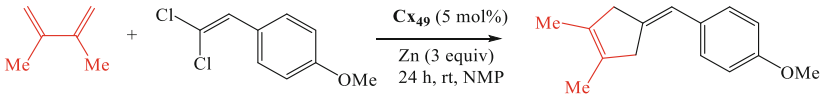

Scheme 44 4 + 1 cyclization with complex **Cx$_{49}$** [104]

DFT calculations revealed that the homodinuclear Ni−Ni catalyst induces a spin crossover mechanism that involves metallacyclopentadiene and nonclassical bridging dimetallacyclooctatriene intermediates (Scheme 43) [103].

Thus, two alkynes bind to two nickel atoms which oxidatively combine to a monometallic metallacyclopentadiene **Cx$_{91}$**. Insertion of the third alkyne gives according to DFT a bimetallic metallacycle via an asymmetric intermediate (not shown), which gives the final product via a rapid bimetallic reductive elimination. This explains the high selectivity for trimerization products rather than tetramerization products. The arene precursor **Cx$_{49}$** has a singlet ground state, but the other intermediates proposed have a triplet ground state accessible via spin cross over. Intermediate **Cx$_{92}$** has a singlet state again and can undergo "spin-allowed" reductive elimination, after the alkyne trimerization.

Uyeda and co-workers have so far reported a range of cyclization reactions (1 + 2, 2 + 2 + 2, 2 + 4) and in 2019 they added to this an example of a 1 + 4 reaction producing 5-membered rings [104]. The dinickel work was reviewed recently by Uyeda and Farley [105].

The catalyst is the same as in the examples before, **Cx$_{49}$**, which undergoes oxidative addition of the C–Cl bonds to form the methylidene (Zn being the stoichiometric reductant) and catalyzing the 1 + 4 addition to the 1,3 diene (for details, see Scheme 44 1 + 2).

Tsai, Yu, and co-workers reported an example of a catalytic process that occurs at a metal−metal multiple bond (see Scheme 45) [106]. The diamagnetic Mo_2 complexes **Cx$_{93}$** feature a metal−metal quintuple bond supported by two bulky amidinate ligands. Complex **Cx$_{93}$** (R = Ph) undergoes a formal [2 + 2]-cycloaddition with 3-hexyne to afford the adduct **Cx$_{94}$**, in which the Mo−Mo bond order is

Scheme 45
Dimolybdenum complexes involved in the trimerization of alkynes

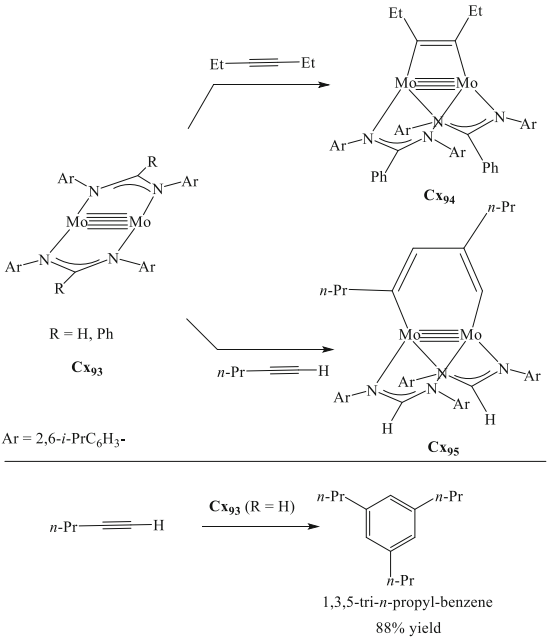

reduced to a quadruple bond. Terminal alkynes such as 1-pentyne undergo double addition to **Cx$_{93}$** (R = H), forming the six-membered metallacycle **Cx$_{95}$** with regioselectivity resulting from head-to-tail coupling of the alkyne. Complexes **Cx$_{93}$** (R = H) and **Cx$_{95}$** were found to be efficient catalysts for the cyclotrimerization of 1-pentyne, forming the 1,3,5-trisubstituted arene product in 88% isolated yield. The reactions of **Cx$_{93}$** with an internal alkyne, 3-hexyne, exclusively yielded the [2 + 2] complexation adducts and no catalytic turnovers.

Carmona and co-workers investigated complex **Cx$_{93}$** and its reactions with dihydrogen to obtain **Cx$_{96}$**, which can be reversed by irradiation [107] (Scheme 46). Complex **Cx$_{96}$** undergoes reversible bimetallic, reversible insertion of ethene without further oligomerization. Reaction with phenylacetylene leads to formation of dihydrogen and the trans-bis-acetylide complex and thus no oligomerization is observed in this instance [108] (Scheme 46).

3.3 Metathesis Using Ru-Ru Complexes

Grubbs and Dias described a bimetallic bisruthenium catalyst that was found to be more active than the Grubbs I catalyst **Cx$_{97}$** (Scheme 47) [109]. Dimer **Cx$_{99}$** was made from Grubbs I and the cymene-ruthenium dichloride dimer **Cx$_{98}$**. The **Cx$_{97}$** catalyst requires dissociation of one PCy_3 ligand before showing activity in the metathesis reaction of alkenes. Complex **Cx$_{99}$** does not require dissociation and is

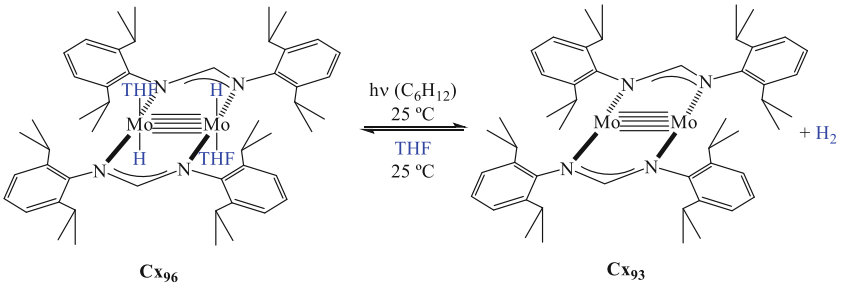

Cx96 **Cx93**

Scheme 46 Reaction of **Cx93** with dihydrogen [107]

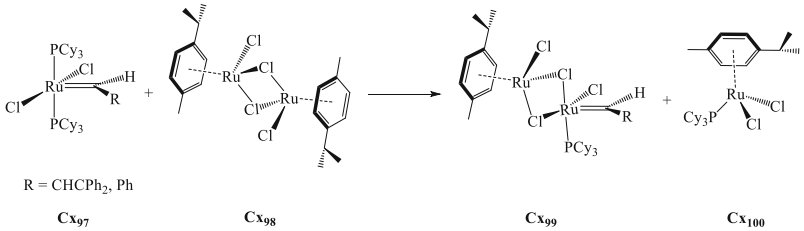

Scheme 47 The formation of an active Ru dimer **Cx99** metathesis catalyst

Scheme 48 Vinylidene diruthenium **Cx101** complex as a catalyst for alkyne and alkene metathesis reactions

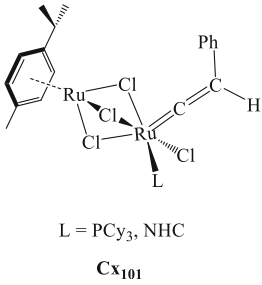

active without incubation time. The spectator [(p-cymene)$RuCl_2$] unit **Cx100** acts as a Lewis acid that enhances the activity of the ruthenium-alkylidene catalyst. The two dimers [(*p*-cymene)$OsCl_2]_2$, and [(*t*Bu_2Cp)$RhCl_2]_2$ can fulfill the same role.

Delaude and co-workers described the use of homobimetallic ruthenium complexes **Cx101** (Scheme 48) as catalysts for metathesis of alkynes and alkenes [110]. The alkylidene complexes can be formed from the ethene adduct precursors via a reaction with terminal alkynes [111]. The catalytic activity of complex **Cx101** was probed in various types of alkene metathesis reactions. The NHC derived catalyst was far more active than the tricyclohexylphosphine complex. The catalytic activity for ROMP and RCM of alkenes could be further enhanced by the addition of catalytic amounts of terminal alkynes. No comparison was made with monometallic systems and the role of the second metal was not investigated.

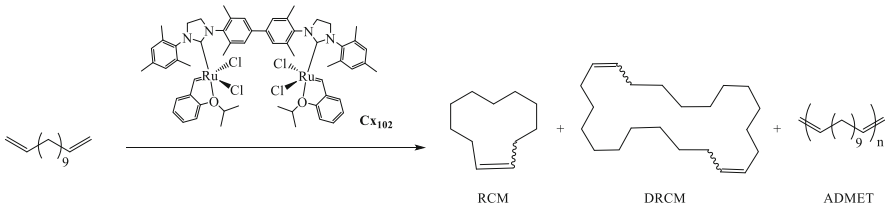

Scheme 49 Ring-closing metathesis of 1,12-tridecadiene catalyzed by the isopropoxystyrene chelated diruthenium complex $\mathbf{Cx_{102}}$

Lemcoff and co-workers linked two Grubbs catalysts via aryl bridges and found an effect of the neighboring metals in ring-closing metathesis (RCM) [112]. In the catalytic screening the Hoveyda–Grubbs variant $\mathbf{Cx_{102}}$ was used as the catalyst precursor (Scheme 49). When 1,12-tridecadiene was used as the substrate catalyst $\mathbf{Cx_{102}}$ gave almost selectively the dimer resulting from the dimer RCM (DRCM) whereas the mononuclear catalysts gave mainly polymers via acyclic diene metathesis (ADMET) under the same conditions. The reactivities for the monometallic and bimetallic catalysts were found to be equal when diethyl diallylmalonate was used in the standard RCM reaction (Scheme 50). Indeed, the two centers are far apart (10.2 Å) for a direct Ru–Ru interaction, but the well-chosen 1,12-tridecadiene nicely bridges between the two centers and gives this peculiar selectivity for the 22-membered carbon ring. Close proximity of two ruthenium-alkylidene species should probably be avoided in bimetallic Ru metathesis catalysts, as Fogg and co-workers have shown that fast, mononuclear Ru catalysts are prone to a bimetallic alkene elimination reaction causing catalyst die-out [113].

4 Reductive Elimination

4.1 Pd-Pd-Catalyzed Functionalization of C–H Reductive Elimination

4.1.1 Pd(III)-Pd(III) Intermediates

Palladium(II) acetate has been long known as an efficient metalating agent of aromatics; one of the older examples of C–H activation with palladium involves the formation of diphenyl when benzene is heated in acetic acid with stoichiometric amounts of palladium salts [114]. The palladium metal formed has to be reoxidized in order to arrive at a catalytic cycle. Palladium(II) acetate, in particular when aided by adjacent, directing functional groups in the substrate (FG-directed activation) has become an efficient catalyst for functionalization of sp^2 C-atoms [115]. As concerns the role of the nuclearity of dimeric and trimeric palladium acetate in the metalation reactions, Váňa et al. concluded in a recent review that there is no single mechanism

Scheme 50 Possible dimer ring-closing metathesis mechanism on the dinuclear ruthenium framework **Cx$_{102}$**

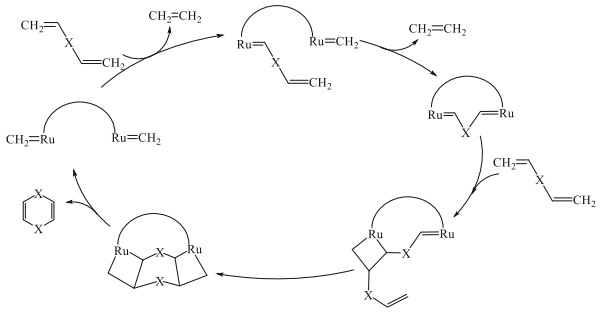

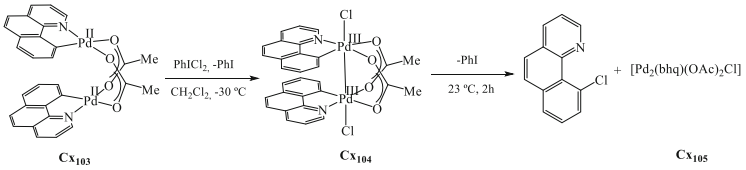

Cx$_{103}$ **Cx$_{104}$** **Cx$_{105}$**

Scheme 51 C–H functionalization by palladium dimer **Cx$_{103}$**

that emerges [116]. The reaction of palladium chloride and an imine with arene substituents such as benzalaniline, 2-phenylpyridine, but also azobenzene, have been known since the 1960s and are referred to as orthometallations, cyclopalladation, C–H activation, etc. [117]. Numerous examples have been published ever since, extended with further stoichiometric reactions such as carbonylations and alkyne insertions, but catalytic use of this rich chemistry dates from the recent period. In the last decade C–H functionalization by palladium has been extended to dimeric compounds of Pd(III). In 2009, Powers and Ritter reported that acetate-bridged binuclear Pd(II) complex **Cx$_{103}$**, the product of cyclopalladation of benzo[*h*]quinoline with $Pd(OAc)_2$, is oxidized at low temperature to binuclear Pd(III) complex **Cx$_{104}$** with $PhICl_2$ (Scheme 51) [118, 119]. Warming to room temperature gave reductive elimination of one molecule of 10-chlorobenzo[*h*]quinoline and Pd (II) dimer **Cx$_{105}$** [120]. With the use of N-chlorosuccinimide as the oxidant the chlorination reaction could be turned into a catalytic one [121]. A close monometallic analog involving Pd(II) and Pd(IV) was reported by Sanford et al. in 2005 for C–C bond and C–O bond formation in an oxidative manner [122, 123]. Monometallic Pd(IV) had been invoked in cross-coupling mechanisms of Pd compounds for decades, although mainstream Pd cross coupling catalysis concerns the Pd(0)/Pd (II) couple. Reductive elimination from intermediates like **Cx$_{104}$** containing Pd(III) dimers may take place in two ways: 1) from one or two metals in the trivalent state, or 2) after disproportionation of $[Pd(III)]_2$ into Pd(II) and Pd(IV) and reductive elimination from Pd(IV). For certain cases it was shown that transformation of symmetric dimers **Cx$_{104}$** to asymmetric dimers Pd(II)/(IV) was a more facile process than reductive elimination from the symmetric dimer [124]. In this joint paper of the

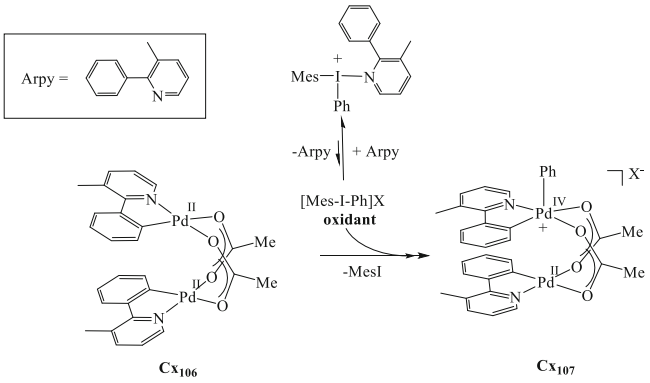

Scheme 52 Asymmetric oxidation of **Cx$_{106}$**

groups of Sanford, Yates, Canty, and Ritter the mechanisms and views were brought together.

The course of the reaction and the involvement of valence states depend on the nature of the ligands and the oxidant. Thus, oxidant [Mes-I-Ph]X (Scheme 52) converts dimeric Pd(II) complexes **Cx$_{106}$** to Pd(II)–Pd(IV) intermediates **Cx$_{107}$** to give the arylated products [125], while electrophilic CF_3-transfer reagents based on hypervalent iodine (CF_3^+ reagent) leads to monometallic Pd(IV) intermediates **Cx$_{108}$** (Scheme 53) [126].

Canty and co-workers describe, with the use of DFT calculations, how the nature of the "axial" ligand influences the course of the reaction of the two metals, whether symmetric (Pd(III)-Pd(III), **Cx$_{104}$** type) or asymmetric (Pd(IV)-Pd(II), **Cx$_{107}$** type) intermediate complexes prevail [127]. For C–C elimination Cl dissociation takes place; for C–Cl elimination, the reaction is direct [128]. For each case the valence states have to be investigated and the whole spectrum can be found.

In the early studies on FG-directed C–H activation by noble metals the reaction had only few applications, but in recent decades the use of electrophilic reagents has given a boost to this area [129]. The current challenges in this area of C–H substitution were discussed recently by Zhang and Ritter [130]. Kozlowski and co-workers reported a DFT study concerning palladium-catalyzed benzylic vs arene C−H activation and found that the oxidation state of the homogeneous palladium species influences the selectivity of C−H activation; Pd(0) and Pd (I) activate the sp^3 C−H bond in toluene, whereas Pd(II) and Pd(III) preferentially activate the sp^2 C−H bond. This selectivity was related to the steric environment of the ligand framework. As the palladium oxidation state increases, the number of ligand sites increases, which relatively favors reaction of the more hindered sp^3 C−H bond [131].

Scheme 53 Symmetric oxidation of **Cx$_{103}$** producing the mononuclear Pd(IV) complex **Cx$_{108}$**

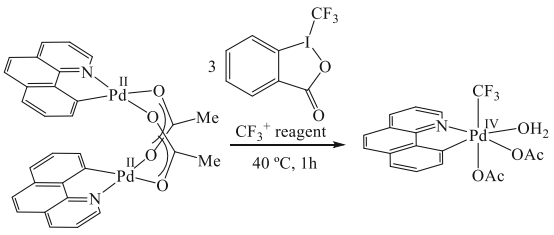

Cx$_{103}$ **Cx$_{108}$**

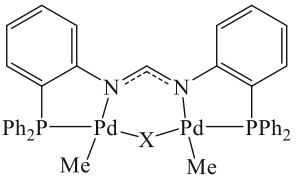

Cx$_{109a-c}$

X= a OH, b Cl, c H

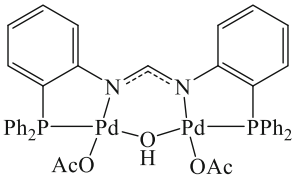

Cx$_{109a}$-OAc

Scheme 54 Structure of the dinuclear palladium(I) complexes **Cx$_{109}$** containing the bridging hydroxy, chloro, and hydrido ligands

4.1.2 Pd(II)-Pd(II) Precursors (C-H Activation and Migratory Insertion)

Tsukada, Inoue, and co-workers introduced a system based on a bridged dipalladium hydride unit held together by a bis-ligand imidinato anion that can be used for the addition of C–H bonds to alkynes without the aid of directing group, a coupling reaction not producing any side product (Schemes 54 and 55) [132]. The precursor for the catalyst is the bridged hydroxide **Cx$_{109a}$** and in situ the bridged hydride **Cx$_{109c}$** is generated with a borane cocatalyst BBu_3 [133]. Benzene gives 100% of the arylated alkenes in 4 h at 100°C, 2% catalyst. Toluene, chlorobenzene, methyl benzoate, and anisole gave mixtures of meta and para isomers in somewhat lower yields. The *cis* addition product was obtained in all cases.

The reaction sequence starts with the insertion of the alkyne in a Pd–C bond on one metal retaining the bridging hydride **Cx$_{110}$**, or insertion in the hydride on one metal, the other metal becoming a spectator **Cx$_{111}$**. Reductive elimination in both cases gives a Pd(0)/Pd(II) species **Cx$_{112}$**, the authors proposed. One could also imagine the formation of a Pd(I) dimer and a bridging hydrocarbyl fragment, similar to the Pd(I) dimers containing a bridging hydride and carbonyl [134]. **Cx$_{112}$** reacts with ArH to regenerate catalyst **Cx$_{113}$**.

Related catalyst **C$_{x109a}$-OAc** catalyzes the β-arylation of thiophenes and furans in modest yield (~50%, silver carbonate as the base), but with remarkable selectivity for the β-position, while most catalysts yield mainly the α-derivative [135–137].

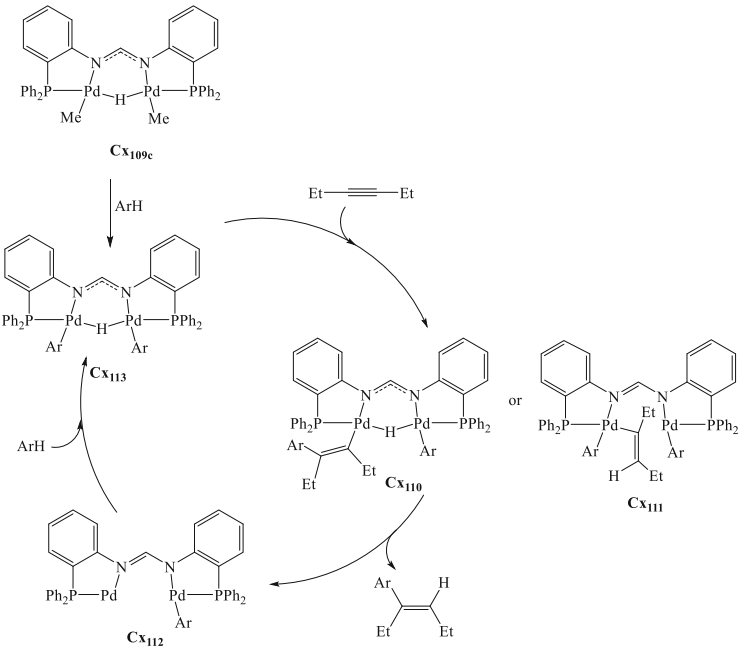

Scheme 55 Catalytic cycle for the addition of C–H bonds to alkynes using catalyst **Cx$_{109c}$**. The reaction was extended by the authors to pyrroles and thiophenes instead of arenes as the substrate with the use of the same catalyst

5 Miscellaneous Reactions

5.1 Michael Reactions (Chiral Nucleophilic Attack)

The Michael addition of cyanoacetate esters as donors and enones as Michael acceptors, as shown in Scheme 56, can be catalyzed by many metal complexes including chiral ones which may provide enantioselectivity as in this case of Jautze and Peters using precatalyst **Cx$_{114}$** [138]. The metal catalyst can activate the donor, the acceptor, or both reagents. The kinetics in general show first order in all three components indicating that in equilibrium a complex of the three entities is formed that undergoes the C–C bond forming as the rate-determining step.

The authors used a chiral bimetallic palladium complex **Cx$_{115}$** as catalyst for the reactions of a range of α-aryl-α-cyanoacetate ester donors with various vinyl ketone acceptors, which proceeded with excellent yield and high enantioselectivity. The bimetallic catalyst was only 2.1 times faster than the monometallic analog, which was ascribed to product inhibition in the former case due to the chelate effect of the two metals forming a complex with the keto and nitrile group. Notably, a quaternary, chiral carbon center is formed in this reaction (Scheme 57). The area of acyclic

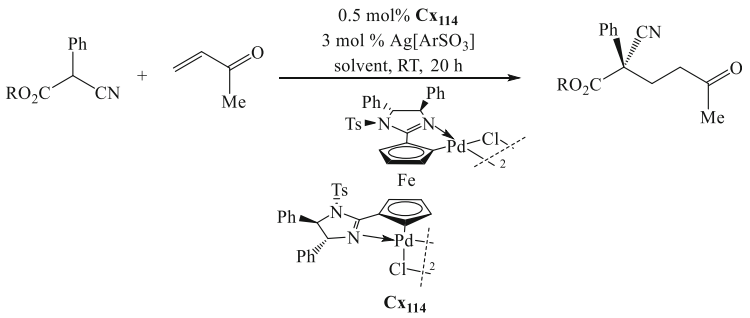

Scheme 56 Michael reaction using the precatalyst **Cx$_{114}$**

Scheme 57 Proposed intermediate **Cx$_{115}$** for the cooperative intramolecular Michael reaction

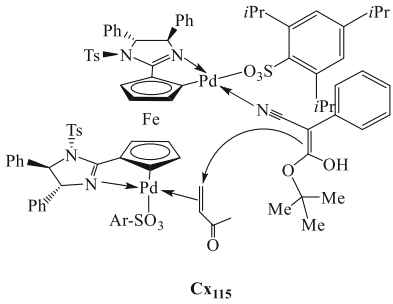

quaternary carbon stereocenters via enantioselective transition metal catalysis was reviewed by Krische and co-workers [139].

Subsequently, catalyst **Cx$_{114}$** was compared with an analogue one based on a ruthenocene instead of a ferrocene, which increases the plane-to-plane distance from 3.29 to 3.58 Å. This has a subtle effect on both the ee and the rate of reaction, depending on the substrate used. This was explained by the different fit of the substrates onto the bimetallic catalyst, which makes it worthwhile to investigate both catalysts although a detailed, molecular explanation is lacking [140].

The acetate derivative of **Cx$_{114}$** (**Cx$_{116}$** in Scheme 58) is a highly efficient enantioselective and fast catalyst for the allylation of aldehydes with allylstannanes [141]. Both conversions and ees increased from 80 s for the monomers to high 90 s for the dimers. More references to related reactions can be found in Ref. [141].

As an example of a heterobimetallic catalyst a Mg-Pd system will be described that was reported by Klein Gebbink and co-workers [142]. A range of complexes **Cx$_{117}$** was synthesized that were used as catalysts for the double Michael addition of α-cyanoacetate esters, Scheme 59.

A comparison was made between various catalysts, e.g. **Cx$_{117}$**-Mg-Pd, pincer-Pd, Mg-porphyrin, etc. The rates observed were Mg-Pd/Pd/Mg/none = 1,900:300:30:6. Thus, a six-fold increase in rate was observed for the bimetallic catalyst **Cx$_{117}$** with respect to pincer-Pd, while Mg alone is a rather poor catalyst. The proposed

Scheme 58 Fast and enantioselective allyl stannylation of aldehydes by **Cx$_{116}$** and a possible mode of action [141]

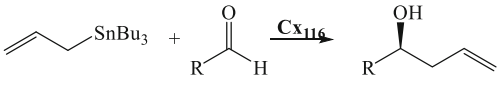

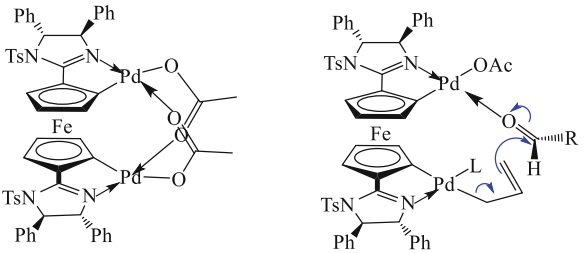

Cx$_{116}$

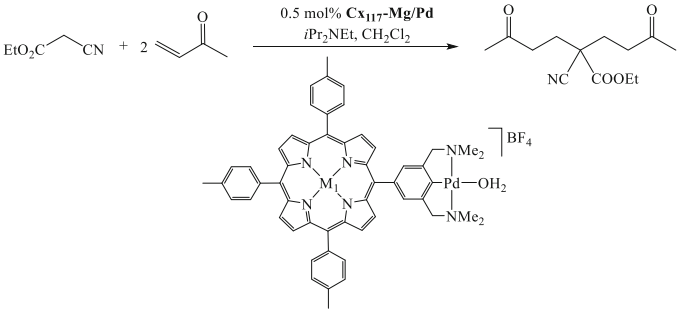

Cx$_{117}$ M_1 = Mg, Ni, Zn

Scheme 59 Double Michael addition catalyzed by the Pd-Mg **Cx$_{117}$** complex

mechanism is the same as that above for Pd–Pd **Cx$_{116}$**; the ketone is activated by the Mg ion, and the cyanoacetate coordinates to Pd via the nitrile functionality.

5.2 Nucleophilic Attack on Alkynes

Bi- and tri-metallic rhodium and iridium complexes containing click derived bi- and tri-topic bis-pyrazolyl and bis-(pyrazolyl-1,2,3-triazolyl) N–N′ donor ligands were described by Messerle and co-workers (Scheme 60) [143]. These systems were applied as catalysts for the tandem two-step dihydroalkoxylation of alkynes. The dirhodium complex **Cx$_{118}$**, appropriately designed to favor cooperativity, showed a

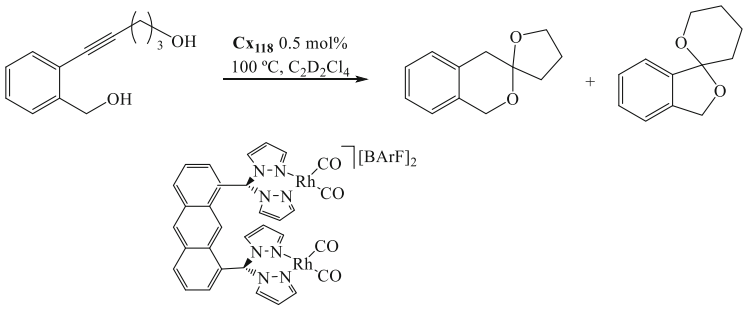

Scheme 60 Dihydroalkoxylation of alkynes using the dirhodium catalyst **Cx$_{118}$**

Scheme 61 Influence of the scaffold on the rate of dihydroalkoxylation of Scheme 60

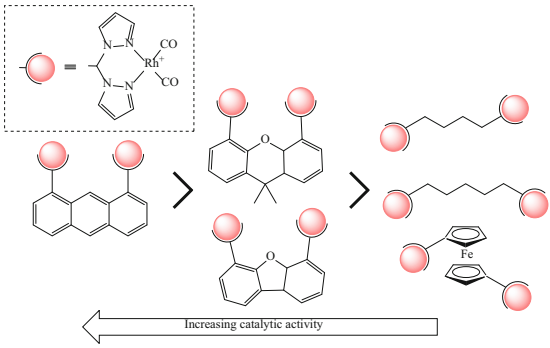

value of TOF 10 times faster than a monometallic analog, but much slower than a monometallic heteroaliphatic carbene Au(I) complex [144, 145].

In a subsequent paper a range of scaffolds was introduced (Scheme 61) and the rate of reaction was strongly influenced by the structure [146]. In all instances the bimetallic motif led to an enhancement of catalyst rate in comparison with that of the mononuclear analog. The highest catalyst activities were obtained with the rigid structures, as indicated in Scheme 61.

5.3 *Ni_2 and Hydrosilylation (Double Oxidative Addition)*

Steiman and Uyeda studied the interaction of a silane with the dinickel complex **Cx$_{49}$** (part IIb), which contains a metal–metal bond sustained by the rigid, redox-active **L$_{12}$** naphthyridine-diimine backbone [147]. According to DFT calculations the system is best described as a Ni(I)-Ni(I) complex. The stable benzene adduct **Cx$_{49}$** reacts with R_2SiH_2 to give the adduct of the latter (**Cx$_{119}$**) by replacement of benzene (Scheme 62).

Scheme 62 Dihydrosilane activation by dinickel complex **Cx$_{49}$**

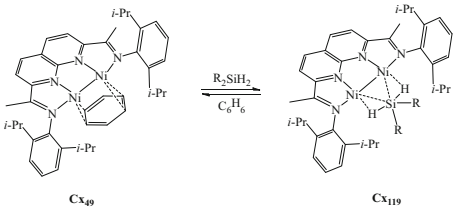

Scheme 63 Deactivation of **Cx$_{119}$** due to the hydride migration to produce **Cx$_{120}$** and proposal of the first step **Cx$_{121}$** for the silane activation by **Cx$_{49}$**

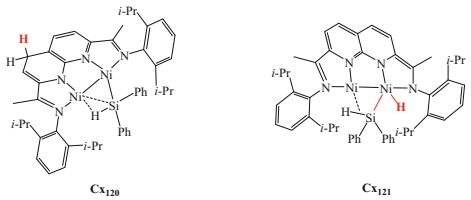

Equilibrium mixtures were obtained as the reaction is sufficiently slow to observe both adducts by NMR at room temperature. The more electron-rich diethylsilane shows weaker binding and trialkylsilanes do not bind at all. Upon crystallization a third compound (R = Ph, **Cx$_{120}$**) forms in addition to **Cx$_{49}$** and **Cx$_{119}$** in which one hydride has been transferred from the silane to the ligand; the X-ray structure clearly shows dearomatization of one side of the molecule. Complex **Cx$_{49}$**(benzene adduct) was found to be a catalyst for alkene hydrosilylation. At 5 mol% the hydrosilylation of 1-octene with Ph_2SiH_2 proceeds to >95% conversion in 22 h at room temperature to provide $CH_3C_7H_{14}SiHPh_2$ in 77% yield. Et_2SiH_2 reacts more slowly, yielding only 35% of the product after the same reaction time. The relative rate of hydrosilylation with Et_2SiH_2 presumably reflects its weaker binding constant to **Cx$_{49}$**. Complex **Cx$_{120}$** was not considered to be relevant to the catalytic activity, but we could consider that the oxidative addition occurred first on one metal center as shown in Scheme 63 with complex **Cx$_{121}$** followed by the migration of the hydride ligand on the ligand **L$_{12}$**. The second nickel atom can interact with the remaining Si-H bond as shown for **Cx$_{121}$** but coordinates the alkene C=C bond along the catalytic cycle.

Styrene, dienes, enones, alkynes, all reacted smoothly and faster than 1-octene. Mononuclear diazadiene nickel complexes gave no conversion and thus we may conclude that silane and alkyne bind to the two adjacent nickel atoms.

5.4 Ni_2 and Azobenzenes from Aryl Azides

Complex **Cx$_{49}$** was also used by Uyeda and co-workers as a catalyst for the dimerization of aryl azide, with loss of two molecules of dinitrogen [148]. At room temperature the complex converted a broad range of aromatic azides in high yields to the corresponding symmetric azo compounds (Scheme 64). The reaction

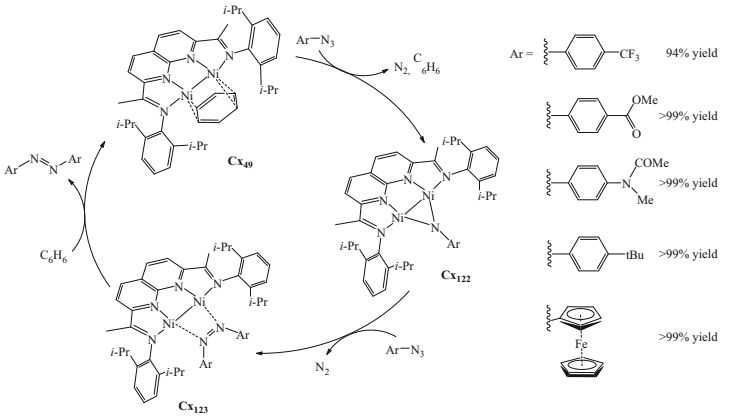

Scheme 64 Proposed catalytic cycle for the dimerization of arylazide on the dinickel $\mathbf{Cx_{49}}$ complex

presumably occurs on one metal center before the azide ligand interacts with the second nickel atom or binds symmetrically the two Ni(II) as shown for $\mathbf{Cx_{122}}$.

Interestingly the monomeric Ni complex $\mathbf{Cx_{124}}$ only showed a stoichiometric conversion to a Ni complex of the *E*-azoarene isomer $\mathbf{Cx_{125}}$ (Scheme 65), which is highly stable, due to the strong binding of the *E*-form of the azoarene to Ni(0), and the substrate does not replace the product.

In the dimeric complex the azides react one by one and after the first reaction a Ni_2 bridging nitrene $\mathbf{Cx_{122}}$ was proposed as intermediate. The second reaction presumably gives two bridging nitrenes that combine to the *Z*-azoarene compound. This complex was observed as the resting state, but since it is much more weakly bound, the *Z*-azo compound in $\mathbf{Cx_{123}}$ can be replaced by the azide or rather a solvent molecule, as the reaction is zero order in azide, which turns the system into a catalytic one. It seems that upon release the *E*-azo is formed, thus avoiding product inhibition.

5.5 *Ru_2 in the Kharasch Reaction (1 Electron Oxidative Addition)*

Dimeric complex $\mathbf{Cx_{126}}$ was found, by Severin et al., to be a fast catalyst for the Kharasch addition of organohalides to alkenes at room temperature and below, also named ATRA reaction (atom-transfer radical addition), see Scheme 66 [149]. The metal catalyst can also be $[Cp^*MCl_2]$, (M = Rh or Ir). It was considerably faster than the routinely used monomeric $[RuCl_2(PPh_3)_3]$ complex, but also faster than the best monomeric complexes studied and compared by Noels, e.g. $[Cp^*RuCl_2(PPh_3)_2]$ [150]. The reaction starts with the abstraction of a chloride atom from the

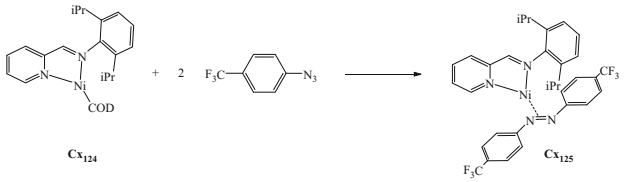

Scheme 65 Dimerization of an arylazide by monomeric nickel complex

Scheme 66 Kharasch addition of organohalides to alkenes

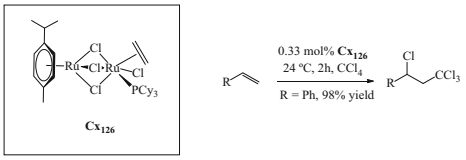

organohalide in which Ru(II) turns to Ru(III), often thought to be the rate-limiting step. The radical $^{\cdot}CCl_3$ formed adds to styrene, methacrylates, and the like, and the newly formed radical recaptures the Cl atom from Ru(III). All catalyst precursors need to create a vacant site before they can start the atom abstraction and Severin ascribed the high activity to the easy loss of ethene from **Cx126**. The electron-accepting spectator metal accelerates the dissociation of ethene, although the reacting metal becomes less electron-donating. In the series of Noels they found, with exceptions, that the more electron rich the Ru center, the faster was the reaction. These systems are very complicated, however, and explanations may be lacking; the concentration of Ru(III) must be sufficiently high to intercept the radical intermediate to prevent polymerization and too high concentrations of organic radicals may lead to undesired dimerizations. Under the latter circumstances, Ru(III) builds up at the cost of Ru(II) and the reaction stops. When the CCl_4 or another initiator concentration is reduced to the level of the Ru concentration (Ru:chloride initiator: MMA = 1:2:800), the acrylate radical will react with another monomer molecule and polymerization is obtained as now the concentration of Ru(III)Cl is low compared to MMA, named ATRP (atom-transfer radical polymerization) [151]. Complex **Cx126** is an excellent catalyst for this reaction at room temperature.

5.6 *Au_2 in Ring Closure Reactions*

Marinetti and co-workers used the light-induced *cis-trans* isomerization of azobenzene in bridged gold-phosphine complexes, providing (***E***)-**Cx127** and (***Z***)-**Cx127** complexes (Scheme 67) to influence their activity in the intramolecular hydroamination reaction of an *N*-alkenylurea [152].

The cationic (***E***)- or (***Z***)-**Cx128** complexes generated by chloride abstraction from the AuCl **Cx127** precursors by addition of $Ag[SbF_6]$ catalyze the ring closure

Scheme 67
Photoisomerization of the two precursors (***E***)-**Cx$_{127}$** and (***Z***)-**Cx$_{127}$** complexes

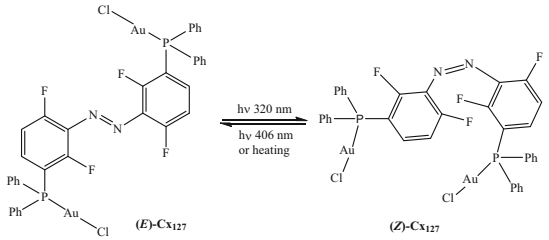

Scheme 68 Intramolecular hydroamination reaction of an *N*-alkenylurea, and double coordination of the substrate to the (***Z***)-**Cx$_{128}$** reactive species

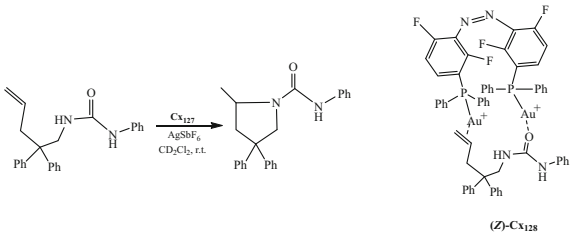

reaction. In bimetallic (***Z***)-**Cx$_{128}$** the two gold centers are closer to one another and the authors aimed at a bimetallic effect on the rate of reaction. A modest enhancement was seen upon irradiation of (***E***)-**Cx$_{128}$**, which is converted to (***Z***)-**Cx$_{128}$**, of about a factor of 2. The authors proposed a chelating coordination of the substrate in the latter complex, as shown in Scheme 68, to explain this effect. The area of photoswitchable catalysts, dinuclear systems included, was recently reviewed, as were photoswitchable phosphines in catalysis [153–155].

5.7 Pd–Ru in Hydrodefluorination

Peris and co-workers discovered the synergistic action of a ruthenium-palladium bimetallic complex in the hydrodefluorination of carbon–fluorine bonds of both aromatics and aliphatics [156]. The three complexes studied are **Cx$_{129}$**, **Cx$_{130}$**, and **Cx$_{131}$**. The latter was made via a stepwise deprotonation of the triazolium salt and adding one by one the metal precursor complexes. Typical catalytic results are presented in Table 6 for the simplest substrate studied, fluorobenzene (Scheme 69).

Thus, Ru_2 **Cx$_{129}$** complex is not active, Pd_2 **Cx$_{130}$** shows slight activity, but catalyst **Cx$_{131}$**, the heterobinuclear complex, gave complete conversion. The mixture of the homobimetallic ones is also active, but less so than the bimetallic complex. It was assumed that palladium is involved in the C–F cleavage, while ruthenium provides hydrogen as a hydrogen transfer catalyst. The high rate of **Cx$_{131}$** relative to the mixture of **Cx$_{129}$** and **Cx$_{130}$** must be explained by the proximity of the two sites involved in the tandem process, although details about the process could not be given.

Table 6 Hydrodefluorination with bimetallic $\mathbf{Cx_{129}}$, $\mathbf{Cx_{130}}$, and $\mathbf{Cx_{131}}$ catalysts

$C_6H_5F \rightarrow C_6H_6$ in *iso*-propanol at 80°C for 1 h; 1% of catalyst with *t*-BuONa	
Catalyst $\mathbf{Cx_{129}}$	0%
Catalyst $\mathbf{Cx_{130}}$	3%
Catalyst $\mathbf{Cx_{131}}$	100%
Catalyst $\mathbf{Cx_{129}}$ + $\mathbf{Cx_{130}}$	49%

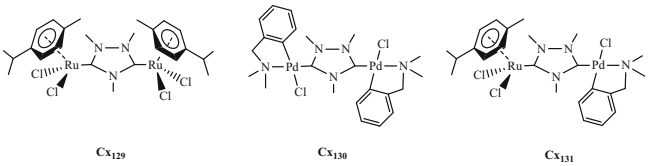

Scheme 69 Diruthenium- ($\mathbf{Cx_{129}}$), dipalladium- ($\mathbf{Cx_{130}}$), and ruthenium-palladium ($\mathbf{Cx_{131}}$) complexes bridged by the triazolyl-di-ylidene ligand

Heterobimetallic complexes in which the two metal centers are bridged by the 1,3-dibutylimidazo{[4,5-*f*][1,10]-phenanthrolin}-2-ylidene ligand are characterized by an extended π-electron system able to interact through a pπ-dπ overlap with them. The ruthenium-palladium $\mathbf{Cx_{132}}$ complex in which ruthenium is coordinated to the two nitrogen atoms of phenanthroline and palladium to the carbene moiety (Scheme 70) is able to perform the dehalogenation/transfer hydrogenation of 4-bromoacetophenone into 1-phenylethanol (99% yield). Similarly, the same $\mathbf{Cx_{132}}$ catalyst allows a 99% yield in 4-phenyl-1-phenylethanol [157]. The Peris and Hahn groups are exploring bridging ligands for coordinating two different metal catalysts inducing a significant cooperativity in order to produce efficient tandem catalysis [158]. Each metal has its own role in the tandem process, and the proximity and the electronic relay played by the bridging ligand provide a high efficiency in terms of activity and selectivity.

Moore and Lu proposed a different bimetallic system Rh/In for hydrodefluorination, catalyst $\mathbf{Cx_{133}}$ that operates at 70°C and 1 bar of H_2 converting fluorobenzene to benzene [159]. It is proposed that the catalytic cycle involves Rh (I) and Rh(–I) and that In stabilizes the low-valent Rh state (Scheme 71).

5.8 *Ir_2 NHC Complexes in Reductions with MeOH*

Li, Hou, and co-workers compared the activity of the dimeric Ir(III)-NHC complex $\mathbf{Cx_{134}}$ with monomeric complexes $\mathbf{Cx_{135}}$ and $\mathbf{Cx_{136}}$ (and 10 more) in several methylations and reductions with the use of MeOH as the hydrogen donor, all reactions employing a hydrogen transfer mechanism [160]. In Table 7 the results for the methylation of aniline are shown. Similar rate differences were found for the methylation of nitrobenzene and the hydrogenation of benzaldehyde. DFT

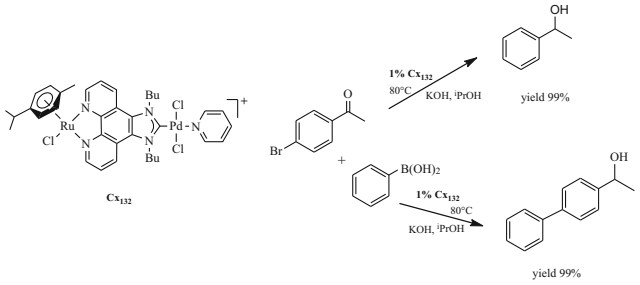

Scheme 70 High yields provided by complex [Ru-Pd] $\mathbf{Cx_{132}}$ in the catalyzed dehalogenation/transfer hydrogenation and Suzuki-Miyaura coupling/transfer hydrogenation reactions

Scheme 71 Bimetallic Rh/In hydrodefluorination catalysts $\mathbf{Cx_{133}}$

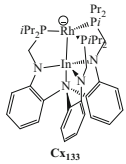

Table 7 1-Methylation of aniline with $\mathbf{Cx_{134}}$, $\mathbf{Cx_{135}}$, and $\mathbf{Cx_{136}}$ catalysts

Yield	
Catalyst $\mathbf{Cx_{134}}$	>99%
Catalyst $\mathbf{Cx_{135}}$	70%
Catalyst $\mathbf{Cx_{136}}$	51%
Catalyst $\mathbf{Cx_{135}}$ + $\mathbf{Cx_{136}}$	65%

Reaction conditions: aniline (0.5 mmol), catalyst (Ir: 0.5 mol%) KOtBu (1 equiv), MeOH (1 mL), 130°C, 4 h

calculations showed that there is a strong NBO interaction between the two Ir centers in $\mathbf{Cx_{134}}$, in spite of the long Ir–Ir distance of 7.58 Å. As a result the relevant Ir–H distances in the intermediates are lengthened, thus creating more active catalysts, in particular in the five-membered irida-ring of $\mathbf{Cx_{134}}$ (Scheme 72).

5.9 Bichromophoric Ru-Pd and Ir-Pd Catalysts

The ruthenium-palladium dinuclear complex $\mathbf{Cx_{137}}$ is particular since the Ru metal center is a visible-light-absorbing unit so that the Pd metal center becomes active under irradiation. As shown by Akita and Inagaki et al., this complex catalyzes the dimerization of α-methylstyrene into 2,4-diphenyl-4-methyl-1-pentene (Scheme 73) and the highest photocatalytic activity was observed for R = Me and X = Br [161]. In this case the Metal-to-Ligand Charge-Transfer transition to the bridging

Scheme 72 Mono- and bimetallic catalysts Ir(III)-NHC **Cx$_{134}$**–**Cx$_{136}$**

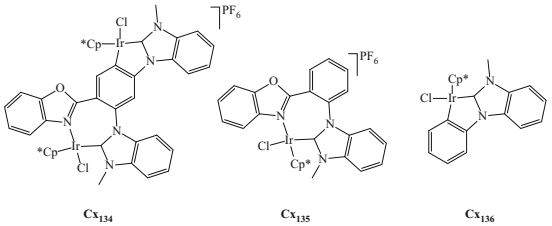

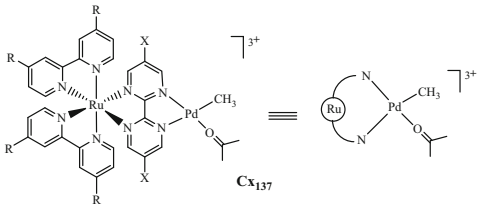

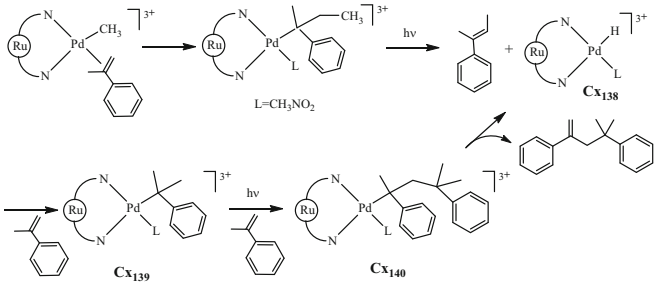

Scheme 73 Photocatalysis induced by the bichromophoric Ru-Pd **Cx$_{137}$** catalyst

ligand is the most efficient. A first coordination of the substrate occurs, followed by methyl migration reaction, before generating the active hydride species **Cx$_{138}$**. Then α-methylstyrene coordinates, forming the alkyl species **Cx$_{139}$** by hydride migration. The rate-determining step concerns the second insertion of the substrate to give **Cx$_{140}$**, for which the electronic structure of the excited species is strongly affected by the photoirradiation, resulting in an elongation of 0.3 Å of the Pd-C bond in **Cx$_{139}$** when α-methylstyrene approaches the Pd center [162].

Similarly, the Ir-Pd complex **Cx$_{141}$** in which the ruthenium metal center of **Cx$_{137}$** has been replaced by the iridium metal (R = 2-naphthyl, X = Br) catalyzes the polymerization of styrene and the copolymerization of styrene and 2,2,2-trifluoroethyl vinyl ether (TFEVE) [163, 164]. The authors checked that no radicals are involved and the reaction proceeds exclusively through a coordination mechanism on the Pd center. Under dark conditions the styrene/TFEVE mixture provides only polymerization of TFEVE and the dimerization of styrene. The long lifetime of the **Cx$_{141}$** complex in its excited-state accelerates the insertion of the monomer [162]. Cu(I) centers are also widely used as chromophores and indeed they can

Scheme 74
Photopolymerization of styrenes using catalyst **Cx$_{142}$**

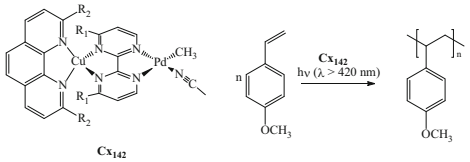

also be used in the Pd-catalyzed styrene polymerization described here. Complex **Cx$_{142}$** containing a sterically congested Cu center catalyzed styrene polymerization under visible-light irradiation to furnish polystyrenes via a nonradical mechanism (Scheme 74) [165].

5.10 Heterogeneous Systems

Recent work deals with the reaction of dimeric iridium(IV) species $[Ir_2(\mu\text{-}O)(H_2O)_2(macac)_2(pyalc)_2]$ **Cx$_{143}$**, where the two bidentate ligands are 2-methyl-2-acetylacetonate and 2-(2′-pyridyl)-2-propane, on an α-Fe_2O_3 substrate through a photochemical treatment to prepare a heterogeneous catalyst **Cx$_{144}$** consisting of two iridium atoms per catalytic site on the surface [166]. The resulting catalytic site (Scheme 75), in which the two Ir(IV) atoms are bridged by two oxygen atoms and are exclusively side-on bonded to the Fe_2O_3 surface through oxygen atoms, presents an outstanding stability against aggregation or detachment and is highly active toward water oxidation (WOC), as already explored [167, 168]. The catalytic activity is considerably higher than that for the corresponding single-atom catalyst and the turnover frequency per Ir(IV) center is around 5 times higher [166]. The same catalyst was studied with WO_3 as a support and now the Ir dimer is end-on immobilized [169].

In a similar approach Macchioni and co-workers studied a dimeric Cp*Ir catalyst in the homogeneous phase and immobilized on a TiO_2 support (Scheme 76) [170]. In this instance the "homogeneous" catalyst remains intact and is not stripped from its ligands. Mononuclear analogs and dinuclear WOCs were tested in homogeneous and heterogeneous water oxidation with sodium periodate as the oxygen source. A remarkable performance was observed for **Cx$_{145}$**@TiO_2, both in terms of TOF (up to 41 min^{-1}) and recyclability, which are significantly higher than those of similar materials derived from mononuclear complexes.

Metal pair site catalysts on surfaces were reviewed recently [171].

6 Conclusions

As shown along this chapter, a reactivity enhancement is observed in many bimetallic catalytic species, when compared with the monometallic counterparts. This phenomenon, described as cooperative effect between the two metal centers,

Scheme 75 Preparation from the $\mathbf{Cx_{143}}$ binuclear complex of the $\mathbf{Cx_{144}}$ heterogeneous catalyst with two Ir(IV) atoms side-on bonded to a Fe_2O_3 surface

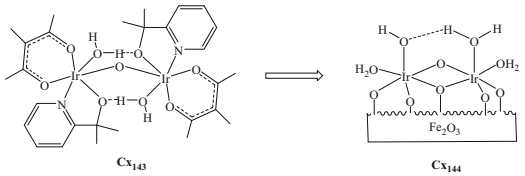

$\mathbf{Cx_{143}}$ $\mathbf{Cx_{144}}$

Scheme 76 Complex $\mathbf{Cx_{145}}$

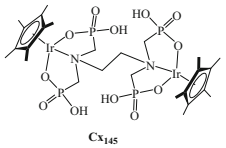

$\mathbf{Cx_{145}}$

requires kinetic studies and theoretical calculations to ascertain that it operates along the catalytic cycle and for each of the different steps occurring along the conversion of the substrates into the expected products.

In some cases, the enhanced activities observed are due to the coexistence of highly reactive mononuclear species and could induce to misleading conclusions, as observed, for instance, in some $[Rh_2(\mu\text{-}Cl)_2(diphos)_2]$ complexes.

When truly dinuclear species are involved along the reaction, the nature of the bridging ligands holding together both metals and their basicity governs the cooperative effect. In this chapter, we have collected bimetallic catalyst systems, in which the nature of the bridging ligand plays an essential role as the distance and orientation of the two metal centers in their ligand environment determine the mutual steric and electronic influences. We have brought to light that there are many ways one metal can influence the reactivity of a neighboring metal, both in stoichiometric and catalytic reactions.

Concerning the structure of the catalyst precursor, it can contain two of the same metals with or without a plane of symmetry or two-fold symmetry axis. When the two metals are different or the same but part of a dissymmetric structure, each metal clearly has its own well-defined role in the reactions with the substrates.

Many examples involve the same metal in symmetric compounds (see, for instance, Schemes 1, 2, 3, 4, 5, and 6 as examples of oxidative addition) in which one metal undergoes the reaction with the substrate electronically enhanced by the presence of the second metal. In Scheme 7, representing a catalytic system for carbonylation of methanol, the electronic interaction between the two rhodium centers unexpectedly enhances the rate of oxidative addition. Subsequent reaction on the second metal is retarded in all cases by electronic factors (Schemes 7, 16, and 17). Changes in free energy of activation may be small, as DFT calculations have shown, but small changes correspond in catalysis to large rate enhancements.

In some examples, only one metal is directly involved in catalysis (i.e., methanol carbonylation with Rh-dimers), but in some cases (i.e., bimetallic rhodium hydroformylation catalyst with two chiral centers, Schemes 9, 10, and 11) after

oxidative addition on one metal center both metals participate in the catalytic cycle. In this case, the orientation of the two centers determines the reactivity, as can be concluded from the much higher reactivity of the species containing the *rac* ligand **L5** compared to that of the species with the *meso* ligand, although this is not understood in detail.

Symmetric bimetallic molecules having a metal–metal bond can be desymmetrized by reaction with a bifunctional substrate and one two-electron oxidative addition may take place (Schemes 18, 19, 20, and 43) or double two-electron oxidative additions (Schemes 62 and 63). For some of these cases two one-electron oxidative additions can be imagined (Scheme 64) as proven also for bimetallic molybdenum containing a metal–metal bond (Scheme 45). In the desymmetrization reactions one functionality precoordinates to one of the metals, which works as a "tug-in" effect. The reaction can start on one metal center and continue on both centers (Scheme 43). The tug-in effect is very common for symmetric bimetallic polymerization catalysts (Scheme 24) and may cause selective rate enhancements in homo- and copolymerizations. Two other effects are observed in symmetric bimetallic polymerization catalysts, an electronic effect exerted by one metal on the other raising the electrophilicity and thus the reactivity, and a steric effect of one metal-ligand moiety on the other, changing the stereoselectivity of the catalyst (Schemes 25, 26, 27, 28, 29, 30, 31, 32, 33, 34, 35, 36, 37, 38, and 39). In the polymerization systems only migratory insertion reactions and chain transfer reactions take place and there are no changes in valency.

This is in contrast with the bis-palladium systems active in C–H activation processes. The binding motive in the palladium complexes is bridging acetates and amidinates (Schemes 51, 52, 53, 54, and 55). The C–H activation takes place on one palladium atom, while often the same metal functions as a tug-in coordinating site. Depending on ligands and substrates various combinations of palladium valence states may occur, from Pd(0) to Pd(IV). The proximity of the two centers leads to strong electronic effects.

All examples require proximity of the two metal centers for electronic and/or steric influences to be effective. The one example reviewed here with rather distant ruthenium centers (Scheme 49) is an exception. There is no direct influence between the metal centers but yet due to the cleverly arranged Ru–Ru distance the catalyst gives selectively the 22-membered cyclic diene.

In heterobimetallic systems the role of the second metal is often that of a tug-in metal and it is especially effective in reaction schemes involving association equilibria, such as the Michael addition (Schemes 56, 57, 58, and 59). The reaction rate can be tuned by adjusting the distance between the two metal centers and choosing the appropriate Lewis acidity.

A catalytic role for both hetero-metals exhibiting a bimetallic effect is rare, but there is one elegant example involving a Zr alkene polymerization catalyst and a Cr ethene oligomerization catalyst that provides the alkene (Scheme 32). In addition to the electronic and steric effects noted above, the proximity of the two catalysts leads to an unusually high effective concentration of hexene reacting at the Zr center. This

is certainly one of the bimetallic effects that deserves attention for future developments.

For a number of cases collected here there is no insight yet available and it should be stressed that progress in this area requires accurate kinetic measurements. In addition, theoretical calculations are today essential to check if the cooperative effect between the two metal centers operates along the catalytic cycle and for each of the different steps occurring along the conversion of the substrates into the expected products. Thanks to the increasing sophistication of surface characterization, we may expect more innovations of bimetallic activity on support materials.

Nevertheless, the design of appropriate ligands to maintain at the right distance the two metal centers and eventually playing a significant role to intended steric effects to adjust the reactivity appears to be essential. Thus, regioselectivity and even enantioselectivity can be achieved using the appropriate ligand. A lot of progress is necessary to anticipate the right way to design the multidentate ligand for a given stoichiometric or catalytic reaction.

References

1. Xiong N, Zhang G, Sun X, Zeng R (2020) Metal-metal cooperation in dinucleating complexes involving late transition metals directed towards organic catalysis. Chin J Chem 38:185–201
2. Wang Q, Brooks SH, Liu T, Tomson NC (2021) Tuning metal–metal interactions for cooperative small molecule activation. Chem Commun 57:2839–2853
3. Charles III RM, Brewster TP (2021) H_2 and carbon-heteroatom bond activation mediated by polarized heterobimetallic complexes. Coord Chem Rev 433:213765
4. Maity R, Birenheide BS, Breher F, Sarkar B (2021) Cooperative effects in multimetallic complexes applied in catalysis. ChemCatChem 13:2337–2370
5. Khoshsefat M, Ma Y, Sun W-H (2021) Multinuclear late transition metal catalysts for olefin polymerization. Coord Chem Rev 434:213788
6. Xu W, Li M, Qiao L, Xie J (2020) Recent advances of dinuclear nickel- and palladium-complexes in homogeneous catalysis. Chem Commun 56:8524–8536
7. Campos J (2020) Bimetallic cooperation across the periodic table. Nat Rev Chem 4:696–702
8. Hosseini FN (2015) Theoretical studies of methyl iodide oxidative addition to adjacent metal centers in diplatinum(II) complexes. Polyhedron 100:67–73
9. Scott JD, Puddephatt RJ (1986) A comparison of the reactivities toward oxidative addition of the dimethylplatinum(II) units in mononuclear and binuclear complexes with bis(diimine) ligands. Organometallics 5:2522–2529
10. Jamali S, Nabavizadeh SM, Rashidi M (2008) Binuclear cyclometalated organoplatinum complexes containing 1,1′-bis(diphenylphosphino)ferrocene as spacer ligand: kinetics and mechanism of MeI oxidative addition. Inorg Chem 47:5441–5452
11. Nabavizadeh SM, Aseman MD, Ghaffari B, Rashidi M, Hosseini FN, Azimi G (2012) Kinetics and mechanism of oxidative addition of MeI to binuclear cycloplatinated complexes containing biphosphine bridges: effects of ligands. J Organomet Chem 715:73–81
12. Raoof F, Esmaeilbeig AR, Nabavizadeh SM, Hosseini FN, Kubicki M (2013) Bridging and chelating roles of bis(2-(diphenylphosphino)ethyl)phenylphosphine in stabilizing binuclear platinum complexes. Organometallics 32:3850–3858
13. Nabavizadeh SM, Sepehrpour H, Kia R, Rheingold AL (2013) Bis(diphenylphosphino)-acetylene as bifunctional ligand in cycloplatinated complexes: synthesis, characterization,

crystal structures and mechanism of MeI oxidative addition. J Organomet Chem:745–746. 148–157
14. Aghakhanpour RB, Rashidi M, Hosseini FN, Raoof F, Nabavizadeh SM (2015) Oxidation of a rollover cycloplatinated(II) dimer by MeI: a kinetic study. RSC Adv 5:66534–66542
15. Haddadi E, Nabavizadeh SM, Hosseini FN (2019) Computational study of the CI bimetallic oxidative addition at PtM (M = Ni, Pd and Pt) reaction centers. Polyhedron 164:35–40
16. Hoseini SJ, Nabavizadeh SM, Jamali S, Rashidi M (2008) Uncommon solvent effect in oxidative addition of MeI to a new dinuclear platinum complex containing a platina(II)-cyclopentane moiety. Eur J Inorg Chem:5099–5105
17. Mayanza A, Kalck P, Poilblanc R (1976) Complexes dinucléaires pontés des métaux d^8. Réactions d'addition oxydante d'halogénures de méthyle aux complexes dinucléaires [RhCl(CO)$(PR_3)]_2$. CR Acad Sci Paris 282:963–966
18. Doyle MJ, Mayanza A, Bonnet J-J, Kalck P, Poilblanc R (1978) Complexes dinucléaires pontés des métaux d^8.VII, réactions d'addition oxydante d'halogénures d'alkyle et d'acyle aux complexes μ-halogénés du rhodium(I) [RhX(CO)$(PR_3)]_2$. Structure cristalline de [RhCl(CO)$(PMe_2Ph)(Me)(Br)]_2$. J Organomet Chem 146:293–310
19. Poilblanc R (1982) Bridged homobimetallic complexes as models of dimetal active centres: the role of metal-metal bonding. Inorg Chim Acta 62:75–86
20. Mayenza A, Bonnet J-J, Galy J, Kalck P, Poilblanc R (1980) Dinuclear-bridged d^8 metal complexes. Part VIII. Study of the oxidative addition reaction at a single metal centre. Crystal structure of $[Rh_2(\mu\text{-}SBu^t)_2(CO)(PMe_2Ph)_2(COCH_3)I]$. J Chem Res 146:2101–2133
21. Bonnet J-J, Kalck P, Poilblanc R (1977) Dinuclear-bridged d^8 metal complexes. 6. Crystal and molecular structure and infrared study of $[Rh(SC_6H_5)(CO)(P(CH_3)_3)]_2$. Inorg Chem 16:1514–1518
22. Jimenez MV, Sola E, Egea MA, Huet A, Francisco AC, Lahoz FJ, Oro LA (2000) Key factors determining the course of methyl iodide oxidative addition to diamidonaphtalene-bridged diiridium(I) and dirhodium(I) complexes. Inorg Chem 39:4868–4878
23. Freixa Z, Kamer PCJ, Lutz M, Spek AL, van Leeuwen PWNM (2005) Activity of SPANphos rhodium dimers in methanol carbonylation. Angew Chem Int Ed 44:4385–4388
24. Lopez-Valbuena JM, Escudero-Adan EC, Benet-Buchholz J, Freixa Z, van Leeuwen PWNM (2010) An approach to bimetallic catalysts by ligand design. Dalton Trans 39:8560–8574
25. Feliz M, Freixa Z, van Leeuwen PWNM, Bo C (2005) Revisiting the methyl iodide oxidative addition to rhodium complexes: a DFT study of the activation parameters. Organometallics 24: 5718–5723
26. Thomas CM, Mafua R, Therrien B, Rusanov E, Stoeckli-Evans H, Süss-Fink G (2002) New diphosphine ligands containing ethyleneglycol and amino alcohol spacers for the rhodium-catalyzed carbonylation of methanol. Chem A Eur J 8:3343–3352
27. Thomas CM, Süss-Fink G (2003) Ligands effects in the rhodium-catalyzed carbonylation of methanol. Coord Chem Rev 243:125–142
28. Burger S, Therrien B, Süss-Fink G (2005) Square-planar carbonylchlororhodium(I) complexes containing trans-spanning diphosphine ligands as catalysts for the carbonylation of methanol. Helv Chim Acta 88:478–486
29. Freixa Z, van Leeuwen PWNM (2008) *Trans*-chelating diphosphines, the elusive ligands. Coord Chem Rev 252:1755–1786
30. Fernando RG, Gasery CD, Moulis MD, Stanley GG (2016) Bimetallic homogeneous hydroformylation. In: Kalck P (ed) Homo- and heterobimetallic complexes in catalysis: cooperative catalysis. Topics organometallic chemistry, vol 59. Springer, pp 1–30
31. Aubry DA, Bridges NN, Ezell K, Stanley GG (2003) Polar phase hydroformylation: the dramatic effect of water on mono- and dirhodium catalysts. J Am Chem Soc 125:11180–11181
32. Nakajima T, Sakamoto M, Kurai S, Kure B, Tanase T (2013) Reversible dioxygen binding on asymmetric dinuclear rhodium centres. Chem Commun 49:5250–5252

33. Nakajima T, Maeda M, Matsui A, Nishigaki M, Kotani M, Tanase T (2022) Unsymmetric dinuclear RhI_2 and RhIRhIII complexes supported by tetraphosphine ligands and their reactivity of oxidative protonation and reductive dechlorination. Inorg Chem 61:1102–1117
34. Patureau FW, de Boer S, Kuil M, Meeuwissen J, Breuil P-AR, Siegler MA, Spek AL, Sandee AJ, de Bruin B, Reek JNH (2009) Sulfonamido−phosphoramidite ligands in cooperative dinuclear hydrogenation catalysis. J Am Chem Soc 131:6683–6685
35. Patureau FW, Gross J, Ernsting JM, van Wüllen C, Reek JNH (2018) P-N bridged dinuclear Rh-METAMORPhos complexes: NMR and computational studies. Eur J Inorg Chem:3761–3769
36. See for example Trzeciak AM, Ziółkowski JJ, Choukroun R (1996) New bimetallic rhodium-zirconium catalysts for homogeneous olefin hydroformylation. J Mol Catal A Chem 110(2): 135–139
37. Nguyen DH, Modrego FJ, Cetina-Casas JM, Gómez-Bautista D, Jiménez MV, Castarlenas R, Lahoz FJ, Oro LA, Pérez-Torrente JJ (2012) Steric effects in the oxidative addition of MeI to a sulfido-bridged $ZrRh_2$ early–late heterobimetallic compound. Organometallics 31(17): 6395–6407
38. Sola E, Bakhmutov VI, Torres F, Elduque A, López JA, Lahoz FJ, Werner H, Oro LA (1998) Cooperative bimetallic effects on new iridium(III) pyrazolate complexes: hydrogen−hydrogen, carbon−hydrogen, and carbon−chlorine bond activations. Organometallics 17(4): 683–696
39. Martín M, Sola E, Tejero S, López JA, Oro LA (2006) Mechanistic investigations of imine hydrogenation catalyzed by dinuclear iridium complexes. Chem A Eur J 12:4057–4068
40. Ciriano MA, Tena MA, Oro LA (1992) Reactions of chloroform and *gem*-dichlorocarbons with binuclear rhodium complexes leading to functionalized methylene-bridged compounds. J Chem Soc Dalton Trans:2123–2124
41. Tejel C, Ciriano MA, Oro LA, Tiripicchio A, Ugozzoli F (2001) Bimetallic reactivity of dirhodium compounds leading to functionalized methylene-bridged compounds. Organometallics 20:1676–1682
42. Tejel C, Ciriano MA, Edwards AJ, Lahoz FJ, Oro LA (2000) Oxidative-addition of organic monochloro derivatives to dinuclear rhodium complexes: mechanistic considerations. Organometallics 19:4968–4976
43. Tejel C, Ciriano MA, Lopez JA, Jimenez S, Bordonaba M, Oro LA (2007) One-electron versus two-electron mechanisms in the oxidative addition reactions of chloroalkanes to amido-bridged rhodium complexes. Chem A Eur J 13:2044–2053
44. Meissner A, Preetz A, Drexler H-J, Baumann W, Spannenberg A, König A, Heller D (2015) In situ synthesis of neutral dinuclear rhodium diphosphine complexes $[\{Rh(diphosphine)(\mu_2\text{-}X)\}_2]$: systematic investigations. ChemPlusChem 80:169–180
45. El Amane M, Maisonnat A, Dahan F, Pince R, Poilblanc R (1985) Double oxidative addition reaction of dihalomethane to dinuclear iridium(I) complexes: preparation and properties of some methylene-bridged diiridium(III) complexes. X-ray structure of $[IrI(\mu\text{-}t\text{-}BuS)(CO)(P(OMe)_3]_2[\mu\text{-}CH_2]$. Organometallics 4:773–780
46. Ball GE, Cullen WR, Fryzuk MD, James BR, Rettig SJ (1991) Oxidative addition of dichloromethane to $[(dppe)Rh]_2(\mu\text{-}Cl)_2$ (dppe=$Ph_2PCH_2CH_2PPh_2$). X-ray structure of $[(dppe)Rh]_2(\mu\text{-}Cl)_2(\mu\text{-}CH_2)$. Organometallics 10:3767–3769
47. Scheetz PM, Blank NF, Gibbons SK, Glueck DS, Rheingold AL (2018) Oxidative addition of methylene chloride to Me-DuPhos complexes of palladium and rhodium. Inorg Chim Acta 483:111–115
48. Brunet JJ, Couillens X, Daran J-C, Diallo O, Lepetit C, Neibecker D (1998) Activation of dichloromethane by $(phosphane)_n$rhodium(I) complexes - X-ray structure of $[\{(PEt_3)_2RhCl\}_2(\mu\text{-}Cl)_2(\mu\text{-}CH_2)]$. Eur J Inorg Chem:349–353
49. Blank B, Glatz G, Kempe R (2009) Single and double C-Cl activation of methylene chloride by P,N-ligand coordinated rhodium complexes. Chem Asian J 4:321–327

50. Mannu A, Drexler H-J, Thede R, Ferro M, Baumann W, Rüger J, Heller D (2018) Oxidative addition of CH_2Cl_2 to neutral dimeric rhodium diphosphine complexes. J Organomet Chem 871:178–184
51. Zhou Y-Y, Hartline DR, Steiman TJ, Fanwick PE, Uyeda C (2014) Dinuclear nickel complexes in five states of oxidation using a redox-active ligand. Inorg Chem 53:11770–11777
52. Rounds HR, Zeller M, Uyeda C (2018) Dinuclear pathways for the activation of strained three-membered rings. Organometallics 37:545–550
53. Behlen MJ, Zhou Y-Y, Steiman TJ, Pal S, Hartline DR, Zeller M, Uyeda C (2017) Dinuclear oxidative addition reactions using an isostructural series of Ni_2, Co_2, and Fe_2 complexes. Dalton Trans 46:5493–5497
54. Hartline DR, Zeller M, Uyeda C (2017) Catalytic carbonylative rearrangement of norbornadiene via dinuclear carbon-carbon oxidative addition. J Am Chem Soc 139:13672–13675
55. Pal S, Zhou Y-Y, Uyeda C (2017) Catalytic reductive vinylidene transfer reactions. J Am Chem Soc 139:11686–11689
56. Stevens H, Duan P-C, Dechert S, Meyer F (2020) Competing H_2 versus intramolecular C–H activation at a dinuclear nickel complex via metal–metal cooperative oxidative addition. J Am Chem Soc 142(14):6717–6728
57. Ahmed SM, Poater A, Childers MI, Widger PCB, LaPointe AM, Lobkovsky EB, Coates GW, Cavallo L (2013) Enantioselective polymerization of epoxides using biaryl-linked bimetallic cobalt catalysts: a mechanistic study. J Am Chem Soc 135:18901–18911
58. McInnis JP, Delferro M, Marks TJ (2014) Multinuclear group 4 catalysis: olefin polymerization pathways modified by strong metal−metal cooperative effects. Acc Chem Res 47:2545–2557
59. Ainooson M, Meyer F (2013) Bimetallic approaches in olefin polymerization and metathesis. In: Reedijk J, Poeppelmeier K (eds) Comprehensive inorganic chemistry II: from elements to applications, vol 8, pp 433–458
60. Cai Z, Xiao D, Do LH (2019) Cooperative heterobimetallic catalysts in coordination insertion polymerization. Comments Inorg Chem 39:27–50
61. Liu S, Invergo AM, McInnis JP, Mouat AR, Motta A, Lohr TL, Delferro M, Marks TJ (2017) Distinctive stereochemically linked cooperative effects in bimetallic titanium olefin polymerization catalysts. Organometallics 36:4403–4421
62. Li H, Li L, Marks TJ, Liable-Sands L, Rheingold AL (2003) Catalyst/cocatalyst nuclearity effects in single-site olefin polymerization. Significantly enhanced 1-octene and isobutene comonomer enchainment in ethylene polymerizations mediated by binuclear catalysts and cocatalysts. J Am Chem Soc 125:10788–10789
63. Li L, Metz MV, Li H, Chen M-C, Marks TJ, Liable-Sands L, Rheingold AL (2002) Catalyst/cocatalyst nuclearity effects in single-site polymerization. Enhanced polyethylene branching and α-olefin comonomer enchainment in polymerizations mediated by binuclear catalysts and cocatalysts via a new enchainment pathway. J Am Chem Soc 124:12725–12741
64. Guo N, Li L, Marks TJ (2004) Bimetallic catalysis for styrene homopolymerization and ethylene−styrene copolymerization. Exceptional comonomer selectivity and insertion regiochemistry. J Am Chem Soc 126:6542–6543
65. Salata MR, Marks TJ (2008) Synthesis, characterization, and marked polymerization selectivity characteristics of binuclear phenoxyiminato organozirconium catalysts. J Am Chem Soc 130:12–13
66. Makio H, Fujita T (2009) Development and application of FI catalysts for olefin polymerization: unique catalysis and distinctive polymer formation. Acc Chem Res 42:1532–1544
67. Liu S, Xing Y, Zheng Q, Jia Y, Li Z (2020) Synthesis of anthracene-bridged dinuclear phenoxyiminato organotitanium catalysts with enhanced activity, thermal stability, and comonomer incorporation ability toward ethylene (Co)polymerization. Organometallics 39(17): 3268–3274

68. Invergo AM, Liu S, Dicken RD, Mouat AR, Delferro M, Lohr TL, Marks TJ (2018) How close is too close? Polymerization behavior and monomer-dependent reorganization of a bimetallic Salphen organotitanium catalyst. Organometallics 37:2429–2436
69. Jüngling S, Rolf Mülhaupt R, Plenio H (1993) Cooperative effects in binuclear zirconocenes: their synthesis and use as catalyst in propene polymerization. J Organomet Chem 460:191–195
70. Lee D-H, Yoon K-B, Noh S-K, Kim S-C, Huh W-S (1996) Polymerization of ethene initiated with a mixture of siloxane-bridged mono- and dinuclear zirconocenes. Macromol Rapid Commun 17:639–644
71. Noh S-K, Kim J, Jung J, Ra CS, Lee D-H, Lee HB, Lee SW, Huh W-S (1999) Syntheses of polymethylene bridged dinuclear zirconocenes and investigation of their polymerization activities. J Organomet Chem 580:90–97
72. Li H, Li L, Marks TJ (2004) Polynuclear olefin polymerization catalysis: proximity and cocatalyst effects lead to significantly increased polyethylene molecular weight and comonomer enchainment levels. Angew Chem Int Ed 43:4937–4940
73. Sampson J, Bruening M, Akhtar MN, Jaseer EA, Theravalappil R, Garcia N, Agapie T (2021) Copolymerization of ethylene and long-chain functional α-olefins by dinuclear zirconium catalysts. Organometallics 40(12):1854–1858
74. van Leeuwen PWNM, Chadwick JC (2011) Homogeneous catalysts: activity – stability – deactivation. Wiley-VCH Verlag GmbH & Co
75. Liu S, Motta A, Mouat AR, Delferro M, Marks TJ (2014) Very large cooperative effects in heterobimetallic titanium-chromium catalysts for ethylene polymerization/copolymerization. J Am Chem Soc 136:10460–10469
76. McGuinness DS, Wasserscheid P, Keim W, Morgan D, Dixon JT, Bollmann A, Maumela H, Hess F, Englert U (2003) First Cr(III)−SNS complexes and their use as highly efficient catalysts for the trimerization of ethylene to 1-hexene. J Am Chem Soc 125:5272–5273
77. Kamigaito M, Lal TK, Waymouth RM (2000) Olefin polymerization with Me_4Cp-amido complexes with electron-withdrawing groups. J Polym Sci A Polym Chem 38:4649–4660
78. Ehm C, Budzelaar PHM, Busico V (2017) Tuning the relative energies of propagation and chain termination barriers in polyolefin catalysis through electronic and steric effects. Eur J Inorg Chem:3343–3349
79. Mu H, Pan L, Song D, Li Y (2015) Neutral nickel catalysts for olefin homo- and copolymerization: relationships between catalyst structures and catalytic properties. Chem Rev 115: 12091–12137
80. Younkin TR, Connor EF, Henderson JI, Friedrich SK, Grubbs RH, Bansleben DA (2000) Neutral, single-component nickel(II) polyolefin catalysts that tolerate heteroatoms. Science 287:460–462
81. Hu T, Tang L-M, Li X-F, Li Y-S, Hu N-H (2005) Synthesis and ethylene polymerization activity of a novel, highly active single-component binuclear neutral nickel(II) catalyst. Organometallics 24:2628–2632
82. Radlauer MR, Day MW, Agapie T (2012) Bimetallic effects on ethylene polymerization in the presence of amines: inhibition of the deactivation by Lewis bases. J Am Chem Soc 134:1478–1481
83. Radlauer MR, Buckley AK, Henling LM, Agapie T (2013) Bimetallic coordination insertion polymerization of unprotected polar monomers: copolymerization of amino olefins and ethylene by dinickel bisphenoxyiminato catalysts. J Am Chem Soc 135:3784–3787
84. Sujith S, Joe DJ, Na SJ, Park YW, Choi CH, Lee BY (2005) Ethylene/polar norbornene copolymerizations by bimetallic salicylaldimine−nickel catalysts. Macromolecules 38: 10027–10033
85. Na SJ, Joe DJ, Sujith S, Han WS, Kang SO, Lee BY (2006) Bimetallic nickel complexes of macrocyclic tetraiminodiphenols and their ethylene polymerization. J Organomet Chem 691: 611–620

86. Wang W-H, Jin G-X (2006) Binuclear neutral nickel complexes bearing bis(bidentate) salicylaldiminato ligands: synthesis, structure and ethylene polymerization behavior. Inorg Chem Commun 9:548–550
87. Wehrmann P, Mecking S (2008) Highly active binuclear neutral nickel(II) catalysts affording high molecular weight polyethylene. Organometallics 27:1399–1408
88. Zhang D, Jin G-X (2006) Bimetallic nickel complexes of trimethyl phenyl linked salicylaldimine ligands: synthesis, structure and their ethylene polymerization behaviors. Inorg Chem Commun 9:1322–1325
89. Chen Q-H, Yu J, Huang J-L (2007) Arene-bridged salicylaldimine-based binuclear neutral nickel(II) complexes: synthesis and ethylene polymerization activities. Organometallics 26: 617–625
90. Rodriguez BA, Delferro M, Marks TJ (2008) Neutral bimetallic nickel(II) phenoxyiminato catalysts for highly branched polyethylenes and ethylene-norbornene copolymerizations. Organometallics 27:2166–2168
91. Shu D, Mouat AR, Stephenson CJ, Invergo AM, Delferro M, Marks TJ (2015) Ligand-unsymmetrical phenoxyiminato dinickel catalyst for high molecular weight long-chain branched polyethylenes. ACS Macro Lett 4:1297–1301
92. Li W-W, Mu H-L, Liu J-Y, Li Y-S (2017) 9,9-Dimethylxanthene-based binuclear phenoxy-imine neutral nickel(II) catalysts for ethylene homo- and copolymerization. J Organomet Chem:836–837. 34–43
93. Speiser F, Braunstein P, Saussine L (2005) Catalytic ethylene dimerization and oligomerization: recent developments with nickel complexes containing P,N-chelating ligands. Acc Chem Res 38:784–793
94. Feng C, Zhou S, Wang D, Zhao Y, Liu S, Li Z, Braunstein P (2021) Cooperativity in highly active ethylene dimerization by dinuclear nickel complexes bearing a bifunctional PN ligand. Organometallics 40:184–193
95. Chen Z, Yao E, Wang J, Gong X, Ma Y (2016) Ethylene (co)polymerization by binuclear nickel phenoxyiminato catalysts with cofacial orientation. Macromolecules 49:8848–8854
96. Chiu H-C, Koley A, Dunn PL, Hue RJ, Tonks IA (2017) Ethylene polymerization catalyzed by bridging Ni/Zn heterobimetallics. Dalton Trans 46:5513–5517
97. Xiao D, Do LH (2018) In situ generated heterometallic nickel–zinc catalysts for ethylene polymerization. Organometallics 37(18):3079–3085
98. Hübel W, Hoogzand C (1960) Die cyclisierende Trimerisierung von Alkinen mit Hilfe von Metallcarbonyl-Verbindungen. Chem Ber 93:103–115
99. Powers IG, Uyeda C (2017) Metal-metal bonds in catalysis. ACS Catal 7:936–958
100. Khand IU, Knox GR, Pauson PL, Watts WE (1971) A cobalt induced cleavage reaction and a new series of arenecobalt carbonyl complexes. J Chem Soc D 36
101. Magnus P, Principe LM (1985) Origins of 1,2- and 1,3-stereoselectivity in dicobaltoctacarbonyl alkene-alkyne cyclizations for the synthesis of substituted bicyclo [3.3.0]octenones. Tetrahedron Lett 26:4851–4854
102. Pal S, Uyeda C (2015) Evaluating the effect of catalyst nuclearity in Ni-catalyzed alkyne cyclotrimerizations. J Am Chem Soc 137:8042–8045
103. Kwon D-H, Proctor M, Mendoza S, Uyeda C, Ess DH (2017) Catalytic dinuclear nickel spin crossover mechanism and selectivity for alkyne cyclotrimerization. ACS Catal 7:4796–4804
104. Zhou Y-Y, Uyeda C (2019) Catalytic reductive [4 + 1]-cycloadditions of vinylidenes and dienes. Science 363:857–862
105. Uyeda C, Farley CM (2021) Dinickel active sites supported by redox-active ligands. Acc Chem Res 54:3710–3719
106. Chen H-Z, Liu S-C, Yen C-H, Yu J-SK, Shieh Y-J, Kuo T-S, Tsai Y-C (2012) Reactions of metal–metal quintuple bonds with alkynes: [2+2+2] and [2+2] cycloadditions. Angew Chem Int Ed 51:10342–10346

107. Carrasco M, Curado N, Maya C, Peloso R, Rodríguez A, Ruiz E, Alvarez S, Carmona E (2013) Interconversion of quadruply and quintuply bonded molybdenum complexes by reductive elimination and oxidative addition of dihydrogen. Angew Chem Int Ed 52:3227–3231
108. Pérez-Jiménez M, Campos J, López-Serrano J, Carmona E (2018) Reactivity of a trans-[H–MoMo–H] unit towards alkenes and alkynes: bimetallic migratory insertion, H-elimination and other reactions. Chem Commun 54:9186–9189
109. Dias EL, Grubbs RH (1998) Synthesis and investigation of homo- and heterobimetallic ruthenium olefin metathesis catalysts exhibiting increased activities. Organometallics 17: 2758–2767
110. Borguet Y, Sauvage X, Zaragoza G, Demonceau A, Delaude L (2011) Synthesis and catalytic evaluation in olefin metathesis of a second-generation homobimetallic ruthenium–arene complex bearing a vinylidene ligand. Organometallics 30:2730–2738
111. Sémeril C, Bruneau C, Dixneuf PH (2001) Ruthenium catalyst dichotomy: selective catalytic diene cycloisomerization or metathesis. Helv Chim Acta 84:3335–3341
112. Tzur E, Ben-Asuly A, Diesendruck CE, Golberg I, Lemcoff NG (2008) Homodinuclear ruthenium catalysts for dimer ring-closing metathesis. Angew Chem Int Ed 47:6422–6425
113. Bailey GA, Foscato M, Higman CS, Day CS, Jensen VR, Fogg DE (2018) Bimolecular coupling as a vector for decomposition of fast-initiating olefin metathesis catalysts. J Am Chem Soc 140:6931–6944
114. van Helden R, Verberg G (1965) The oxidative coupling of aromatic compounds with palladium salts. Rec Trav Chim Pays-Bas 84:1263–1273
115. Boele MDK, van Strijdonck GPF, de Vries AHM, Kamer PCJ, de Vries JG, van Leeuwen PWNM (2002) Selective Pd-catalyzed oxidative coupling of anilides with olefins through C−H bond activation at room temperature. J Am Chem Soc 124:1586–1587
116. Váňa J, Hanuseka J, Sedláka M (2018) Bi and trinuclear complexes in palladium carboxylate-assisted C–H activation reactions. Dalton Trans 47:1378–1382
117. Molnar SP, Orchin M (1969) The synthesis and infrared spectra of di-μ-chlorobis [o-(N-phenylformimidoyl)phenyl]dipalladium(II) and related complexes. J Organomet Chem 16:196–200
118. Powers DC, Ritter T (2009) Bimetallic Pd(III) complexes in palladium-catalysed carbon–heteroatom bond formation. Nat Chem 1:302–309
119. Powers DC, Ritter T (2012) Bimetallic redox synergy in oxidative palladium catalysis. Acc Chem Res 45:840–850
120. Powers DC, Benitez D, Tkatchouk E, Goddard III WA, Ritter T (2010) Bimetallic reductive elimination from dinuclear Pd(III) complexes. J Am Chem Soc 132:14092–14103
121. Powers DC, Xiao DY, Geibel MAL, Ritter T (2010) On the mechanism of palladium-catalyzed aromatic C−H oxidation. J Am Chem Soc 132:14530–14536
122. Kalyani D, Deprez NR, Desai LV, Sanford MS (2005) Oxidative C−H activation/C−C bond forming reactions: synthetic scope and mechanistic insights. J Am Chem Soc 127:7330–7331
123. Dick AR, Kampf JW, Sanford MS (2005) Unusually stable palladium(IV) complexes: detailed mechanistic investigation of C−O bond-forming reductive elimination. J Am Chem Soc 127: 12790–12791
124. Powers DC, Lee E, Ariafard A, Sanford MS, Yates BF, Canty AJ, Ritter T (2012) Connecting binuclear Pd(III) and mononuclear Pd(IV) chemistry by Pd–Pd bond cleavage. J Am Chem Soc 134:12002–12009
125. Deprez NR, Sanford MS (2009) Synthetic and mechanistic studies of Pd-catalyzed C-H arylation with diaryliodonium salts: evidence for a bimetallic high oxidation state Pd intermediate. J Am Chem Soc 131:11234–11241
126. Ye Y, Ball ND, Kampf JW, Sanford MS (2010) Oxidation of a cyclometalated Pd(II) dimer with "CF_3^{+}": formation and reactivity of a catalytically competent monomeric Pd(IV) aquo complex. J Am Chem Soc 132:14682–14687
127. Ariafard A, Hyland CJT, Canty AJ, Sharma M, Brookes NJ, Yates BF (2010) Ligand effects in bimetallic high oxidation state palladium systems. Inorg Chem 49:11249–11253

128. Ariafard A, Hyland CJT, Canty AJ, Sharma M, Yates BF (2011) Theoretical investigation into the mechanism of reductive elimination from bimetallic palladium complexes. Inorg Chem 50: 6449–6457
129. Lyons TW, Sanford MS (2010) Palladium-catalyzed ligand-directed C−H functionalization reactions. Chem Rev 110:1147–1169
130. Zhang L, Ritter T (2022) A perspective on late-stage aromatic C–H bond functionalization. J Am Chem Soc 144(6):2399–2414
131. Amadeo P, Bhaskararao B, Yang Y-F, Kozlowski MC (2021) Inherent selectivity of Pd C–H activation from different metal oxidation states. Organometallics 40:2290–2294
132. Tsukada N, Mitsuboshi T, Setoguchi H, Inoue Y (2003) Stereoselective cis-addition of aromatic C−H bonds to alkynes catalyzed by dinuclear palladium complexes. J Am Chem Soc 125:12102–12103
133. Tsukada N, Setoguchi H, Mitsuboshi T, Inoue Y (2006) Hydroalkenylation of alkynes catalyzed by dinuclear palladium complexes via C–H bond activation. Chem Lett 35:1164–1165
134. Portnoy M, Frolow F, Milstein D (1991) Methanol reduces an organopalladium(II) complex to a palladium(I) hydride. Crystallographic characterization of a hydrido-bridged palladium complex. Organometallics 10:3960–3962
135. Tsukada N, Murata K, Inoue Y (2005) Selective cis-addition of C–H bonds of pyrroles and thiophenes to alkynes catalyzed by a dinuclear palladium complex. Tetrahedron Lett 46:7515–7517
136. Maki Y, Goto T, Tsukada N (2016) Selective β-arylation of thiophenes with aryl iodides catalyzed by dinuclear palladium carboxylate complexes. ChemCatChem 8:699–702
137. Goto T, Kato H, Tsukada N (2017) Direct β-arylation of furans with aryl iodides catalyzed by dinuclear palladium complexes. Heterocycles 94:2222–2228
138. Jautze S, Peters R (2008) Enantioselective bimetallic catalysis of Michael additions forming quaternary stereocenters. Angew Chem Int Ed 47:9284–9288
139. Feng J, Holmes M, Krische MJ (2017) Acyclic quaternary carbon stereocenters via enantioselective transition metal catalysis. Chem Rev 117:12564–12580
140. Hellmuth T, Rieckhoff S, Weiss M, Dorst K, Frey W, Peters R (2014) Cooperative bimetallic asymmetric catalysis: comparison of a planar chiral ruthenocene bis-palladacycle to the corresponding ferrocene. ACS Catal 4:1850–1858
141. Heberle M, Legendre S, Wannenmacher N, Weber M, Frey W, Peters R (2022) Bispalladacycle catalyzed nucleophilic enantioselective allylation of aldehydes by allylstannanes. ChemCatChem:e202200093
142. Suijkerbuijk BMJM, Schamhart DJ, Kooijman H, Spek AL, van Koten G, Klein Gebbink RJM (2010) Mono(NCN-pincer palladium)-metalloporphyrin catalysts: evidence for supramolecular bimetallic catalysis. Dalton Trans 39:6198–6216
143. Ho JHH, Choy SWS, Macgregor SA, Messerle BA (2011) Cooperativity in bimetallic dihydroalkoxylation catalysts built on aromatic scaffolds: significant rate enhancements with a rigid anthracene scaffold. Organometallics 30:5978–5984
144. Vuong KQ, Wong CM, Bhadbhadea M, Messerle BA (2014) Bi- and tri-metallic Rh and Ir complexes containing click derived bis- and tris-(pyrazolyl-1,2,3-triazolyl) N–N' donor ligands and their application as catalysts for the dihydroalkoxylation of alkynes. Dalton Trans 43:7540–7553
145. Blanco Jaimes MC, Böhling CRN, Serrano-Becerra JM, Hashmi ASK (2013) Highly active mononuclear NAC–gold(I) catalysts. Angew Chem Int Ed 52:7963–7966
146. Timerbulatova MG, Gatus MRD, Vuong KQ, Bhadbhade M, Algarra AG, Macgregor SA, Messerle BA (2013) Bimetallic complexes for enhancing catalyst efficiency: probing the relationship between activity and intermetallic distance. Organometallics 32:5071–5081
147. Steiman TJ, Uyeda C (2015) Reversible substrate activation and catalysis at an intact metal–metal bond using a redox-active supporting ligand. J Am Chem Soc 137:6104–6110

148. Powers IG, Andjaba JM, Luo X, Mei J, Uyeda C (2018) Catalytic azoarene synthesis from aryl azides enabled by a dinuclear Ni complex. J Am Chem Soc 140:4110–4118
149. Quebatte L, Solari E, Scopelliti R, Severin K (2005) A bimetallic ruthenium ethylene complex as a catalyst precursor for the Kharasch reaction. Organometallics 24:1404–1406
150. Simal F, Wlodarczak L, Demonceau A, Noels AF (2001) New, highly efficient catalyst precursors for Kharasch additions – $[RuCl(Cp^*)(PPh_3)_2]$ and $[RuCl(Ind)(PPh_3)_2]$. Eur J Org Chem:2689–2695
151. Haas M, Solari E, Nguyen QT, Gautier S, Scopelliti R, Severin K (2006) A bimetallic ruthenium complex as a catalyst precursor for the atom transfer radical polymerization of methacrylates at ambient temperature. Adv Synth Catal 348:439–442
152. Arif T, Cazorla C, Bogliotti N, Saleh N, Blanchard F, Gandon V, Metivier R, Xie J, Voituriez A, Marinetti A (2018) Bimetallic gold(I) complexes of photoswitchable phosphines: synthesis and uses in cooperative catalysis. Cat Sci Technol 8:710–715
153. Freixa Z (2020) Photoswitchable catalysis using organometallic complexes. Cat Sci Technol 10(10):3122–3139
154. Cazorla C, Casimiro L, Arif T, Deo C, Goual N, Retailleau P, Métivier R, Xie J, Voituriez A, Marinetti A, Bogliotti N (2021) Synthesis and properties of photoswitchable diphosphines and gold(i) complexes derived from azobenzenes. Dalton Trans 50:7284–7292
155. Medici F, Goual N, Delattre V, Voituriez A, Marinetti A (2020) Photoswitchable phosphines in catalysis. ChemCatChem 12:5573–5589
156. Sabater S, Mata JA, Peris E (2013) Hydrodefluorination of carbon-fluorine bonds by the synergistic action of a ruthenium-palladium catalyst. Nat Commun 4:2553
157. Pezük LG, Şen B, Hahn FE, Türkmen H (2019) Heterobimetallic complexes bridged by imidazol{[4,5-f][1,10]-phenanthrolin}-2-ylidene: synthesis and catalytic activity in tandem reactions. Organometallics 38:593–601
158. Mata JA, Hahn FE, Peris E (2014) Heterometallic complexes, tandem catalysis and catalytic cooperativity. Chem Sci 5:1723–1732
159. Moore JT, Lu CC (2020) Catalytic hydrogenolysis of aryl C–F bonds using a bimetallic rhodium–indium complex. J Am Chem Soc 142:11641–11646
160. Huang S, Hong X, Cui H-Z, Zhan B, Li Z-M, Hou X-F (2020) Bimetallic bis-NHC-Ir(III) complex bearing 2-arylbenzo[d]oxazolyl ligand: synthesis, catalysis, and bimetallic effects. Organometallics 39:3514–3523
161. Nitadori H, Takahashi T, Inagaki A, Akita M (2012) Enhanced photocatalytic activity of α-methylstyrene oligomerization through effective metal-to-ligand charge-transfer localization on the bridging ligand. Inorg Chem 51:51–62
162. Kikuchi S, Saito K, Akita M, Inagaki A (2018) Nonradical light-controlled polymerization of styrene and vinyl ethers catalyzed by an iridium–palladium photocatalyst. Organometallics 37: 359–366
163. Murata K, Saito K, Kikuchi S, Akita M, Inagaki A (2015) Visible-light-controlled homo- and copolymerization of styrenes by a bichromophoric Ir–Pd catalyst. Chem Commun 51:5717–5720
164. Ohyama R, Mishima M, Inagaki A (2021) Syntheses and structure of dinuclear metal complexes containing naphthyl-Ir bichromophore. Dalton Trans 50:12716–12722
165. Fujiwara T, Nomura K, Inagaki A (2020) Cu–Pd dinuclear complexes with earth-abundant Cu photosensitizer: synthesis and photopolymerization. Organometallics 39:2464–2469
166. Zhao Y, Yang KR, Wang Z, Yan X, Cao S, Ye Y, Dong Q, Zhang X, Thorne JE, Jin L, Materna KL, Trimpalis A, Bai H, Fakra SC, Zhong X, Wang P, Pan X, Guo J, Flytzani-Stephanopoulos M, Brudvig GW, Batista VS, Wang D (2018) Stable iridium dinuclear heterogeneous catalysts supported on metal-oxide substrate for solar water oxidation. Proc Natl Acad Sci U S A 115:2902–2907
167. Sheehan SW, Thomsen JM, Hintermair U, Crabtree RH, Brudvig GW, Schmuttenmaer CA (2015) A molecular catalyst for water oxidation that binds to metal oxide surfaces. Nat Commun 6(6469):1–9

168. Yang KR, Matula AJ, Kwon G, Hong J, Sheehan SW, Thomsen JM, Brudvig GW, Crabtree RH, Tiede DM, Chen LX, Batista VS (2016) Solution structures of highly active molecular Ir water-oxidation catalysts from density functional theory combined with high-energy X-ray scattering and EXAFS spectroscopy. J Am Chem Soc 138:5511–5514
169. Zhao Y, Yan X, Yang KR, Cao S, Dong Q, Thorne JE, Materna KL, Zhu S, Pan X, Flytzani-Stephanopoulos M, Brudvig GW, Batista VS, Wang D (2018) End-on bound iridium dinuclear heterogeneous catalysts on WO_3 for solar water oxidation. ACS Central Sci 4:1166–1172
170. Domestici C, Tensi L, Zaccaria F, Kissimina N, Valentini M, D'Amato R, Costantino F, Zuccaccia C, Macchioni A (2020) Molecular and heterogenized dinuclear Ir-Cp* water oxidation catalysts bearing EDTA or EDTMP as bridging and anchoring ligands. Sci Bull 65:1614–1625
171. Guan E, Ciston J, Bare SR, Runnebaum RC, Katz A, Kulkarni A, Kronawitter CX, Gates BC (2020) Supported metal pair-site catalysts. ACS Catal 10(16):9065–9085

Top Organomet Chem (2023) 70: 67–98
https://doi.org/10.1007/3418_2022_79

Published online: 3 January 2023

Chemical Transformations in Heterobimetallic Complexes Facilitated by the Second Coordination Sphere

R. Malcolm Charles III and Timothy P. Brewster

Contents

Abstract This chapter is dedicated to heterobimetallic complexes in which the two metal centers are not directly bound. Complexes are described in which the second metal resides in the second coordination sphere of the first metal and enables bond activation processes via synergistic activity with the first metal that are not available to the corresponding monometallic complexes. Both stoichiometric and catalytic bond activations are analyzed in the light of the type of reactions (e.g., H_2 activation, polymerization, etc.). Both steric and electronic effects appear to play significant roles in many cases, and as such, they are examined when applicable. Indeed, spatial proximity between the two metal centers as well as electronic environment can allow for modification and tuning of reactivity. This realization has led to the development of switchable catalytic systems which are highlighted and discussed in terms of how they are manipulated (e.g., redox-switchable systems and cation-responsive systems). While significant progress has been made toward furthering our collective understanding of the behavior of these types of heterobimetallic complexes, this area

R. Malcolm Charles III
Department of Chemistry, The University of Memphis, Memphis, TN, USA
e-mail: rmchrles@memphis.edu

T. P. Brewster (✉)
Department of Chemistry, Faculty of Chemistry, The University of Memphis, Memphis, TN, USA
e-mail: tbrwster@memphis.edu

is still ripe for future development. Additional systematic work is necessary to continue to push this area of chemistry forward.

Keywords Bimetallic · Bond activation · Catalysis · Heterobimetallic · Migratory insertion · Oxidative addition · Reactivity · Reductive elimination · Second coordination sphere

1 Introduction

As the field of bimetallic chemistry continues to develop, it can be beneficial to separate bimetallic structures into two structural categories. In the first category the two metals are covalently bound to each other. Positioning a second metal in the primary coordination sphere of a metal center allows for strong electronic modulation and positions the system for cooperative bond-breaking events. Structures of this type have been widely explored and feature in a number of review articles as well as other chapters within this volume [1–5].

The second category of complex contains bimetallic structures in which the two metal centers are not bound to each other, *but rather exert second coordination sphere effects on each other*. Electronic influence between the two sites is weaker than in directly bound systems, which allows the two metal centers to operate with more independence and to retain properties that these metals would be likely to exhibit in monomeric complexes. However, being tied together in a bimetallic construct can help to overcome kinetic and/or stability issues that can arise in tandem catalytic systems.

Our chapter focuses on this second class of bimetallic complex, with a particular focus on complexes that have been structurally characterized. As an introduction, we will first discuss representative applications of such complexes in stoichiometric bond activations, then move on to explore select, instructive catalytic applications, before finally discussing an emerging area of research in which one metal center is used to switchably attenuate the reactivity at the second metal site. While not designed as an exhaustive literature review of bond activation or catalysis mediated by bimetallic complexes (this has been done elsewhere) [2, 6–8], this chapter will provide a tutorial review sampling the breadth of reactivity that is available in second-sphere systems.

2 Stoichiometric Bond Activation Mediated by the Second Coordination Sphere

Second coordination sphere effects manifest in a number of different ways. The section below will highlight examples that are both unique and instructive. When considering stoichiometric bond activations in bimetallic systems, it is important to distinguish between systems in which the two metal centers act cooperatively and systems in which the two metal centers function somewhat independently. We will consider as "cooperative" bond activations those in which both metal centers are (or likely are) active participants in the elementary step during which the key bond-breaking event occurs. Other systems, where a single metal center is responsible for bond breaking and the second metal serves a separate function (electronic modifier, steric blocking, etc.), will be considered as non-cooperative. Both motifs are frequently encountered.

Our first instructive example, a heterobimetallic potassium-aluminum dimer that, remarkably, functions as a nucleophile, falls into the non-cooperative category (Scheme 1) [9]. In this system the presence of the potassium cation stabilizes a formally Al(I) center bearing a nucleophilic lone pair. The cation is not directly bound to the aluminum center, but rather interacts with aromatic substituents on the sterically bulky pincer ligand employed. Only a strongly electropositive, reducing metal center would be able to stabilize an Al(I) aluminyl in a bimetallic construct. The nucleophilic K-Al heterobimetallic construct was found to activate H_2 and oxidatively add benzene via C–H bond activation. This study represents the first example of intermolecular oxidative addition of a C–H bond in benzene at a single, well-defined, main-group metal center (Scheme 2), with reactivity made possible by the outer-sphere stabilization imparted by the potassium cation.

In a mechanistically similar example, hydrogen activation by heterobimetallic iridium-aluminum and rhodium-aluminum complexes was reported, as shown in Scheme 3 [10]. This system is comprised of a late transition metal center bound to a second-sphere aluminum functionality. In the solid state the two metal centers are separated by over 4 Angstroms preventing the formation of a direct metal–metal bond [11]. Despite the long internuclear distance and relatively weak electronic effect the aluminum site exerts on the transition metal, the system is still able to achieve reactivity that the late transition metal center could not achieve

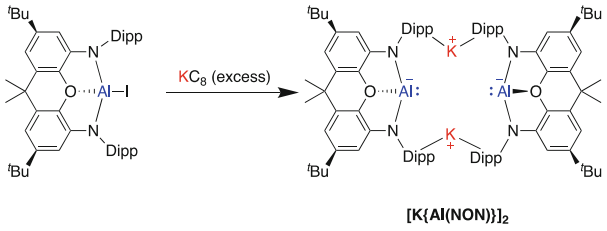

Scheme 1 Synthesis of K-Al heterobimetallic dimer

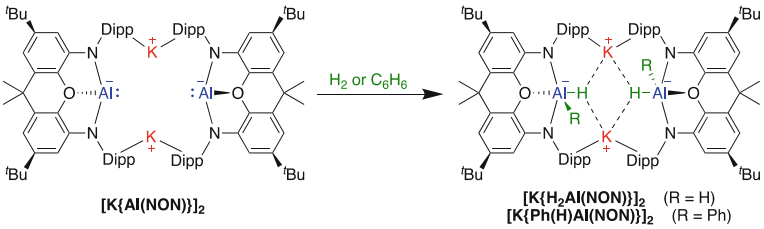

Scheme 2 H_2 activation and oxidative addition of benzene by K-Al heterobimetallic

Scheme 3 General H_2 activation and hydrogenolysis reaction

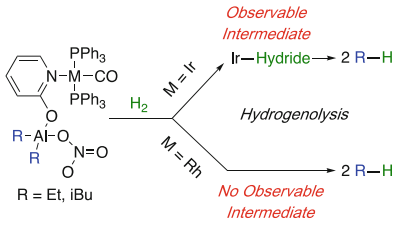

independently. Both Ir and Rh were found to react with hydrogen to generate the observed final product of alkane gas.

A series of kinetic experiments were undertaken to distinguish between several possible, plausible reaction mechanisms (Scheme 4). The authors determined proposed mechanism 1 to be the most likely reaction mechanism, based on derivation of a second-order rate and, in the case of Ir, observation of a stable intermediate resulting from oxidative addition of hydrogen to the transition metal. The transition metal facilitates a classical oxidative addition reaction and subsequently transfers hydrides to the aluminum alkyls, functioning as acceptors, in the second coordination sphere. Notably, while 16-electron Ir centers are well known to oxidatively add H_2, the corresponding oxidative addition reaction with the utilized Rh complexes is endergonic. The reaction proceeds only because the strongly basic aluminum alkyls provide a thermodynamic driving force. The overall mechanics of this stoichiometric reactivity are akin to a tandem catalytic process.

The remaining examples discussed in this section focus on cooperative reactivity. In cooperative second-sphere reactions the two metal centers can function in a manner similar to a Frustrated Lewis Pair (FLP) [12–17], such that they can be considered "masked FLPs." The result is a heterolytic bond cleavage. A beautiful example of this concept is a platinum-aluminum heterobimetallic complex, synthesized in 2016. The Z-type complex was shown to sequester CO_2, CS_2, and to stoichiometrically activate molecular hydrogen via oxidative addition of H–H bonds at elevated temperature (80°C) and pressure (3 bar) (Scheme 5) [18].

At first glance, this reaction may not appear to be a second-sphere process. However, DFT calculations revealed that each step in the reaction is facilitated by

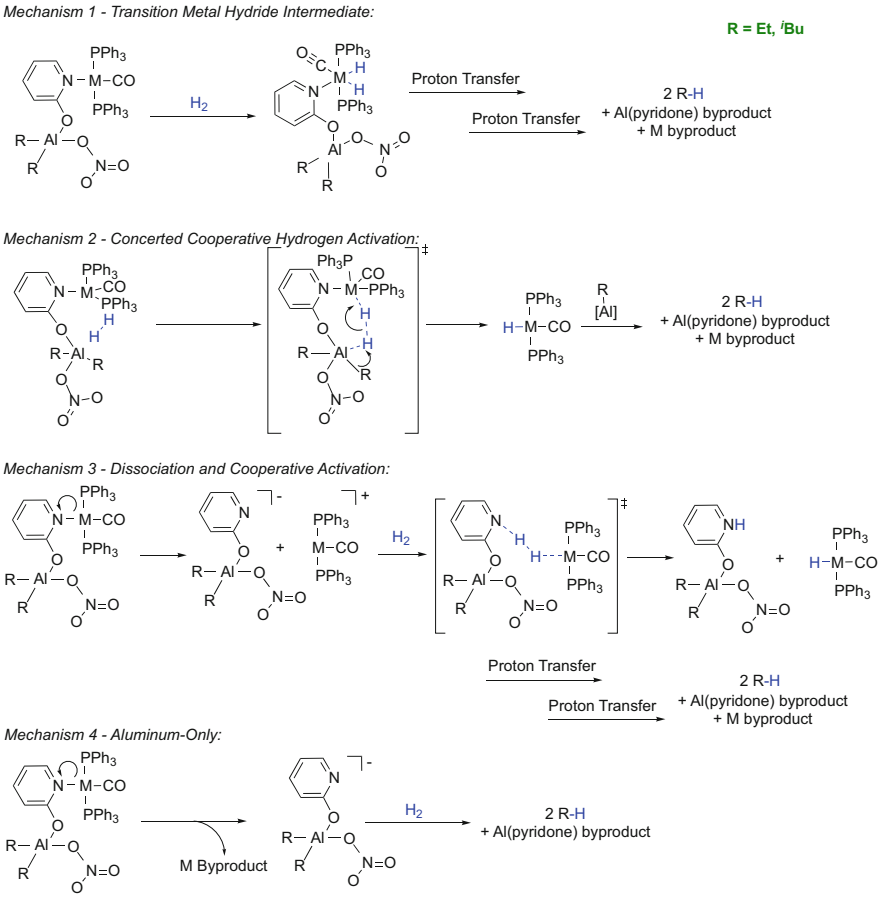

Scheme 4 Considered reaction mechanisms for the reaction of Rh/Ir-Al heterobimetallics with hydrogen

Scheme 5 Hydrogen activation by Pt-Al heterobimetallic

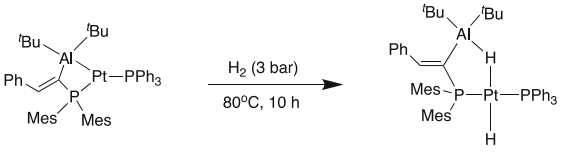

stabilizing interactions with the Al moiety; thus, cooperative interaction between the two metal centers is required for successful H_2 activation. Indeed, the formal Z-type bond between the Pt center and Al is cleaved first, followed by subsequent H_2 coordination. This results in a bridged dihydrogen complex, making this a true second-sphere effect.

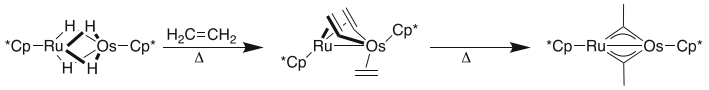

Scheme 6 Reaction of Ru-Os heterobimetallic with ethylene

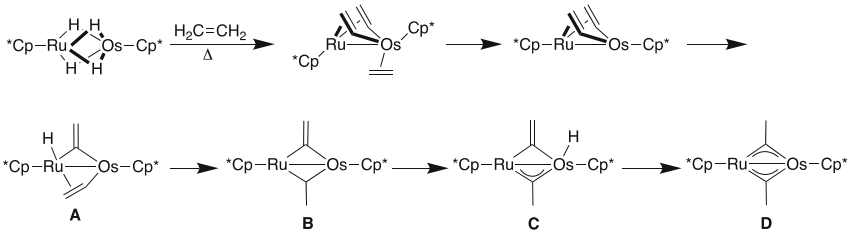

Scheme 7 Proposed mechanism for reaction of Ru-Os heterobimetallic with ethylene

The examples described above beautifully illustrate how a second metal in the second coordination sphere can modulate reactivity. In the first example, the aluminum center is able to access a reactivity manifold (oxidative addition) that is otherwise very unlikely to occur due to the instability of Al(I) complexes. In the second, a tandem-like system is generated in which each metal undergoes a more "standard" reactivity pattern. Finally, our third example demonstrates cooperative bond activation. The final highlighted examples of stoichiometric reactivity that we will present illustrate a different type of cooperative reactivity. As a direct contrast to this system, two metal centers which are initially separated by a bridging ligand are found to be directly bound in the final product.

An Ru-Os tetrahydrido heterobimetallic complex that reacts with ethylene to exclusively generate a divinyl-ethylene complex is shown in Scheme 6 [19]. This report is reminiscent of earlier work from the authors on a related Ru-Ru homobimetallic system [20–22].

The authors proposed a mechanism for this reaction (Scheme 7) in which emancipation of the coordinated η [2]-ethylene, followed by oxidative addition of the C(α) − H bond of one of the two vinyl groups at Ru, produces μ-vinylidene species **A**. **A** then undergoes insertion of the remaining vinyl group into an Ru − H bond giving μ-ethylidene-μ-vinylidene intermediate **B**. Subsequent α-H elimination from the μ-ethylidene ligand followed by insertion of the μ-vinylidene moiety into an Os−H bond would afford the final bis-ethylidyne product **D**, via intermediary μ-vinylidene-μ-ethylidyne complex **C**. This report represents the first example of a heterobimetallic tetrahydrido-bridged complex having neither phosphine nor carbonyl ligands, and the heterobimetallic product **D** contains a newly formed M-M bond between Ru and Os.

This work was extended further with the advent of an Ir-Zr heterobimetallic complex bridged by hydrides (Scheme 8) [23]. These heterobimetallics, the authors demonstrated, were able to facilitate H/D exchange reactions between C_6D_6 and

Scheme 8 Ir-Zr heterobimetallic complex

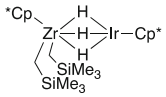

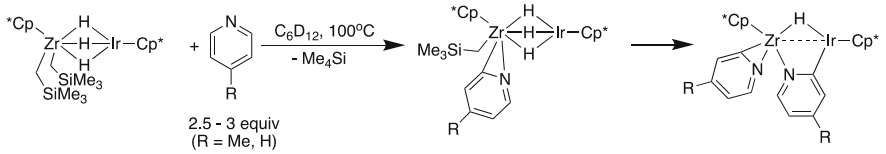

Scheme 9 Reaction of Ir-Zr heterobimetallic with pyridine derivatives

methoxyarenes as well as C–H activation of pyridine derivatives. Interestingly, as with their previously mentioned Ru-Os report [19], the heterobimetallic product resulting from the pyridine C–H activation reactions contains a newly formed bond between the Zr and Ir metal centers (Scheme 9).

3 Catalysis Mediated by the Second Coordination Sphere

The general reaction motifs encountered above can be extended into catalytic applications. In each of the catalytic reactions discussed below, the role of the "secondary" metal in modulating the reactivity of the "primary" catalytic metal will be presented in the context of the stoichiometric reactions above.

A common application of bimetallic complexes in catalysis is polymerization [24–35]. The prevalence of metallocene and other homogeneous transition metal olefin polymerization catalysts that are activated by methylalumoxane (MAO) has historically been a significant driver for this work. With the goal of removing the stoichiometric (or often superstoichiometric) MAO activator from the system, homogeneous polymerization catalysts tethered to Lewis Acid activators have been sought after for some time. In many cases, the Lewis Acid activator (typically aluminum) is directly bound to the early metal center [36–39]. The examples presented here extend beyond simple catalyst activation protocols. These systems contain two potentially active catalyst sites in constrained environments. The result is a synergistic effect akin to the second stoichiometric example above: each metal is performing a task it is known to achieve in monometallic systems, but the *overall processes,* in these cases the properties of the obtained polymers, are enforced by the bimetallic construct.

In 2004, a Ti-Zr heterobimetallic complex was synthesized and its ability to catalyze ethylene polymerization was demonstrated (Scheme 10) [40]. The heterobimetallic catalyst is highly active for the generation of high-molecular-weight, long-chain branched polyethylene. In contrast, control experiments

Scheme 10 Heterobimetallic Ti-Zr catalyst for ethylene polymerization

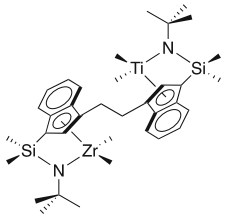

Scheme 11 Ti-W olefin polymerization catalyst

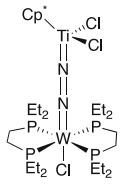

Scheme 12 Ti-Cr ethylene polymerization catalysts

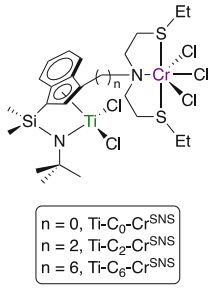

involving mixtures of monomolecular Ti and Zr complexes generate polymeric products with negligible branching. The authors attributed this to the covalent linkage between the two transition metal centers. Due to the covalent linkage, the two metals are sterically constrained such that the oligomer/macromonomer capture/enchainment is significantly enhanced.

Around the same time, a Ti-W heterobimetallic was reported that functions as a catalyst for olefin polymerization (Scheme 11) [41]. The Ti-W catalyst exhibited a remarkably high activity for the copolymerization of 1-hexene and ethylene of 510 kg mmol(cat)$^{-1}$ h^{-1}. In fact, even at reaction temperatures as high as 150°C, the catalyst was highly active for several minutes. Also, the Ti-W heterobimetallic was found to be a more active ethylene homopolymerization catalyst than a structurally similar constrained geometry catalyst (CGC).

More recently, in 2014, a series of three Ti-C_n-Cr heterobimetallic complexes were found to catalyze ethylene polymerization (Scheme 12) [42]. All three catalysts afford linear low-density polyethylenes (LLDPEs) containing exclusive *n*-butyl branches under identical conditions. The Ti-C_0-Cr^{SNS} catalyst is more active and yields polyethylenes with higher branch density than the Ti-C_2-Cr^{SNS} and Ti-C_6-Cr^{SNS}. Moreover, the authors performed additional studies which further indicate

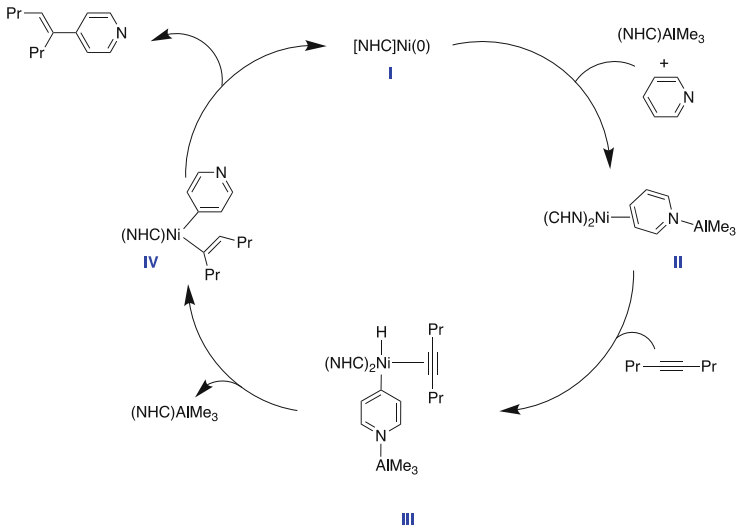

Scheme 13 Proposed catalytic cycle for *p*-selective pyridine alkenylation

that decreased spatial proximity between the two metal centers results in lower catalytic activity. That is, the further away the two metals are from each other (the longer the bridging carbon chain, C_n), the less catalytically active the heterobimetallic complex, which the authors attributed to diminished chain transfer rates.

Second-sphere effects are not limited to polymerization reactions. Applications in C-H functionalization have also been explored. The ability of one metal to *sterically direct* reactivity in such systems is a promising avenue that is now beginning to bear fruit.

A Ni-Al heterobimetallic was developed that catalyzed *para*-selective alkenylation of pyridine [43]. The authors described a possible catalytic cycle (Scheme 13). Heterobimetallic complex **II** is generated via addition of pyridine and (NHC)$AlMe_3$ (NHC = N-heterocyclic carbene) to (NHC)Ni (**I**). Ni-H intermediate **III** is then produced by oxidative addition of the alkyne to **II**. Subsequent alkyne insertion into the Ni-H bond yields **IV**. Subsequent reductive elimination yields alkenylated product and regenerates **I**. Of note, proposed Ni-Al intermediate **II** proved to be isolable and structurally characterizable, thereby serving as the first structurally isolated example of C–H activation via a synergistic effect resulting from a Ni–Al interaction.

Direct C-4-selective pyridine alkylation catalyzed by a Ni-Al heterobimetallic was reported around the same time. Furthermore, in their report, a plausible catalytic cycle similar to that described above (Scheme 13) was proposed as well (Scheme 14) [44]. The aluminum center is determined to activate the pyridine ring and to sterically compel reactivity at the electronically activated *para* position. Oxidative

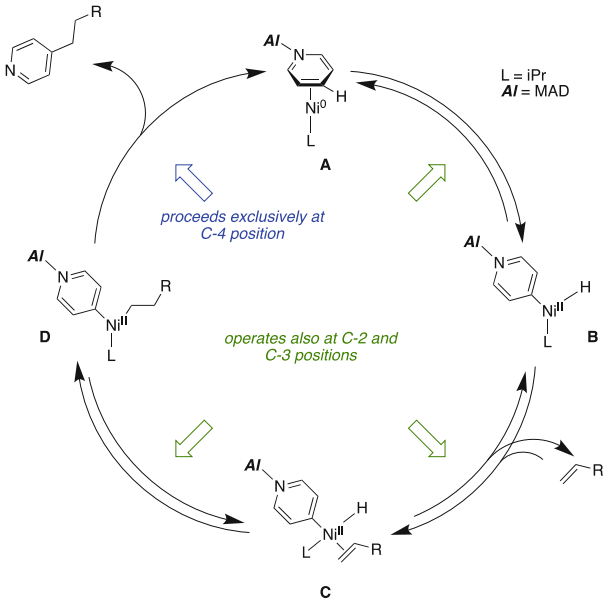

Scheme 14 Proposed catalytic cycle for C-4-selective alkylation of pyridine catalyzed by Ni-Al heterobimetallic

addition of the pyridine C(4)-H bond of **A** affords **B**. Subsequent alkene coordination yields **C**, which then undergoes migratory alkene insertion into the Ni-H bond to give **D**. Finally, reductive elimination releases C-4-alkylated pyridine and regenerates **A**. The bulky NHC ligands and (2,6-*t*-Bu_2-4-Me-$C_6H_2O)_2$AlMe (MAD) were found to be critical for promoting C-4 selectivity in both the oxidative addition and reductive elimination steps. This represents the first example of direct C-4-selective alkylation of pyridines by a Ni-Al catalyst.

The ability of a Ni-Al heterobimetallic to catalyze dehydrogenative [4 + 2] cycloaddition of formamides with alkynes has been investigated and an accompanying catalytic cycle was proposed (Scheme 15) [45].

The proposed catalytic cycle begins with η^2 coordination of Al-bound formamide to Ni, affording **A**, which then oxidatively adds the formyl C–H bond to generate **B**. Alkyne coordination followed by migratory insertion yields **C** and **D**, respectively. A second C–H activation via concerted cyclometalation results in **E**. This is followed by a second migratory insertion of a coordinating alkyne to give **F**. Subsequent reductive elimination of the $AlMe_3$-containing cycloadduct follows. Finally, decomplexation of $AlMe_3$ from the cycloadduct-generated product followed by recomplexation of $AlMe_3$ with another molecule of formamide enables regeneration of **A** via η^2 coordination.

The ability of a Ni-Al heterobimetallic to promote regioselective C–H activation of benzimidazole has also been discovered [46]. The heterobimetallic structure produces a steric restriction for the realization of the linear insertion product of

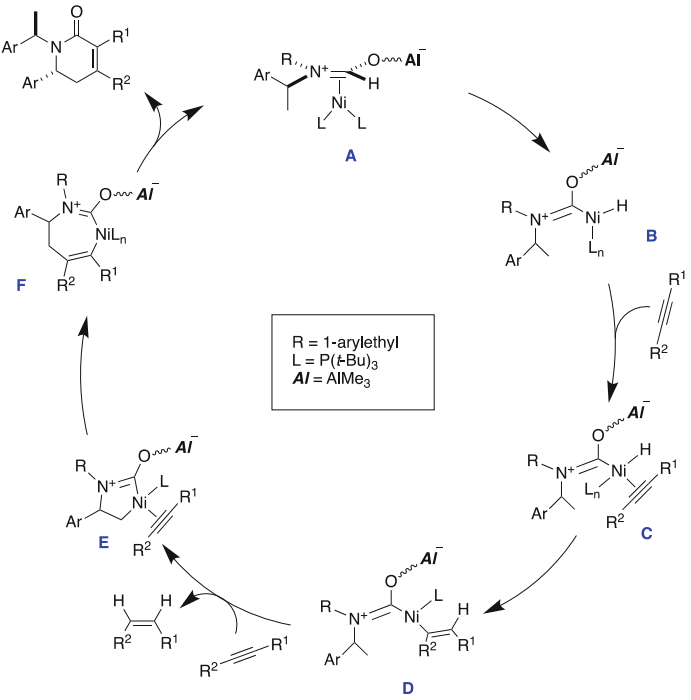

Scheme 15 Proposed catalytic cycle for dehydrogenative [4 + 2] cycloaddition of formamides with alkynes

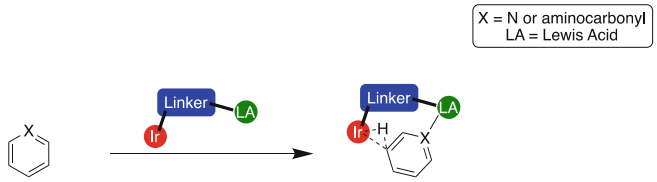

Scheme 16 Overall reaction scheme for *m*-selective C–H borylation of benzamides and pyridines

benzimidazole into styrene, while the employment of monometallic $Ni(COD)_2$ as the catalyst generates a change in favor of the branched product.

More recently, an Ir-Al heterobimetallic was described that catalyzes *meta*-selective benzamide and pyridine C–H borylation [47]. Various functional groups – N-containing, O-containing, amine, ether, and carbonyl functionalities – were well tolerated without experiencing a decline in selectivity, yielding the respective functionalized pyridylborates. Significantly, this report highlights the potential of Lewis acid–base interactions to serve as powerful instruments for manipulating site-selectivities of catalytic C–H functionalization reactions at remote positions (Scheme 16).

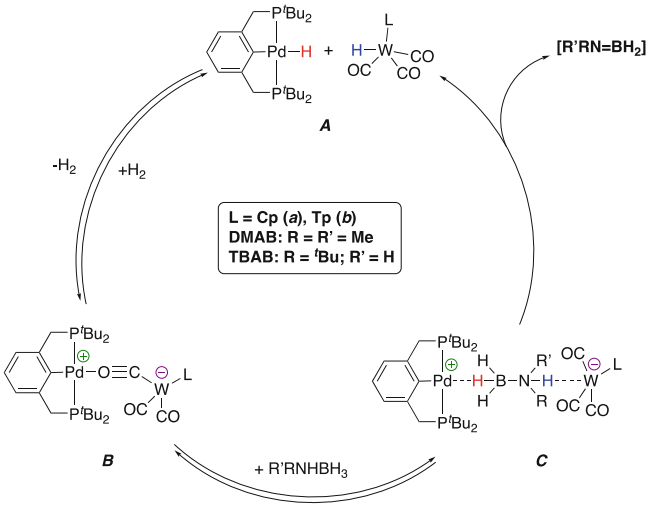

Scheme 17 Proposed catalytic cycle for amine-borane dehydrogenation by W-Pd heterobimetallic

Scheme 18 Ir-Os heterobimetallic catalyst for acceptorless and base-free dehydrogenation of secondary alcohols

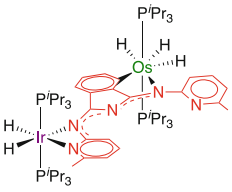

The next catalytic example presented in this section features a cooperative bond-breaking step. Similar to the example above (Scheme 5), each metal is involved in substrate activation in a manner akin to a Frustrated Lewis Pair (FLP). A W-Pd heterobimetallic complex was reported that catalyzes the dehydrogenation of amine-borane. The authors were able to propose a plausible catalytic cycle (Scheme 17) [48]. First, independent monometallic Pd-hydride and W-hydride complexes, collectively labeled **A**, react with each other to release H_2 and generate heterobimetallic complex **B**. Then, the amine-borane substrate inserts into **B** to generate **C**. Subsequent proton transfer from NH to W and hydride transfer from the BH group to Pd results in elimination of the $BH_2 = NMe_2$ product and the formation of bimetallic hydride species **C**. Finally, **C** ejects H_2 to yield **A** which interacts again to regenerate catalytically active heterobimetallic complex **B**.

In 2020, an Ir-Os heterobimetallic complex was described that catalyzes the acceptorless and base-free dehydrogenation of secondary alcohols (Scheme 18) [49]. During the course of their investigation, the authors synthesized monometallic and homobimetallic Ir analogues. Interestingly, these analogues also serve as catalysts for acceptorless and base-free secondary alcohol dehydrogenation, yet the homobimetallic is more efficient than the monometallic, and the heterobimetallic

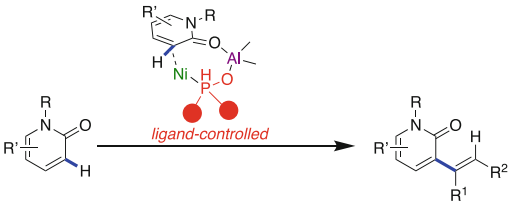

Scheme 19 General 2-pyridone C_3–H alkenylation reaction catalyzed by Ni-Al heterobimetallic

Ir-Os catalyst is more efficient than the homo- and monometallic analogues (i.e., Ir-Os > Ir-Ir > Ir).

The superior efficiency of the heterobimetallic catalyst compared to the other analogues is attributed by the authors, and we believe correctly so, to the synergistic behavior between the two different metal sites. Indeed, as mentioned before, this type of increased efficiency, along with new modes of reactivity, is a major driving force behind the interest in heterobimetallic research overall.

Recently, a Ni-Al heterobimetallic was reported to catalyze C_3–H alkenylation of 2-pyridones with alkynes (Scheme 19) [50].

A series of control experiments were performed which reinforced the importance of the PO ligand bound heterobimetallic catalyst to reaction success, as the reaction did not proceed in the absence of Ni, Al, or PO ligand. Furthermore, it was determined that the structure of the PO itself also had a profound impact on the reactivity, which is not without precedent [51]. The PO ligand needed to be sterically bulky enough to promote C–H cleavage by forcing the Ni center to approach the reaction site more closely. This is yet another fine example of how sterics should always be contemplated when considering possible reactivities and designing potential catalysts.

The breadth of potential catalytic reactivity in second-sphere bimetallic systems is immense. Reactivity patterns and motifs which have been discovered in stoichiometric reactions have been found to translate directly into catalytic systems. With the field in its relative infancy, there is a huge amount of space for future development in the coming years.

3.1 Switchable Systems

We finally turn our attention to an emergent area of research, switchable catalysis. Bimetallic systems are ideal for switchable systems. With highly differentiated metal centers, one can predictably change the structure (coordination sphere, oxidation state, etc.) at one metal center selectively. The structural or electronic change at this second-sphere metal center is "felt" by the catalytically active metal site. If the felt change is large enough, the catalyst can be turned on and off, or the nature of the obtained catalysis product can be altered. Potential applications for this technology are vast. In this last section we will give a brief overview of two forms of second-

sphere catalyst switching: redox-switchable catalysts and cation-responsive catalysts.

3.1.1 Redox-Switchable Systems

The reader will notice that ferrocene and cobaltocene are overwhelmingly utilized as the "switch" in ligand-based redox-switchable systems. This is due to the fact that they are both redox-active moieties at moderate electrochemical potentials so their electronics can be readily tuned without interference from the catalytically active site. Their redox changes are also highly reversible (ferrocene is a normal electrochemistry standard). Finally, they are substitutionally inert [52]. That is to say, upon changing their electronics, the metallocene remains attached to the scaffold containing the second metal in the bimetallic system. All of these properties, when combined make them ideal choices for a redox switch.

In 1995, a seminal study in the field of redox-switchable catalysis utilizing a metallocene switch was published [53]. In their investigation, the authors showed that an Rh-Co heterobimetallic containing cobaltocene in its reduced form $[Rh\text{-}Co]^{red}$ was a better olefin hydrogenation catalyst than its oxidized analogue $[Rh\text{-}Co]^{ox}$ (Scheme 20). In contrast, they found the opposite to be true in the case of acetone hydrosilylation, in which case $[Rh\text{-}Co]^{ox}$ was a superior catalyst than $[Rh\text{-}Co]^{red}$. The authors attributed the differences in catalytic activity to multiple possibilities, including difference in electron "donicity" as well as phosphine basicity, both of which have literature precedent [54–59].

Extension of redox-switchable behavior to olefin metathesis has been achieved. Redox switching can control the reactivity of a Grubbs–Hoveyda-type olefin metathesis catalyst that has been tagged with redox-active ferrocene (Scheme 21) [60]. Interestingly, the authors were able to use the redox-active ferrocene moieties not only to switch catalytic activity for Ring-Closing Metathesis (RCM) of *N*-tosyldiallylamide on and off, but also to control the solubility of the catalyst. By oxidizing the ferrocenyl tags, the resulting inactive dicationic catalyst precipitates out within seconds, allowing for the product to be easily separated by filtration. The

Scheme 20 Rh-Co olefin hydrogenation and acetone hydrosilylation catalysts (oxidized, red; reduced, green)

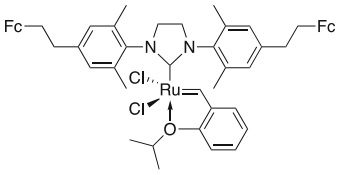

Scheme 21 Ferrocene-tagged redox-switchable Grubbs–Hoveyda type olefin metathesis catalyst

Scheme 22 Redox-switchable heterobimetallic Ru-Fe catalyst for ring-closing metathesis

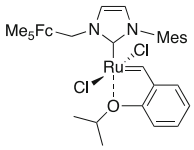

Scheme 23 Redox-switchable Ru-Fe ring-opening metathesis polymerization catalyst

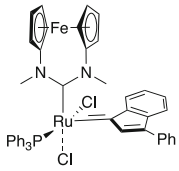

catalyst can then be switched back on via reduction, allowing for easy catalyst recycling.

Building upon this report, in 2013 an Ru-Fe heterobimetallic was prepared that served as a redox-switchable catalyst for RCM of diethyl diallylmalonate (Scheme 22) [61].

The authors showed that oxidation of the catalyst caused a dramatic decrease in catalytic activity, presumably due to reduced electron density at the metal center. Subsequent reduction with decamethylferrocene resulted in a greater than 94% return to initial catalytic activity. Thus, following one full redox cycle, the catalyst still functions at greater than 94% of its original catalytic activity. Also significant, this work represents the first example of a homogeneous, redox-switchable, NHC-supported Ru catalyst used to control RCM via modification of ligand electronics.

Around the same time, a different redox-switchable Ru-Fe heterobimetallic complex was reported that catalyzed the RCM of diethyl diallylmalonate as well as the ring-opening metathesis polymerization (ROMP) of 1,5-cyclooctadiene (COD) (Scheme 23) [62]. At 80°C in toluene, quantitative formation of poly (1,4-butadiene) was generated in less than 1 h from the ROMP of COD. Oxidation by 2,3-dichloro-5,6-dicyanoquinone (DDQ) resulted in a significant decrease in catalytic activity, and subsequent reduction by decamethylferrocene restored catalytic activity. As with the previously mentioned study [61], the weaker electron density at the metal center of the oxidized catalyst is believed to be the cause of its decreased catalytic activity.

One of the most important applications of switchable catalysis has been in polymerization. Nearly a decade after the first redox-active system for olefin polymerization was proposed, the viability of a ferrocene-containing Fe-Ti heterobimetallic complex to function as a switchable redox-active polymerization catalyst was demonstrated [63, 64]. Moreover, the authors investigated the effects of location of the redox-active moiety on catalysis.

Contrary to a previously reported Fe-Ti polymerization catalyst in which the ferrocenyl moiety is located distal to the Ti metal center [64], an Fe-Ti catalyst was synthesized in which the ferrocenyl moiety is proximal to the active Ti metal center

Scheme 24 Comparison of catalysts containing a redox-active ferrocenyl moiety proximal to the metal center (red; right) and ferrocenyl moieties distal to the metal center (purple; left)

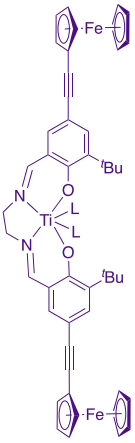

Gibson and Long., 2006

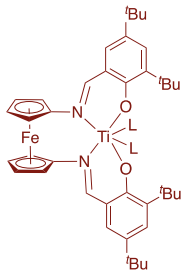

Long et al., 2015

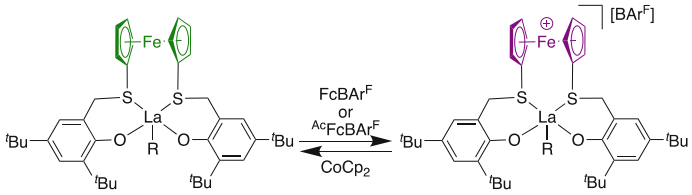

Scheme 25 Thiol-containing La-Fe catalysts

(Scheme 24). The authors found not only that their proximal ferrocenyl-containing heterobimetallic catalyzed the redox-switchable polymerization of LA, but also that the positioning of the redox-active ferrocenyl moiety in closer proximity to the active Ti metal center resulted in an improved redox switch in polymerization activity compared to the previously reported Fe-Ti catalyst.

The following year, two heterobimetallic thiol-containing La-Fe catalysts were synthesized in an effort to expand redox-switchable catalysts to include rare-earth-metal analogues as well as to investigate the effect of non-alkoxide versus alkoxide ancillary ligands on catalytic performance (Scheme 25) [65].

In their investigation, the authors found that both catalysts **A** and **B** were more active for ROP of *rac*-LA (*rac*-lactide) than their oxidized counterparts ($\mathbf{A_{ox}}$/$\mathbf{B_{ox}}$), with **A** achieving higher percent monomer conversion than **B**. As such, their results suggest that both non-alkoxide and alkoxide ancillary ligands may be employed for these redox-switchable catalysts while those catalysts containing non-alkoxide moieties might result in lower polymerization rates.

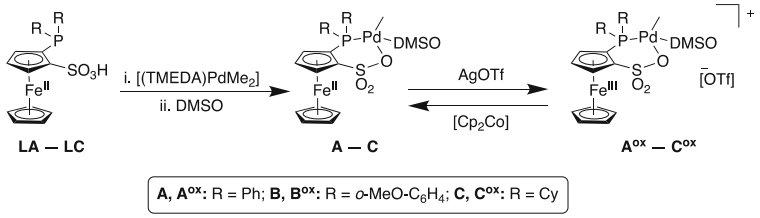

Scheme 26 Synthesis of 3 analogous redox-switchable Pd-Fe heterobimetallics

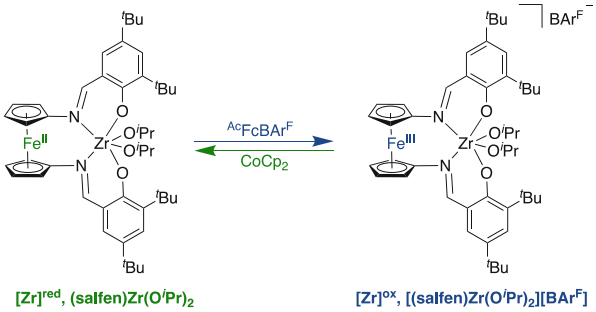

Scheme 27 Interconversion between [Fe-Zr]^{red} and [Fe-Zr]^{ox} redox states of redox-switchable Fe-Zr catalyst

Also in 2016, a set of 3 analogous redox-switchable Pd-Fe heterobimetallic complexes was reported that catalyze the copolymerization of olefins including norbornene oligomerization, ethylene homopolymerization, and ethylene/methyl acrylate copolymerization (Scheme 26) [66].

The catalytic activity of these heterobimetallics is controllable via redox switching. Particularly in norbornene oligomerization, the neutral heterobimetallic complexes were catalytically inactive while the oxidized complexes displayed significant catalytic activity. Hence, switching between the neutral and oxidized states in situ leads to corresponding on and off switching for norbornene oligomerization.

In 2019, the ability of an Fe-Zr heterobimetallic to function as a redox-switchable catalyst for the ring-opening polymerization and copolymerization of cyclic esters and ethers was detailed (Scheme 27) [67].

The authors tested several monomers for homopolymerization reactions with both the reduced [Fe-Zr]^{red} and oxidized [Fe-Zr]^{ox} states of the catalyst. CHO and PO (propylene oxide) were polymerizable via [Fe-Zr]^{ox}, while LA, VL, and TMC were polymerizable via [Fe-Zr]^{red}. Additionally, 16e block- and triblock-copolymers were synthesized by the redox-switchable Fe-Zr catalyst.

Later in 2019, an Fe-Al heterobimetallic complex was reported that functions as a redox-switchable catalyst for the ring-opening polymerization of cyclic esters and cyclohexene oxide (Scheme 28) [68].

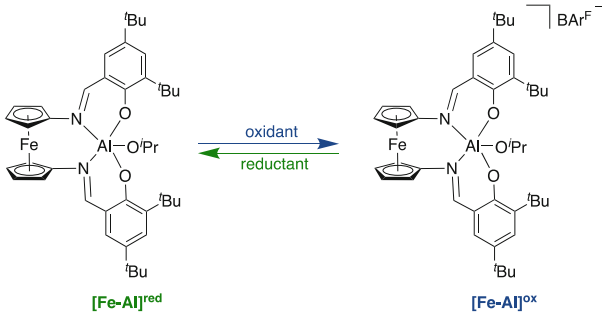

Scheme 28 Redox-switchable Fe-Al heterobimetallic polymerization catalyst. Note $[Fe\text{-}Al]^{red}$ is reduced state, and $[Fe\text{-}Al]^{ox}$ is oxidized state

Scheme 29 Synthesis of redox-switchable Au-Fe heterobimetallic cyclization catalyst

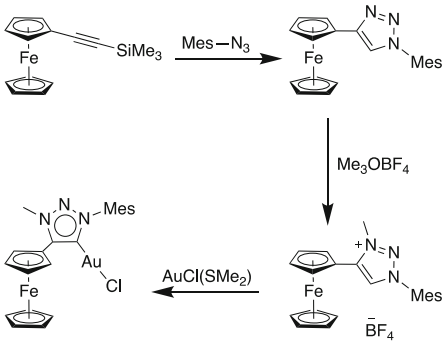

$[Fe\text{-}Al]^{red}$ polymerized LA (L-lactide), TMC (1,3-trimethylene carbonate), and BBL (b-butyrolactone), while $[Fe\text{-}Al]^{ox}$ did not. In fact, the only observed activity for $[Fe\text{-}Al]^{ox}$ was with CHO (cyclohexene oxide), and there was no observed selectivity between the two redox states for CL (e-caprolactone) and VL (d-valerolactone). Finally, the successful synthesis of AB and ABC-type block copolymers of CHO, TMC, and LA was performed via switching redox states of the Fe-Al heterobimetallic and sequential monomer addition.

Despite the prevalence of systems developed with polymerization applications in mind, redox-switchable metallocenes have been employed in a range of other reaction manifolds. A ferrocenyl-substituted mesoionic carbene-containing Au-Fe heterobimetallic complexes was presented in 2015 (Scheme 29) [69].

The authors were able to demonstrate that the oxidized form of the catalyst $[Au\text{-}Fe]^{ox}$ catalyzes the cyclization of *N*(2-propyn-1-yl)benzamide to 5-methylene-2-phenyl-4,5-dihydrooxazole while the unoxidized neutral form reduced [Au-Fe] was catalytically inactive (Scheme 30).

This shows that oxidation of the catalyst can be used to switch the catalyst on and off. Also of note, this report represents the first example of a heterobimetallic complex containing a redox-active ferrocenyl-triazolylidene metalloligand.

The ability of an Fe-Co heterobimetallic to catalyze the hydroalkoxylation of styrenes has been demonstrated as well (Scheme 31) [70].

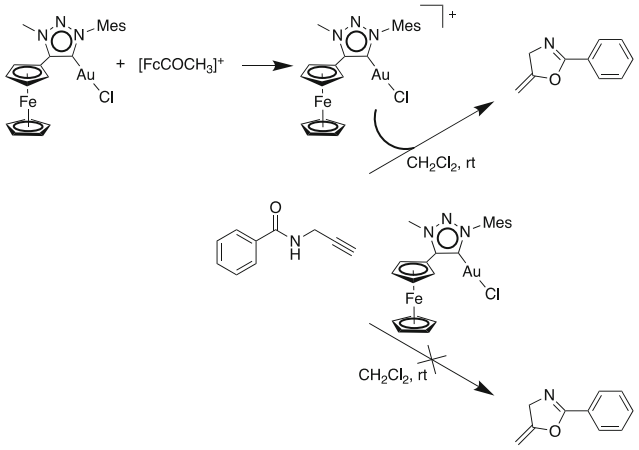

Scheme 30 Redox-switchable formation of 4,5-dihydrooxazole catalyzed by [Au-Fe]^{ox}

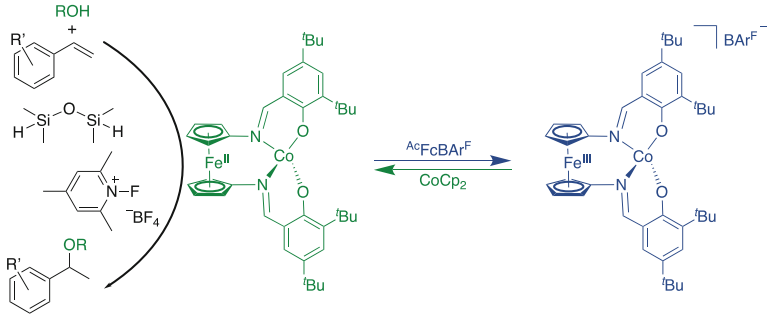

Scheme 31 Fe-Co heterobimetallic hydroalkoxylation catalyst

The one-electron-oxidized species was shown to be inactive toward hydroalkoxylation, and, as such, the hydroalkoxylation reactivity is able to be switched on and off in situ via redox chemistry.

Recently, the potential utility of this scaffold was demonstrated to extend beyond solely polymerization into additional reaction systems. In 2019, the ability of a sulfur-containing Fe-Zr heterobimetallic complex to function as a redox-switchable catalyst for intramolecular hydroamination was discovered (Scheme 32) [71].

The authors found that the reduced form of the complex catalyzes the hydroamination of primary aminoalkenes. Contrarily, the oxidized state of the heterobimetallic was shown to catalyze the hydroamination of secondary aminoalkenes. By switching between the two redox states, they were able to selectively catalyze primary aminoalkene hydroamination over secondary, and vice versa.

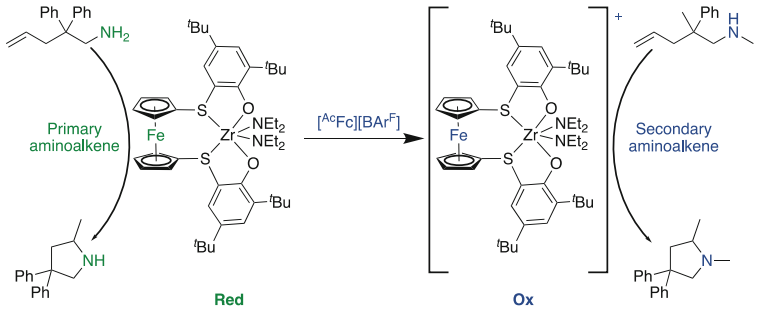

Scheme 32 Redox-switchable Fe-Zr heterobimetallic catalyst for hydroamination reactions

Scheme 33 Structure of Th_2-arene (arene: benzene, naphthalene, anthracene)

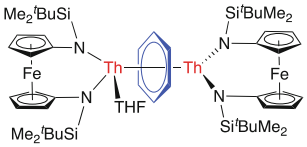

Most recently, in late 2020, dimeric Th-Fe heterobimetallics (Th_2-arene; arene: benzene, naphthalene, anthracene) were shown to reduce select arenes as well as alkynes (Scheme 33) [72].

It was found that all Th_2-arene served as reductants for azobenzene or cyclooctatetraene. Interestingly, all Th_2-arene were able to reduce diphenylacetylene, yet only the most reactive Th_2-naph could reduce bis (trimethylsilyl)acetylene (Scheme 34).

In 2016, an Fe-Au heterobimetallic complex was revealed to have the ability to behave as a redox-switchable catalyst for alkyne cyclization with furans (Scheme 35) [73].

It was determined that the neutral heterobimetallic $[Fe\text{-}Au]^{neut}$ was catalytically inactive. However, upon addition of acetylferrocenium tetrafluoroborate as the oxidant, the oxidized form of the heterobimetallic complex $[Fe\text{-}Au]^{ox}$ generated moderate to good yields of the final products (Scheme 36).

The authors attribute the catalytic activity of the oxidized heterobimetallic catalyst $[Fe\text{-}Au]^{ox}$ to the increased electrophilicity of the Au metal center resulting from the production of a cationic ligand due to oxidation. Thus, switching from neutral $[Fe\text{-}Au]^{neut}$ to oxidized $[Fe\text{-}Au]^{ox}$ affords a corresponding switch in alkyne cyclization catalysis from off to on.

A subsequent report detailed an Ru-Fe heterobimetallic complex analogous to their previously reported Fe-Au system (Scheme 37) [74]. The investigators discovered that the Ru-Fe heterobimetallic complex [Ru-Fe] functions as a redox-switchable catalyst for the transfer hydrogenation of imines and ketones. It was found that, while the neutral heterobimetallic [Ru-Fe] was highly active for reducing

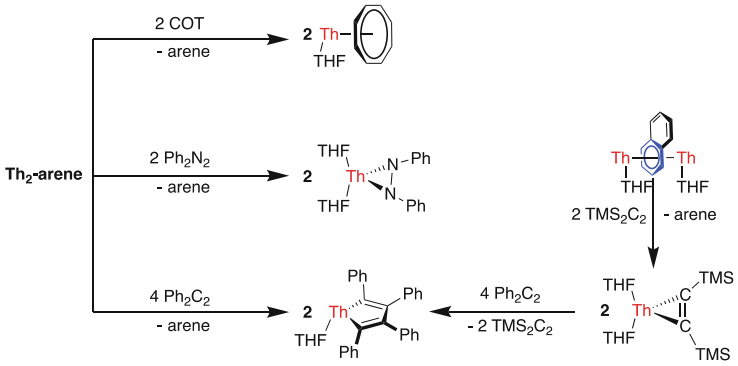

Scheme 34 Reduction reactivity studies of Th_2-arene

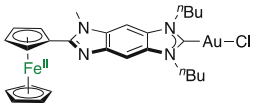

Scheme 35 Redox-switchable Fe-Au heterobimetallic catalyst in neutral state $[Fe\text{-}Au]^{neut}$

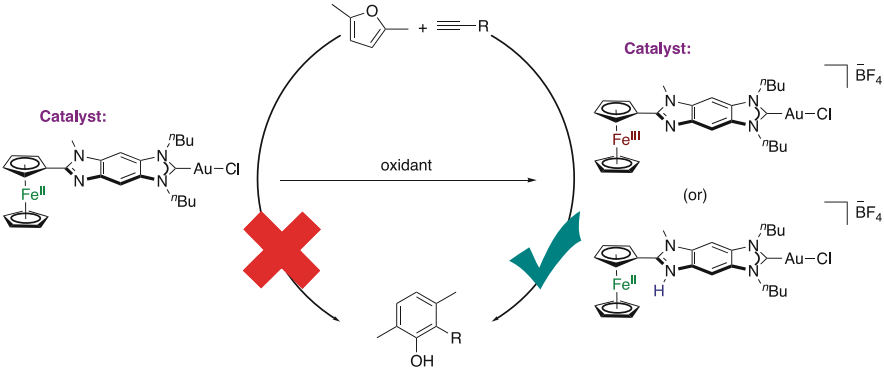

Scheme 36 Effect of redox switching on catalysis of alkyne cyclization with furans

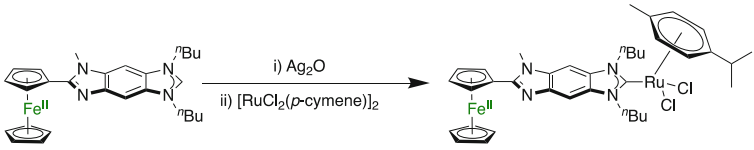

Scheme 37 Synthesis of Ru-Fe heterobimetallic catalyst [Ru-Fe] for transfer hydrogenation

Table 1 Transfer hydrogenation of imines and ketones using redox-switchable [Ru-Fe][a]

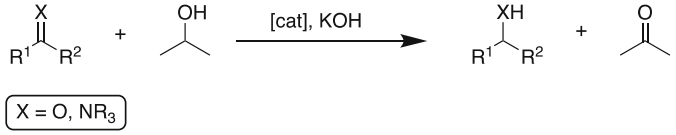

Entry	Substrate	Catalyst	Yield [%][b]
1	acetophenone	**[Ru-Fe]**	94
2	acetophenone	**[Ru-Fe]** + oxidant	24
3	cyclohexanone	**[Ru-Fe]**	75
4	cyclohexanone	**[Ru-Fe]** + oxidant	66
5	hexanophenone	**[Ru-Fe]**	94
6	hexanophenone	**[Ru-Fe]** + oxidant	20
7	2-acetophenone	**[Ru-Fe]**	60
8	2-acetophenone	**[Ru-Fe]** + oxidant	6
9	4-bromoacetophenone	**[Ru-Fe]**	68
10	4-bromoacetophenone	**[Ru-Fe]** + oxidant	51
11	4-methoxyacetophenone	**[Ru-Fe]**	40
12	4-methoxyacetophenone	**[Ru-Fe]** + oxidant	18
13	*N*-benzylideneaniline	**[Ru-Fe]**	85
14	*N*-benzylideneaniline	**[Ru-Fe]** + oxidant	81

[a] Reaction conditions: 0.5 mmol ketone or imine, 0.05 mmol KOH, 0.5 mol% of [Ru-Fe], 0.5 mol% of acetylferrocenium tetrafluoroborate (oxidant), and 2 mL of isopropanol at 80°C for 2 h
[b] Yields determined by GC using anisole (0.5 mmol) as an internal standard

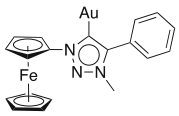

Scheme 38 Redox-switchable Au-Fe heterobimetallic cyclization catalyst

all tested substrates, the oxidized species [Ru-Fe]^{ox} showed reduced activity for ketone reduction (Table 1).

Moreover, the authors demonstrated that the rate of hexaphenone reduction could actually be modulated via addition of subsequent amounts of reductant and oxidant. Addition of acetylferrocenium tetrafluoroborate (oxidant) leads to decreased catalytic activity, while subsequent addition of cobaltocene (reductant) leads to restoration of catalytic activity to pre-oxidation levels.

The first example of redox-switchable catalysis with a gold(I) complex was described in a 2017 report on an Au-Fe heterobimetallic (Scheme 38) [75].

The authors demonstrated the ability of their Au-Fe heterobimetallic to catalyze cyclization reactions, including the formation of furan, phenol, and oxazoline (Scheme 39).

Scheme 39 Formation of oxazoline (top), furan (middle), and phenol (bottom) catalyzed by redox-switchable [Au-Fe]

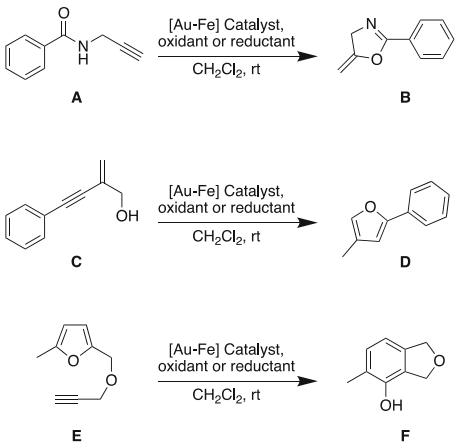

Scheme 40 Back and forth switching during [Au-Fe] catalyzed phenol formation

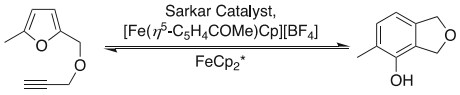

Scheme 41 Redox-switchable Rh-Fe catalyst for terminal alkyne hydrosilylation

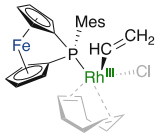

Moreover, the authors showed that switching from the unoxidized native form of the catalyst [Au-Fe] to the oxidized form $[Au\text{-}Fe]^{ox}$ turns the catalytic activity from off to on, respectively. In addition, the addition of decamethylferrocene to the active catalyst $[Au\text{-}Fe]^{ox}$ is shown to turn catalysis back off via reduction back to the native unoxidized heterobimetallic [Au-Fe]. Interestingly, in the case of the phenol formation, a different kind of switching was observed. As with the furan and oxazoline formation before, $[Au\text{-}Fe]^{ox}$ leads to phenol formation. However, reduction with decamethylferrocene leads to back-conversion of the phenol to starting material (Scheme 40).

Independent control experiments suggest this back and forth switching is inherently connected to the entire catalytic mixture.

The same year, an Rh-Fe heterobimetallic that serves as a redox-responsive catalyst for hydrosilylation of terminal alkynes was also reported (Scheme 41) [76]. It was shown that all hydrosilylation reactions were drastically accelerated with the catalyst in its oxidized form $[Rh\text{-}Fe]^{ox}$ instead of its reduced form $[Rh\text{-}Fe]^{red}$. Perhaps even more significantly, the authors discovered that both the selectivity and the product distribution of the catalysis changed appreciably upon switching from $[Rh\text{-}Fe]^{ox}$ to $[Rh\text{-}Fe]^{red}$.

Scheme 42 Redox-responsive Au-Fe heterobimetallic catalyst for alkyne hydroamination

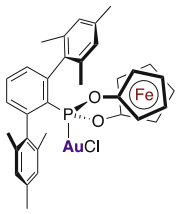

More recently, in 2019, a redox-responsive Au-Fe heterobimetallic complex was described that catalyzed alkyne hydroamination (Scheme 42) [77]. The authors discovered that the hydroamination reaction generally occurs approximately two times faster when the catalyst is switched to its oxidized form $[Au\text{-}Fe]^{ox}$ instead of its reduced form $[Au\text{-}Fe]^{red}$.

Additionally, the researchers examined the hydroamination of electron-poor, electron-rich, and aliphatic alkynes in their study and found that the electronic nature of the alkyne actually had a meaningful impact on the efficiency of the reaction, with electron-donating groups slowing the reaction down (Table 2).

Similar to the aforementioned work, a redox-switchable Au-Fe heterobimetallic cyclization catalyst was recently reported (Scheme 43) [78].

The authors demonstrated that, while the oxidized heterobimetallic $[Au\text{-}Fe]^{ox}$ was catalytically active for the cyclization of N(2-propyn-1-yl)benzamide to 2-phenyl-5-vinylidene-2-oxazoline, the reduced form $[Au\text{-}Fe]^{red}$ is inactive. Further, redox switching between $[Au\text{-}Fe]^{ox}$ and $[Au\text{-}Fe]^{red}$ switches catalytic turnover on and off.

3.1.2 Cation-Responsive Systems

In 2014, a heterobimetallic Ir-crown ether complex, in which the crown either moiety contains either Na^+ or Li^+, was reported to catalyze H_2 activation and facilitate H/D exchange (Scheme 44) [79].

The main-group cation is thought to sequester the crown ether and prevent an oxygen atom from competing with H_2 for an open site at the iridium center. Interestingly, it was determined that the rate of H_2 activation can be controlled by cation selection. Reactions containing lithium proceed approximately 10 times faster than those reactions involving sodium. Moreover, the H/D exchange reaction rate can be increased up to 250-fold upon addition of catalytic amounts of Li^+. Thus, modification of the identity and concentration of the main-group cation results in corresponding modification of the reaction.

This type of cation-responsive system has been extended beyond hydrogen activation and into the field of olefin isomerization [80]. Simple halide abstraction switched the monometallic Ir catalyst from inactive to active (i.e., off to on) (Scheme 45).

From that point, it was found that the catalyst activity could be tuned by converting the monometallic Ir catalyst to a heterobimetallic Ir-M (M = K, Na, Li)

Table 2 Scope of alkyne hydroamination catalyzed by Au-Fe

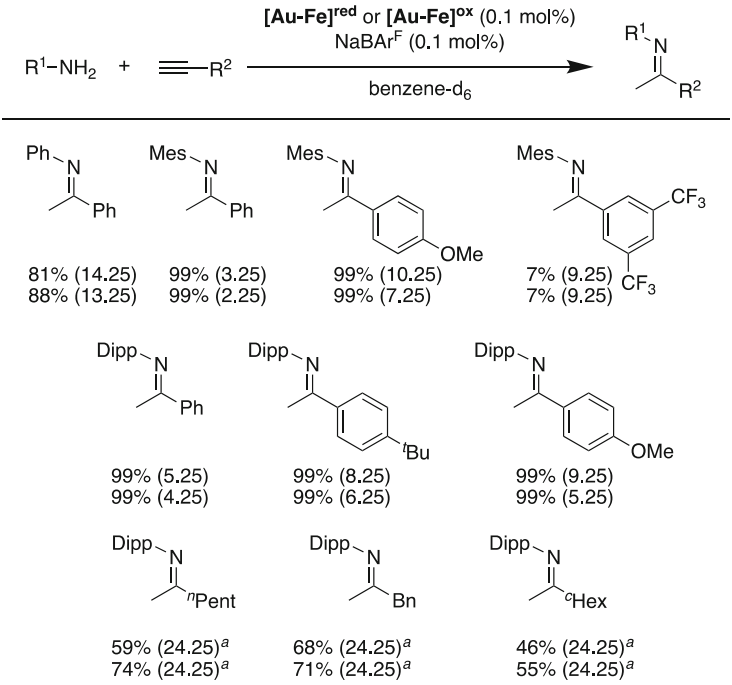

Hydroamination of alkynes. Yields are given for [Au-Fe]^{red} (upper value) and [Au-Fe]^{ox} (lower value); numbers in parentheses correspond to reaction times in [h]. Reactions were conducted on a 0.1 mmol scale in d_6-benzene with 0.1 mol% [Au-Fe]^{red} and 0.1 mol% $NaBAr^F$ as activating agents. [Au-Fe]^{ox} was generated in situ prior to the reaction by addition of 0.1 mol% [Fc(Oac)][Al{OC$(CF_3)_3$}$_4$]. The yields were determined using 1,3,5-$(MeO)_3C_6H_3$ as an internal standard

[a] Reactions were conducted using a 1 mol% catalyst/activator

Scheme 43 Switchable gold-catalyzed cyclization of *N*(2-propyn-1-yl) benzamide to 2-phenyl-5-vinylidene-2-oxazoline

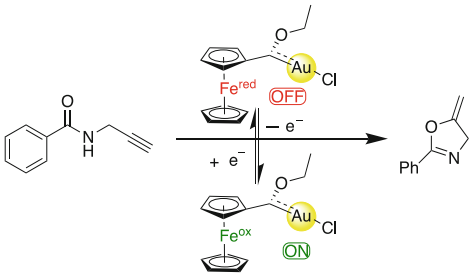

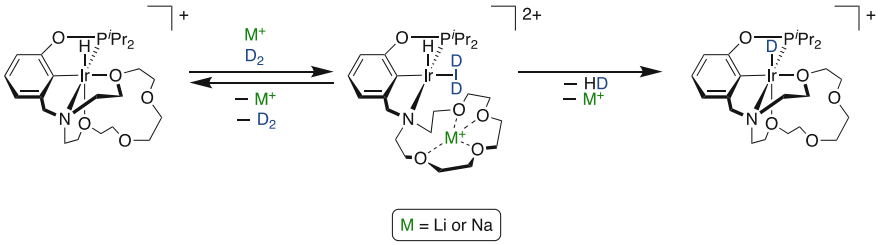

Scheme 44 Overall H_2 activation and H/D exchange reaction

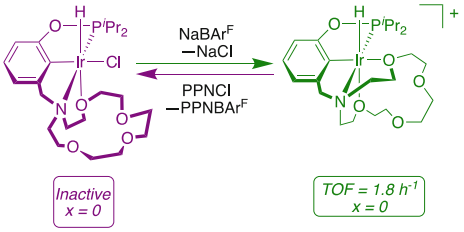

Scheme 45 Interconversion between inactive (purple; left) and active (green; right) olefin isomerization catalyst

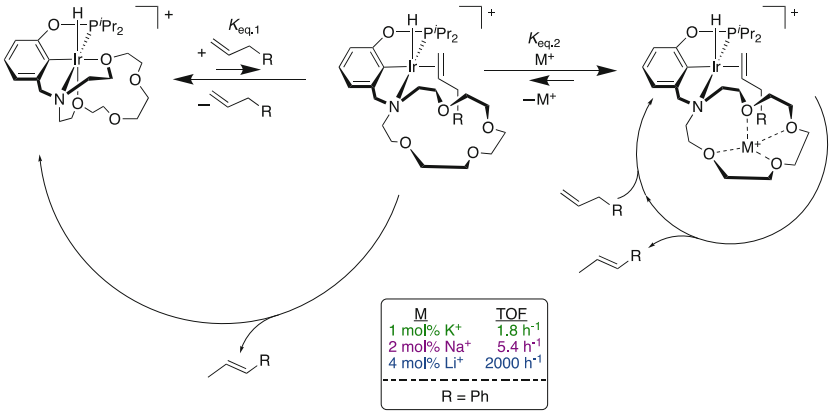

Scheme 46 Proposed mechanism for cation-controlled olefin isomerization via heterobimetallic catalysis

catalyst via addition of main-group metal salts. Turnover frequency (TOF) for olefin isomerization increased upon changing M such that TOF: K < Na < Li (Scheme 46).

Further still, the authors demonstrated that addition of chloride salts completely halts catalytic activity, allowing for the catalyst to be switched off and on using chloride salts (off) and sodium salts (on).

It is also worth noting that redox-switchable catalytic ability of crown ether-containing Ir-M (M = metal salt) heterobimetallic complexes extends to modulate methanol carbonylation [81, 82]. In these systems, structurally analogous to previously mentioned heterobimetallics [79, 80], changing the metal cation results in corresponding changes to the turnover number (TON) for the methanol carbonylation. Rather than a simple on and off switch, the authors demonstrate the potential for cation-controlled reaction tunability.

4 Conclusions

As displayed throughout this chapter, a specific class of heterobimetallic complexes in which each metal center resides in the second coordination sphere of the other has recently emerged as an area of increased interest. This is undoubtedly due to the unique reactivity manifolds afforded by these complexes as a result of the presence of two different metal centers. Stoichiometric bond activation is observed in heterobimetallic species that is otherwise not seen without both metals present. In some examples, activation is achieved in a manner not dissimilar to Lewis pair-type chemistry in which the two metals form an adduct with a new M–M' bond following bond activation. Catalytic bond activation ranging from alkenylation to polymerization facilitated by these heterobimetallics has been observed, with some examples showing regioselectivity. Ongoing progress continues in the development of catalytically useful second-sphere bimetallic systems. Of particular note is the recent emergence of switchable heterobimetallic complexes. In this chapter, we have discussed both redox-switchable and cation-responsive heterobimetallic systems.

In redox-switchable systems, changing the oxidation state of one of the metals is used to modify catalytic activity. In many systems, oxidizing or reducing one of the metals switches catalysis from "off" to "on" and vice versa. While polymerization is the centerpiece of redox-switchable heterobimetallics, switchable systems have had application in additional reactions such as alkyne cyclization, hydroamination, and hydrosilylation. Similarly, cation-responsive systems utilize cation manipulation to influence catalytic activity with some evidence to suggest size of the cation could have an appreciable effect on catalysis. Future directions in this area include the generation of "multi-state" switches, systems that can exist in states beyond the currently standard "on" and "off."

Though perhaps not as commonly encountered for bond activation and catalysis as systems containing formal metal–metal bonds, the field of second-sphere bimetallic chemistry is certain to grow over the coming years. Potential applications are limitless, as the metals can function cooperatively or in tandem to achieve desired reactivity. We look forward to watching the field mature and are excited for what is yet to come!

References

1. Stephan DW (1989) Early-late heterobimetallics. Coord Chem Rev 95(1):41–107. https://doi.org/10.1016/0010-8545(89)80002-5
2. Charles III RM, Brewster TP (2021) H2 and carbon-heteroatom bond activation mediated by polarized heterobimetallic complexes. Coord Chem Rev 433:213765. https://doi.org/10.1016/j.ccr.2020.213765
3. Cotton FA, Lecture C (1975) Quadruple bonds and other multiple metal to metal bonds. Chem Soc Rev 4(1):27–53. https://doi.org/10.1039/CS9750400027
4. Cotton FA (1978) Discovering and understanding multiple metal-to-metal bonds. Acc Chem Res 11(6):225–232. https://doi.org/10.1021/ar50126a001
5. Cooper BG, Napoline JW, Thomas CM (2012) Catalytic applications of early/late heterobimetallic complexes. Catal Rev 54(1):1–40. https://doi.org/10.1080/01614940.2012.619931
6. Wheatley N, Kalck P (1999) Structure and reactivity of early−late heterobimetallic complexes. Chem Rev 99(12):3379–3420. https://doi.org/10.1021/cr980325m
7. Campos J (2020) Bimetallic cooperation across the periodic table. Nat Rev Chem 4(12):696–702. https://doi.org/10.1038/s41570-020-00226-5
8. Park J, Hong S (2012) Cooperative bimetallic catalysis in asymmetric transformations. Chem Soc Rev 41(21):6931–6943. https://doi.org/10.1039/C2CS35129C
9. Hicks J, Vasko P, Goicoechea JM, Aldridge S (2018) Synthesis, structure and reaction chemistry of a nucleophilic aluminyl anion. Nature 557(7703):92–95. https://doi.org/10.1038/s41586-018-0037-y
10. Charles III RM, Yokley TW, Schley ND, DeYonker NJ, Brewster TP (2019) Hydrogen activation and hydrogenolysis facilitated by late-transition-metal–aluminum heterobimetallic complexes. Inorg Chem 58(19):12635–12645. https://doi.org/10.1021/acs.inorgchem.9b01359
11. Brewster TP, Nguyen TH, Li Z, Eckenhoff WT, Schley ND, DeYonker NJ (2018) Synthesis and characterization of heterobimetallic iridium–aluminum and rhodium–aluminum complexes. Inorg Chem 57(3):1148–1157. https://doi.org/10.1021/acs.inorgchem.7b02601
12. Stephan DW (2015) Frustrated Lewis pairs: from concept to catalysis. Acc Chem Res 48(2):306–316. https://doi.org/10.1021/ar500375j
13. Stephan DW (2016) The broadening reach of frustrated Lewis pair chemistry. Science 354(6317). https://doi.org/10.1126/science.aaf7229
14. Stephan DW, Erker G (2015) Frustrated Lewis pair chemistry: development and perspectives. Angew Chem Int Ed 54(22):6400–6441. https://doi.org/10.1002/anie.201409800
15. Bouhadir G, Bourissou D (2016) Complexes of ambiphilic ligands: reactivity and catalytic applications. Chem Soc Rev 45(4):1065–1079. https://doi.org/10.1039/C5CS00697J
16. Flynn SR, Wass DF (2013) Transition metal frustrated Lewis pairs. ACS Catal 3(11):2574–2581. https://doi.org/10.1021/cs400754w
17. Navarro M, Campos J (2021) Chapter three – bimetallic frustrated Lewis pairs. In: Pérez PJ (ed) Advances in organometallic chemistry, vol 75. Academic Press, pp 95–148. https://doi.org/10.1016/bs.adomc.2021.01.001
18. Devillard M, Declercq R, Nicolas E, Ehlers AW, Backs J, Saffon-Merceron N, Bouhadir G, Slootweg JC, Uhl W, Bourissou D (2016) A significant but constrained geometry Pt→Al interaction: fixation of CO2 and CS2, activation of H2 and PhCONH2. J Am Chem Soc 138(14):4917–4926. https://doi.org/10.1021/jacs.6b01320
19. Shima T, Suzuki H (2005) Heterobimetallic polyhydride complex, Cp*Ru(μ-H)4OsCp* (Cp* = H5-C5Me5). Synthesis and reaction with ethylene. Organometallics 24(16):3939–3945. https://doi.org/10.1021/om0503996
20. Suzuki H, Omori H, Moro-Oka Y (1988) Activation of the carbon-hydrogen bond of ethylene by a dinuclear tetrahydride-bridged ruthenium complex. Organometallics 7(12):2579–2581. https://doi.org/10.1021/om00102a031

21. Omori H, Suzuki H, Morooka Y (1989) Preparation and structure determination of a dinuclear ruthenacyclopentadiene complex. Coupling of coordinated vinyl ligands. Organometallics 8(6): 1576–1578. https://doi.org/10.1021/om00108a039
22. Suzuki H, Omori H, Lee DH, Yoshida Y, Fukushima M, Tanaka M, Moro-oka Y (1994) Synthesis, structure, and chemistry of a dinuclear tetrahydride-bridged complex of ruthenium, (. Eta.5-C5Me5)Ru(.Mu.-H)4Ru(.Eta.5-C5Me5). C-H bond activation and coupling reaction of ethylene on dinuclear complexes. Organometallics 13(4):1129–1146. https://doi.org/10.1021/om00016a017
23. Oishi M, Kato T, Nakagawa M, Suzuki H (2008) Synthesis and reactivity of early−late heterobimetallic hydrides of group 4 metals and iridium supported by mono(H5-C5Me5) ancillary ligands: bimetallic carbon−hydrogen bond activation. Organometallics 27(23): 6046–6049. https://doi.org/10.1021/om800715b
24. Cai Z, Xiao D, Do LH (2019) Cooperative heterobimetallic catalysts in coordination insertion polymerization. Comments Inorg Chem 39(1):27–50. https://doi.org/10.1080/02603594.2019.1570165
25. Boulho C, Zijlstra HS, Harder S (2015) Oxide-bridged heterobimetallic aluminum/zirconium catalysts for ethylene polymerization. Eur J Inorg Chem 2015(12):2132–2138. https://doi.org/10.1002/ejic.201500123
26. Boulho C, Zijlstra HS, Hofmann A, Budzelaar PHM, Harder S (2016) Insight into oxide-bridged heterobimetallic Al/Zr olefin polymerization catalysts. Chem Eur J 22(48): 17450–17459. https://doi.org/10.1002/chem.201602674
27. Chiu H-C, Koley A, Dunn PL, Hue RJ, Tonks IA (2017) Ethylene polymerization catalyzed by bridging Ni/Zn heterobimetallics. Dalton Trans 46(17):5513–5517. https://doi.org/10.1039/C7DT00222J
28. Nakamura T, Suzuki K, Yamashita M (2018) A Zwitterionic aluminabenzene–alkylzirconium complex having half-zirconocene structure: synthesis and application for additive-free ethylene polymerization. Chem Commun 54(33):4180–4183. https://doi.org/10.1039/C8CC02186D
29. Bhattacharjee H, Müller J (2016) Metallocenophanes bridged by group 13 elements. Coord Chem Rev 314:114–133. https://doi.org/10.1016/j.ccr.2015.09.008
30. Suo H, Solan GA, Ma Y, Sun W-H (2018) Developments in compartmentalized bimetallic transition metal ethylene polymerization catalysts. Coord Chem Rev 372:101–116. https://doi.org/10.1016/j.ccr.2018.06.006
31. Tanabiki M, Tsuchiya K, Motoyama Y, Nagashima H (2005) Monometallic and heterobimetallic azanickellacycles as ethylene polymerization catalysts. Chem Commun 27: 3409–3411. https://doi.org/10.1039/B502942B
32. Gurubasavaraj PM, Nomura K (2010) Hetero-bimetallic complexes of titanatranes with aluminum alkyls: synthesis, structural analysis, and their use in catalysis for ethylene polymerization. Organometallics 29(16):3500–3506. https://doi.org/10.1021/om100119g
33. Kulangara SV, Jabri A, Yang Y, Korobkov I, Gambarotta S, Duchateau R (2012) Synthesis, X-ray structural analysis, and ethylene polymerization studies of group IV metal heterobimetallic aluminum-pyrrolyl complexes. Organometallics 31(17):6085–6094. https://doi.org/10.1021/om300453a
34. Barisic D, Lebon J, Maichle-Mössmer C, Anwander R (2019) Pentadienyl migration and abstraction in yttrium aluminabenzene complexes including a single-component catalyst for isoprene polymerization. Chem Commun 55(49):7089–7092. https://doi.org/10.1039/C9CC02857A
35. Barisic D, Buschmann DA, Schneider D, Maichle-Mössmer C, Anwander R (2019) Rare-earth-metal pentadienyl half-sandwich and sandwich tetramethylaluminates–synthesis, structure, reactivity, and performance in isoprene polymerization. Chem A Eur J 25(18):4821–4832. https://doi.org/10.1002/chem.201900108
36. Tritto I, Li SX, Sacchi MC, Locatelli P, Zannoni G (1995) Titanocene-Methylaluminoxane catalysts for olefin polymerization: a 13C NMR study of the reaction equilibria and polymerization. Macromolecules 28(15):5358–5362. https://doi.org/10.1021/ma00119a028

37. Fischer D, Mülhaupt R (1994) The influence of Regio- and Stereoirregularities on the crystallization behaviour of isotactic poly(propylene)s prepared with homogeneous group IVa metallocene/Methylaluminoxane Ziegler-Natta catalysts. Macromol Chem Phys 195(4): 1433–1441. https://doi.org/10.1002/macp.1994.021950426
38. Endo K, Uchida Y, Matsuda Y (1996) Polymerizations of butadiene with Ni(Acac)2-methylaluminoxane catalysts. Macromol Chem Phys 197(11):3515–3521. https://doi.org/10.1002/macp.1996.021971102
39. Endo K, Yamanaka Y (2001) Polymerization of butadiene with V(Acac)3-methylaluminoxane catalyst. Macromol Chem Phys 202(1):201–206. https://doi.org/10.1002/1521-3935(20010101)202:1<201::AID-MACP201>3.0.CO;2-D
40. Wang J, Li H, Guo N, Li L, Stern CL, Marks TJ (2004) Covalently linked heterobimetallic catalysts for olefin polymerization. Organometallics 23(22):5112–5114. https://doi.org/10.1021/om049481b
41. Ishino H, Takemoto S, Hirata K, Kanaizuka Y, Hidai M, Nabika M, Seki Y, Miyatake T, Suzuki N (2004) Olefin polymerization catalyzed by titanium−tungsten heterobimetallic dinitrogen Complexes1. Organometallics 23(20):4544–4546. https://doi.org/10.1021/om049447x
42. Liu S, Motta A, Mouat AR, Delferro M, Marks TJ (2014) Very large cooperative effects in heterobimetallic titanium-chromium catalysts for ethylene polymerization/copolymerization. J Am Chem Soc 136(29):10460–10469. https://doi.org/10.1021/ja5046742
43. Tsai C-C, Shih W-C, Fang C-H, Li C-Y, Ong T-G, Yap GPA (2010) Bimetallic nickel aluminun mediated para-selective alkenylation of pyridine: direct observation of H2,H1-pyridine Ni(0)−Al(III) intermediates prior to C−H bond activation. J Am Chem Soc 132(34):11887–11889. https://doi.org/10.1021/ja1061246
44. Nakao Y, Yamada Y, Kashihara N, Hiyama T (2010) Selective C-4 alkylation of pyridine by nickel/Lewis acid catalysis. J Am Chem Soc 132(39):13666–13668. https://doi.org/10.1021/ja106514b
45. Nakao Y, Morita E, Idei H, Hiyama T (2011) Dehydrogenative [4 + 2] cycloaddition of formamides with alkynes through double C−H activation. J Am Chem Soc 133(10): 3264–3267. https://doi.org/10.1021/ja1102037
46. Shih W-C, Chen W-C, Lai Y-C, Yu M-S, Ho J-J, Yap GPA, Ong T-G (2012) The regioselective switch for amino-NHC mediated C–H activation of benzimidazole via Ni–Al synergistic catalysis. Org Lett 14(8):2046–2049. https://doi.org/10.1021/ol300570f
47. Yang L, Uemura N, Nakao Y (2019) Meta-selective C–H borylation of benzamides and pyridines by an Iridium–Lewis acid bifunctional catalyst. J Am Chem Soc 141(19): 7972–7979. https://doi.org/10.1021/jacs.9b03138
48. Osipova ES, Gulyaeva ES, Gutsul EI, Kirkina VA, Pavlov AA, Nelyubina YV, Rossin A, Peruzzini M, Epstein LM, Belkova NV, Filippov OA, Shubina ES (2021) Bifunctional activation of amine-boranes by the W/Pd bimetallic analogs of "Frustrated Lewis Pairs". Chem Sci 12(10):3682–3692. https://doi.org/10.1039/D0SC06114J
49. Buil ML, Esteruelas MA, Izquierdo S, Nicasio AI, Oñate E (2020) N–H and C–H bond activations of an isoindoline promoted by iridium- and osmium-polyhydride complexes: a noninnocent bridge ligand for acceptorless and base-free dehydrogenation of secondary alcohols. Organometallics 39(14):2719–2731. https://doi.org/10.1021/acs.organomet.0c00316
50. Yin G, Li Y, Wang R-H, Li J-F, Xu X-T, Luan Y-X, Ye M (2021) Ligand-controlled Ni(0)–Al(III) bimetal-catalyzed C3–H alkenylation of 2-pyridones by reversing conventional selectivity. ACS Catal 11(8):4606–4612. https://doi.org/10.1021/acscatal.1c00750
51. Donets PA, Cramer N (2013) Diaminophosphine oxide ligand enabled asymmetric nickel-catalyzed hydrocarbamoylations of alkenes. J Am Chem Soc 135(32):11772–11775. https://doi.org/10.1021/ja406730t
52. Slone CS, Mirkin CA, Yap GPA, Guzei IA, Rheingold AL (1997) Oxidation-state-dependent reactivity and catalytic properties of a Rh(I) complex formed from a redox-switchable hemilabile ligand. J Am Chem Soc 119(44):10743–10753. https://doi.org/10.1021/ja9723601

53. Lorkovic IM, Duff RR, Wrighton MS (1995) Use of the redox-active ligand 1,1'-bis (Diphenylphosphino)cobaltocene to reversibly alter the rate of the rhodium(I)-catalyzed reduction and isomerization of ketones and alkenes. J Am Chem Soc 117(12):3617–3618. https://doi.org/10.1021/ja00117a033
54. Schrock RR, Osborn JA (1970) Rhodium catalysts for the homogeneous hydrogenation of ketones. J Chem Soc D 9:567–568. https://doi.org/10.1039/C29700000567
55. Schrock RR, Osborn JA (1976) Catalytic hydrogenation using cationic rhodium complexes. I. Evolution of the catalytic system and the hydrogenation of olefins. J Am Chem Soc 98(8):2134–2143. https://doi.org/10.1021/ja00424a020
56. Tolman CA (1977) Steric effects of phosphorus ligands in organometallic chemistry and homogeneous catalysis. Chem Rev 77(3):313–348. https://doi.org/10.1021/cr60307a002
57. Jacobsen EN, Zhang W, Guler ML (1991) Electronic tuning of asymmetric catalysts. J Am Chem Soc 113(17):6703–6704. https://doi.org/10.1021/ja00017a069
58. RajanBabu TV, Casalnuovo AL (1992) Tailored ligands for asymmetric catalysis: the hydrocyanation of vinyl arenes. J Am Chem Soc 114(15):6265–6266. https://doi.org/10.1021/ja00041a066
59. RajanBabu TV, Ayers TA, Casalnuovo AL (1994) Electronic amplification of selectivity in rh-catalyzed hydrogenations: D-glucose-derived ligands for the synthesis of D- or L-amino acids. J Am Chem Soc 116(9):4101–4102. https://doi.org/10.1021/ja00088a065
60. Süßner M, Plenio H (2005) Redox-switchable phase tags for recycling of homogeneous catalysts. Angew Chem Int Ed 44(42):6885–6888. https://doi.org/10.1002/anie.200502182
61. Arumugam K, Varnado Jr CD, Sproules S, Lynch VM, Bielawski CW (2013) Redox-switchable ring-closing metathesis: catalyst design, synthesis, and study. Chem A Eur J 19(33):10866–10875. https://doi.org/10.1002/chem.201301247
62. Varnado Jr CD, Rosen EL, Collins MS, Lynch VM, Bielawski CW (2013) Synthesis and study of olefin metathesis catalysts supported by redox-switchable diaminocarbene[3] ferrocenophanes. Dalton Trans 42(36):13251–13264. https://doi.org/10.1039/C3DT51278A
63. Brown LA, Rhinehart JL, Long BK (2015) Effects of ferrocenyl proximity and monomer presence during oxidation for the redox-switchable polymerization of l-lactide. ACS Catal 5(10):6057–6060. https://doi.org/10.1021/acscatal.5b01434
64. Gregson CKA, Gibson VC, Long NJ, Marshall EL, Oxford PJ, White AJP (2006) Redox control within single-site polymerization catalysts. J Am Chem Soc 128(23):7410–7411. https://doi.org/10.1021/ja061398n
65. Hermans C, Rong W, Spaniol TP, Okuda J (2016) Lanthanum complexes containing a bis (phenolate) ligand with a ferrocene-1,1′-diyldithio backbone: synthesis, characterization, and ring-opening polymerization of Rac-lactide. Dalton Trans 45(19):8127–8133. https://doi.org/10.1039/C6DT00272B
66. Chen M, Yang B, Chen C (2015) Redox-controlled olefin (Co)polymerization catalyzed by ferrocene-bridged phosphine-sulfonate palladium complexes. Angew Chem Int Ed 54(51): 15520–15524. https://doi.org/10.1002/anie.201507274
67. Dai R, Diaconescu PL (2019) Investigation of a zirconium compound for redox switchable ring opening polymerization. Dalton Trans 48(9):2996–3002. https://doi.org/10.1039/C9DT00212J
68. Lai A, Hern ZC, Diaconescu PL (2019) Switchable ring-opening polymerization by a ferrocene supported aluminum complex. ChemCatChem 11(16):4210–4218. https://doi.org/10.1002/cctc.201900747
69. Hettmanczyk L, Manck S, Hoyer C, Hohloch S, Sarkar B (2015) Heterobimetallic complexes with redox-active mesoionic carbenes as metalloligands: electrochemical properties, electronic structures and catalysis. Chem Commun 51(54):10949–10952. https://doi.org/10.1039/C5CC01578B
70. Shepard SM, Diaconescu PL (2016) Redox-switchable hydroelementation of a cobalt complex supported by a ferrocene-based ligand. Organometallics 35(15):2446–2453. https://doi.org/10.1021/acs.organomet.6b00317

71. Shen Y, Shepard SM, Reed CJ, Diaconescu PL (2019) Zirconium complexes supported by a ferrocene-based ligand as redox switches for hydroamination reactions. Chem Commun 55(39): 5587–5590. https://doi.org/10.1039/C9CC01076A
72. Yu C, Liang J, Deng C, Lefèvre G, Cantat T, Diaconescu PL, Huang W (2020) Arene-bridged dithorium complexes: inverse sandwiches supported by a δ bonding interaction. J Am Chem Soc 142(51):21292–21297. https://doi.org/10.1021/jacs.0c11215
73. Ibáñez S, Poyatos M, Dawe LN, Gusev D, Peris E (2016) Ferrocenyl-imidazolylidene ligand for redox-switchable gold-based catalysis. A detailed study on the redox-switching abilities of the ligand. Organometallics 35(16):2747–2758. https://doi.org/10.1021/acs.organomet.6b00517
74. Ibáñez S, Poyatos M, Peris E (2016) A ferrocenyl-benzo-fused imidazolylidene complex of ruthenium as redox-switchable catalyst for the transfer hydrogenation of ketones and imines. ChemCatChem 8(24):3790–3795. https://doi.org/10.1002/cctc.201601025
75. Klenk S, Rupf S, Suntrup L, van der Meer M, Sarkar B (2017) The power of ferrocene, mesoionic carbenes, and gold: redox-switchable catalysis. Organometallics 36(10): 2026–2035. https://doi.org/10.1021/acs.organomet.7b00270
76. Feyrer A, Armbruster MK, Fink K, Breher F (2017) Metal complexes of a redox-active [1] phosphaferrocenophane: structures, electrochemistry and redox-induced catalysis. Chem A Eur J 23(31):7402–7408. https://doi.org/10.1002/chem.201700868
77. Deck E, Wagner HE, Paradies J, Breher F (2019) Redox-responsive phosphonite gold complexes in hydroamination catalysis. Chem Commun 55(37):5323–5326. https://doi.org/10.1039/C9CC01492F
78. Veit P, Volkert C, Förster C, Ksenofontov V, Schlicher S, Bauer M, Heinze K (2019) Gold (II) in redox-switchable gold(I) catalysis. Chem Commun 55(32):4615–4618. https://doi.org/10.1039/C9CC00283A
79. Kita MR, Miller AJM (2014) Cation-modulated reactivity of iridium hydride pincer-crown ether complexes. J Am Chem Soc 136(41):14519–14529. https://doi.org/10.1021/ja507324s
80. Kita MR, Miller AJM (2017) An ion-responsive pincer-crown ether catalyst system for rapid and switchable olefin isomerization. Angew Chem Int Ed 56(20):5498–5502. https://doi.org/10.1002/anie.201701006
81. Gregor LC, Grajeda J, Kita MR, White PS, Vetter AJ, Miller AJM (2016) Modulating the elementary steps of methanol carbonylation by bridging the primary and secondary coordination spheres. Organometallics 35(17):3074–3086. https://doi.org/10.1021/acs.organomet.6b00607
82. Gregor LC, Grajeda J, White PS, Vetter AJ, Miller AJM (2018) Salt-promoted catalytic methanol carbonylation using iridium pincer-crown ether complexes. Cat Sci Technol 8(12): 3133–3143. https://doi.org/10.1039/C8CY00328A

Top Organomet Chem (2023) 70: 99–156
https://doi.org/10.1007/3418_2022_77

Published online: 10 December 2022

Role of a Redox-Active Ligand Close to a Dinuclear Activating Framework

Catherine Elleouet, François Y. Pétillon, and Philippe Schollhammer

Contents

Abstract The main advances, over the last two decades, on dinuclear complexes featuring a redox-active ligand close to the bimetallic core are presented in this chapter. At the end of the nineties, the discovery of the structure of the active site of [FeFe]-hydrogenases has led to a revival of the chemistry of dithiolato/bis-thiolato bridged carbonyl di-iron complexes with the aim of understanding the functioning, at the molecular level, of this family of metallo-enzymes and to reproduce their activity towards the reversible H^+/H_2 conversion. The progress in the knowledge of the H-cluster reveals that its high activity is due to an efficient and subtle Nature's engineering that involves a dinuclear activating framework and its cooperativity with redox-active ligand and proton-relay. If initially the development of this chemistry has been centred on the preparation of rudimentary di-iron compounds in order to study their ability to reduce protons electrochemically or photochemically, more sophisticated systems with a relay of protons, for promoting proton transfers, have rapidly emerged. Paradoxically, it is only quite recently that an increasing number of derivatives incorporating a redox-active ligand has been elaborated. To date, there are only a few di-iron compounds capable of reproducing H-cluster activity. These

C. Elleouet, F. Y. Pétillon, and P. Schollhammer (✉)
UMR CNRS 6521 'Chimie, Electrochimie Moléculaires et Chimie Analytique', Université de Bretagne Occidentale, Brest, France
e-mail: Philippe.Schollhammer@univ-brest.fr

researches are still ongoing and they have contributed to develop the chemistry of dinuclear complexes with redox ligands.

The first part of this chapter is dedicated to the advances in this di-iron bio-inspired chemistry, which has led to consider the combination of carbonyl di-iron platforms with a large series of redox ligands and the different ways for introducing them near the di-iron core. Examples of hetero-bimetallic [NiFe] species featuring a redox group, considered as models of the [NiFe]-hydrogenases, are also presented.

Considering the renewal of the interest in using bimetallic systems for molecular activation in order to develop novel catalytic processes, the second part of this chapter presents selected examples of bimetallic derivatives featuring chelating redox-active ligands. Their properties/activities, often original or unexpected, in connection with the presence of the redox-active ligand in the coordination sphere of a dinuclear framework, are described. These results, even if their presentation in this chapter may appear somewhat scattered, demonstrate that the combination of "non-innocent" ligands (redox-active in this chapter but also proton-responsive) with dinuclear sites offers interesting perspectives in the field of molecular activation with transition metal complexes.

Keywords Bio-inspired complexes · Catalysis · Cooperative effects · Dinuclear complexes · Electron reservoir · Non-innocence · Redox-active ligand · Small molecules activation · Transition metal

1 Introduction

Numerous reviews and perspective articles have been dedicated to redox-active ligands and their "non-innocence" [1–28]. The combination of such ligands with metal frameworks affords important perspectives in the field of catalysis and molecular materials. A plethoric number of metal compounds combining redox ligands has been reported, but the building of such devices for the activation of small molecules is still in its infancy, especially with polymetallic derivatives, and is highly promising in reason of the possibility to produce, using such combinations, efficient catalysts based on earth-abundant first-row transition metals instead of expensive noble metals. One of the main roles, that a redox-active ligand may display, is to behave as an electron reservoir into the vicinity of a metallic active site and to allow electron transfers during the chemical transformation process of substrates. Depending on the nature of the metallic framework, this ability to store or to release electrons also induces other interesting processes such as the transfer of single electron to the substrate, the stabilization of reactive radicals or the control of Lewis acid/base character of the metal centre.

During these decades, a renewed and growing attractiveness for the chemistry of bimetallic systems has also emerged in reason of the interest that cooperative and

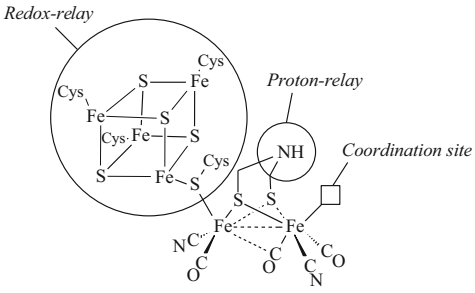

Scheme 1 Schematical view of the H-cluster of [FeFe]-hydrogenases

synergistic effects between two metal centres in close proximity may have for bond activation and catalysis, thus affording a complementary and efficient approach to the single-metal reactivity and catalysis [29–44]. Compared to monometallic systems, much fewer bimetallic systems including a redox ligand have been described until now. However, there is an important interest for catalysis in the design of first-row transition bimetallic systems with a nearby redox-active ligand in order to explore and to find new reactional processes, which do not take place at a single metal centre. They may be favoured by a higher electronic flexibility of the bimetallic site and a better control of multi-electron transfers, through metal-ligand cooperativity. The development of such bimetallic systems has been stimulated by the existence of efficient natural systems, which has led to a bio-inspired approach. Indeed, multielectron transfers are ubiquitous in biologically important activation processes, such as hydrogen production/uptake, nitrogen fixation or CO_2 reduction…, which are catalyzed by metalloenzymes with multimetallic active sites (hydrogenases, nitrogenases or CO-dehydrogenase, respectively) [45–49].

One of the most outstanding examples is the H-cluster (Scheme 1), the active site of [FeFe]-hydrogenases, that is a natural sophisticated archetype for bimetallic activation involving metal-metal and metal-ligand cooperativities [50–53].

The high bidirectional catalytic efficiency of [FeFe]-hydrogenases towards H^+/H_2 conversion is governed by fine structural and electronic rearrangements that are controlled by electron and proton transfers, mediated by the amine of the azadithiolato bridge, acting as a proton-relay, and the redox-actif $[Fe_4S_4]$ cubane, occuring throughout the catalytic cycle [45, 53–55]. Principally, two mechanisms for the functioning of the H-cluster are currently proposed (Scheme 2). They are still under debate and the question of protonation and redox steps sequences, involving separate proton- and electron-transfers or PCETs, still remains open. These mechanism highlight the structural and electronic synergy between the two iron atoms in the di-iron subsite. The role of the $[Fe_4S_4]$ sub-cluster is evidenced as essential, acting as an electron reservoir during catalysis, cycling between $[Fe_4S_4]^+$ and $[Fe_4S_4]^{2+}$ states, but also being proton-responsive and thus allowing to adjust the electronic balance between the cubane and the di-iron subsite for a high catalytic activity.

Despite the syntheses and studies of hundreds di-iron complexes bio-inspired by the H-cluster, a limited number of efficient di-iron species containing ligands with

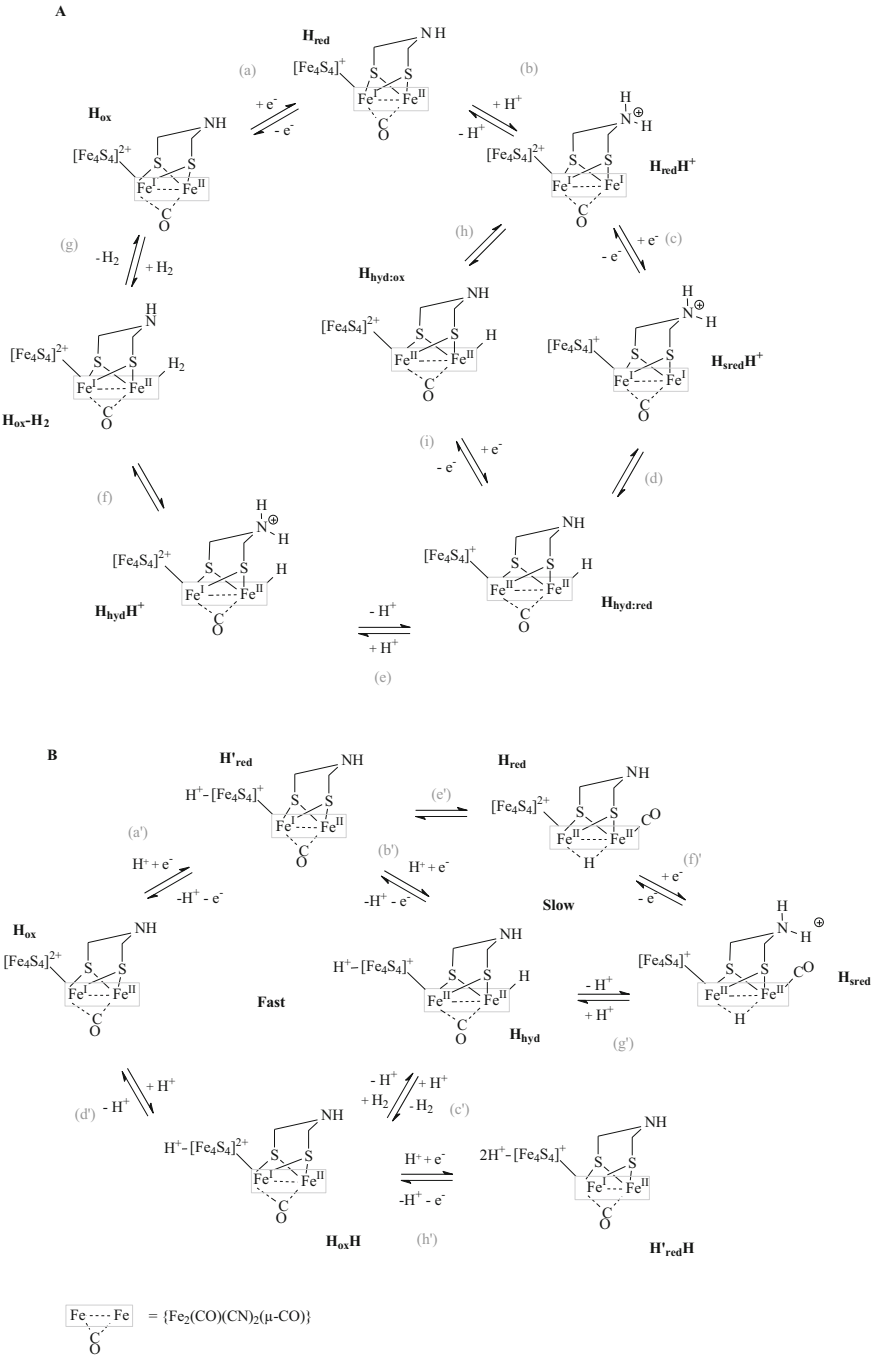

Scheme 2 Two current models proposed for the catalytic cycle of [FeFe]-hydrogenases

redox properties, modelling the role of the electron reservoir played by the $[Fe_4S_4]$ subcluster, has been reported. Moreover, the redox activity of such ligands at a di-iron site has been very scarcely observed or demonstrated [55–61].

The first section of this chapter is specifically dedicated to a state of the art of dinuclear molecules with redox ligands bio-inspired by hydrogenases. Homo-dinuclear [FeFe] complexes have been considered as well as some rare examples of hetero-bimetallic [NiFe] species. The second section is an overview of dinuclear systems containing various chelating redox ligands in order to illustrate the effect that such ligands may have on the structure of bimetallic complexes, on their electronic properties and redox chemistry as well as on their chemical activity.

An arbitrary choice has been made to subdivide each section according to the nature of the redox ligands rather than that of the metal or according to the activity that is induced (bond formation or cleavage, electron storage or releasing upon redox processes, generation of radical based-ligand, structural effect on metal-metal interaction, redox isomerism. . .) or according to the chemical process that is concerned (H^+/H_2 conversion, H_2O oxidation, N_2 reduction, O_2 reduction. . .).

The scope of the topic tackled in this chapter is delimited to the d-transition metal chemistry. Most of the reported examples in this chapter involve dinuclear compounds with metal centres in close proximity and a redox ligand linked by covalent interactions in the first or second coordination sphere of the bimetallic core. Examples of dinuclear species associated to photosystems or grafted in electrode materials as well as those used for the design of molecular electronic/magnetic devices have not been considered in the scope of this chapter.

2 Hydrogenases-Bio-Inspired Dinuclear Complexes Featuring a Redox Ligand

Strategies for introducing an electron reservoir into the vicinity of a bimetallic site are nicely exemplified by the chemistry of di-iron complexes comprising a surrogate of the $[Fe_4S_4]$ sub-cluster of the H-cluster. Redox ligands have been introduced in the coordination sphere of the dinuclear site either by the replacement of one or two terminal carbonyl groups in carbonyl di-iron precursors $[Fe_2(CO)_{6-x}L_x(\mu\text{-dithiolato})]$ ($x = 1, 2$) or by the functionalization of the dithiolato bridge through the use of preformed dithiols, or cyclic disulfides, respectively [55, 56, 58]. Other strategies, based on the combination of mononuclear precursors, have been also developed. Various redox ligands or groups, such as nitrosyl, phosphole, fullerene, nitrogen and dinitrogen ligands (pyridine, bipyridine, phenanthroline, azopyridine. . .), phosphine and diphosphine functionalized, or not, with a ferrocenyl moiety have been combined with a di-iron core through the substitution of CO. Simplified and general strategies for the preparation of homo-bimetallic species with a redox ligand are illustrated in the Scheme 3. Similar strategies have been used for the synthesis of hetero-bimetallic species.

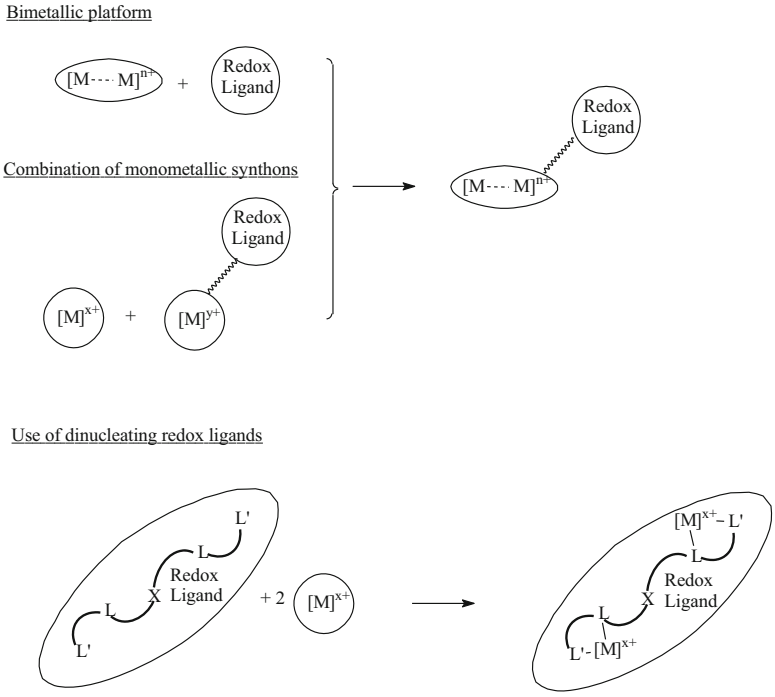

Scheme 3 General strategies for the preparation of homo-bimetallic species featuring a redox ligand

2.1 Complexes with a Non-Metal Based Redox Ligand

2.1.1 Introduction of a Redox Ligand Through Monodentate Coordination

NO ligand. The coordination chemistry of NO is well known and its role is crucial as a signaling molecule (gasotransmitter) in numerous physiological and pathological events in biology [62, 63]. NO presents an ambidentate mode of coordination by varying its (M-N-O) bond angle depending on its donor/acceptor ability towards a metallic framework. It can behave as a strong π-electron acceptor nitrosyl cation NO^+ (linear M-N ≡ O), a neutral nitric oxide radical $NO^{\bullet}$ (bent M-NO) or a strong electron donor when considered as the nitroxide anion NO^- (bent [M-N=O]).

A series of nitrosyl di-iron complexes (**1**-**6**) (Scheme 4) was prepared by reacting $NOBF_4$ with various precursors such as $[Fe_2(CO)_{6-2y}(\kappa^2\text{-dppv})_y(\mu\text{-xdt})]$ (y = 1 or 2; dppv = cis-1,2-bis(diphenylphosphinoethylene); xdt = 1,2-ethanedithiolato (edt) or 1,3-propanedithiolato (pdt)) and by a further CO substitution with PMe_3 or CN^- [64]. Complexes $[Fe_2(CO)_{6-y}(PMe_3)_y(\mu\text{-xdt})]$ (y = 1 or 2) also react with $NOBF_4$ affording the parent nitrosyl complexes $[Fe_2(CO)_{5-y}(PMe_3)_y(NO)(\mu\text{-xdt})](BF_4)$ (**7**-**10**) (Scheme 4) by releasing one CO [65]. Apparently, NO does not alter the formal

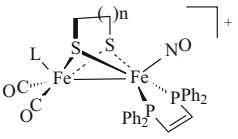

L = CO ; n = 1 (**1**), 2 (**2**);
L = PMe_3 ; n = 1 (**3**)

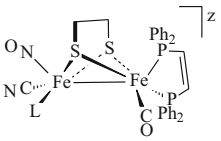

z = 1- ; L = CN **4**
z = 0 ; L = PMe_3 **5**

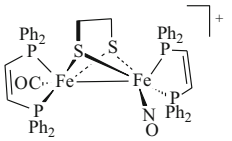

6

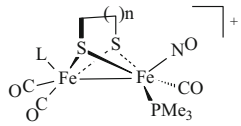

L = CO ; n = 1 (**7**), 2 (**8**)
L = PMe_3 ; n = 1 (**9**), 2 (**10**)

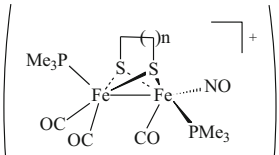

distorted geometry of **9**, **10**

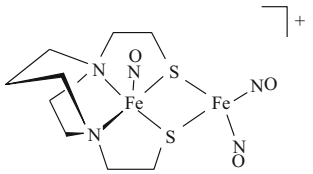

11

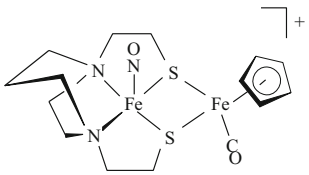

12

Scheme 4 Various di-iron nitrosyl complexes

oxidation state $Fe^{I}Fe^{I}$ of the di-iron core in these compounds despite two facts. Firstly, complexes $[Fe_2(CO)_{5-y}(PMe_3)_y(NO)(\mu\text{-xdt})](BF_4)$ adopt a distorted rotated structure, especially when $y = 2$, resembling to the structure of the redox state H_{ox} of [FeFe]-hydrogenases, which has a mixed valent subunit $Fe^{II}Fe^{I}$. Secondly, DFT calculations show that the charge density at iron atoms in the disubstituted derivative $[Fe_2(CO)_3(PMe_3)_2(NO)(\mu\text{-pdt})](BF_4)$ (**10**) fits better with that of the monocationic $Fe^{II}Fe^{I}$ complex $[Fe_2(CO)_4(PMe_3)_2(\mu\text{-pdt})]^+$ than with that of the neutral $Fe^{I}Fe^{I}$ species $[Fe_2(CO)_4(PMe_3)_2(\mu\text{-pdt})]$. Although it has been shown that an asymmetrical substitution of terminal ligands at di-iron centres combined with a steric crowding bridge may cause geometric distortions [66], the difficulty in giving a clear electronic description of the di-iron site in terms of oxidation state suggests a redox "non-innocent" role of NO. Moreover, this ambivalence is also suggested by the formation of the nitrosyl species $[Fe_2(CO)(\kappa^2\text{-dppv})_2(NO)(\mu\text{-edt})]^+$ (**6**) by reacting the preformed cationic radical $[Fe_2(CO)_2(\kappa^2\text{-dppv})_2(\mu\text{-edt})]^+$ ($Fe^{II}Fe^{I}$) with NO. Upon reduction of $[Fe_2(CO)_3(\kappa^2\text{-dppv})(NO)(\mu\text{-edt})]^+$ (**1**) into its neutral form by treatment with the decamethylcobaltocene at low temperature (−78°C), IR recordings show an important shift of *ca* 180 cm^{-1} at lower wavenumbers of the

Scheme 5 N-Heterocyclic Carbene and arylisocyanide complexes

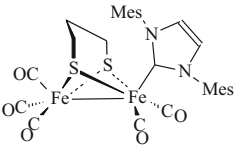

13

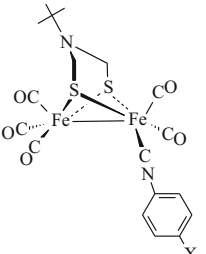

14

ν(NO) band, which corroborates the redox behaviour of NO, that is also shown by EPR measurements [64].

Such accommodation of redox level for regulation of electronic density through electron uptake and storage by a {FeNO} moiety was also exemplified by experiments and calculations in compounds $[Fe_2(bme\text{-}dach)(NO)_3](BF_4)$ (**11**; bme-dach = N,N′-bis(2-mercaptoethyl)-1,4-diazacycloheptane) and $[Fe_2(Cp)(bme\text{-}dach)(CO)(NO)](BF_4)$ (**12**; Cp = η^5-C_5H_5) (Scheme 4), in which the {MN2S2} core is also reminiscent of the active site of acetyl CoA synthase [67–69]. In the case of **11**, a single electron reduction assigned to the mono-nitrosyl iron takes place at −0.78 V vs. (Fc^+/Fc), while the other di-iron moiety reduces at −1.41 V. After the transfer of the first electron at −0.78 V, the reduced species becomes active in the presence of acid, leading to a cationic complex which is again reduced at this potential.

N-Heterocyclic Carbene (NHC) and isocyanide (RNC) ligands. A possible role of a N-Heterocyclic Carbene (NHC), as a redox ligand, in the complex $[Fe_2(CO)_5(\kappa^1\text{-}IMes)(\mu\text{-}pdt)]$ (**13**; IMes = 1,3-bis(2,4,6-trimethylphenyl)imidazol-2-ylidene) (Scheme 5) has been explored by DFT in order to rationalize the two-electron reduction of this species at the same potential. These calculations proposed that, after the first electron transfer centred on the di-iron core, the addition of a second electron at the IMes ligand would afford a triplet state that is more stable than the singlet one arising from the double reduction at the di-iron site [70]. Until now, no other example of di-iron species featuring NHC ligands, non-functionalized with a redox group, has displayed such a behaviour [71, 72].

In the series of arylisocyanide (ArNC; Ar = pC_5H_5X) monosubstituted derivatives $[Fe_2(CO)_5(\kappa^1\text{-}ArNC)(\mu\text{-}S_2\{CH_2\}_2N^tBu)]$ (**14**) (Scheme 5), the LUMO can be either purely ligand centred (X = NO_2) or distributed over the isocyanide and the di-iron centre (X = CF_3, CN), or quasi fully metal centred (X = OCH_3, CH_3, H, I). These results suggest that a simple tuning of such common ligands allows to control the transfer of an electron at the ligand or at the metal centre as well as to find intermediate electronic situations where the redox ligand would become "non-innocent" [73].

Phosphole ligand. The compound $[Fe_2(CO)_5(\kappa^1\text{-phosphole})(\mu\text{-bdt})]$ (**15**; bdt = 1,2-benzenedithiolato) is a scarce example of an aqueous-soluble complex

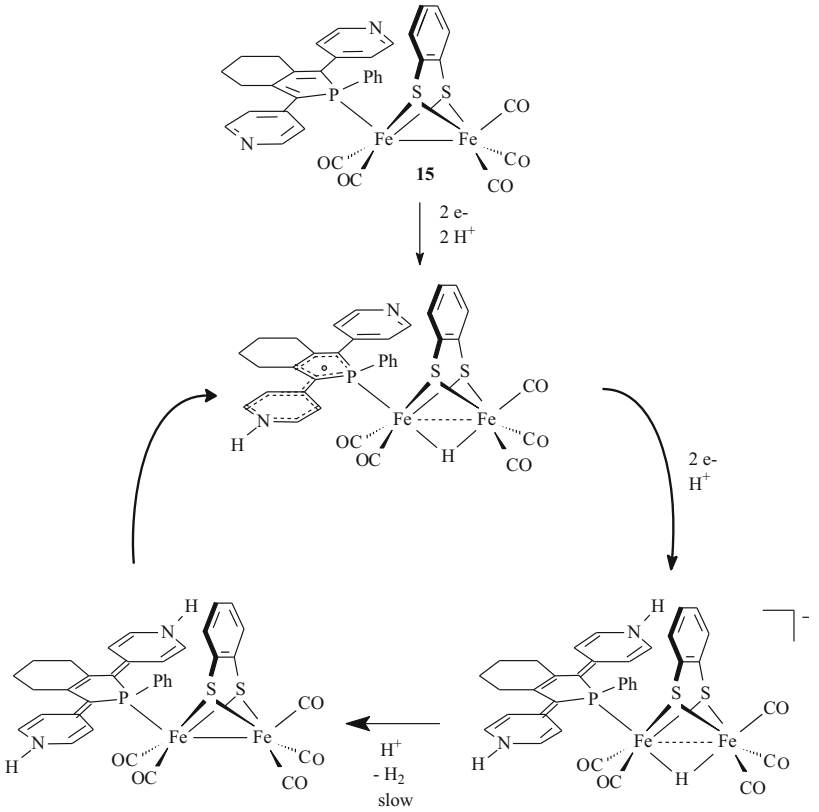

Scheme 6 Involvement of a di-iron compound featuring a redox-active phosphole ligand in HER process

containing a dipyridylphosphole ligand with a redox-active behaviour. It has been prepared from the hexacarbonyl compound [$Fe_2(CO)_6(\mu$-bdt)] in which a carbonyl group is displaced by the phosphole ligand. Upon reduction, the monoanion retains the structure of the neutral parent complex, the added electron being localized on the phosphole ligand. The addition of a second electron occurs at the di-iron core, weakening the Fe-S bond and leading to the formation of a dianionic species able to accept a further electron. Spectroelectrochemistry and time-resolved IR spectroscopy studies strongly suggest that the phosphole ligand is involved in the proton reduction process, acting as an electron reservoir and also being proton-responsive through the presence of pyridyl moieties. These properties allow a well-suited leveling of redox potentials during the catalytic cycle due to a balance of charges induced by protonation of the redox ligand and electron transfers (Scheme 6) [74, 75]. Using H_2SO_4 (1 M), efficient HER catalysis in water occurs at −0.66 V vs. NHE with a turnover frequency (TOF) of 70,000 s^{-1} and a catalytic rate constant of 3.5×10^4 M^{-1} s^{-1}.

Scheme 7 The di-iron complex **16** with a redox fullerene moiety

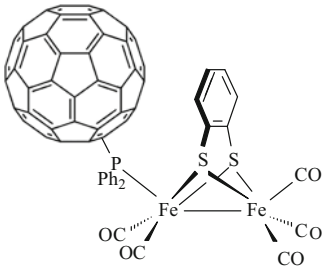

16

Scheme 8 Terminal or bridged dithioformate phosphine at a di-iron site

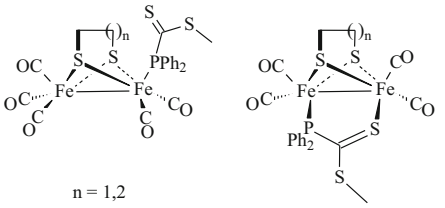

17 **18**

Functionalized phosphine ligand. Phosphine linkers can be used to introduce a redox-active ligand in the vicinity of a bimetallic core, but the electronic communication between subsets is generally weak. The C_{60} fullerene is known to be able to uptake up to six electrons [76, 77]. The fullerene complex $[Fe_2(CO)_5(\kappa^1\text{-}PPh_2C_{60}{}^H)(\mu\text{-bdt})]$ (**16**) (Scheme 7) was prepared to study the interplay between such a potential electron reservoir and a di-iron site [78, 79]. Four reversible reductions were detected by cyclic voltammetry, three of them (the first, the second and the fourth) were assigned to the fullerene reduction and the third was proposed to be centred at the di-iron core. Spectroscopic and DFT studies suggest that, depending on the redox state of the dinuclear centre, its electron density is modulated by the presence of the fullerene. Indeed, in contrast to the monoanion where the electron density is mainly on the fullerene subset, the spin density of the dianion, in its triplet state, displays a significant extent of spin delocalization onto the di-iron centre, the potential of the second reduction being however ascribed to the C_{60} based-reduction. These results indicate that the electron acceptance by the redox partner with a more accessible LUMO, followed by an electron transfer to the di-iron centre may facilitate the lowering of potential for proton reduction [60, 78].

Di-iron complexes featuring a phosphine with a dithioformate group PPh_2CS_2Me (Scheme 8) were prepared by reaction of ^{n}BuLi/CS_2/MeI with $[Fe_2(CO)_5(\kappa^1\text{-}PPh_2H)(\mu\text{-xdt})]$ (xdt = edt, pdt) [79]. Depending on the mode of coordination of this phosphine, terminal in $[Fe_2(CO)_5(\kappa^1\text{-}PPh_2CS_2Me)(\mu\text{-xdt})]$ (**17**) or bridged in $[Fe_2(CO)_4(\mu\text{-}PPh_2CS_2Me)(\mu\text{-xdt})]$ (**18**), the dithioformate component displays, or not, redox behaviour. DFT calculations revealed that the LUMO of **18** is mainly

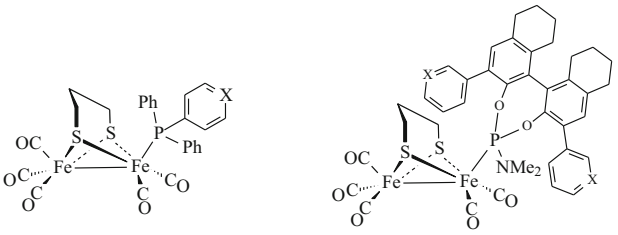

		k_{obs} (s^{-1})		k_{obs} (s^{-1})
X = N	**19**	580	**20**	6340
X = CH	**21**	130	**22**	240

Scheme 9 Pyridyl-, phenyl-phosphine and -phosphoramidite based di-iron complexes. The observed rate constants (k_{obs}) for proton reduction (acetic acid 7 mM) are given

distributed (> 85%) on the dithioformate moiety of the bridging phosphine ligand confirming that the first reduction arises on the bridging ligand and thus affords a thiolato-thiyl state upon reduction of the thione function. The electrocatalytic activity of **17**, **18** towards proton reduction was not reported, preventing to evaluate the impact of the change in the coordination of the dithioformate phosphine ligand in connection with the related concomitant redox-non-active → redox-active switching.

Interestingly, the presence of a pyridyl group in monodentate phosphine and phosphoramidite ligands strongly enhances the rate constant of proton reduction (k_{obs}) of mono-substituted di-iron species (**19, 20**) (Scheme 9) compared to that of their analogous derivatives (**21**, **22**) with a phenyl group instead of a pyridyl one [80]. If the dimethylamino group, in **20**, **22**, may act as a proton relay, the role of the pyridyl functionalities has not been clearly demonstrated but their presence may favour electronic communication between the phosphine and the di-iron site or may contribute to stabilize reduced species.

2.1.2 Introduction of a Redox Ligand via Chelating Coordination

Diphosphine. The 2,3-bis(diphenylphosphino) maleic anhydride (bma) is a redox-active ligand that affords a reversible single-electron reduction at −1.10 V vs. (Fc^+/Fc) followed by an irreversible one at −1.89 V [81]. A similar cyclic voltammetry with a positive shift of 0.2 V is obtained for the complex $[Fe_2(CO)_4(\kappa^2\text{-bma})(\mu\text{-pdt})]$ (**23**) (Scheme 10) [81]. The first reduction of **23** is bma-centred, the electron residing in its π* orbital. The presence of the oxygen atom favours delocalization through resonance effects, preventing the charge transfer to the di-iron centre. The lack of electronic communication between the redox diphosphine and the di-iron core is obvious and prevents the protonation of this latter upon reduction of bma [82]. DFT calculations highlight that an electron transfer would not take place even if the

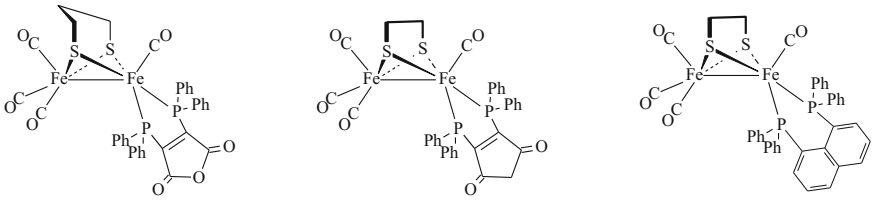

23 24 25

Scheme 10 Di-iron complexes with redox diphosphines

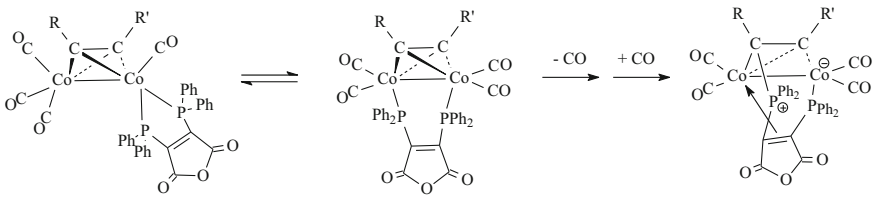

26 27 28

Scheme 11 Interconversion of "bma di-cobalt" complexes

di-iron centre was protonated. Therefore, the reduced diphosphine appears to be an innocent bystander. The same conclusions are drawn in the case of the complex $[Fe_2(CO)_4(\kappa^2\text{-bpcd})(\mu\text{-edt})]$ (**24**) (bpcd = 4,5-bis(diphenylphosphino)-4-cyclopenten-1,3-dione). It is nevertheless worth noting that, unlike **23**, this complex catalyses the proton reduction due to the greater stability of the bpcd moiety compared to that of bma after the uptake of the second electron [83]. DFT calculations predict that, when the oxygen atom of the bma cycle is replaced by a less electronegative sulfur atom, an intramolecular charge transfer from the redox-active ligand to the di-iron core should be triggered by protonation at the di-iron site [82]. These results strongly suggest that a fine rational tuning of the redox diphosphine may induce an electronic communication with the di-iron core. They also highlight that the presence of a redox ligand in the coordination sphere of a bimetallic site is not a sufficient condition to observe a tight coupling between proton and electron transfers.

Interestingly, κ^2-bma → μ-bma isomerization was studied in di-cobalt complexes $[Co_2(CO)_4(bma)(\mu\text{-RCCR'})]$ (**26**, **27**) (Scheme 11) [84–87]. The transient loss of a carbonyl group in the μ-bma complex **27** triggers a change in the coordination of the diphosphine which leads to a zwitterionic product **28** through the formation of a P-C bond with the bridging alkyne. It has been shown that the π^* orbital contribution of the bma ligand into the LUMO of these complexes varies accordingly to its coordination mode to the di-cobalt core. The character of the LUMO is fully centred on the bma ligand in complexes $[Co_2(CO)_4(bma)(\mu\text{-RCCR'})]$ (**26**, **27**) while it acquires a mixed-metal-ligand character in the zwitterionic species **28**. The examination of

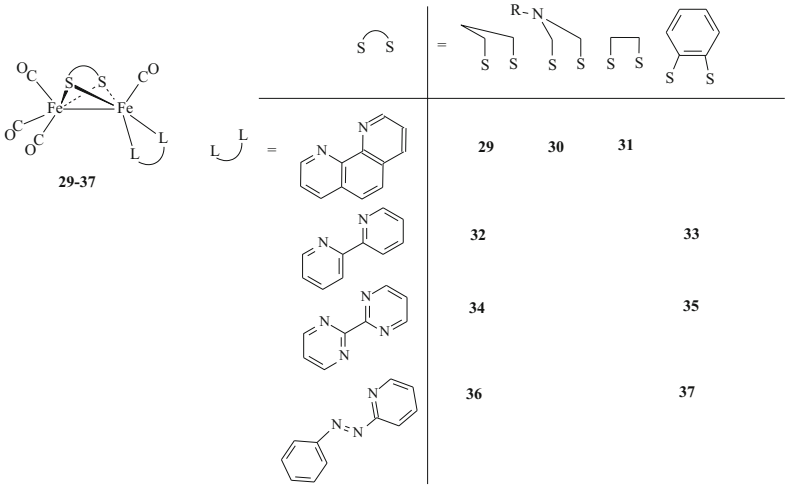

Scheme 12 Di-iron complexes with chelating nitrogen-donor ligands

redox potentials of **26**-**28** confirms the electronic description suggested by theoretical calculations and the contribution of the bma group in a consistent stabilization of the reduced forms. Furthermore, adjusting the coordination mode of bma affords the possibility to tune the redox behaviour of the dinuclear systems.

The complex $[Fe_2(CO)_4(\kappa^2\text{-dppn})(\mu\text{-edt})]$ (**25**), with dppn =1,8-bis (diphenylphosphino) naphthalene, a diphosphine bearing an extended π-system, was also studied (Scheme 10). The LUMO of this complex can be described as a delocalized π-naphthalene-based orbital with an antibonding Fe-Fe contribution. In contrast to the bma di-iron species **23**, it turned out to be an efficient electrocatalyst towards proton reduction, suggesting that the redox-active dppn plays a still unclear crucial role in this process [88].

Nitrogen-donor ligands. Several di-iron complexes with various chelating nitrogen-donor ligands, such as bipyridine, phenanthroline, bipyrimidine, azopyridine, have been reported (Scheme 12). The examination of the redox behaviour of the complexes $[Fe_2(CO)_4(\kappa^2\text{-phen})(\mu\text{-xdt})]$ (**29**, **30**) (xdt = pdt or adt with adt = azadithiolato), through recent electrochemical studies and DFT calculations, reveals the control that a redox-active chelate like phenanthroline exerts on the electronic properties of a dinuclear site with a $\{Fe_2(CO)_4(\mu\text{-dithiolato})\}$ framework [89]. Its electron acceptor properties are involved and direct the reduction of the complex towards a two-electron process with a potential inversion unlike other chelate ligands (diphosphine, bis-carbene). The phenanthroline ligand ensures electronic communication with the di-iron site and allows an almost total or partial redistribution of the two electrons leading to the existence of two isomers with either a cleavage of a Fe-S bond or the retention of the {Fe2S2} core with a concomitant stretching of the Fe-Fe bond. This indicates that, depending on the isomer, such a

ligand prevents, or not, a Fe-S disruption and may induce alternative mechanisms in HER catalysis.

DFT calculations were also carried out for a series of complexes featuring ethanedithiolato bridge and phenanthroline/bipyridine ligands and they similarly show that the reduction of these complexes implies the di-iron centre and the diazo ligand [90]. Upon reduction of **31**, giving the anionic species $[Fe_2(CO)_4(\kappa^2\text{-phen})(\mu\text{-edt})]^-$ (**31**$^-$), the first electron is added to the N-chelate into an orbital with significant π* character while the second electron transfer, leading to the doubly reduced species $[Fe_2(CO)_4(\kappa^2\text{-phen})(\mu\text{-edt})]^{2-}$ (**31**$^{2-}$), arises into an orbital with a significant σ*(Fe-Fe) character affording an electronic state for the dianion described as an open-shell triplet [90].

A comparison of the four complexes **32**-**35**, bearing either a propanedithiolato (pdt) or a benzenedithiolato (bdt) bridge and a bipyridine or a bipyrimidine as chelating ligand (bipy = 2,2′-bipyridine; bpym = 2,2′-bipyrimidine) (Scheme 12) shows that the effect of the N-chelating ligand depends on a fine electronic balance with the dithiolato di-iron moiety. Thus, the replacement of diazo chelates, bipy → bpym, does not lead to similar observations depending on whether the complex contains a pdt or a bdt bridge. The complexes **33** and **35**, in the bdt series, are characterized by a two-electron reduction. The bipy → bpym replacement leads to a shift of the potentials values (~130 mV) towards more positive ones in reason of the stronger electron π-acceptor character of the bipyrimidine group [91, 92]. In the case of complexes carrying a propanedithiolato bridge (**32**, **34**), the reductive process is different. Indeed, while the bipyridine complex **32** presents a two-electron reduction (one electron reduction is centred on the metal and the second is proposed to occur on the chelating ligand), the bipyrimidine analogue **34** is characterized by two separate reductions with a ΔE_p of 520 mV. The first monoelectronic reduction is centred on the bpym ligand and the second one would involve two electron transfers, one centred on the metal atom and the other on the ligand ($bpym^{1-}$/$bpym^{2-}$). The formal replacement of two CH groups by a nitrogen atom (bipy vs. bpym) lowers the energy of the molecular orbitals of the ligand making bpym easier to reduce than bipy. Moreover, bpym is a better π-acceptor which stabilizes the reduced metal centre by delocalizing the electronic density into the lower vacant π* orbital. Such a tuning modifies the electronic properties of the complexes but in this case, the benefit on the efficiency towards catalytic HER activity is disappointingly non-existent. The complexes with bpym (**34**, **35**) do not catalyze the reduction of protons probably due to an unwell-suited site of protonation (unbound nitrogen of bpym vs. di-iron centre). For **33**, in the presence of acetic acid, TOF values up to 1.170 s^{-1} have been determined by cyclic voltammetry with an overpotential of *ca* 620 mV (electrocatalytic event at *ca* −2.0 V), close to that of **32**.

The use of azopyridine, as a chelating ligand, has been also reported [93]. The benzenedithiolato complex $[Fe_2(CO)_4(\kappa^2\text{-pap})(\mu\text{-bdt})]$ (**37**) (pap = 2-phenylazopyridine) was prepared and its electronic structure investigated by DFT calculations. A decrease of the HOMO-LUMO gap is found in comparison with that observed for the hexacarbonyl analogue. While the frontier orbitals (HOMO-LUMO) of this latter compound are distributed over the {Fe2S2} core, the HOMO

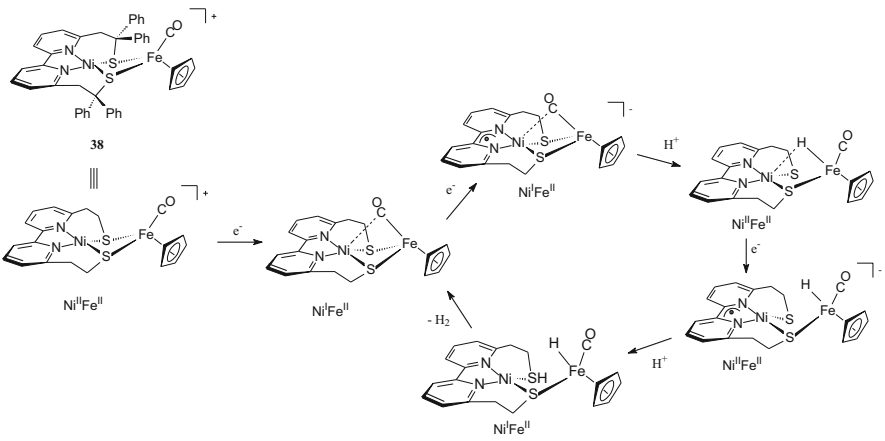

Scheme 13 Mechanism of proton reduction induced by a NiFe featuring a tetradentate redox bipyridine bis-thiolato ligand

of **37** is almost entirely localized on the iron atoms bearing the redox ligand. On the other hand, the LUMO has a mixed metal-ligand character but it mainly remains localized on the chelating ligand (π orbital), which explains the metal-to-ligand charge transfer transition observed (~600 nm) in the UV-visible spectrum (CH_2Cl_2). An identical observation is made for the propanedithiolato analogue [$Fe_2(CO)_4(\kappa^2$-pap)(μ-pdt)] (**36**), in reason of similar frontier orbitals. Such observations suggest a facile communication between the di-iron centre and the azopyridine which should help the protonation at the di-iron site while avoiding an overly negative reduction potential, thus affording catalysts operating with low overpotential. Unfortunately, the electrochemical behaviour towards proton reduction being not studied, the benefit of the presence of the azopyridine in these complexes is not established.

The mechanism of H_2 evolution from the heterodinuclear $Ni^{II}Fe^{II}$ complex **38** featuring a tetradentate bipyridine bis-thiolato ligand N2S2 is presented in the Scheme 13. **38** undergoes, near its second reduction potential (−1.90 V vs. Fc^+/Fc), an electrocatalytic event, in the presence of weak acid ($(Et_3NH)(BF_4)$), with relatively high rates (TOF ~ 250 s^{-1}) [94–96]. The mechanism details of this catalytic process and the role of the redox-active bipyridine ligand have been explored. After a one-electron reduction of the starting $[Ni^{II}Fe^{II}L]^+$ system (mimic of Ni-SIa state) into $[Ni^{I}Fe^{II}L]$ state (Ni-L), a further reduction is centred on the bipyridine ligand affording a radical species $[Ni^{I}Fe^{II}L^{\bullet}]^-$. Then, protonation step affords a Fe-hydride $[(Ni^{II})(HFe^{II})L]$ (Ni-R). A third electron is accommodated by the bipyridine giving a $[Ni^{II}(HFe^{II})L^{\bullet}]$ state, that is enough basic to be S-protonated on a thiolato group, thus affording "hydride-proton" intermediate $[Ni^{I}(HFe^{II})(SH)]$ able to release H_2.

2.1.3 Redox Bridging Ligands

Disulfido complexes, such as $[Fe_2(CO)_6(\mu\text{-}S_2)]$ and $[MnMo(Cp)(CO)_5(\mu\text{-}S_2)]$, are used in reason of the reactivity of the disulfido bridge and its ability to be functionalized with various reagents, such as alkyne, alkene as well as organic halides or metal moieties [97]. Such reactivity has been exploited to prepare a series of hexacarbonyl di-iron complexes containing dithiolato bridges with 1,4-benzoquinone, substituted (Me, OMe, Cl, ^{t}Bu)-1,4-benzoquinones, 1,4-naphthoquinone and 1,4 anthraquinone, as well as some of their disubstituted phosphine derivatives, in order to examine their electronic behaviours (Scheme 14) [98, 99].

Quinones are among the earliest redox-active ligands that have been described and whose reduction involves two one-electron transfers coupled with proton additions leading to hydroquinones (Scheme 15). The electronic communication between the di-iron centre and quinone moiety has been evidenced by EPR investigations and computational studies. These studies have shown that the one-electron reduction leads to anions in which the electron is delocalized between the semiquinone and the {Fe2S2} core, suggesting the "non-innocent" behaviour of such bridged ligands [98]. It is worth noting that in the presence of acetic acid, the formation of the hydroquinone species arises prior to any reduction of proton that

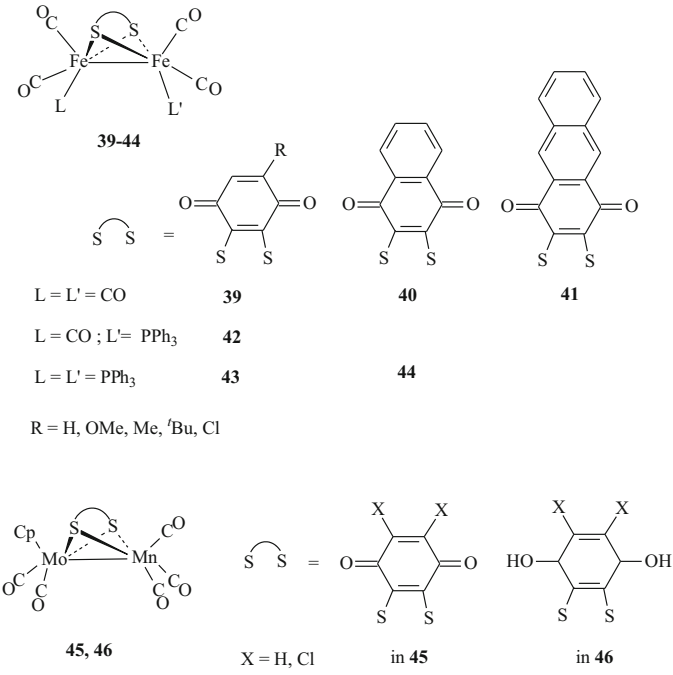

Scheme 14 Examples of quinone-containing di-iron and hetero-bimetallic [MnMo] complexes

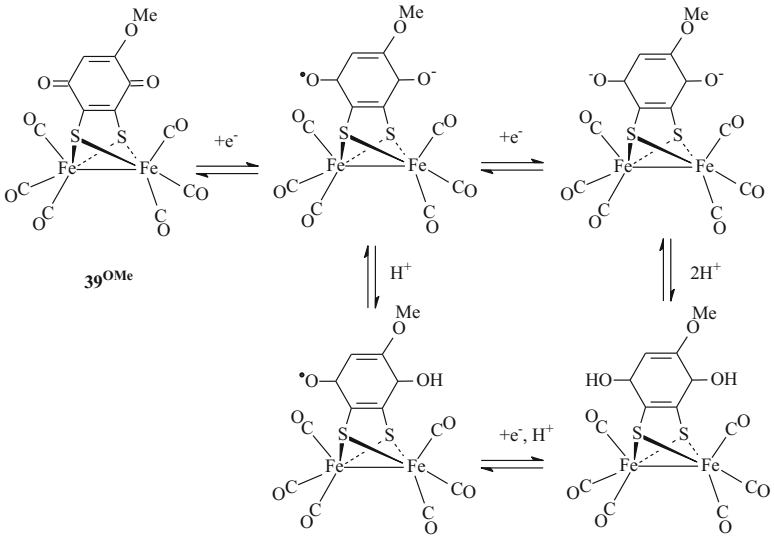

Scheme 15 Reduction process of a benzoquinone di-iron complexe in protic medium

appears at a more negative potential. The replacement of one or two carbonyl(s) by PPh_3 does not alter the first reduction of complexes **39**, **42**, **43** that is assigned to the one-electron reduction of the quinone redox couple (quinone /quinone^{1-}).

The use of dithiolato or thiolato bridges based on a naphthalene framework has been also explored (Scheme 16) [100–103]. In the case of the pyridyl-functionalized di-iron dithiolato naphthalene monoimide (**48**), a self-assembled complex was formed in the presence of zinc tetraphenylporphyrin (ZnTTP) through the pyridyl coordination. Combined time-resolved and spectroelectrochemical IR, EPR and DFT studies reveal that after the transfer of the first electron, the spin density of the reduced species is both delocalized over the di-iron core and the naphthalene monoimide (NMI) group [100]. This delocalization would explain the observed low catalytic efficiency towards proton reduction. Extension of this study to propargyl instead of pyridyl group confirms the properties of the NMI moiety upon the reduction and suggests that the second electron transfer arises at the di-iron site [101]. Recently, the combination of tetrathiafulvalene (TTF) groups with $[Fe_2(CO)_6(\mu\text{-}S_2)]$ (Scheme 16) was examined in reason of the electron-donating properties of TTF moieties and their specific redox behaviour in acid media generating protonated TTF species involved in the four-electron reduction of O_2 [104]. Differences in the location of the LUMO of complexes **55**-**57** were observed depending on the level of the π-extension of the TTF systems in the dithiolato bridge. The LUMO is centred on the di-iron core in **55** with a tetrathiafulvalene bridge while it is delocalized on the π-extended TTF, anthracenyl or tetracenyl, in **56** and **57**.

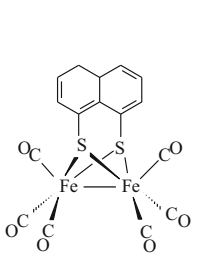

47

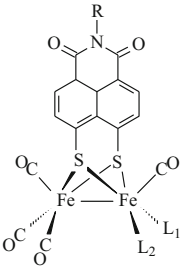

48-53

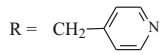

R = CH_2 N $L_1 = L_2 = CO$ **48**

L_1-L_2 = dppv **49**

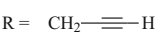

R = CH_2 H $L_1 = L_2 = CO$ **50**

$L_1 = CO$, $L_2 = PPh_3$ **51**

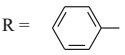

R = $L_1 = L_2 = CO$ **52**

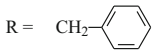

R = CH_2 $L_1 = L_2 = CO$ **53**

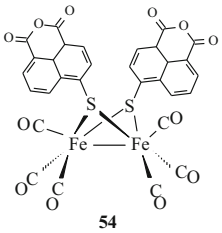

54

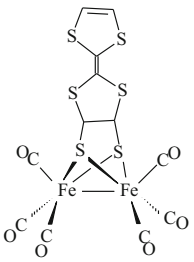

55

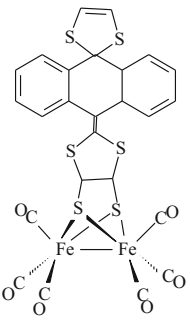

56

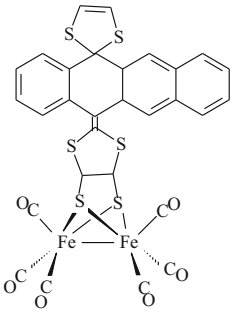

57

Scheme 16 Thiolato and dithiolato di-iron compounds with sulfur-bridges based on a naphthalene or tetrathiafulvalene backbone

The reaction of $[Fe_2(CO)_6(\mu\text{-}S_2)]$ with the C_{60} fullerene also allowed to introduce a redox group in the dithiolato bridge affording the hexacarbonyl complex $[Fe_2(CO)_6(\mu\text{-}S_2C_{60})]$ [105, 106].

Otherwise, the benzene-1,2 dithiolato (bdt) bridge has been widely used in di-iron models of the H-cluster in order to benefit of its electron-withdrawing effect on bimetallic site [55, 56, 58]. It is considered as a potential redox-active ligand in

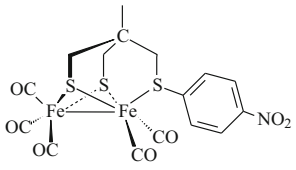

58

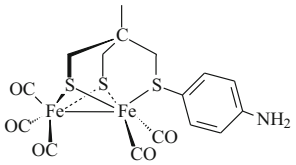

59

Scheme 17 Complexes with a remote non-metallic redox function bound to a linking S-atom at a {Fe2S3} site

reason of the possible oxidation of the dianion bdt^{2-} into the radical anion $bdt^{\bullet-}$ [107]. Such properties have not been evidenced in the case of complexes $[Fe_2(CO)_{6-x}L_x(\mu\text{-bdt})]$.

The influence of a remote non-metallic redox-active group bound to a linking S-atom in a similar fashion, as the redox cubane in the H-cluster, has been explored by studying the compounds **58** and **59** (Scheme 17) [108]. The first reduction is centred on the NO_2 group in **58** and further reductions in the presence of proton then afford the complex **59** with an amine function. The presence of the pendant NO_2 redox group and its redox/protic modifications have a straight effect on the strength of the thioether coordination and its ability to compete with CO coordination.

2.2 *Complexes with a Metal-Based Redox Ligand*

Fe_4S_4 cubane. There are very few examples of di-iron complexes in which the entire structure of the H-cluster is modelled. $[Fe_4S_4]$ cubanes, as a sub-cluster in the coordination sphere of a di-iron site, have been introduced following the pathway described for the preparation of the species $[Fe_2(CO)_5(CH_3C(CH_2S)_3\{Fe_4S_4(SR)_3\}]^{2-}$ (R = Me, 1,3,5-tris(4,6-dimethyl-3-mercaptophenylthio)-2,4,6-tris(*p*-tolyl-thio)benzene) (**60**) (Scheme 18) through the coordination of a thio-ether as a linker [109]. Theoretical and electrochemical studies showed evidences for an interplay of redox states of the di-iron site and the $[Fe_4S_4]$ sub-cluster and significant delocalization of frontier molecular orbitals on all the "6Fe" H-cluster [110, 111].

To date, **60** is the sole model incorporating a cubane cluster at a di-iron site. Electrochemical studies reveal that **60** is capable to electrocatalyze proton reduction. The rationalization of the electrochemical behaviour suggests that upon reduction, the $[Fe_4S_4]^{2+}$ moiety is reduced into $[Fe_4S_4]^{+}$, then an intramolecular electron transfer to the di-iron subsite arises concomitantly with the opening of the thioether bridge. The cubane remains linked to the dithiolato bridge and an open coordination site is thus generated at the di-iron site.

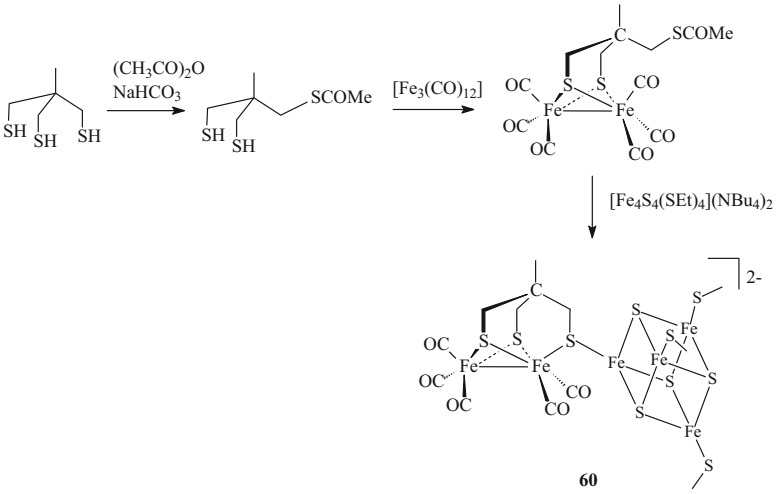

Scheme 18 A $[Fe_4S_4]$ cubane-based model of the H-cluster

Metallocene-based redox ligand. Several complexes featuring ferrocenyl group have been synthesized with the aim of modelling the role of the electron reservoir played by the $[Fe_4S_4]$ sub-cluster in the H-cluster.

A way for introducing the ferrocenyl group is to used the diphosphine $[Fe(\eta^5\text{-}C_5H_4PPh_2)_2]$ (dppf = 1,10-bis(diphenylphosphino)ferrocene) which can adopt a bridging or a terminal position (see selected examples **61-68** in Scheme 19) [112–117]. This is interesting insofar as small changes in the mode of coordination and in the bite angles of such diphosphine have an influence on the reactivity and the electronic behaviour.

In the complex $[Fe_2(CO)_4(\mu\text{-dppf})(\mu\text{-pdt})]$ (**61**$^{\mathbf{Ph}}$), the dppf oxidation ($Fe^{II} \rightarrow Fe^{III}$) at +0.685 V vs. ($Fc^+$/Fc) is strongly affected by the oxidation of the di-iron centre ($Fe^IFe^I \rightarrow Fe^{II}Fe^I$) that arises at 0.05 V (ΔE_p = 60 mV) in MeCN-$[Bu_4N][PF_6]$ [112]. Complexes **63** and **64** have similar electrochemical behaviours than **61**$^{\mathbf{Ph}}$ [115]. The level of cooperativity between the ferrocenyl group and the di-iron site in $[Fe_2(CO)_4(\mu\text{-dppf})(\mu\text{-pdt})]$ has not been clearly defined despite the fact that the two redox centres are about 4.5–4.7 Å apart in solid state, which is comparable with the distance between the $[Fe_4S_4]$ cluster and the di-iron subsite in the H-cluster (~4 Å) [117]. There is neither electron transfer induced by protonation, nor protonation induced by a charge transfer [112]. However, the presence of a mixed-valence $Fe^{II}Fe^I$ di-iron centre in proximity of a surrogate of the $[Fe_4S_4]$ cluster, such as dppf, may be suitable to trigger electron delocalization upon H_2 binding. Indeed, the activation of H_2 by such a complex has been observed in the presence of pyridine as an external base, and rationalized by DFT (Scheme 20). It was evidenced that the ground state of the $\{Fe^{II}Fe^I\}Fe^{III}$ dication has a rotated conformation close in energy to the unrotated isomer, thus affording either a site for H_2 binding in the apical position at one iron atom or in the Fe-Fe region [117, 118]. Moreover, further

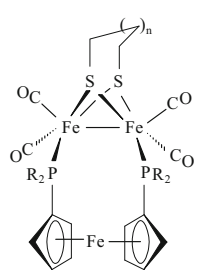

n = 1 ; R = Ph, Cy **61**
n = 0 ; R = Ph **62**

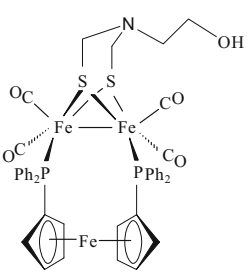

63

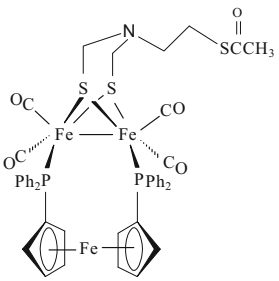

64

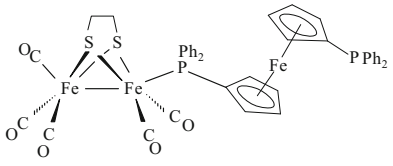

65

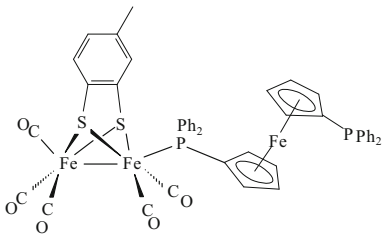

66

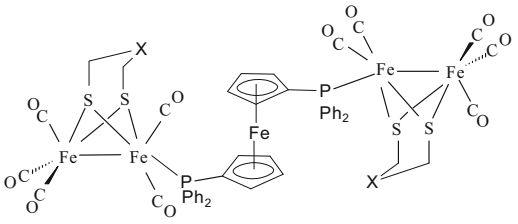

X = O, CH_2

67

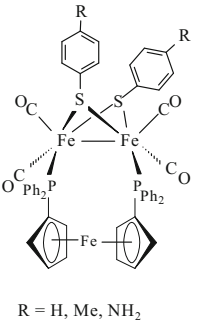

R = H, Me, NH_2

68

Scheme 19 Selected examples of di-iron complexes with dppf ligand

investigations suggest that the ferrocenyl group itself may promote the heterolytic cleavage of H_2.

Another way for introducing a ferrocenyl moiety is to use a phosphino-functionalized ferrocene such as mppf (mppf = $[Fe(\eta^5\text{-}C_5H_5)(\eta^5\text{-}C_5H_4PPh_2)]$). The comparison of the electrochemical behaviours of the complexes $[Fe_2(CO)_5(\kappa^1\text{-mppf})(\mu\text{-pdt})]$ (**69**) (Scheme 21) and $[Fe_2(CO)_5(PPh_3)(\mu\text{-pdt})]$ shows that although PPh_3 and mppf have similar σ-donating abilities, their oxidative behaviours are very different. The $Fe^IFe^I \rightarrow Fe^{II}Fe^I$ oxidation of the di-iron core occurs at 0.47 V vs. (Fc^+/Fc) in MeCN-$[Bu_4N](BAr^F{}_4)$ ($[BAr^F{}_4]^-$ = $[B(3,5\text{-}C_6H_3(CF_3)_2)_4]^-$) for **69** vs. 0.32 V in the case of $[Fe_2(CO)_5(PPh_3)(\mu\text{-pdt})]$.

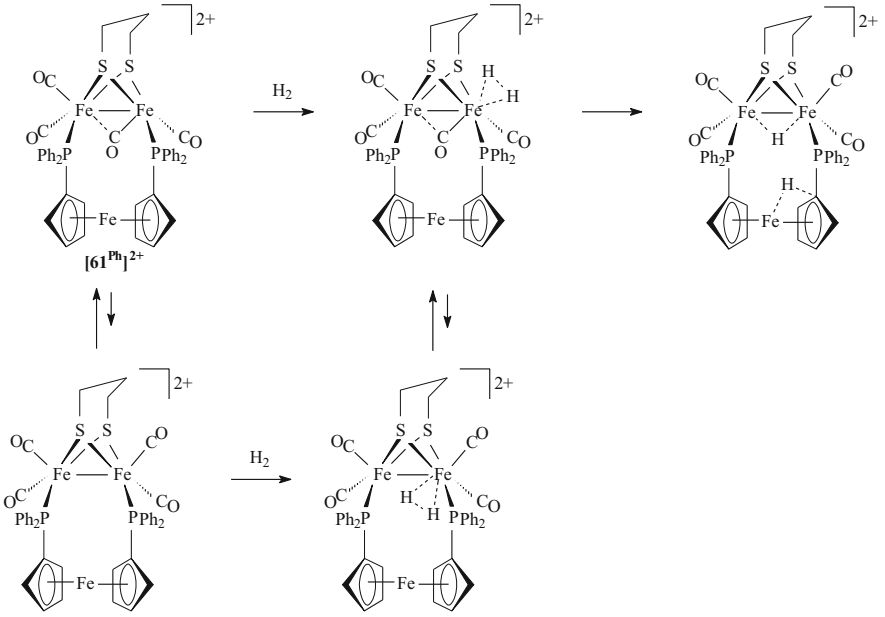

Scheme 20 Possible mechanisms for the activation of H_2 by $[Fe_2(CO)_4(\mu\text{-dppf})(\mu\text{-pdt})]^{2+}$

Scheme 21 A complex with a phosphino-functionalized ferrocene

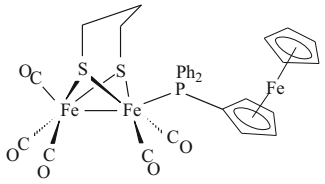

69

This shift is the consequence of the oxidation of the ferrocenyl group that arises at 0.16 V in **69** [60, 119].

The complex $[Fe_2(CO)_3(\kappa^1\text{-Fc'})(\kappa^2\text{-dppv})(\mu\text{-adt}^{Bn})]$ (**70**) (Fc' = $[Fe(\eta^5\text{-}C_5Me_5)\{\eta^5\text{-}C_5Me_4(CH_2PEt_2)\}]$ and $adt^{Bn} = (SCH_2)_2NCH_2C_6H_5$) is a rare example in which an intramolecular electron transfer between the di-iron centre and a ferrocenyl-phosphine arises [120–122]. The presence of the electroactive Fc' ligand in the coordination sphere of the azadithiolato complex **70**, as an electron reservoir, allows bidirectional H^+/H_2 catalysis. In the presence of $[H(OEt_2)_2](BAr^F{}_4)$, **70** undergoes a protonation of the amine function followed by the formation of a terminal hydride at one iron atom (Scheme 22) [121]. Then the release of H_2 is proposed to be induced by an intramolecular electron transfer from the ferrocene ligand to the di-iron core. Further studies have shown that no catalysis occurs without the presence of a ferrocenyl-phosphine. Its presence would impede the isomerization of the terminal

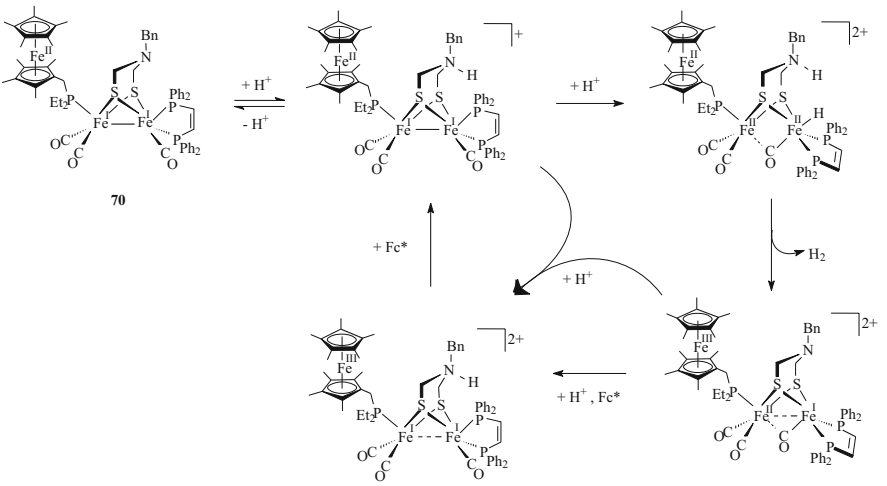

Scheme 22 Proposed mechanism for HER activity of $[Fe_2(CO)_2(\kappa^1\text{-Fc'})(\kappa^2\text{-dppv})(\mu\text{-adt}^{Bn})]$ (**70**) in the presence of Fc* = $[Fe(\eta^5\text{-}C_5Me_5)_2]$

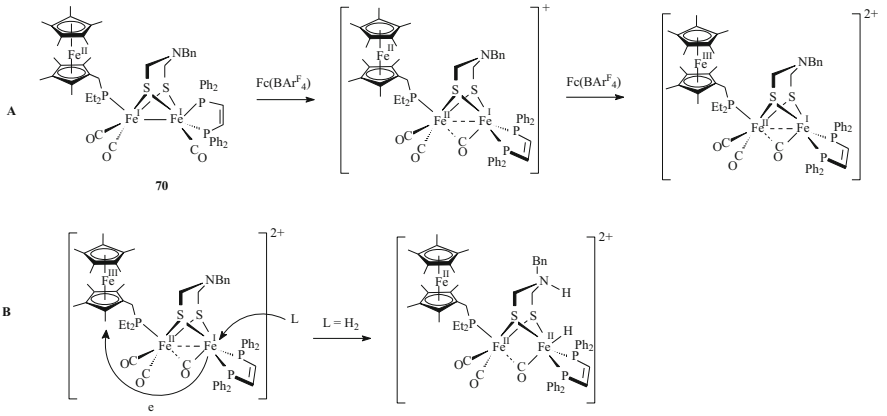

Scheme 23 Oxidation of $[Fe_2(CO)_3(\kappa^1\text{-Fc'})(\kappa^2\text{-dppv})(\mu\text{-adt}^{Bn})]$ (**70**) and activation of H_2

hydride isomer into its inactive bridged-hydride form [121]. A turnover rate of 6.6 h^{-1} was determined in CH_2Cl_2 with an overpotential of *ca* 0.54 V vs. (Fc*$^+$/Fc*) (Fc* = $[Fe(\eta^5\text{-}C_5Me_5)_2]$).

Conversely, the oxidation of **70** leads to a dicationic species in which the $\{Fe^{II}Fe^{I}\}$ core exhibits an inverted conformation while the iron atom of the Fc' ligand is in the oxidation state III (Scheme 23a). The coordination of H_2 to the dication triggers an intramolecular electron transfer from the di-iron core to the oxidized ferrocenyl group and leads to the heterolytic cleavage of H_2 (Scheme 23b) [122]. A rate of 0.4 turnover/h is reported for H_2 oxidation.

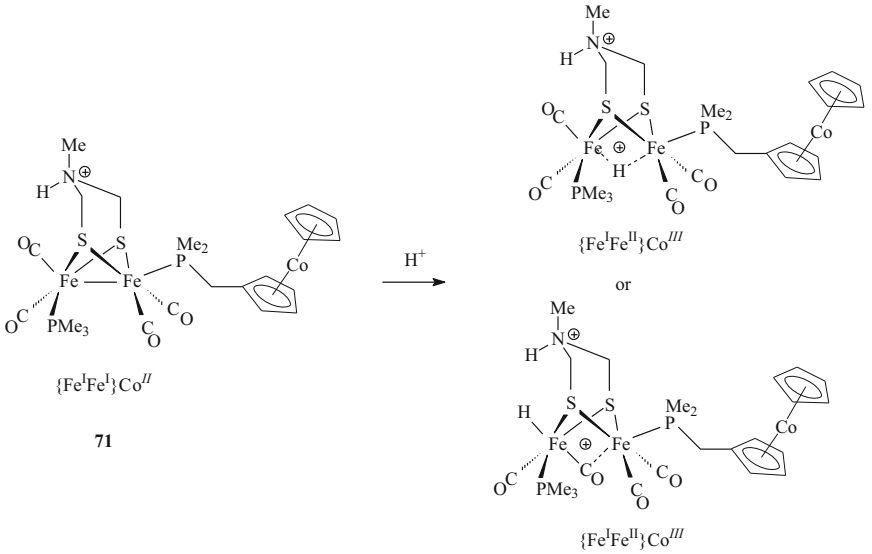

Scheme 24 A theoretical model of a di-iron compound featuring a cobaltocenyl group

DFT calculations predict that the theoretical model **71** featuring a cobaltocenyl group attached through a phosphine linker $\{Co(\eta^5\text{-}C_5H_5)(\eta^5\text{-}C_5H_4CH_2PMe_2)\}$ to a di-iron core $\{Fe_2(CO)_4(PMe_3)(\mu\text{-}\{SCH_2\}_2NH(Me))\}^+$ (Scheme 24) provides a suitable electronic balance for undergoing, upon protonation, a facile electron transfer from the cobaltocenyl group to the di-iron site, giving thus an interesting model for the functioning of the H-cluster [82, 123].

Many studies on hetero-bimetallic NiFe complexes have aimed to mimic [NiFe]-hydrogenases but synthetic models featuring redox-active auxiliaries are scarce [124], certainly in reason of the absence of a direct covalent coordination between a redox ligand and the {NiFe} core in the active site of these enzymes. However, a series of NiFe species $[NiFe(CO)_2(\kappa^2\text{-diphosphine})(\kappa^1\text{-ferrocenylphosphine})(\mu\text{-pdt})]^+$ (**72**) featuring dppf or mppf ligands was reported (Scheme 25). A promising rich redox chemistry was revealed notably for the hydride species $[NiFe(CO)_2(\kappa^2\text{-dppe})(\kappa^1\text{-mppf})(\mu\text{-pdt})(\mu\text{-H})]^+$ (**73**) which exhibits four accessible redox states from $\{Ni^{II}Fe^{II}\}Fe^{II}$, $\{Ni^{II}Fe^{I}\}Fe^{II}$, $\{Ni^{II}Fe^{I}\}Fe^{III}$ to $\{Ni^{I}Fe^{I}\}Fe^{II}$ due to the introduction of the ferrocenylphosphine. Moreover, **73** turned out to be more efficient for the production of H_2 than its analogue $[NiFe(CO)_2(\kappa^2\text{-dppe})(PPh_3)(\mu\text{-pdt})(\mu\text{-H})]^+$ for reasons that still remain unclear but that should be related to the introduction of the redox ligand mppf [124].

Theoretical NiFe models featuring substituted isocyanoferrocene were also studied by a DFT approach (Scheme 26a) [125]. The results of these theoretical studies have demonstrated that the coordination of H_2 and its activation at a NiFe site can arise with adequate substituted isocyanoferrocenes in reason of their ability to

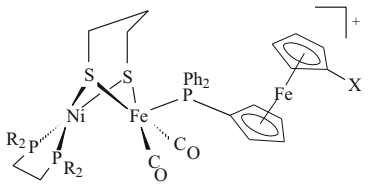

72

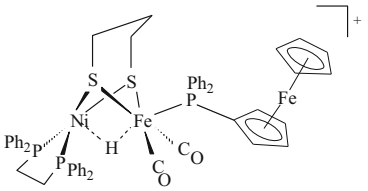

73

X = H (mppf) or PPh_2 (dppf)
R = Ph, Cy

Scheme 25 Examples of NiFe systems with mppf and dppf redox ligand

undergo intramolecular electron transfers upon substrate binding (Scheme 26b). Moreover, the formation of hydride species after H_2 binding at the Ni atom of a $\{Ni^{II}Fe^{II}\}Fe^{III}$ core is facilitated by the presence of an amine in the dithiolato bridge or carried by a functionalized cyclopentadienyl group [125]. It is worth noting that the dicyano species **76**, with a $Ni^{II}Fe^{II}$ redox state, is not able to activate H_2 (Scheme 26c).

Ferrocenyl groups can be introduced through dithiolato or phosphido bridges, as it has been reported for complexes featuring phosphido, ethanedithiolato or 1,8-naphthalenedithiolato bridges (**77**-**83**) (Scheme 27) [126–129]. In the case of the 1,8-naphthalenedithiolato bridge, the ferrocenyl group serves as a probe for calibrating the electron number during electrochemical experiments. Two reductions and two oxidations were observed in dichloromethane, one of which corresponds to the oxidation of the incorporated ferrocenyl group [127]. In the case of the bis-phosphido bridged complexes, *syn*-$[Fe_2(CO)_6\{\mu\text{-}PH(CH_2Fc)\}_2]$ ($\mathbf{77^H}$) and *anti-/syn*-$[Fe_2(CO)_6\{\mu\text{-}PMe(CH_2Fc)\}_2]$ ($\mathbf{77^{Me}}$), two ferrocenyl groups were introduced into the bridges [128]. An original proton reduction mechanism involving an homolytic cleavage of a P-H bond in the radical monoanion $[\mathbf{77^H}]^{\bullet-}$ was proposed for explaining the higher efficiency of $\mathbf{77^H}$ compared to that of $\mathbf{77^{Me}}$, but no cooperative effect involving the ferrocenyl groups and the di-iron centre was evidenced.

Recently, the preparation of hexacarbonyl di-iron systems (**80**, **81**) from ferrocenyl α-thienyl thioketone and $[Fe_3(CO)_{12}]$ was reported (Scheme 27), but the redox benefit of introducing one or two ferrocenyl groups in the coordination sphere towards catalytic activity was not highlighted [130]. Finally, recent works show the possibility to introduce a 1,1′-dithiolato (/selenato) ferrocenyl bridge in di-iron compounds $[Fe_2(CO)_6(\mu\text{-}E_2\{Fe(\eta^5\text{-}C_5H_4)_2\})]$ (E = S, Se; **83**) (Scheme 27), thus affording species with a redox moiety in close proximity of the di-iron site [131, 132].

Other redox metal frameworks. A redox ligand based on acenaphthene-1,2 diimine (Bian) has attracted interest [133, 134]. It was combined to a platform

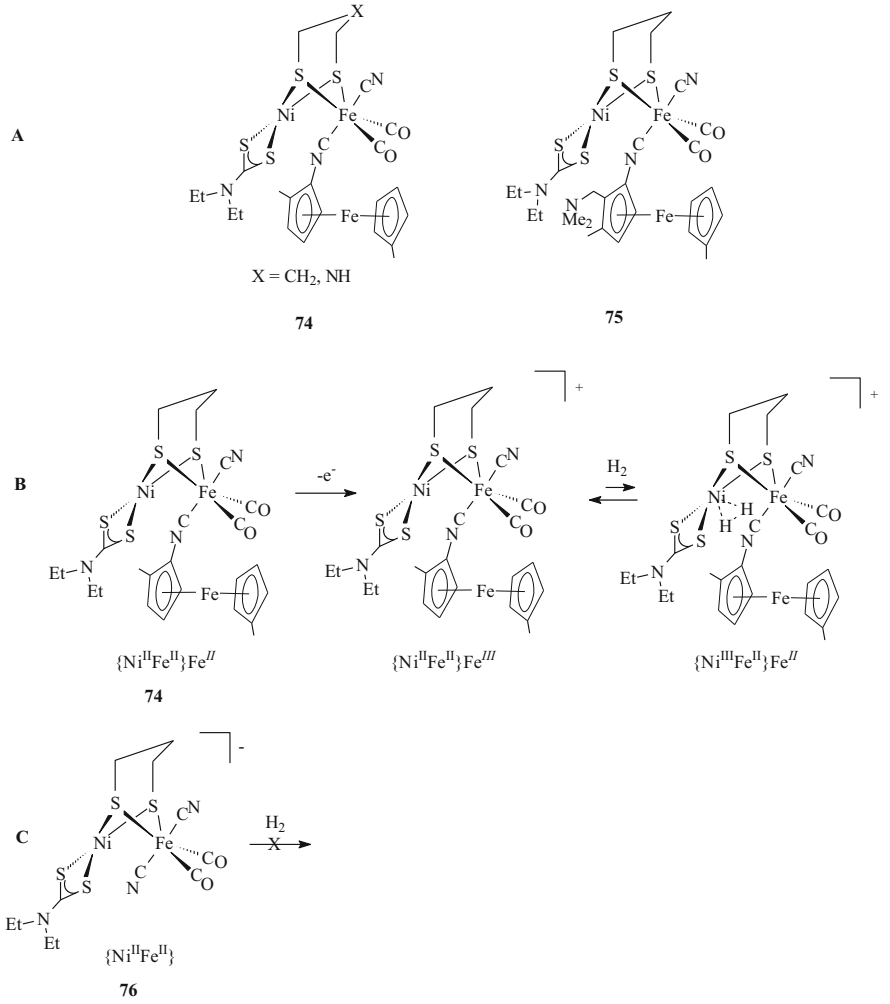

Scheme 26 Theoretical hetero-bimetallic NiFe species with an isocyanoferrocene group (**a**, **b**) and dicyano analogue (**c**) and their activity towards H_2

$\{Fe_2(CO)_6(\mu\text{-}X)_2\}$ (X = S or Te) via a metalloligand $\{M(\kappa^2\text{-dpp-Bian})\}$ (M = {Fe-CO}, Al, Ga; dpp-Bian = N,N′-bis(2,6-di-*iso*propylphenylacenaphthene-1,2-diimine)) linked to the bridging chalcogen atoms (Scheme 28). The reduction of $[Fe_2(CO)_6(\mu\text{-}S_2)]$ with the complex $[Ga^{II}(\text{dpp-Bian})]_2$ afforded the species $[Fe_2(CO)_6(\mu_3\text{-}S)_2\{Ga(\kappa^2\text{-dpp-Bian})\}]$ (**84**) [133]. EPR and DFT studies confirm that the Bian moiety takes part to the reduction of the di-iron core and show that the dpp-Bian ligand is a radical, acting as a redox group.

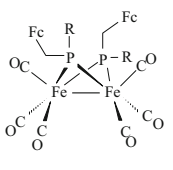

R = H, CH_3

77

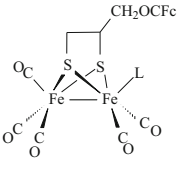

L = CO, PR_3

78

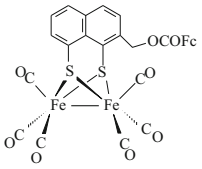

79

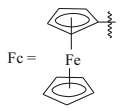

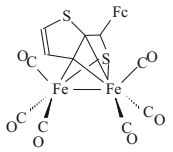

80

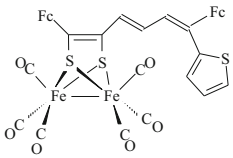

81

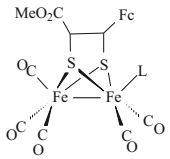

82

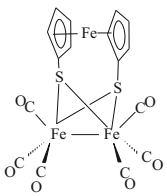

83

Scheme 27 Selected examples of di-iron complexes with ferrocenyl introduced into the bridge

Scheme 28 Di-iron complexes bearing a Bian-metal framework

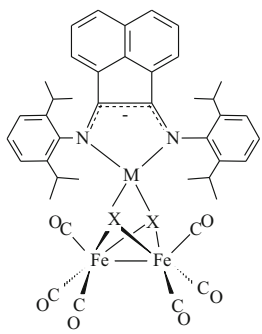

M = Ga, Al ; X = S **84**, **85**

M = {Fe(CO)} : X = Te **86**

3 Illustrations of Various Bimetallic Complexes with a Redox Ligand for Molecular Activation

A wide variety of other redox ligands have been used in order to build bimetallic systems for preparing molecular materials or catalysts. Nitrogen donor ligands with extended π-systems (e.g. based on pyridine-diimines, pyridine-bis(oxazolines), α-diimines, iminopyridine...) allow to expand the scope of accessible oxidation states in transition metal complexes by acting as electron reservoirs. Some illustrations are proposed below.

Polypyridines-based complexes. The role of potentially redox-active tridentate pincers based on pyridyl groups has been explored for the reduction of N_2 by transition metal in order to check if cooperative metal-ligand effects can stabilize intermediates in such processes [135]. For this purpose, the di-molybdenum dinitrogen compound with terpyridine ligands $[\{(^{Ph}Tpy)(PPh_2Me)_2Mo\}_2(\mu_2\text{-}N_2)](BAr^F{}_4)_2$ (**87**) (^{Ph}Tpy = 4'-Ph-2,2′,6′,2″-terpyridine) has been prepared. The cyclic voltammetry of **87** in THF-$[Bu_4N][PF_6]$ 0.1 M features two reversible oxidations at −0.22 V and −0.77 V and two reversible reductions at −1.65 V and −1.86 V vs. (Fc^+/Fc). The chemical oxidation and reduction of $[\{(^{Ph}Tpy)(PPh_2Me)_2Mo\}_2(\mu_2\text{-}N_2)]^{2+}$, Raman and ^{15}N NMR spectroscopic studies highlighted the fact that the {Mo-N-N-Mo} core remains unchanged across five oxidation states due to the π* orbitals of the terpyridine which are energetically suitable to store additional electrons (Scheme 29). While the SOMO of the one-electron-oxidized species $[\{(^{Ph}Tpy)(PPh_2Me)_2Mo\}_2(\mu_2\text{-}N_2)]^{3+}$ is essentially metal-based, the unpaired electron is principally chelate-based in the reduced monocationic complex $[\{(^{Ph}Tpy)(PPh_2Me)_2Mo\}_2(\mu\text{-}N_2)]^+$.

The introduction of a ferrocenyl group at the 4-position in the pyridine cycle of the PNP-pincer ligands in the dinitrogen-bridged di-molybdenum–dinitrogen complexes $[Mo(N_2)_2(4\text{-Fc-PNP})]_2(\mu\text{-}N_2)$ (**88**) (4-Fc-PNP = 4-ferrocenyl-2,6-bis(di-tert-butylphosphinomethyl pyridine) (Scheme 30a) improves the activity of such well-known complexes towards the reduction of N_2 into NH_3 compare to that of the unsubstituted analogues [136]. Spectroscopic data suggest that the introduction of the metallocene moieties does not affect the electronic density at the molybdenum atoms in **88**, but DFT calculations propose that their presence may increase the rate of the reduction steps of the coordinated nitrogeneous ligand on the molybdenum atom (Scheme 30b). It would promote a charge transfer from the iron atom of the ferrocenyl group to the molybdenum centre in the proposed hydrazidium intermediate $\{[Mo(4\text{-Fc-PNP})(OTf)(NNH_3)\text{–}N{\equiv}N\text{–}Mo(4\text{-Fc-PNP})(N_2)_2]^+\}$ (Scheme 30b), which may assist the cleavage of the N-N bond in the hydrazidium ligand N-NH_3 and accelerate the reduction step affording a nitride species. In the case of the complex **89** (Scheme 30a), the position of the ferrocenyl group between the two molybdenum moieties is not suitable for N_2 activation and its transformation into NH_3 [137].

A series of homodinuclear complexes $[M_2(PMe_3)_2(^3PDI_2)(\mu\text{-Cl})]^{n+}$ (n = 1 for M = Fe, n = 1–3 for M = Co, n = 1–2 for M = Ni) was prepared with a dinucleating

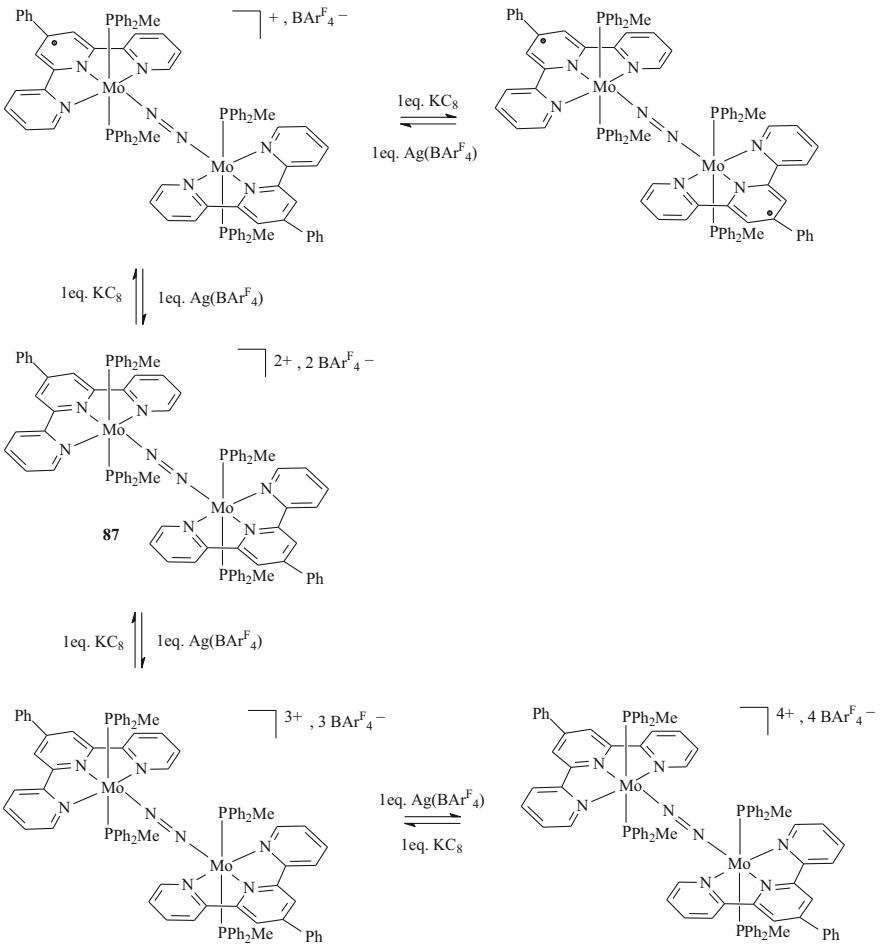

Scheme 29 Redox processes involving the terpyridine complex **87**

macrocyclic ligand ($^3PDI_2$) derived from pyridyldiimine (PDI) ($^3PDI_2$ is a macrocyclic ligand containing two p-^{t}Bu-pyridyldiimine moieties, linked through their imino nitrogen with three catenated CH_2 units) (Scheme 31) [138]. The characterization of these complexes, spanning five redox levels from 34 to 38 electrons, showed that they have similar structures but it also revealed noticeable differences in the metal-metal bonding and anomalies compared to the expected evolution of the metal-metal distances. This is due to the redox ability of the $^3PDI_2$ ligand to store electrons. Structural characteristics were correlated to electron distribution in the complexes through the filling of a redox-active σ* orbital with an M-M antibonding character. The order of the σ(MM) bond is 1 for $[Fe_2(PMe_3)_2(^3PDI_2)(\mu\text{-}Cl)]^+$ (**90$^+$**) and $[Co_2(PMe_3)_2(^3PDI_2)(\mu\text{-}Cl)]^{3+}$ (**91^{3+}**), 0.5 for $[Co_2(PMe_3)_2(^3PDI_2)(\mu\text{-}Cl)]^{2+}$ (**91^{2+}**) and $[Ni_2(PMe_3)_2(^3PDI_2)(\mu\text{-}Cl)]^{2+}$ (**92^{2+}**) and 0 for $[Co_2(PMe_3)_2(^3PDI_2)$

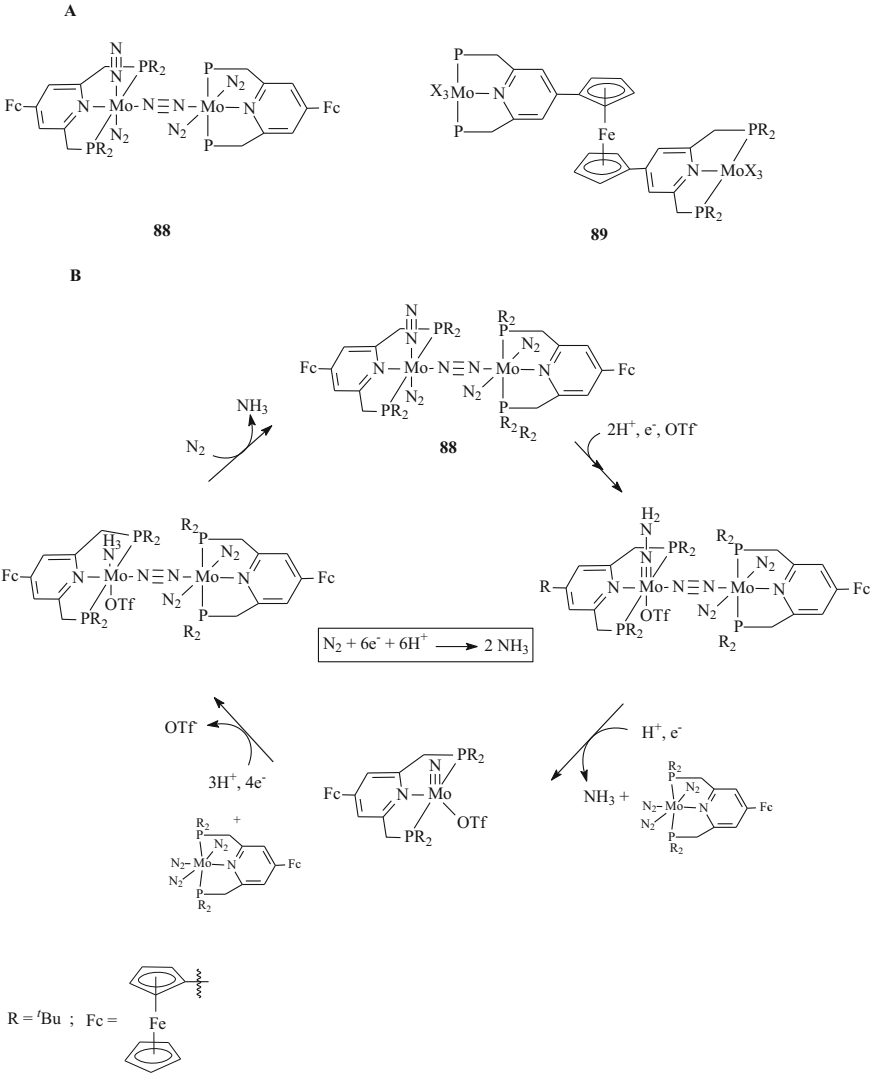

Scheme 30 Ferrocene-based di-molybdenum systems for dinitrogen activation

$(\mu\text{-Cl})]^+$ (**91**$^+$) and $[Ni_2(PMe_3)_2(^3PDI_2)(\mu\text{-Cl})]^+$ (**92**$^+$). Whereas the expected lengthening is observed upon successive one-electron reductions for the cobalt complex, an unexpected decrease of the M-M bond distance is observed in the case of the nickel species. Calculations revealed that this shortening results from a change of the spin multiplicity in the σ* orbital, this one being half-occupied. Significant changes in M-($^3PDI_2$) distances also provided indirect information on the spin states of the metal centre as well as the electronic density delocalization into the pyridyldiimine ligand. The results suggest that pyridyldiimine has a $^3PDI_2^{3-}$ charge in **90**$^+$

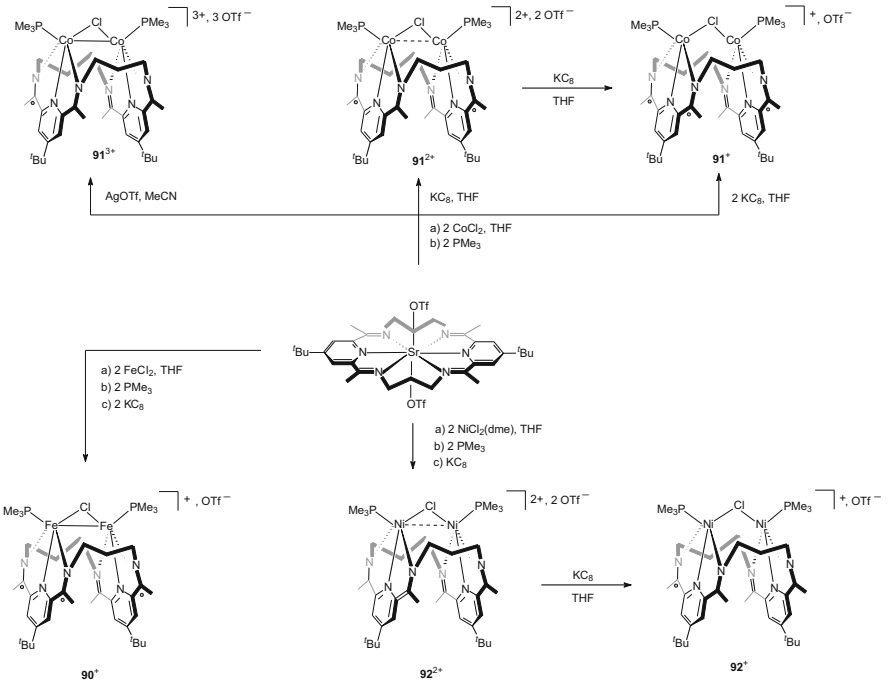

Scheme 31 Homobimetallic complexes of iron, nickel and cobalt built on a macrocyclic pyridyldiimine backbone

($\{Fe_2Cl\}^+$ core). A singly reduced $^3PDI_2^-$ is proposed for the complex with the isoelectronic $\{Co_2Cl\}^{3+}$ core (**91**$^{3+}$) while a neutral $^3PDI_2$ is considered in the di-nickel species **92**$^{2+}$ ($\{Ni_2Cl\}^{2+}$ core). It is worth noting that the cleavage of Co-Co and Ni-Ni bonds appears without changing the apparent redox state of the metal centres in reason of a mainly centred ligand-based reduction. The reactivity of these $^3PDI_2$-supported bimetallic complexes towards substrates (such as N_2, MeCN, N_3^-, Ph-C ≡ C-Ph. . .) has been explored. Original results showed their ability for small molecule activation due to the redox aptitude of macrocyclic pyridyldiimine ligands and the geometrical control that they enforce on the coordination sphere of metal centres, thus allowing the tuning of the intermetallic distances [30, 139].

Similarly, the reactivity of a series of di-nickel complexes supported by binucleating naphthyridine diimine (NDI) ligands was studied [140]. In THF solution, the complex $[Ni_2(^{i\text{-Pr}}NDI)(C_6H_6)]$ (**93**) (Scheme 32) affords two reversible reductions and two reversible oxidations. Species in five oxidation states have been characterized, showing that the Ni-Ni bond is preserved since the bimetallic platform can accommodate a range of oxidative addition and reductive removal processes. Thus, such complexes promote a broad range of two-electron redox processes in which the NDI ligand manages electron equivalents, while the metals remain in a Ni^INi^I state with minimal electronic disruption of the σ(M − M) bond.

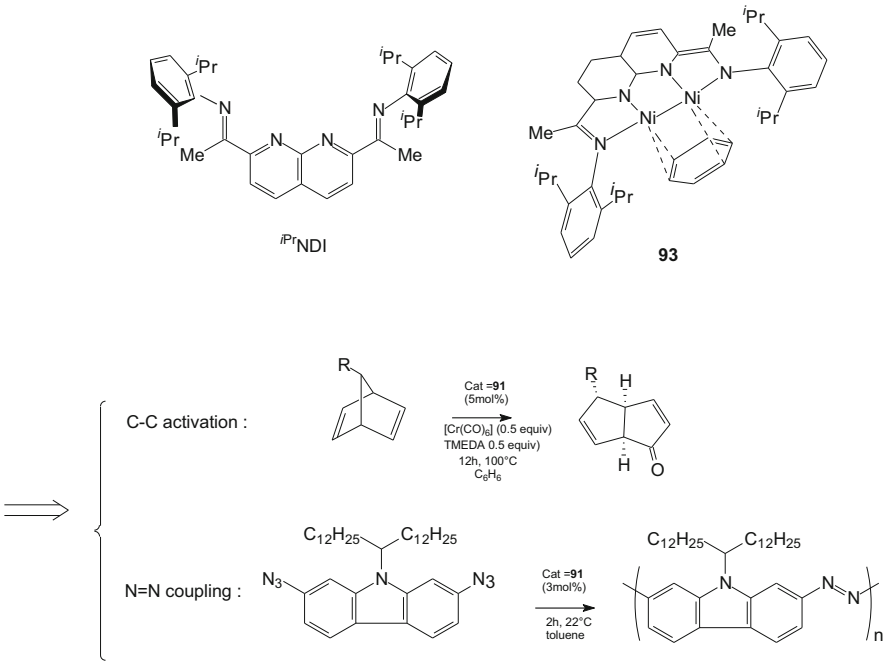

Scheme 32 The based-naphthyridine diimine (NDI) complex $[Ni_2(^{i\text{-}Pr}NDI)(C_6H_6)]$ and two examples of reactivity

Such a dinuclear catalyst contributes to solve catalytic problems as, for instance, dimerization of aryl azides to form azoarenes or catalytic carbonylation of norbornadiene.

Other complexes having dinucleating polypyridine scaffolds with redox properties were reported (Scheme 33) [141, 142]. For example, the ligand 1-N,1-N-bis (pyridine-2-ylmethyl)-3-N-(pyridine-2-ylmethylidene) benzene-1,3-diamine (L), with both an α-iminopyridine redox-active moiety and an innocent bis (2-pyridylmethyl)amino part, was reacted with $Fe(OTf)_2$, $Cu(OTf)_2$ and $ZnCl_2$ and afforded symmetrical or asymmetrical dinuclear compounds, $[Fe_2(OTf)_2(L)_2](OTf)_2$ (**94**) and $[Cu_2(L)_2](OTf)_4$ (**95**), $[Zn_2Cl_4(L)]$ (**96**), respectively. Important differences affecting redox behaviours of **94**, **96** arise depending on the metal centre [141]. The cyclic voltammetry of **94** shows two one-electron reductions corresponding to both metal- and ligand-centred processes, while a one-electron reduction is assigned to $L/L^{\bullet -}$ for **96** and the reduction of **95** metal-centred. Compounds **94** and **95** display a similar penta-coordination of the ligand L at each metal centre. The main structural difference lies in the M...M distance that is longer in the di-iron complex (7.5–7.7 Å) than in the di-copper species (3.4–3.7 Å) due to π-stacking effect in the latter. This suggests that electronic properties may be different in reason of alternative pathway for electronic communication between the two metal centres mainly depending on, more or less, geometric constraint of the encapsulating polypyridine ligand L.

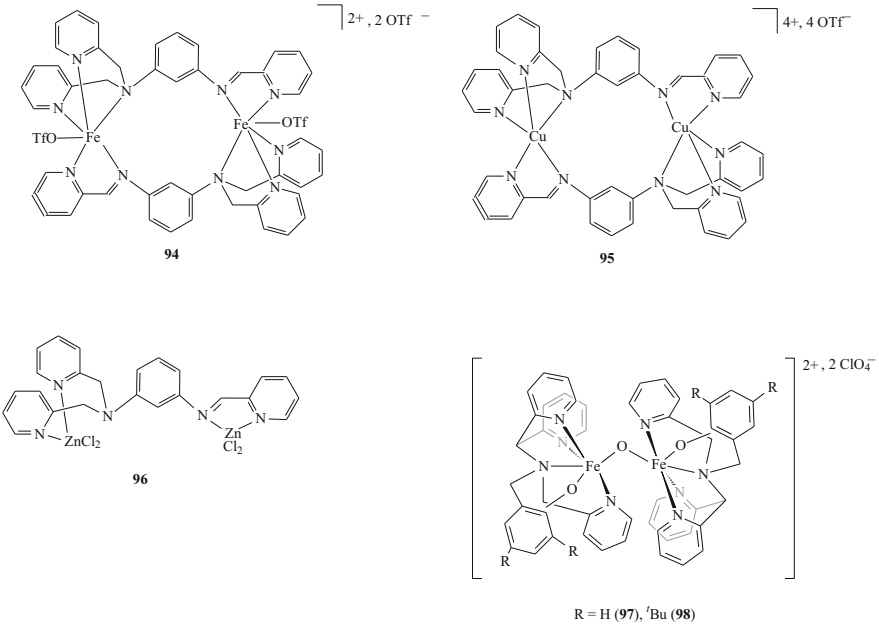

Scheme 33 Other examples of complexes with dinucleating polypyridine scaffolds with redox properties

The oxidative behaviours of pentadentate polypyridyl phenolato based μ-oxodi-iron(III) complexes $[LFe(\mu\text{-}O)FeL]^{2+}$ (L = 2-(((di(pyridin-2-yl)methyl)-(pyridin-2-ylmethyl)amino)-methyl)phenol (**97**) or 3,5-di-tertbutyl-2-(((di(pyridin-2-yl)methyl)(pyridin-2-ylmethyl)amino)-methyl)phenol (**98**)) (Scheme 33) have been explored [142]. The dimerization of **97**, affording a 4,4′-bisphenolato bridged-bis-μ-oxo-di-iron(III) polypyridyl species, results from its oxidation (Scheme 34a). The irreversible oxidation of **97** in dichloromethane initially yields a phenoxyl radical cation $\mathbf{97}^{+\bullet}$, which undergoes dimerization via aryl C − C coupling in *para* position of the phenol moiety. Then, deprotonation affords a tetranuclear oligomer. This last species undergoes two further reversible one-electron oxidations which are localized on the {4,4-bisphenolato} core (Scheme 34b). DFT calculations indicate that the occupation of d-orbitals of the iron(III) centres for both **97** and $\mathbf{97}^{+\bullet}$ is unaffected over the oxidation process. The presence of ^{t}Bu groups in **98** prevents the dimerization.

An interesting example of a di-ruthenium(II) complex, $[\{Ru(_L\text{-}N_4Me_2)\}_2(\mu\text{-tape})](PF_6)_4$ ($\mathbf{99}^{4+}$) ($_L$-N_4Me_2 = N,N′-dimethyl-2,11-diaza[3.3](2,6)-pyridinophane), was reported (Scheme 35) [143]. It features a bridging 1,6,7,12-tetraazaperylene (tape) that is a highly π-conjugated polyheteroaromatic planar bis-chelating bridging ligand, called "large-surface" ligand, particularly attractive for electron storage as well as electron shuttling. It is based on rigid bis(α,α'-diimine). Such a ligand has an efficient metal-metal bridging capacity combined with a strong π-accepting nature due to a low lying highly delocalized π* molecular orbital for reversibly storing two

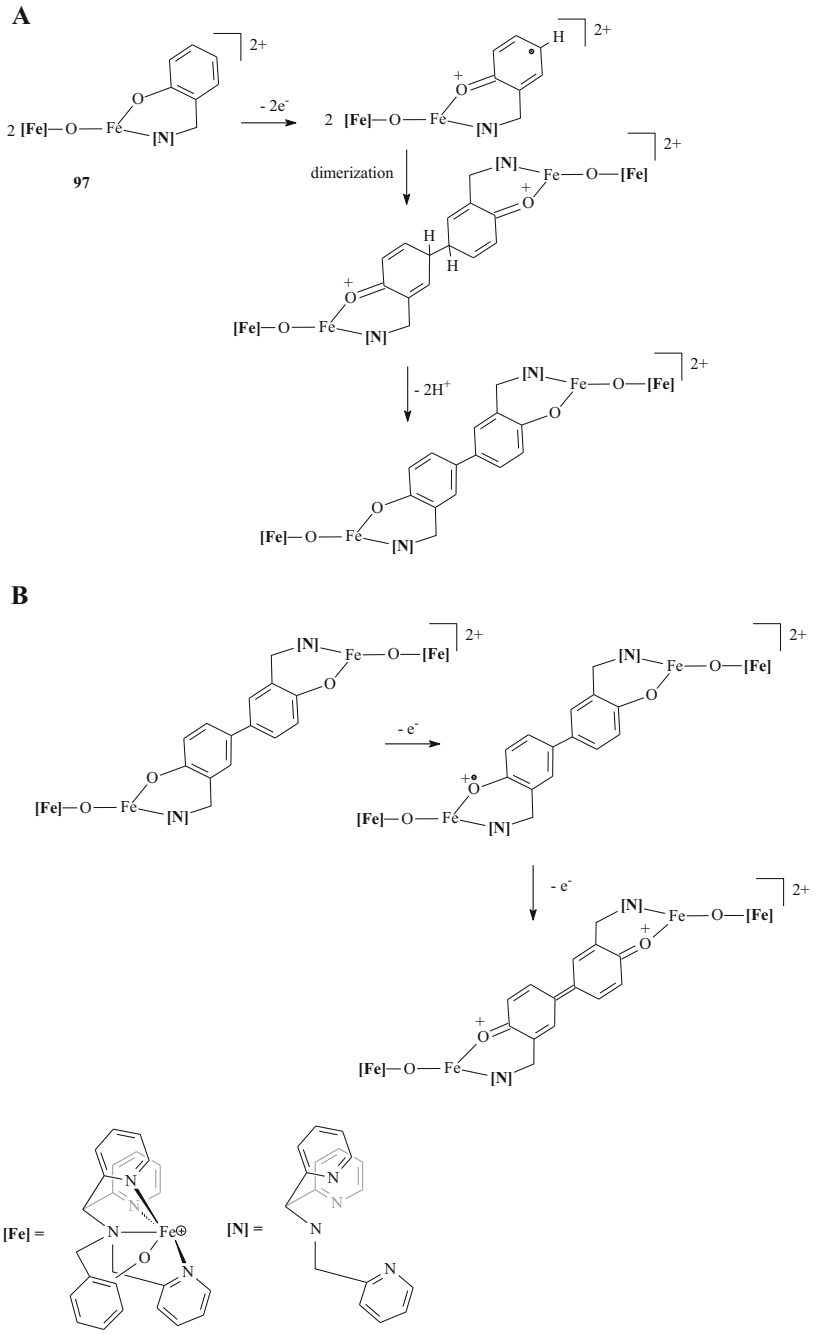

Scheme 34 Mechanism proposed for oxidative dimerization of **97**

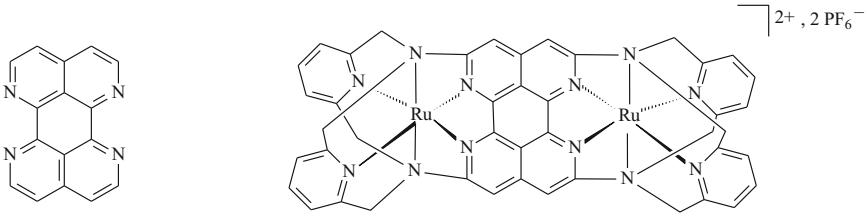

tape

$\mathbf{99}^{2+}$

Scheme 35 Structure of 1,6,7,12-tetraazaperylene (tape) and of the di-ruthenium complex $\mathbf{99}^{2+}$ featuring a tetraazaperylene bridging ligand as an electron reservoir

electrons. $\mathbf{99}^{2+}$ presents two reversible reductions at −0.13 V and −0.73 V vs. SCE in MeCN. Single- and double-reduced species can be isolated. Their respective EPR spectra suggested that the two added electrons fill up the LUMO of the bridging ligand affording the reduction of tape^0 into tape$^{\bullet-}$ and tape^{2-}. Expected shortening of the C-$C_{diimine}$ bond and elongation of C-$N_{diimine}$ bonds upon reduction are observed which is consistent with the filling of the LUMO of neutral tape^0 that has π(C-$C_{diimine}$) and π*(C-$N_{diimine}$) character. Finally, disulfonato derivative [{Ru($_L$-N_4Me_2)}$_2${μ-tape-$(SO_3)_2$}]$(PF_6)_2$ ($\mathbf{99}^{\mathbf{SO3}}$) may find applications as a redox mediator in voltammetric enzyme-electrode processes.

Tetrakisguanidine-based complexes. Redox-active 1,2,4,5-tetrakis (tetramethylguanidino) benzene (or pyridine, naphthalene), called Guanidino-Functionalized Aromatic (GFA), have been used to elaborate dinuclear entities in reason of their interesting coordinating capacity [144]. They are able to undergo two-electron oxidation. Redox isomerism processes, depending on intrinsic and extrinsic effects, have been observed for di-copper complexes [145]. According to the polarity of the solvent, complexes [GFA($CuCl_2$)$_2$] (**100**, **101**) exhibit different magnetic behaviours that are associated to a valence tautomerism between the two following redox forms [Cu^I–GFA^{2+}–Cu^I] and [Cu^{II}–GFA^0–Cu^{II}] (Scheme 36a). In contrast, the complex [GFA($CuBr_2$)$_2$] (**102**) is diamagnetic both in solution and in solid state. This redox switching reveals the influence of the ancillary ligands (Cl vs. Br) lying in the first coordination sphere on the electronic behaviours of such complexes. These behaviours can be rationalized with the HSAB theory, predicting the stabilization of higher oxidation states by harder chloro ligands. The GFA bridge allows to retain the dinuclear entities without any modification of the coordination number of the copper atoms, and connectivity. Extensions to GFA ligand based on tetrakisguanidine dibenzo-[1,4]-dioxine moiety (**103** in Scheme 36b) have been recently reported [146].

Diimino-quinone- and quinone -based complexes. Numerous molecular mixed-valence dinuclear compounds with similar geometries [M]-(redox-active bridged ligand)-[M] have been built with 2,5-dihydroxy-1,4-benzoquinone, quinonoid, "imino"quinonoid and other various redox bridged ligands (Scheme 37a) [147–

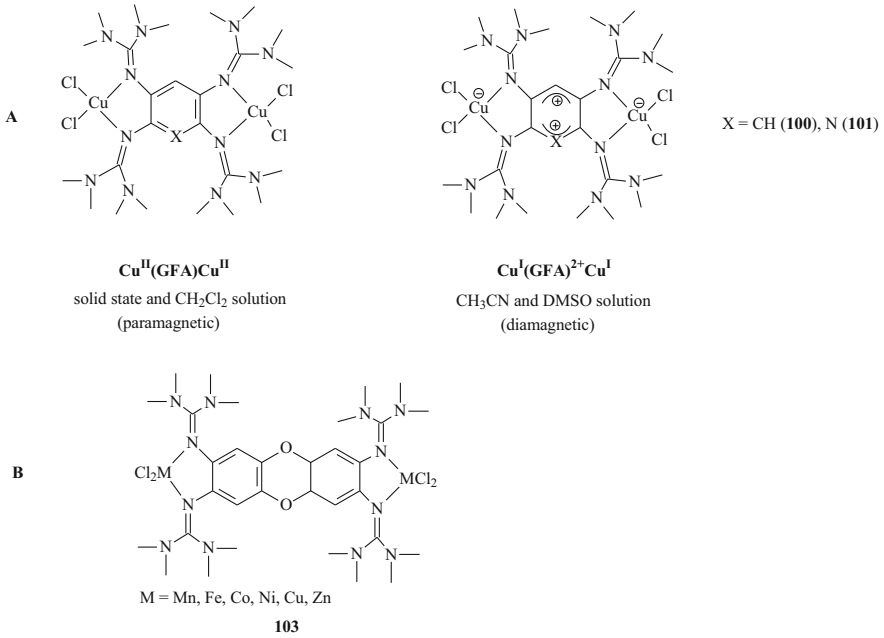

Scheme 36 Example of redox-isomerism with dinuclear tetrakisguanidine-based compounds (**a**) and the structure of complexes built on tetrakisguanidine dibenzo-[1,4]-dioxine ligands (**b**)

152] in view to find applications in the development of molecular electronic devices for optical and/or magnetic data storage involving intramolecular electron-transfer phenomena induced by external stimuli. It is noteworthy that some dinuclear complexes with large metal-metal distances, in which the two metal centres are separated with π-conjugated spacer, have shown enhanced catalytic activities compared to their mononuclear counter parts [31].

The dinuclear platinum complex **104**, based on the 2,5-di-[2,6-Dipp-anilino]-1,4-benzoquinone (Dipp = di-isopropyl), as a dinucleating ligand, and two C–H activated 1,5-cyclooctadiene (cod), affords a nice example of cooperativity between decoupled redox-active and proton-responsive ligands, working in tandem as electron and proton reservoir, which affords the possibility of multi-proton and -electron transfers to a substrate (Scheme 37b) [153]. As a proof of concept, 3,5-di-*tert*-butyl-benzoquinone is transformed into catechol upon sequential action of (HDMF)(OTf) and cobaltocene.

The di-ruthenium complex $[Ru_2(OH)_2(3,6\text{-}^tBu_2\text{-qui})_2(btpyan)]^{2+}$ (**105**) (3,6-^{t}Bu$_2$-qui = 3,6-di-*tert*-butyl-1,2-benzoquinone; btpyan = 1,8-bis(2,2′:6′,2″--terpyridyl)anthracene), featuring two ruthenium metal centres, each coordinated to a terpyridine group bound to a rigid anthracene scaffold (btpyan), a redox-active quinone (3,6-^{t}Bu$_2$qui) and an hydroxy group, (Scheme 38) has revealed its ability to mediate water oxidation catalysis. [154–159] Cyclic voltammetry studies showed a ligand-centred oxidation at $E_{1/2}$ = +0.40 V vs. (AgCl/Ag) and a metal-centred

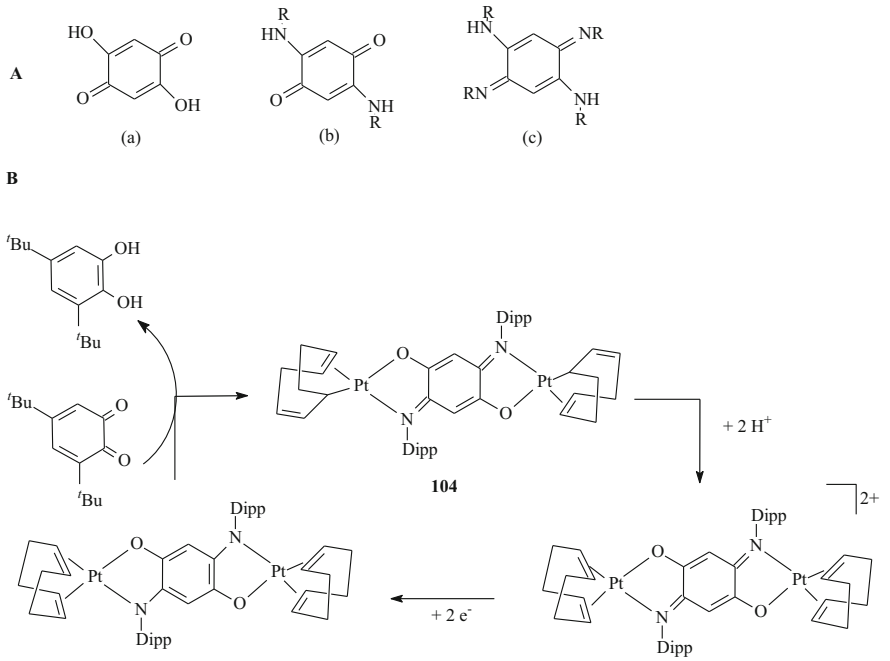

Scheme 37 (**a**) Representations of 2,5-dihydroxy-1,4-benzoquinone, quinonoid, "imino"quinonoid framework and (**b**) illustration of the cooperativity between a redox-active and proton-responsive ligand in a dinuclear platinum complex

oxidation at +1.2 V in trifluoroethanol containing 10% water. Controlled potential electrolysis of **105** at a potential of +1.70 V in the presence of H_2O in CF_3CH_2OH resulted in electrocatalytic oxidation of water and dioxygen evolution with a current efficiency of 91% (21 turnovers). Efficient water oxidation activity with turnover numbers higher than 30,000, over a period of 40 h, were determined in optimized conditions. A mechanism involving sequential two-electron and two-proton transfers is proposed for the $4H^+/4e^-$ electrocatalytic cycle in which the redox couple (quinone/semi-quinone) plays a key role in maintaining the ruthenium centres in low oxidation state of II/III (or only II) unlike other analogous processes involving high oxidation state oxo-ruthenium species [157]. It is worth noting that an analogous complex in which quinone is replaced with bipyridine ligands does not undergo deprotonation, preventing the O–O bond formation. This highlights the crucial role of the redox-active quinone/semi-quinone couple in this process. A possible role of bipyridine as a redox-active ligand in the water oxidation process induced by the blue ruthenium dimer $[Ru_2(bipy)_2(H_2O)_2(\mu\text{-}O)]^{4+}$ (**106**) was also considered [160, 161].

The presence of the reduced catecholate (or aminophenolato) ligand in the rhenium(V) complex $[Re(O)(\kappa^2\text{-}cat)_2]^-$ (**107**) (cat^{2-} = 1,2-catecholate) assists the activation of O_2 which affords the *cis*-dioxo rhenium(VII) species $[Re(O)_2(\kappa^2\text{-}$

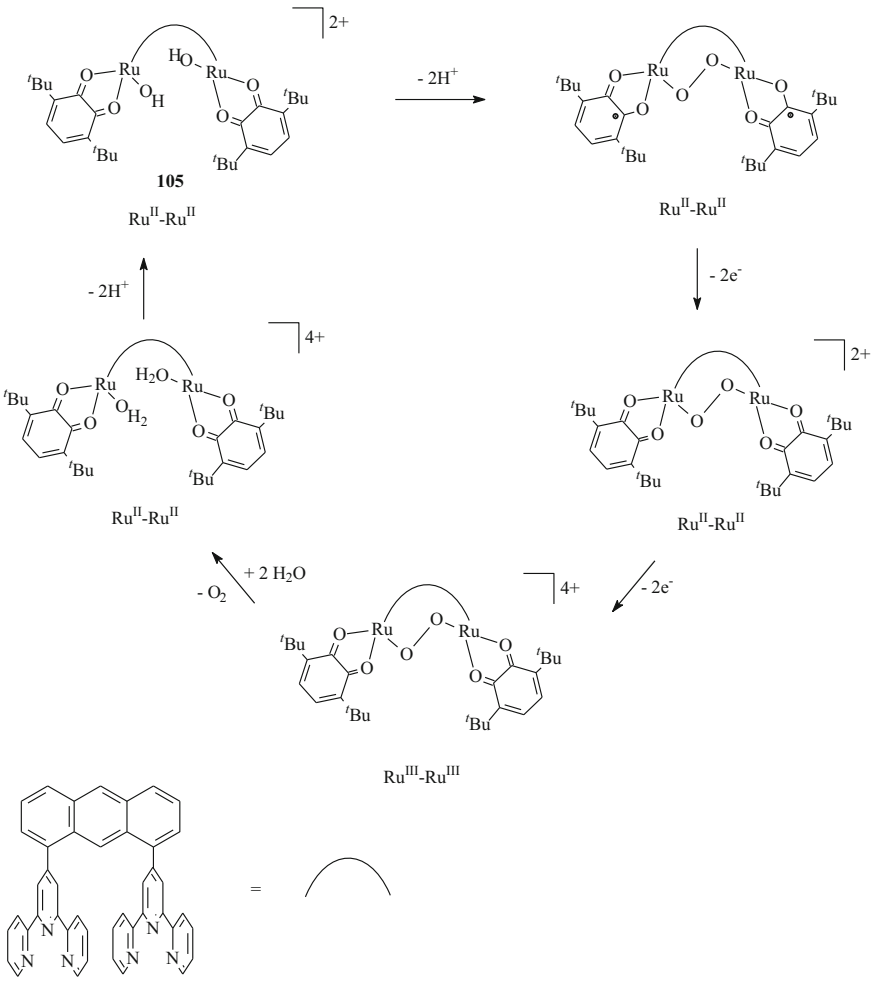

Scheme 38 Proposed mechanism for the water oxidation process mediated by the di-ruthenium benzoquinone complex $[Ru_2(OH)_2(3,6\text{-}^tBu_2\text{-qui})_2(btpyan)]^{2+}$ (**105**)

cat)$_2$]$^-$ (**108**) upon treatment with air (Scheme 39) [162]. The oxalate analogue of **107** does not display any activity towards O_2, thus showing the specific influence of the redox-active catecholate. The proposed mechanism on the basis of kinetic experiments and computational studies (Scheme 39), suggests that the redox-active ligand favours the formation of the rhenium(V) superoxide radical, thus allowing to circumvent the formation of unusual rhenium(VI) species through the transfer of a single electron to the metal centre. Then, it enables a bimetallic homolysis of O_2 via the formation of a di-rhenium(V) intermediate, featuring a trans-μ-1,2-peroxo O_2^{2-} linkage, $[\{Re(O)(\kappa^2\text{-cat})(\kappa^2\text{-sq}^\bullet)\}_2(\mu\text{-}O_2)]^{2-}$ ($sq^\bullet$ = semiquinonate) (**109**). Moreover,

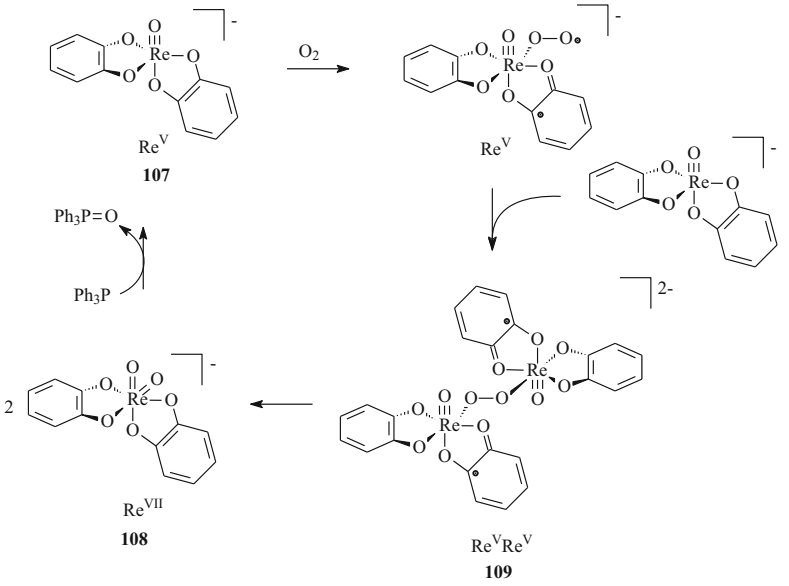

Scheme 39 Bimetallic homolysis of O_2 via the formation of a di-rhenium(V) intermediate

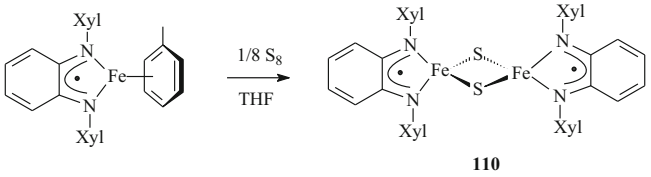

Scheme 40 Synthesis of a model of ferredoxin/Rieske clusters-type featuring a redox ligand

the two-electron oxygen-atom transfer process is not prevented by the presence of catecholate ligands.

N,N-chelating ligands: o-phenylenediamide (pda)- and diazadienes (dads)-based complexes. Small iron-sulfur systems with a {Fe2S2} core mimick the role of similar clusters found in ferredoxins and Rieske-type proteins that are involved in one-electron-transfer processes. The combination of such metallic entities with redox-active ligands enhances their electron storage capacity in view of mediation of multielectron chemical transformations. An interesting example of a complex featuring a {Fe2S2} core with a redox-active bidentate N,N-bis(2,6-dimethylphenyl)-o-phenylene diamide (^{Xyl}pda) ligand (Scheme 40) allows the reversible storage up to four electrons [163]. Cyclic voltammetry, spectroscopic and crystallographic studies of [$Fe_2(\kappa^2$-^{Xyl}pda)$_2(\mu$-S)$_2$] (**110**) indicate four reduction events, the two first ones being ligand-based and the two others metal-based. A mixed valence {$Fe^{III}Fe^{II}$}, with a localized single electron, and an unstable super reduced state are obtained after the third and fourth reduction, respectively. This rich redox chemistry is

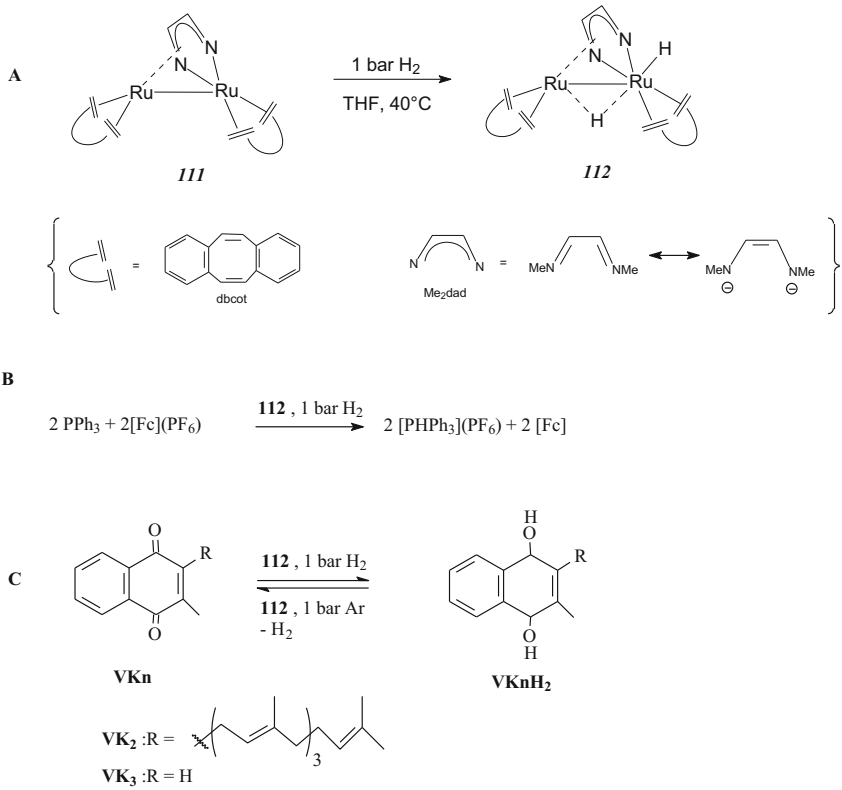

Scheme 41 Complexes with a diazadiene bridge **111**, **112** (**a**) and their catalytic activity towards H_2 (**b**) and vitamins K_n (**c**)

allowed by the fact that the well-known phenylene diamide group (^{Xyl}pda) can exist in three different redox states (closed-shell dianion/open-shell π-radical monoanion (S = 1/2)/closed shell neutral form). The catalytic activity of **110** towards N_2 silylation, with Me_3SiCl and KC_8, produced up to 88 (± 2) equivalents of N $(SiMe_3)_3$ per Fe atom but no N_2-intermediate species was observed and the multi-electron mechanism involving the phenylene diamide chelates, as electron reservoir, in this catalytic process was not evidenced.

The chemical and redox "non-innocent" properties of a bridging dimethyl diazadiene (MeN=CH-CH=NMe; 1,4-dimethyl-diazabuta-1,3-diene; Me_2dad) in the di-ruthenium complex $[Ru_2(Me_2dad)(dbcot)_2]$ (dbcot = dibenzocyclooctatetraene) (**111**) have been also reported (Scheme 41a) [164]. **111** reacts with H_2 (1 bar) to afford the dihydride species $[Ru_2(t\text{-}H)(Me_2dad)(dbcot)_2(\mu\text{-}H)]$ (**112**). The C–N and C–C bonds, ~1.38 Å and 1.39 Å, respectively, in the bridged Me_2dad in **111** and **112** are very close indicating a reduced form of the ligand MeN=CH-CH=NMe. C–N and C–C distances are *ca* 1.33 Å and 1.38 Å, respectively, in the diazadiene radical anion, and *ca* 1.38 Å and 1.35 Å in the dianionic bis-amido olefin form while they

are shorter *ca* 1.29 Å for the C-N bond and longer, *ca* 1.46 Å, for the C-C bond in the neutral diimine form. Thus, these distances reflect the "level of redox involvement" of the diazo bridge. **112** catalyzes the oxidation of H_2 to protons and electrons, using PPh_3 and [Fc](PF_6) as proton and electron acceptors, respectively (Scheme 41b), as well as the reversible and selective hydrogenation of vitamins K_2/K_3 (VK_2/VK_3) forming VK_2 hydroquinone (VK_2H_2) or dihydrovitamin K_3 (VK_3H_2) while preserving the C=C bonds of the side chain of VK_2 (Scheme 41c). In these processes, the {Ru_2(Me_2dad)} moiety evidently serves as an electron reservoir, with a possible chemically "non-innocent" role of the diazo bridge, conferring to **112** an hydrogenase-like as well as an hydrogen:quinone oxidoreductase-like activity.

Tridendate pincers (LXL)-based complexes. Various dinucleating tridentate pincers LXL with a bridging amido/phosphido group and featuring coordinating phosphine or thioether (L) (LXL = 2-*tert*-butylsulfanylphenyl)amide (SNS), bis(2-di-*iso*-butylphosphinophenyl)amide (PNP), bis(2-di-*iso*-propylphosphinophenyl)phosphide (PPP)) have served for preparing di-copper systems $[Cu_2(\mu\text{-}XL_2)_2]^{n+}$ (**113**-**117**) (n = 0, 1, 2 and X = N or P) (Scheme 42a) as models of diamond cores {$Cu_2(\mu$-$SR)_2$} of CuA sites found in cytochrome c oxidases and nitrous oxide reductases [165–168]. The involvement of the bridging ligand X = N or P during the two-electron oxidation process induced by these complexes has been demonstrated by X-ray crystallography, X-ray absorption spectroscopy (XAS), and density functional theory (DFT) for complexes $\mathbf{113}^{t\mathbf{Bu}}$ and **114** [167–170]. These studies revealed that the oxidation of $\mathbf{113}^{t\mathbf{Bu}}$ and **114** are predominantly centred on the amino or phosphido group affording a contribution of aminyl and phosphinyl radicals for the description of these complexes, thus highlighting the redox-active behaviour of the pincer ligands (Scheme 42b). It is worth noting that if the *tert*-butyl groups, in *para* position, are replaced by H in **113**, the dimerization of the aminyl radical through a C-C coupling arises at the aromatic cycle. The second oxidation of $\mathbf{113}^{t\mathbf{Bu}}$ is substantially ligand-based. It affords a dication, with two unpaired electrons predominantly located on the nitrogen atoms, that is assigned to a diradical species which is structurally characterized by a strong asymmetrical distortion of the {$Cu_2(\mu$-$NL_2)_2$} core. Recently, an analogous dianionic di-copper complex (**116**) was prepared with a tridentate ligand based on the triamine bis-(2-aminophenyl) amine (Scheme 42a) [171]. X-Ray diffraction, NMR and UV-visible characterizations of **116** suggest, as reported for previous $[Cu_2(\mu\text{-}XL_2)_2]$ systems, an ambivalent redox state for the di-copper site suggesting the redox activity of the bridging NNN ligand.

Ditopic tridentate ligands (PNP) have been also used for pre-organizing the structure of dinuclear gold complexes. An original example of ligand-to-metal two-electron transfer was highlighted (Scheme 43) [172, 173]. A chloride abstraction in the mixed-valent Au^I-Au^{III} complex **117**, using Ag(NTf_2), results in an unusual reactivity involving two-electron ligand oxidation, generating the chloro-bridged Au^I–Au^I species **118** bearing a carbazolyl backbone upon C-H activation and C-C coupling.

A redox-active tridentate bis-phenolato amido ligand ONO, derived from bis (3,5-di-*tert*-butyl-2-phenol)amine) has allowed the synthesis of saturated

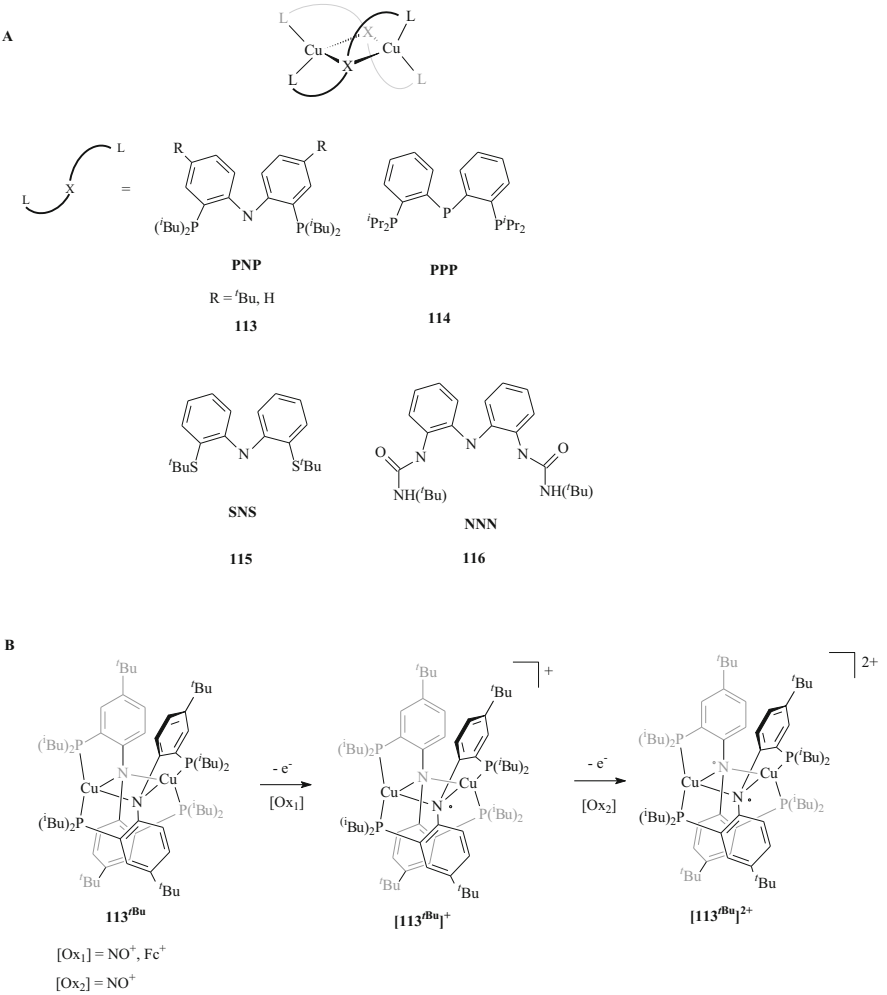

Scheme 42 Complexes $[Cu_2(\mu\text{-}XL_2)_2]^{n+}$ (**113**-**116**) (**a**) and two-electron oxidative process of $\mathbf{113}^{t\mathbf{Bu}}$ affording cations with predominantly aminyl radical and diradical character (**b**)

six-coordinate compounds $[M(ONO)_2]$ which often display a limited reactivity. The original formation of homo- and hetero-bimetallic complexes, $[Fe_2(ONO)_3]$ (**119**) and $[FeZn(ONO)_3]$ (**120**) (Scheme 44a) [174], has been obtained by reacting the formally reduced species $[Fe^{II}(ONO^{sq\bullet})(ONO^{q})]^{-}$ (see Scheme 44b for the representations of $(ONO^{sq\bullet})^{2-}$ and $(ONO^{q})^{-}$ ligands) which acts as a chelating metalloligand towards a second metal centre through the formation of bridging phenoxide oxygen atoms, thus affording a modular strategy for the preparation of such dinuclear systems. Compounds **119** and **120** display original redox properties, the former being a double mixed-valence complex (ligand $(ONO^{sq\bullet}/ONO^{q})$ and metal

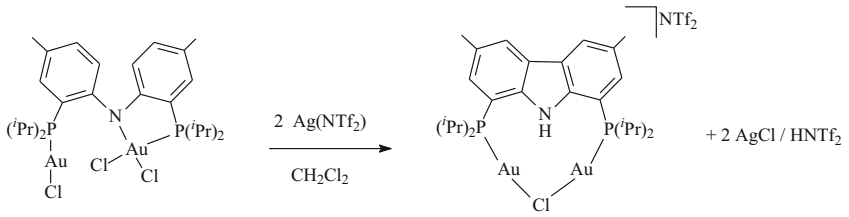

Scheme 43 Ligand-to-metal two-electron transfer during $Au^{I}Au^{III}$ /$Au^{I}Au^{I}$ species conversion

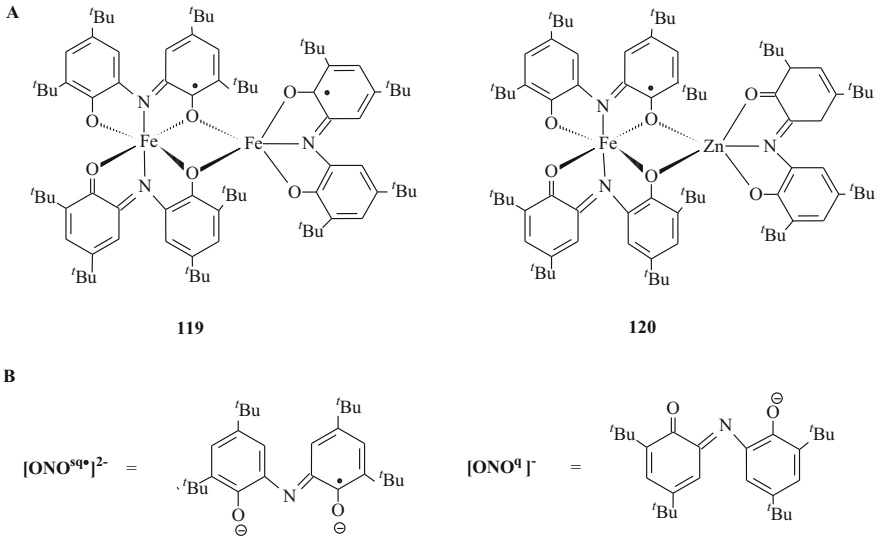

Scheme 44 Complexes featuring ONO pincer ligand

(Fe^{III}/Fe^{II})) best described as [Fe^{II}($ONO^{sq\bullet}$)(ONO^{q})Fe^{III}($ONO^{sq\bullet}$)], and the second, [Fe^{II}($ONO^{sq\bullet}$)(ONO^{q})Zn^{I}(ONO^{q})], displaying a ligand-based mixed-valency.

The oxidation of the di-tantalum(V) complex [Ta_2(ONO^{red})$_2$(py)$_2${μ-N(*p*tolyl)}] (**121**) with two equivalents of $PhICl_2$ (Scheme 45) resulting in the elimination of (*p*tolyl)N=N(*p*tolyl) affords an example of a multi-electron reaction, in which the oxidation leads to bond formation. The oxidation state of the metallic centre does not vary throughout the process [175]. The oxidation-induced elimination of aryl diazene is a four-electron process leading to the formation of a N=N double bond, that is allowed by the presence of the redox-active $[ONO^{red}]^{3-}$ ligands providing up to four electrons for the formation of the diazene.

A wide diversity of pincer ligands featuring a central diarylamido were used in dinuclear species. The extension to various complexes (**122-124**) with bis-mercapto amido SNS ligands based on the backbone of bis(2-mercapto-*p*-tolyl)amine has been

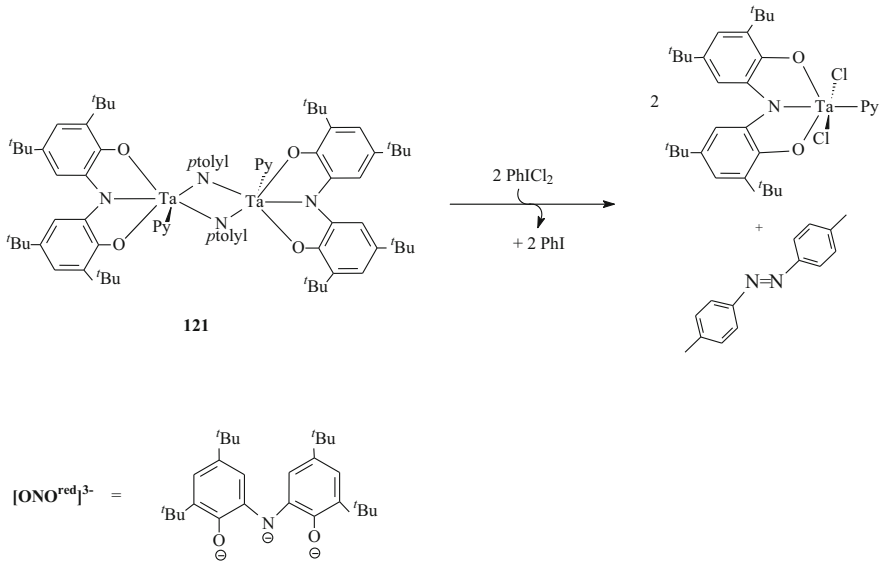

Scheme 45 Four-electron oxidative formation of an aryl diazene with a di-tantalum(V) complex **121** featuring ONO ligands

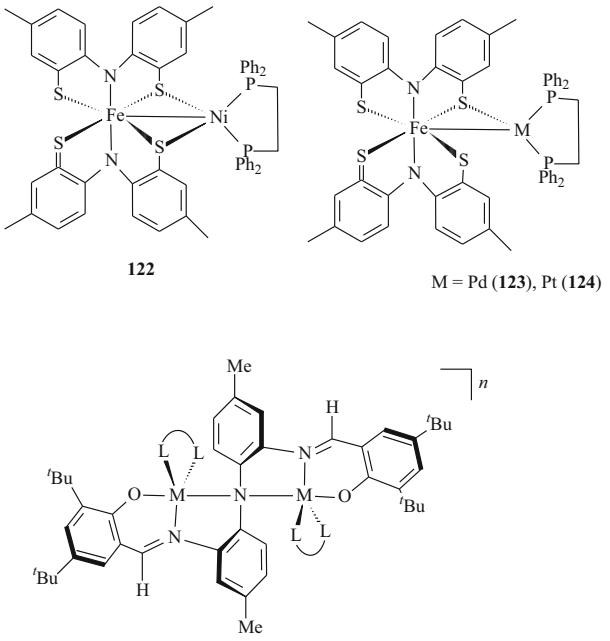

Scheme 46 Complexes featuring SNS and N3O2 pincers ligands

reported (Scheme 46) [176–178]. Moreover, the original trianionic pentadentate ligand N3O2, which merges two NNO units through a central diarylamido, is able to chelate M(II) ions (M = Co, Cu, Zn) affording homo-bimetallic compounds such as the bipyridine species $[Co_2(N3O2)(\kappa^2\text{-bipy})_2](ClO_4)$ (**125**) (Scheme 46) [179]. The electrochemical study of **125** shows six redox couples over a range of 3.0 V arising from metal- and ligand-based events. EPR and DFT studies suggest that the one-electron oxidation is centred at the bridging diarylamido, thus inducing the formation of a N3O2-based radical and revealing its possible role as electron reservoir.

The di-copper(II) complex **126**, featuring the redox-active thio-bis-phenolato OSO ligand (2,2′-thiobis(2,4-di-*tert*-butylphenol), mimicks the activity of the galactose oxidase [180, 181]. In addition to the conversion of primary alcohols to aldehydes in the presence of O_2, **126** catalyzes the oxidation of secondary alcohols into diols (Scheme 47) through the formation, upon treatment with O_2, of an oxygen-centred bi-radical intermediate which assists the transfer of hydrogen atoms before dimerization via C-C coupling and release of the diol. A seleno-analogue of **126** allows catalytic dealkylation of primary amine, such as benzylamine, through the proposed formation of a similar radical intermediate [182].

Scheme 47 Oxidation of secondary alcohols into diols catalyzed by **126**

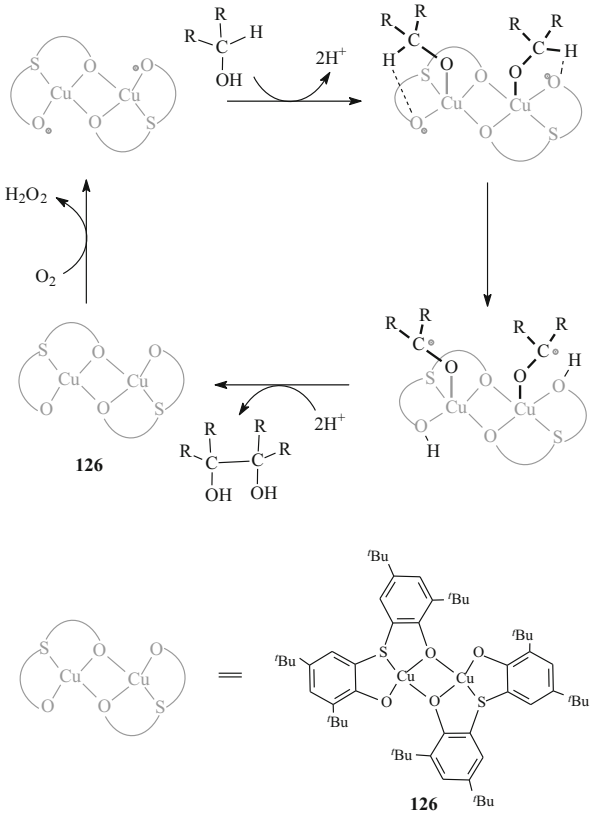

4 Conclusions

The structural characterization of the active sites of [FeFe]- and [NiFe]-hydrogenases and the search for understanding their functioning have stimulated the development of novel bio-inspired di-iron (and nickel-iron) compounds with a redox ligand in the coordination sphere of the bimetallic site. A wide variety of redox surrogates of the $[Fe_4S_4]$ cubane was combined to a di-iron core for modelling the H-cluster. For now, the benefit of introducing a redox-active ligand has been only demonstrated in few examples. Indeed, a limited number of catalytically efficient di-iron complexes containing a redox-active ligand has been reported but, the whole of the compounds described in the first section of this chapter has contributed to significant advances in the knowledge of the interplay between a dinuclear site and a close redox group as well as the design of such devices. These results show that the introduction of such a ligand, in a bridged or terminal position, requires a fine tuning of the electronic and steric properties of the entire dinuclear molecular device in order to have a well-adjusted electronic balance between the dinuclear site and the redox ligand.

An enhancement of the activity of some complexes, compared to that of their analogues lacking redox-active ligand, has been reported but often, the reasons for this improvement turned out difficult to be rationalized. In other compounds, the electronic communication between a potentially redox-active ligand and metal centres is established without improving their activity. This highlights the confused use, sometimes, of the redox "non-innocent" term to describe some ligands, that are not redox-active and behave rather as "trivial" spectator ligands contributing to the steric and electronic control of the metal centres through their electron-donating/-withdrawing properties.

Among all the redox ligands used, the ferrocenyl-phosphine and the pyridinyl-phosphole have afforded interesting progresses by modelling, in part, the role of the $[Fe_4S_4]$ cluster. In the complex $[Fe_2(CO)_2(\kappa^1\text{-Fc'})(\kappa^2\text{-dppv})(\mu\text{-adt}^{Bn})]$ (**70**), the modified ferrocene $[Fe(\eta^5\text{-}C_5Me_5)\{\eta^5\text{-}C_5Me_4(CH_2PEt_2)\}]$ acts as an electron reservoir and allows bidirectional electrocatalysis for reversible H^+/H_2 conversion. The activity of the derivative $[Fe_2(CO)_5(\kappa^1\text{-phosphole})(\mu\text{-bdt})]$ (**15**) towards HER relies on a proton-responsive dipyridyl-phosphole that can also act as an electron reservoir. The derivative $[Fe_2(CO)_4(\mu\text{-dppf})(\mu\text{-pdt})]$ ($\mathbf{61^{Ph}}$) is one of the few di-iron compounds reported as being able to activate H_2. It is also worth noting that NO displays an effective "non-innocent" behaviour according to the definition of Jørgensen and it allows a distortion of the geometry around one iron centre mimicking the geometry of the active site. From all of these results emerges a basic knowledge that should make possible the design of efficient di-iron catalysts having an hydrogenases-like activity.

The second section shows the diversity of dinuclear complexes designed for molecular activation with simple well-known redox chelates or highly sophisticated encapsulating and dinucleating, polydentate redox-active ligands. Such species are able to favour multi-electronic processes, involving bonds formation or cleavage, at

a bimetallic site as well as the stabilization of reactive radical species. They generally play the essential role of electron reservoir but they may also have a crucial influence on metal-metal interactions. Some complexes display redox isomerism which may have an effect on the orientation of their reactivity.

Finally, the combination of redox-active ligands, and more generally of "non-innocent" ligands, with a bimetallic core, especially with abundant metals of the first transition series, opens a wide and promising field of possibilities and perspectives for molecular catalysis.

References

1. van Leest NP, de Zwart FJ, Zhou M, de Bruin B (2021) Controlling radical-type single-electron elementary steps in catalysis with redox-active ligands and substrates. JACS Au 1: 1101–1115. https://doi.org/10.1021/jacsau.1c00224
2. Drosou M, Kamatsos F, Mitsopoulou CA (2020) Recent advances in the mechanisms of the hydrogen evolution reaction by non-innocent sulfur-coordinating metal complexes. Inorg Chem Front 7:37–71. https://doi.org/10.1039/C9QI01113G
3. van der Vlugt JI (2019) Radical-type reactivity and catalysis by single-electron transfer to or from redox-active ligands. Chem A Eur J 25:2651–2662. https://doi.org/10.1002/chem.201802606
4. Chirila A, Das BG, Kuijpers PF, Sinha V, de Bruin B (2019) Application of stimuli-responsive and "non-innocence" ligands in base metal catalysis. In: Klein Gebbink RJM, Moret M-E (eds) Non-Noble metal catalysis: molecular approaches and reactions. Wiley-VCH, pp 1–31. https://doi.org/10.1002/9783527699087.ch1
5. Costentin C, Savéant J-M, Tard C (2018) Ligand "non-innocence" in coordination complexes vs. kinetic, mechanistic, and selectivity issues in electrochemical catalysis. Proc Natl Acad Sci 115:9104–9109. https://doi.org/10.1073/pnas.1810255115
6. Storr T, Mukherjee R (2018) Preface for the forum on applications of metal complexes with ligand-centered radicals. Inorg Chem 57:9577–9579. https://doi.org/10.1021/acs.inorgchem.8b02171
7. Luo G-G, Zhang H-L, Tao Y-W, Wu Q-Y, Tian D, Zhang Q (2019) Recent progress in ligand-centered homogeneous electrocatalysts for hydrogen evolution reaction. Inorg Chem Front 6: 343–354. https://doi.org/10.1039/C8QI01220B
8. de Bruin B, Gualco P, Paul ND (2016) Redox-non-innocent ligands: reactivity and catalysis. In: Stradiotto M, Lundgren RJ (eds) Ligand design in metal chemistry: reactivity and catalysis1st edn. Wiley, pp 46–65. https://doi.org/10.1002/9781118839621.ch7
9. Jacquet J, Desage-El Murr M, Fensterbank L (2016) Metal-promoted coupling reactions implying ligand-based redox changes. ChemCatChem 8:3310–3316. https://doi.org/10.1002/cctc.201600616
10. Broere DLJ, Plessius R, van der Vlugt JI (2015) New avenues for ligand-mediated processes – expanding metal reactivity by the use of redox-active catechol, o-aminophenol and o-phenylenediamine ligands. Chem Soc Rev 44:6886–6915. https://doi.org/10.1039/c5cs00161g
11. Berben LA, de Bruin B, Heyduk AF (2015) Non-innocent ligands. Chem Commun 51:1553–1554. https://doi.org/10.1039/C4CC90480J
12. Olivos Suarez AI, Lyaskovskyy V, Reek JNH, van der Vlugt JI, de Bruin B (2013) Complexes with nitrogen-centered radical ligands: classification, spectroscopic features, reactivity, and catalytic applications. Angew Chem Int Ed 52:12510–12529. https://doi.org/10.1002/anie.201301487

13. Luca OR, Crabtree RH (2013) Redox-active ligands in catalysis. Chem Soc Rev 42:1440–1459. https://doi.org/10.1039/c2cs35228a
14. Hindson K, de Bruin B (2012) Cooperative & redox non-innocent ligands in directing organometallic reactivity. Eur J Inorg Chem 3:340–342. https://doi.org/10.1002/ejic.201290001
15. Blanchard S, Derat E, Desage-El Murr M, Fensterbank L, Malacria M, Mouriès-Mansuy V (2012) Non-innocent ligands: new opportunities in iron catalysis. Eur J Inorg Chem:376–389. https://doi.org/10.1002/ejic.201100985
16. Kaim W (2012) The shrinking world of innocent ligands: conventional and non-conventional redox-active ligands. Eur J Inorg Chem:343–348. https://doi.org/10.1002/ejic.201101359
17. Lyaskovskyy V, de Bruin B (2012) Redox non-innocent ligands: versatile new tools to control catalytic reactions. ACS Catal 2:270–279. https://doi.org/10.1021/cs200660v
18. Praneeth VKK, Ringenberg MR, Ward TR (2012) Redox-active ligands in catalysis. Angew Chem Int Ed 51:10228–10234. https://doi.org/10.1002/anie.201204100
19. Chirik PJ (2011) Preface: forum on redox-active ligands. Inorg Chem 50:9737–9740. https://doi.org/10.1021/ic201881k
20. Kaim W (2011) Manifestations of non-innocent ligand behavior. Inorg Chem 50:9752–9765. https://doi.org/10.1021/ic2003832
21. Eisenberg R, Gray HB (2011) Non-innocence in metal complexes: a dithiolene dawn. Inorg Chem 50:9741–9751. https://doi.org/10.1021/ic2011748
22. Chirik PJ, Wieghardt K (2010) Radical ligands confer nobility on base-metal catalysts. Science 327:794–795. https://doi.org/10.1126/science.1183281
23. Kaim W, Schwederski B (2010) Non-innocent ligands in bioinorganic chemistry – an overview. Coord Chem Rev 254:1580–1588. https://doi.org/10.1016/j.ccr.2010.01.009
24. Knijnenburg Q, Gambarotta S, Budzelaar PHM (2006) Ligand-centred reactivity in diiminepyridine complexes. Dalton Trans:5442–5448. https://doi.org/10.1039/b612251e
25. Butin KP, Beloglazkina EK, Zyk NV (2005) Metal complexes with non-innocent ligands. Russ Chem Rev 74:531–553. https://doi.org/10.1070/RC2005v074n06ABEH000977
26. Ward MD, McCleverty JA (2002) Non-innocent behaviour in mononuclear and polynuclear complexes: consequences for redox and electronic spectroscopic properties. J Chem Soc Dalton Trans:275–288. https://doi.org/10.1039/b110131p
27. Allgeier AM, Mirkin CA (1998) Ligand design for electrochemically controlling stoichiometric and catalytic reactivity of transition metals. Angew Chem Int Ed 37:894–908. https://doi.org/10.1002/(SICI)1521-3773(19980420)37:7<894::AID-ANIE894>3.0.CO;2-L
28. Jørgensen CK (1966) Differences between the four halide ligands, and discussion remarks on trigonal-bipyramidal complexes, on oxidation states, and on diagonal elements of one-electron energy. Coord Chem Rev 1:164–178. https://doi.org/10.1016/S0010-8545(00)80170-8
29. van Beek CB, van Leest NP, Lutz M, de Vos SD, Klein Gebbink RJM, de Bruin B, Broere DLJ (2022) Combining metal–metal cooperativity, metal–ligand cooperativity and chemical non-innocence in diiron carbonyl complexes. Chem Sci 13:2094–2104. https://doi.org/10.1039/d1sc05473b
30. Wang Q, Brooks SH, Liu T, Tomson NC (2021) Tuning metal–metal interactions for cooperative small molecule activation. Chem Commun 57:2839–2853. https://doi.org/10.1039/d0cc07721f
31. Maity R, Birenheide BS, Breher F, Sarkar B (2021) Cooperative effects in multimetallic complexes applied in catalysis. ChemCatChem 13:2337–2370. https://doi.org/10.1002/cctc.202001951
32. Xiong N, Zhang G, Sun X, Zeng R (2020) Metal-metal cooperation in dinucleating complexes involving late transition metals directed towards organic catalysis. Chin J Chem 38:185–201. https://doi.org/10.1002/cjoc.201900371
33. Campos J (2020) Bimetallic cooperation across the periodic table. Nat Rev Chem 4:696–702. https://doi.org/10.1038/s41570-020-00226-5

34. Farley CM, Uyeda C (2019) Organic reactions enabled by catalytically active metal–metal bonds. Trends Chem 1:497–509. https://doi.org/10.1016/j.trechm.2019.04.002
35. Mankad NP (2019) Catalysis with multinuclear complexes. In: Klein Gebbink RJM, Moret M-E (eds) Non-Noble metal catalysis: molecular approaches and reactions. Wiley-VCH, pp 49–68. https://doi.org/10.1002/9783527699087.ch3
36. Rej S, Tsurugi H, Mashima K (2018) Multiply-bonded dinuclear complexes of early-transition metals as minimum entities of metal cluster catalysts. Coord Chem Rev 355:223–239. https://doi.org/10.1016/j.ccr.2017.08.016
37. Powers IG, Uyeda C (2017) Metal–metal bonds in catalysis. ACS Catal 7:936–958. https://doi.org/10.1021/acscatal.6b02692
38. Pye DR, Mankad NP (2017) Bimetallic catalysis for C–C and C–X coupling reactions. Chem Sci 8:1705–1718. https://doi.org/10.1039/c6sc05556g
39. Kalck P (ed) (2016) Homo- and heterobimetallic complexes in catalysis. Topics in organometallic chemistry. Springer, Cham. ISBN-13: 978-3319816951
40. Mankad NP (2016) Selectivity effects in bimetallic catalysis. Chem A Eur J 22:5822–5829. https://doi.org/10.1002/chem.201505002
41. Iglesias M, Sola E, Oro LA (2016) Binuclear iridium complexes in catalysis. In: Kalck P (ed) Homo- and heterobimetallic complexes in catalysis: cooperative catalysis. Springer, Cham, pp 31–58
42. Buchwalter P, Rosé J, Braunstein P (2015) Multimetallic catalysis based on heterometallic complexes and clusters. Chem Rev 115:28–126. https://doi.org/10.1021/cr500208k
43. van der Vlugt JI (2012) Cooperative catalysis with first-row late transition metals. Eur J Inorg Chem:363–375. https://doi.org/10.1002/ejic.201100752
44. Khusnutdinova JR, Milstein D (2015) Metal–ligand cooperation. Angew Chem Int Ed 54:12236–12273. https://doi.org/10.1002/anie.201503873
45. Ghosh AC, Duboc C, Gennari M (2021) Synergy between metals for small molecule activation: enzymes and bio-inspired complexes. Coord Chem Rev 428:213606. https://doi.org/10.1016/j.ccr.2020.213606
46. Bullock RM, Chen JG, Gagliardi L, Chirik PJ, Farha OK, Hendon CH, Jones CW, Keith JA, Klosin J, Minteer SD, Morris RH, Radosevich AT, Rauchfuss TB, Strotman NA, Vojvodic A, Ward TR, Yang JY, Surendranath Y (2020) Using nature's blueprint to expand catalysis with earth-abundant metals. Science 369:eabc3183. https://doi.org/10.1126/science.abc3183
47. Klein Gebbink RJM, Morret M-E (eds) (2019) Non-Noble metal catalysis. Molecular approaches and reactions. Wiley-VCH, p 590. ISBN: 978-3-527-69908-7
48. Weigand W, Schollhammer P (eds) (2015) Bioinspired catalysis, metal-sulfur complexes. Wiley-VCH, Weinheim, p 417. ISBN: 978-3-527-33308-0
49. Lindahl PA (2012) Metal–metal bonds in biology. J Inorg Biochem 106:172–178. https://doi.org/10.1016/j.jinorgbio.2011.08.012
50. Peters JW, Lanzilotta WN, Lemon BJ, Seefeldt LC (1998) X-ray crystal structure of the Fe-only hydrogenase (Cpl) from clostridium pasteurianum to 1.8 angstrom resolution. Science 282:1853–1858. https://doi.org/10.1126/science.282.5395.1853
51. Nicolet Y, Piras C, Legrand P, Hatchikian CE, Fontecilla-Camps JC (1999) Desulfovibrio desulfuricans iron hydrogenase: the structure shows unusual coordination to an active site Fe binuclear center. Structure 7:13–23. https://doi.org/10.1016/s0969-2126(99)80005-7
52. Lubitz W, Ogata H, Rüdiger O, Reijerse E (2014) Hydrogenases. Chem Rev 114:4081–4148. https://doi.org/10.1021/cr4005814
53. Birell JA, Rodriguez-Macia P, Reijerse EJ, Martini MA, Lubitz W (2021) The catalytic cycle of [FeFe] hydrogenase: a tale of two sites. Coord Chem Rev 449:214191–214213. https://doi.org/10.1016/j.ccr.2021.214191
54. Wittkamp F, Senger M, Stripp ST, Apfel U-P (2018) [FeFe]-hydrogenases: recent developments and future perspectives. Chem Commun 54:5934–5942. https://doi.org/10.1039/c8cc01275j

55. Kleinhaus JT, Wittkamp F, Yadav S, Siegmund D, Apfel U-P (2021) [FeFe]-Hydrogenases: Maturation and reactivity of enzymatic systems and overview of biomimetic models. Chem Soc Rev 50:1668–1784. https://doi.org/10.1039/D0CS01089H
56. Apfel U-P, Pétillon FY, Schollhammer P, Talarmin J, Weigand W (2015) [FeFe] hydrogenase models: an overview. In: Weigand W, Schollhammer P (eds) Bioinspired catalysis: metal-sulfur complexes. Wiley-VCH, Weinheim, pp 79–103. https://doi.org/10.1002/9783527664160.ch4
57. Elleouet C, Pétillon FY, Schollhammer P (2019) [FeFe]-hydrogenases models. In: Hirao T, Moriuch T (eds) Advances in bioorganometallic chemistry: [FeFe]-hydrogenases models. Elsevier, pp 347–359. ch. 17 ISBN: 9780128141984
58. Schilter D, Camara JM, Huynh MT, Hammes-Schiffer S, Rauchfuss TB (2016) Hydrogenase enzymes and their synthetic models: the role of metal hydrides. Chem Rev 116:8693–8749. https://doi.org/10.1021/acs.chemrev.6b00180
59. Simmons TR, Berggren G, Bacchi M, Fontecave M, Artero V (2014) Mimicking hydrogenases: from biomimetics to artificial enzymes. Coord Chem Rev:270–271., 127–150. https://doi.org/10.1016/j.ccr.2013.12.018
60. Liu Y-C, Yen T-H, Chu K-T, Chiang M-H (2016) Utilization of non-innocent redox ligands in [FeFe]-hydrogenase modeling for hydrogen production. Comments Inorg Chem 36:141–181. https://doi.org/10.1080/02603594.2015.1115397
61. Sun L, Duboc C, Shen K (2022) Bioinspired molecular electrocatalysts for H_2 production: chemical strategies. ACS Catal 12:9159–9170. https://doi.org/10.1021/acscatal.2c02171
62. Lehnert N, Kim E, Dong HT, Harland JB, Hunt AP, Manickas EC, Oakley KM, Pham J, Reed GC, Alfaro VS (2021) The biologically relevant coordination chemistry of iron and nitric oxide: electronic structure and reactivity. Chem Rev 121:14682–14905. https://doi.org/10.1021/acs.chemrev.1c00253
63. Hirst DG, Robson T (2011) Chapter 1: nitric oxide physiology and pathology. In: McCarthy HO, Coulter JA (eds) Nitric oxide, methods and protocols, methods in molecular biology, vol 704, pp 1–13. ISBN: 978-1-61737-963-5 978-1-61737-964-2
64. Olsen MT, Justice AK, Gloaguen F, Rauchfuss TB, Wilson SR (2008) New nitrosyl derivatives of diiron dithiolates related to the active site of the [FeFe]-hydrogenases. Inorg Chem 47:11816–11824. https://doi.org/10.1021/ic801542w
65. Olsen MT, Bruschi M, De Gioia L, Rauchfuss TB, Wilson SR (2008) Nitrosyl derivatives of diiron(I) dithiolates mimic the structure and Lewis acidity of the [FeFe]-hydrogenase active site. J Am Chem Soc 130:12021–12030. https://doi.org/10.1021/ja802268p
66. Hsieh C-H, Erdem ÖF, Harman SD, Singleton ML, Reijerse E, Lubitz W, Popescu CV, Reibenspies JH, Brothers SM, Hall MB, Darensbourg MY (2012) Structural and spectroscopic features of mixed valent $Fe^{II}Fe^{I}$ complexes and factors related to the rotated configuration of diiron hydrogenase. J Am Chem Soc 134:13089–13102. https://doi.org/10.1021/ja304866r
67. Hsieh C-H, Darensbourg MY (2010) A $\{Fe(NO)_3\}^{10}$ trinitrosyliron complex stabilized by an N-heterocyclic carbene and the cationic and neutral $\{Fe(NO)_2\}^{9/10}$ products of its NO release. J Am Chem Soc 132:14118–14125. https://doi.org/10.1021/ja104135x
68. Hsieh C-H, Ding S, Erdem ÖF, Crouthers DJ, Liu T, McCrory CCL, Lubitz W, Popescu CV, Reibenspies JH, Hall MB, Darensbourg MY (2014) Redox active iron nitrosyl units in proton reduction electrocatalysis. Nat Commun 5:3684. https://doi.org/10.1038/ncomms4684
69. Ding S, Ghosh P, Lunsford AM, Wang N, Bhuvanesh N, Hall MB, Darensbourg MY (2016) Hemilabile bridging thiolates as proton shuttles in bioinspired H_2 production electrocatalysts. J Am Chem Soc 138:12920–12927. https://doi.org/10.1021/jacs.6b06461
70. Tye JW, Lee J, Wang H-W, Mejia-Rodriguez R, Reibenspies JH, Hall MB, Darensbourg MY (2005) Dual electron uptake by simultaneous iron and ligand reduction in an N-heterocyclic carbene substituted [FeFe] hydrogenase model compound. Inorg Chem 44:5550–5552. https://doi.org/10.1021/ic050402d

71. Mele A, Bertini S, Albrecht M, Elleouet C, Pétillon FY, Schollhammer P (2020) A diiron hydrogenase mimic featuring a 1,2,3-triazolylidene. Chimia 74:499–503. https://doi.org/10.2533/chimia.2020.499
72. Mele A, Arrigoni F, Elleouet C, Pétillon FY, Schollhammer P, Zampella G (2022) Insights into triazolylidene ligands behaviour at a di-iron site related to [FeFe]-hdrogenases. Molecules 27:4700. https://doi.org/10.3390/molecules27154700
73. Collado A, Torres A, Gómez-Gallego M, Casarrubios L, Sierra MA (2020) A model for the prediction of the redox potentials in [FeFe]-clusters from the electronic properties of isocyanide ligands. ChemistrySelect 5:7177–7182. https://doi.org/10.1002/slct.202001820
74. Becker R, Amirjalayer S, Li P, Woutersen S, Reek JNH (2016) An iron-iron hydrogenase mimic with appended electron reservoir for efficient proton reduction in aqueous media. Sci Adv 2:e1501014. https://doi.org/10.1126/sciadv.1501014
75. Zaffaroni R, Dzik WI, Detz RJ, van der Vlugt JI, Reek JNH (2019) Proton relay effects in pyridyl-appended hydrogenase mimics for proton reduction catalysis. Eur J Inorg Chem:2498–2509. https://doi.org/10.1002/ejic.201900072
76. Xie Q, Pérez-Cordero E, Echegoyen L (1992) Electrochemical detection of C_{60}^{6-} and C_{70}^{6-}: enhanced stability of fullerenes in solution. J Am Chem Soc 114:3978–3980. https://doi.org/10.1021/ja00036a056
77. Echegoyen L, Echegoyen LE (1998) Electrochemistry of fullerenes and their derivatives. Acc Chem Res 31:593–601. https://doi.org/10.1021/ar970138v
78. Liu Y-C, Yen T-H, Tseng Y-J, Hu C-H, Lee G-H, Chiang M-H (2012) Electron delocalization from the fullerene attachment to the diiron core within the active-site mimics of [FeFe]-hydrogenase. Inorg Chem 51:5997–5999. https://doi.org/10.1021/ic3007298
79. Yen T-H, He Z-C, Lee G-H, Tseng M-C, Shen Y-H, Tseng T-W, Liaw W-F, Chiang M-H (2017) Reduced thione ligation is preferred over neutral phosphine ligation in diiron biomimics regarding electronic functionality: a spectroscopic and computational investigation. Chem Commun 53:332–335. https://doi.org/10.1039/C6CC08042A
80. Derossi S, Becker R, Li P, Hartl F, Reek JNH (2014) A phosphoramidite-based [FeFe]H_2ase functional mimic displaying fast electrocatalytic proton reduction. Dalton Trans 43:8363–8367. https://doi.org/10.1039/c3dt53471e
81. Si Y, Charreteur K, Capon J-F, Gloaguen F, Pétillon FY, Schollhammer P, Talarmin J (2010) Non-innocent bma ligand in a dissymetrically disubstituted diiron dithiolate related to the active site of the [FeFe] hydrogenases. J Inorg Biochem 104:1038–1042. https://doi.org/10.1016/j.jinorgbio.2010.05.011
82. Greco C, De Gioia L (2011) A theoretical study on the enhancement of functionally relevant electron transfers in biomimetic models of [FeFe]-hydrogenases. Inorg Chem 50:6987–6995. https://doi.org/10.1021/ic200297d
83. Ghosh S, Hollingsworth N, Warren M, Hrovat DA, Richmond MG, Hogarth G (2019) Hydrogenase biomimics containing redox-active ligands: $Fe_2(CO)_4(\mu\text{-edt})(\kappa^2\text{-bpcd})$ with electron-acceptor 4,5-bis(diphenylphosphino)-4-cyclopenten-1,3-dione (bpcd) as a potential $[Fe_4–S_4]_H$ surrogate. Dalton Trans 48:6051–6060. https://doi.org/10.1039/C8DT04906H
84. Yang K, Bott SG, Richmond MG (1994) Intramolecular phosphine attack on a coordinated alkyne ligand in $Co_2(CO)_4$(bma)(μ-PhC≡CH). Characterization of the zwitterionic hydrocarbyl complex $Co_2(CO)_4[\mu\text{-}\eta^2\text{:}\eta^2\text{:}\eta^1\text{:}\eta^1\text{-PhC=C(H)PPh}_2\text{C=C(PPh}_2\text{)C(O)OC(O)}]$. Organometallics 13:3767-3769. https://doi.org/10.1021/om00022a007
85. Yang K, Bott SG, Richmond MG (1994) Reversible chelate-to-bridge ligand exchange in $Co_2(CO)_4$(μ-PhC≡CPh)(bma) and alkyne-diphosphine ligand coupling. Synthesis, reactivity, and molecular structures of $Co_2(CO)_4$(μ-PhC≡CPh)(bma), $Co_2(CO)_4$(μ-PhC≡CPh){(Z)-Ph_2PCH=CHPPh_2}, and $Co_2(CO)_4\{\eta^2,\eta^2,\eta^1,\eta^1\text{-(Z)-Ph}_2\text{PC(Ph)=(Ph)CC=C(PPh}_2\text{)C(O)OC(O)}\}$. Organometallics 13:3788–3799. https://doi.org/10.1021/om00022a013
86. Yang K, Bott SG, Richmond MG (1996) Regioselective phosphine attack on the coordinated alkyne in $Co_2(\mu\text{-alkyne})$ complexes Reactivity studies and X-ray diffraction structures of $Co_2(CO)_4$(bma)(μ-PhC≡C^{t}Bu) and the zwitterionic hydrocarbyl complexes $Co_2(CO)_4[\mu$-

$\eta^2,\eta^2,\eta^1,\eta^1$-RC=C(R')$PPh_2$C=C($PPh_2$)C(O)OC(O)}. J Organomet Chem 516:65-80. https://doi.org/10.1016/0022-328X(95)06090-J

87. Bott SG, Yang K, Talafuse KA, Richmond MG (2003) Phosphine ligand attack at both the methylidyne cap and the CpNi center in $HCCo_2NiCp(CO)_6$ by 2,3-Bis(diphenylphosphino)-maleic anhydride (bma): P-C bond cleavage reactivity, kinetics, and X-ray structures of the zwitterionic clusters $Co_2NiCp(CO)_4(\mu\text{-CO})[\mu_2,\eta^2,\eta^1\text{-C(H)}PPh_2C{=}C(PPh_2)C(O)OC(O)]$ and $Co_2NiCp(CO)_4[\mu_2\ ,\eta^2,\sigma\text{-C(H)}PPh_2C{=}CC(O)OC(O)](\mu_2\text{-}PPh_2)$. Organometallics 22:1383–1390. https://doi.org/10.1021/om0209273
88. Ghosh S, Rana S, Hollingsworth N, Richmond MG, Kabir SE, Hogarth G (2018) Hydrogenase biomimetics with redox-active ligands: synthesis, structure, and electrocatalytic studies on $[Fe_2(CO)_4(\kappa^2\text{-dppn})(\mu\text{-edt})]$ (edt = ethanedithiolate; dppn = 1,8-bis(diphenylphosphino)-naphthalene). Inorganics 6:122. https://doi.org/10.3390/inorganics6040122
89. Arrigoni F, Elleouet C, Mele A, Pétillon FY, De Gioia L, Schollhammer P, Zampella G (2020) Insights into the two-electron reductive process of [FeFe]H_2ase biomimetics: cyclic voltammetry and DFT investigation on chelate control of redox properties of $[Fe_2(CO)_4(\kappa^2\text{-chelate})(\mu\text{-dithiolate})]$. Chem A Eur J 26:17536–17545. https://doi.org/10.1002/chem.202003233
90. Ghosh S, Rahaman A, Holt KB, Nordlander E, Richmond MG, Kabir SE, Hogarth G (2016) Hydrogenase biomimetics with redox-active ligands: electrocatalytic proton reduction by $[Fe_2(CO)_4(\kappa^2\text{-diamine})(\mu\text{-edt})]$ (diamine = 2,2′-bipy, 1,10-phen). Polyhedron 116:127–135. https://doi.org/10.1016/j.poly.2016.05.015
91. Roy S, Laureanti JA, Groy TL, Jones AK (2017) Synthesis and electrocatalytic activity of [FeFe]-hydrogenase model complexes with non-innocent chelating nitrogen-donor ligands. Eur J Inorg Chem:2942–2950. https://doi.org/10.1002/ejic.201700123
92. Roy S, Groy TL, Jones AK (2013) Biomimetic model for [FeFe]-hydrogenase: asymmetrically disubstituted diiron complex with a redox-active 2,2′-bipyridyl ligand. Dalton Trans 42:3843–3853. https://doi.org/10.1039/c2dt32457a
93. Seidel RA, Hall MB, Swenson MT, Nichol GS, Lichtenberger DL, Evans DH, Glass RS (2013) Synthesis and characterization of [FeFe]-hydrogenase mimics appended with a 2-phenylazopyridine ligand. J Sulfur Chem 34:566–579. https://doi.org/10.1080/17415993.2013.796553
94. Brazzolotto D, Gennari M, Queyriaux N, Simmons TR, Pécaut J, Demeshko S, Meyer F, Orio M, Artero V, Duboc C (2016) Nickel-centred proton reduction catalysis in a model of [NiFe] hydrogenase. Nat Chem 8:1054–1060. https://doi.org/10.1038/nchem.2575
95. Wang L, Gennari M, Barrozo A, Fize J, Philouze C, Demeshko S, Meyer F, Olio M, Artero V, Duboc C (2020) Role of the metal ion in bio-inspired hydrogenase models: investigation of a homodinuclear FeFe complex vs its heterodinuclear NiFe analogue. ACS Catal 10:177–186. https://doi.org/10.1021/acscatal.9b03212
96. Tang H, Hall MB (2017) Biomimetics of [NiFe]-hydrogenase: nickel- or iron-centered proton reduction catalysis? J Am Chem Soc 139:18065–18070. https://doi.org/10.1021/jacs.7b10425
97. Adams RD, Miao S (2004) Metal carbonyl derivatives of sulfur-containing quinones and hydroquinones: synthesis, structures, and electrochemical properties. Inorg Chem 43:8414–8426. https://doi.org/10.1021/ic048880w
98. Hall MB, Chen J, Mebi CA, Okumura N, Swenson MT, Ossowski SE, Zakai UL, Nichol GS, Lichtenberger DL, Evans DH, Glass RS (2013) Redox chemistry of noninnocent quinones annulated to 2Fe2S cores. Organometallics 32:6605–6612. https://doi.org/10.1021/om400913p
99. Chen J, Vannucci AK, Mebi CA, Okumura N, Borowski SC, Swenson M, Lockett LT, Evans DH, Glass RS, Lichtenberger DL (2010) Synthesis of diiron hydrogenase mimics bearing hydroquinone and related ligands. Electrochemical and computational studies of the mechanism of hydrogen production and the role of O−H···S hydrogen bonding. Organometallics 29:5530–5340. https://doi.org/10.1021/om100396j

100. Li P, Amirjalayer S, Hartl F, Lutz M, de Bruin B, Becker R, Woutersen S, Reek JNH (2014) Direct probing of photoinduced electron transfer in a self-assembled biomimetic [2Fe2S]-hydrogenase complex using ultrafast vibrational spectroscopy. Inorg Chem 53:5373–5383. https://doi.org/10.1021/ic500777d
101. Oudsen JPH, Venderbosch B, Korstanje TJ, Tromp M (2020) Electronic characterization of redox (non)-innocent Fe2S2 reference systems: a multi K-edge X-ray spectroscopic study. RSC Adv 10:729–738. https://doi.org/10.1039/c9ra08903a
102. Benndorf S, Hofmeister E, Wächtler M, Görls H, Liebing P, Peneva K, Gräfe S, Kupfer S, Dietzek-Ivanšić B, Weigand W (2022) Unravelling the mystery: enlightenment of the uncommon electrochemistry of naphthalene monoimide [FeFe]-hydrogenase mimics. Eur J Inorg Chem:e202100959. https://doi.org/10.1002/ejic.202100959
103. Mebi CA, Labrecque JH, Williams AA (2020) Metalloenzyme mimic: diironhexacarbonyl cluster coupled to redox-active 4-mercapto-1,8-naphthalic anhydride ligands. Transit Met Chem 45:577–581. https://doi.org/10.1007/s11243-020-00410-y
104. Torres A, Collado A, Gómez-Gallego M, Ramírez de Arellano C, Sierra MA (2022) Electrocatalytic behavior of tetrathiafulvalene (TTF) and extended tetrathiafulvalene (exTTF) [FeFe]- hydrogenase mimics. ACS Org Inorg Au 2:23–33. https://doi.org/10.1021/acsorginorgau.1c00011
105. Westmeyer MD, Galloway CP, Rauchfuss TB (1994) Photoaddition of $Fe_2S_2(CO)_6$ to C_{60}. Inorg Chem 33:4615–4616. https://doi.org/10.1021/ic00099a005
106. Westmeyer MD, Rauchfuss TB, Verma AK (1996) Iron sulfido derivatives of the fullerenes C_{60} and C_{70}. Inorg Chem 35:7140–7147. https://doi.org/10.1021/ic960728+
107. Chen S, Luo L, Li Y, Yang D, Qu J, Luo Y (2016) Electronic structure of thiolate-bridged diiron complexes and a single-electron oxidation reaction: a combination of experimental and computational studies. Chin J Chem 34:915–924. https://doi.org/10.1002/cjoc.201600262
108. Tard C, Borg SJ, Fairhurst SA, Pickett CJ, Best SP (2019) Electronic communication between dithiolato-bridged diiron carbonyl and S-bridged redox-active centres. Inorganics 7:37. https://doi.org/10.3390/inorganics7030037
109. Tard C, Liu X, Ibrahim SK, Bruschi M, De Gioia L, Davies SC, Yang X, Wang L-S, Sawers G, Pickett CJ (2005) Synthesis of the H-cluster framework of iron-only hydrogenase. Nature 433:610–613. https://doi.org/10.1038/nature03298
110. Schwab DE, Tard C, Brecht E, Peters JW, Pickett CJ, Szilagyi RK (2006) On the electronic structure of the hydrogenase H-cluster. Chem Commun:3696–3698. https://doi.org/10.1039/b604994j
111. Brushi M, Greco C, Zampella G, Ryde U, Picket CJ, De Gioia L (2008) A DFT investigation on structural and redox properties of a synthetic Fe6S6 assembly closely related to the [FeFe]-hydrogenases active site. CR Chimie 11:834–841. https://doi.org/10.1016/j.crci.2008.04.010
112. Ghosh S, Hogarth G, Hollingsworth N, Holt KB, Kabir SE, Sanchez BE (2014) Hydrogenase biomimetics: $Fe_2CO)_4(\mu$-dppf)(μ-pdt) (dppf = 1,1′-bis(diphenylphosphino)ferrocene) both a proton-reduction and hydrogen oxidation catalyst. Chem Commun 50:945–947. https://doi.org/10.1039/C3CC46456C
113. Rana S, Ghosh S, Hossain MK, Rahaman A, Hogarth G, Kabir SE (2016) Hydrogenase biomimetics: structural and spectroscopic studies on diphosphine-substituted derivatives of $Fe_2(CO)_6$(μ-edt) (edt = ethanedithiolate) and $Fe_2(CO)_6$(μ-tdt) (tdt = 1,3-toluenedithiolate). Transit Met Chem 41:933–942. https://doi.org/10.1007/s11243-016-0097-5
114. Song L-C (2005) Investigations on butterfly Fe/S cluster S-centered anions $(\mu\text{-}S^-)_2Fe_2(CO)_6$, $(\mu\text{-}S^-)(\mu\text{-RS})Fe_2(CO)_6$, and related species. Acc Chem Res 38:21–28. https://doi.org/10.1021/ar030004j
115. Li C-G, Wang S-L, Shang J-Y (2016) Bis(diphenylphosphino)ferrocene as an intramolecular bridging ligand in *N*-functionally substituted 1,3-azapropanedithiolate diiron complexes: synthesis and catalysis of proton reduction. J Coord Chem 69:2845–2854. https://doi.org/10.1080/00958972.2016.1225296

116. Kaur-Ghumaan S, Sreenithya A, Sunoj RB (2015) Synthesis, characterization and DFT studies of 1, 1′-bis(diphenylphosphino)ferrocene substituted diiron complexes: bioinspired [FeFe] hydrogenase model complexes. J Chem Sci 127:557–563. https://doi.org/10.1007/s12039-015-0809-y
117. Orton GRF, Ghosh S, Alker L, Sarker JC, Pugh D, Richmond MG, Hartl F, Hogarth G (2022) Biomimics of [FeFe]-hydrogenases incorporating redox-active ligands: synthesis, redox properties and spectroelectrochemistry of diiron-dithiolate complexes with ferrocenyl-diphosphines as Fe_4S_4 surrogates. Dalton Trans 51:9748–9769. https://doi.org/10.1039/D2DT00419D
118. Arrigoni F, Bertini L, Bruschi M, Greco C, De Gioia L, Zampella G (2019) H_2 activation in [FeFe]-hydrogenase cofactor versus diiron dithiolate models: factors underlying the catalytic success of nature and implications for an improved biomimicry. Chem A Eur J 25:1227–1241. https://doi.org/10.1002/chem.201804687
119. Liu Y-C, Lee C-H, Lee G-H, Chiang M-H (2011) Influence of a redox-active phosphane ligand on the oxidations of a diiron core related to the active site of Fe-only hydrogenase. Eur J Inorg Chem:1155–1162. https://doi.org/10.1002/ejic.201000972
120. Camara JM, Rauchfuss TB (2012) Combining acid–base, redox and substrate binding functionalities to give a complete model for the [FeFe]-hydrogenase. Nat Chem 4:26–30. https://doi.org/10.1038/nchem.1180
121. Lansing JC, Camara JM, Gray DE, Rauchfuss TB (2014) Hydrogen production catalyzed by bidirectional, biomimetic models of the [FeFe]-hydrogenase active site. Organometallics 33:5897–5906. https://doi.org/10.1021/om5004013
122. Rauchfuss TB (2015) Diiron azadithiolates as models for the [FeFe]-hydrogenase active site and paradigm for the role of the second coordination sphere. Acc Chem Res 48:2107–2116. https://doi.org/10.1021/acs.accounts.5b00177
123. Greco C (2013) H_2 binding and splitting on a new-generation [FeFe]-hydrogenase model featuring a redox-active decamethylferrocenyl phosphine ligand: a theoretical investigation. Inorg Chem 52:1901–1908. https://doi.org/10.1021/ic302118h
124. Schilter D, Gray DL, Fuller AL, Rauchfuss TB (2017) Synthetic models for nickel–iron hydrogenase featuring redox-active ligands. Aust J Chem 70:505–515. https://doi.org/10.1071/CH16614
125. Greco C (2013) Towards [NiFe]-hydrogenase biomimetic models that couple H_2 binding with functionally relevant intramolecular electron transfers: a quantum chemical study. Dalton Trans 42:13845–13854. https://doi.org/10.1039/c3dt50836f
126. Lu D-T, He J, Yu X-Y, Liu X-F, Li Y-L, Jiang Z-Q (2018) Diiron ethanedithiolate complexes with pendant ferrocene: synthesis, characterization and electrochemistry. Polyhedron 149:1–6. https://doi.org/10.1016/j.poly.2018.04.015
127. Qian G, Wang H, Zhong W, Liu X (2015) Electrochemical investigation into the electron transfer mechanism of a diiron hexacarbonyl complex bearing a bridging naphthalene moiety. Electrochim Acta 163:190–195. https://doi.org/10.1016/j.electacta.2015.02.163
128. Gimbert-Suriñach C, Bhadbhade M, Colbran SB (2012) Bridgehead hydrogen atoms are important: unusual electrochemistry and proton reduction at iron dimers with ferrocenyl-substituted phosphido bridges. Organometallics 31:3480–3491. https://doi.org/10.1021/om201126w
129. Aguado S, Casarrubios L, Ramírez de Arellano C, Sierra MA (2020) Revisiting the photochemical synthesis of [FeFe]-hydrogenase mimics: reaction optimization, mechanistic study and electrochemical behaviour. RSC Adv 10:29855–29867. https://doi.org/10.1039/d0ra06002j
130. Daraosheh AQ, Abul-Futouh H, Murakami N, Ziems KM, Görls H, Kupfer S, Gräfe S, Ishii A, Celeda M, Mlostoń G, Weigand W (2022) Novel [FeFe]-hydrogenase mimics: unexpected course of the reaction of ferrocenyl α-thienyl thioketone with $[Fe_3(CO)_{12}]$. Materials 15:2867–2879. https://doi.org/10.3390/ma15082867

131. Häßner M, Fiedler J, Ringenberg MR (2019) (Spectro)electrochemical and electrocatalytic investigation of 1,1′-dithiolatoferrocene–hexacarbonyldiiron. Inorg Chem 58:1742–1745. https://doi.org/10.1021/acs.inorgchem.8b02971
132. Orton GRF, Ringenberg MR, Hogarth G (2022) Biomimics of [FeFe]-hydrogenases incorporating redox-active ligands: ferrocene-bridged dithiolate complexes $[Fe_2(CO)_6(-\mu\text{-}EC_5H_4FeC_5H_4E)]$ (E = S, se). J Organomet Chem 978:122472. https://doi.org/10.1016/j.jorganchem.2022.122472
133. Ogienko MA, Pushkarevsky NA, Smolentsev AI, Nadolinny VA, Ketkov SY, Konchenko SN (2014) Metal- and ligand-supported reduction of the $\{Fe_2S_2\}$ cluster as a path to formation of molecular group 13 element complexes $\{Fe_2S_2M\}$ (M = Al, Ga). Organometallics 33:2713–2720. https://doi.org/10.1021/om401237x
134. Piryazev DA, Ogienko MA, Virovets AV, Pushkarevsky NA, Konchenko SN (2012) [N,N'-Bis(2,6-diisopropylphenyl)-acenaphthene-1,2-diimine-κ^2N,N']-heptacarbonyl-1κC,2κ^3C,3κ^3C-di-μ3-tellurido-triiiron(II)(2 *Fe–Fe*). Acta Crystallogr C68:m320–m322. https://doi.org/10.1107/S0108270112040012
135. Bezdek MJ, Guo S, Chirik PJ (2016) Terpyridine molybdenum dinitrogen chemistry: synthesis of dinitrogen complexes that vary by five oxidation states. Inorg Chem 55:3117–3127. https://doi.org/10.1021/acs.inorgchem.6b00053
136. Kuriyama S, Arashiba K, Nakajima K, Tanaka H, Yoshizawa K, Nishibayashi Y (2015) Nitrogen fixation catalyzed by ferrocenesubstituted dinitrogen-bridged dimolybdenum–dinitrogen complexes: unique behavior of ferrocene moiety as redox active site. Chem Sci 6:3940–3951. https://doi.org/10.1039/c5sc00545k
137. Itabashi T, Arashiba K, Tanaka H, Konomi A, Eizawa A, Nakajima K, Yoshizawa K, Nishibayashi Y (2019) Synthesis and catalytic reactivity of bis(molybdenum-trihalide) complexes bridged by ferrocene skeleton toward catalytic nitrogen fixation. Organometallics 38:2863–2872. https://doi.org/10.1021/acs.organomet.9b00263
138. Wang Q, Zhang S, Cui P, Weberg AB, Thierer LM, Manor BC, Gau MR, Carroll PJ, Tomson NC (2020) Interdependent metal–metal bonding and ligand redox-activity in a series of dinuclear macrocyclic complexes of iron, cobalt, and nickel. Inorg Chem 59:4200–4214. https://doi.org/10.1021/acs.inorgchem.9b02339
139. Liu T, Murphy RP, Carroll PJ, Gau MR, Tomson NC (2022) C–C σ-bond oxidative addition and hydrofunctionalization by a macrocycle-supported diiron complex. J Am Chem Soc 144:14037–14041. https://doi.org/10.1021/jacs.2c06266
140. Uyeda C, Farley CM (2021) Dinickel active sites supported by redox-active ligands. Acc Chem Res 54:3710–3719. https://doi.org/10.1021/acs.accounts.1c00424
141. Lindsay S, Lo SK, Maguire OR, Bill E, Probert MR, Sproules S, Hess CR (2013) Syntheses and electronic structure of bimetallic complexes containing a flexible redox-active bridging ligand. Inorg Chem 52:898–909. https://doi.org/10.1021/ic302087f
142. Unjaroen D, Swart M, Browne WR (2017) Electrochemical polymerization of iron(III) polypyridyl complexes through C–C coupling of redox non-innocent phenolato ligands. Inorg Chem 56:470–479. https://doi.org/10.1021/acs.inorgchem.6b02378
143. Brietzke T, Dietz T, Kelling A, Schilde U, Bois J, Kelm H, Reh M, Schmitz M, Körzdörfer T, Leimkühler S, Wollenberger U, Krüger H-J, Holdt H-J (2017) The 1,6,7,12-tetraazaperylene bridging ligand as an electron reservoir and its disulfonato derivative as redox mediator in an enzyme-electrode process. Chem A Eur J 23:15583–15587. https://doi.org/10.1002/chem.201703639
144. Himmel H-J (2013) Guanidinyl-functionalized aromatic compounds (GFAs) – charge and spin density studies as starting points for the development of a new class of redox-active ligands. Z Anorg Allg Chem 639:1940–1952. https://doi.org/10.1002/zaac.201200496
145. Wiesner S, Wagner A, Kaifer E, Himmel H-J (2016) The control of the electronic structure of dinuclear copper complexes of redox-active tetrakisguanidine ligands by the environment. Dalton Trans 45:15828–15839. https://doi.org/10.1039/c6dt02128j

146. Steuer L, Kaifer E, Himmel H-J (2021) On the metal–ligand bonding in dinuclear complexes with redox-active guanidine ligands. Dalton Trans 50:9467–9482. https://doi.org/10.1039/d1dt01354h
147. Evangelio E, Ruiz-Molina D (2005) Valence tautomerism: new challenges for electroactive ligands. Eur J Inorg Chem:2957–2971. https://doi.org/10.1002/ejic.200500323
148. Tezgerevska T, Alley KG, Boskovic C (2014) Valence tautomerism in metal complexes: stimulated and reversible intramolecular electron transfer between metal centers and organic ligands. Coord Chem Rev 268:23–40. https://doi.org/10.1016/j.ccr.2014.01.014
149. Miller JS, Min KS (2009) Oxidation leading to reduction: Redox-induced electron transfer (RIET). Angew Chem Int Ed 48:262–272. https://doi.org/10.1002/anie200705138
150. Sarkar B, Schweinfurth D, Deibel N, Weisser F (2015) Functional metal complexes based on bridging "imino"-quinonoid ligands. Coord Chem Rev:293–294., 250–262. https://doi.org/10.1016/j.ccr.2015.01.015
151. Kaim W, Lahiri GK (2007) Unconventional mixed-valent complexes of ruthenium and osmium. Angew Chem Int Ed 46:1778–1796. https://doi.org/10.1002/anie.200602737
152. Kaim W, Sarkar B (2007) Mixed valency in ruthenium complexes – coordinative aspects. Coord Chem Rev 251:584–594. https://doi.org/10.1016/j.ccr.2006.06.003
153. Deibel N, Hohloch S, Schweinfurth D, Weisser F, Grupp A, Sarkar B (2014) Three-way cooperativity in d^8 metal complexes with ligands displaying chemical and redox non-innocence. Chem A Eur J 20:15178–15187. https://doi.org/10.1002/chem.201403276
154. Boyer JL, Rochford J, Tsai M-K, Muckerman JT, Fujita E (2010) Ruthenium complexes with non-innocent ligands: electron distribution and implications for catalysis. Coord Chem Rev 254:309–330. https://doi.org/10.1016/j.ccr.2009.09.006
155. Wada T, Tsuge K, Tanaka K (2001) Syntheses and redox properties of bis(hydroxoruthenium) complexes with quinone and bipyridine ligands. Water-oxidation catalysis. Inorg Chem 40:329–337. https://doi.org/10.1021/ic000552i
156. Muckerman JT, Polyansky DE, Wada T, Tanaka K, Fujita E (2008) Water oxidation by a ruthenium complex with non-innocent quinone Lligands: possible formation of an O-O bond at a low oxidation state of the metal. Inorg Chem 47:1787–1802. https://doi.org/10.1021/ic701892v
157. Ghosh S, Baik M-H (2011) Redox properties of Tanaka's water oxidation catalyst: redox. Non-innocent ligands dominate the electronic structure and reactivity. Inorg Chem 50:5946–5957. https://doi.org/10.1021/ic102427g
158. Ghosh S, Baik M-H (2012) The mechanism of O-O bond formation in Tanaka's water oxidation catalyst. Angew Chem 124:1247–1250. https://doi.org/10.1002/ange.201106337
159. Isobe H, Tanaka K, Shen J-R, Yamagushi K (2014) Water oxidation chemistry of a synthetic dinuclear ruthenium complex containing redox-active quinone ligands. Inorg Chem 53:3973–3984. https://doi.org/10.1021/ic402340d
160. Conception JJ, Jurss JW, Brennaman MK, Hoertz PG, Patrocinio AOT, Murakami NY, Iha NYM, Templeton JL, Meyer TJ (2009) Making oxygen with ruthenium complexes. Acc Chem Res 42:1954–1965. https://doi.org/10.1021/ar9001526
161. Hurst JK, Cape JL, Clark AE, Das S, Qin C (2008) Mechanisms of water oxidation catalyzed by ruthenium diimine complexes. Inorg Chem 47:1753–1764. https://doi.org/10.1021/ic700724h
162. Lippert CA, Arnstein SA, Sherrill CD, Soper JD (2010) Redox-active ligands facilitate bimetallic O_2 homolysis at five-coordinate oxorhenium(V) centers. J Am Chem Soc 132:3879–3892. https://doi.org/10.1021/ja910500a
163. Liang Q, DeMuth JC, Radović A, Wolford NJ, Neidig ML, Song D (2021) [2Fe–2S] cluster supported by redox-active *o*-phenylenediamide ligands and its application toward dinitrogen reduction. Inorg Chem 60:13811–13820. https://doi.org/10.1021/acs.inorgchem.1c00683
164. Yang X, Gianetti TL, Wörle MD, van Leest NP, de Bruin B, Grützmacher H (2019) A low-valent dinuclear ruthenium diazadiene complex catalyzes the oxidation of dihydrogen

and reversible hydrogenation of quinones. Chem Sci 10:1117–1125. https://doi.org/10.1039/c8sc02864h

165. Harkins SB, Peters JC (2004) Amido-bridged Cu2N2 diamond cores that minimize structural reorganization and facilitate reversible redox behavior between a $Cu^{1}Cu^{1}$ and a class III delocalized $Cu^{1.5}Cu^{1.5}$ species. J Am Chem Soc 126:2885–2893. https://doi.org/10.1021/ja037364m
166. Mankad NP, Rivard E, Harkins SB, Peters JC (2005) Structural snapshots of a flexible Cu_2P_2 core that accommodates the oxidation states $Cu^{I}Cu^{I}$, $Cu^{1.5}Cu^{1.5}$, and $Cu^{II}Cu^{II}$. J Am Chem Soc 127:16032–16033. https://doi.org/10.1021/ja056071l
167. Harkins SB, Mankad NP, Miller AJM, Szilagyi RK, Peters JC (2008) Probing the electronic structures of $[Cu_2(\mu\text{-}XR_2)]^{n+}$ diamond cores as a function of the bridging X atom (X = N or P) and charge ($n = 0, 1, 2$). J Am Chem Soc 130:3478–3485. https://doi.org/10.1021/ja076537v
168. Mankad NP, Harkins SB, Antholine WE, Peters JC (2009) Multifrequency EPR studies of $[Cu^{1.5}Cu^{1.5}]^{+}$ for $Cu_2(\mu\text{-}NR_2)_2$ and $Cu_2(\mu\text{-}PR_2)_2$ diamond cores. Inorg Chem 48:7026–7032. https://doi.org/10.1021/ic801864z
169. Rhee YM, Head-Gordon M (2008) A delicate electronic balance between metal and ligand in [Cu-P-Cu-P] diamondoids: oxidation state dependent plasticity and the formation of a singlet diradicaloid. J Am Chem Soc 130:3878–3887. https://doi.org/10.1021/ja0764916
170. Olivos Suarez AI, Lyaskovskyy V, Reek JNH, van der Vlugt JI, de Bruin B (2013) Complexes with nitrogen-centered radical ligands: classification, spectroscopic features, reactivity, and catalytic applications. Angew Chem Int Ed 52:12510–12529. https://doi.org/10.1002/anie.201301487
171. Wu T, Musgrove J, Siegler MA, Garcia-Bosch I (2021) Mononuclear and dinuclear copper complexes of tridentate redox-active ligands with tunable H-bonding donors: structure, spectroscopy and H^{+}/e^{-} reactivity. Chem Asian J 16:1608–1618. https://doi.org/10.1002/asia.202100286
172. Vreeken V, Broere DLJ, Jans ACH, Lankelma M, Reek JNH, Siegler MA, van der Vlugt JI (2016) Well-defined dinuclear gold complexes for preorganization-induced selective dual gold catalysis. Angew Chem Int Ed 55:10042–10046. https://doi.org/10.1002/anie.201603938
173. Vreeken V, Siegler MA, van der Vlugt JI (2017) Controlled interconversion of a dinuclear Au species supported by a redox-active bridging PNP ligand facilitates ligand-to-gold electron transfer. Chem A Eur J 23:5585–5594. https://doi.org/10.1002/chem.201700360
174. Wong JL, Higgins RF, Bhowmick I, Xi Cao D, Szigethy G, Ziller JW, Shores MP, Heyduk AF (2016) Bimetallic iron–iron and iron–zinc complexes of the redox-active ONO pincer ligand. Chem Sci 7:1594–1599. https://doi.org/10.1039/c5sc03006d
175. Zarkesh RA, Ziller JW, Heyduk AF (2008) Four-electron oxidative formation of aryl diazenes using a tantalum redox-active ligand complex. Angew Chem Int Ed 47:4715–4718. https://doi.org/10.1002/anie.200800812
176. Wojnar MK, Ziller JW, Heyduk AF (2017) Heterobimetallic and heterotrimetallic clusters containing a redox-active metalloligand. Eur J Inorg Chem:5571–5575. https://doi.org/10.1002/ejic.201701222
177. Rosenkoetter KE, Ziller JW, Heyduk AF (2017) Heterobimetallic complexes of palladium and platinum containing a redox-active $W[SNS]_2$ metalloligand. Dalton Trans 46:5503–5507. https://doi.org/10.1039/c6dt04451d
178. Rosenkoetter KE, Ziller JW, Heyduk AF (2016) A heterobimetallic W−Ni complex containing a redox-active $W[SNS]_2$ metalloligand. Inorg Chem 55:6794–6798. https://doi.org/10.1021/acs.inorgchem.6b01164

179. Wang D, Linderman SV, Fiedler AT (2015) Bimetallic complexes supported by a redox-active ligand with fused pincer-type coordination sites. Inorg Chem 54:8744–8754. https://doi.org/10.1021/acs.inorgchem.5b01380
180. Que L, Tolman WB (2008) Biologically inspired oxidation catalysis. Nature 455:333–340. https://doi.org/10.1038/nature07371
181. Chaudhuri P, Hess M, Flörke U, Wieghardt K (1998) From structural models of galactose oxidase to homogeneous catalysis: efficient aerobic oxidation of alcohols. Angew Chem Int Ed 37:2217–2220. https://doi.org/10.1002/(SICI)1521-3773(19980904)37:16<2217::AID-ANIE2217>3.0.CO;2-D
182. Chaudhuri P, Wieghardt K, Weyhermüller T, Paine TK, Mukherjee S, Mukherjee C (2005) Biomimetic metal-radical reactivity: aerial oxidation of alcohols, amines, aminophenols and catechols catalyzed by transition metal complexes. Biol Chem 386:1023–1033. https://doi.org/10.1515/BC.2005.118

Top Organomet Chem (2023) 70: 157–206
https://doi.org/10.1007/3418_2023_88

Published online: 25 April 2023

Dinuclear Reactivity Between the Two Metal Centers

Laurent Maron and Philippe Kalck

Contents

Abstract In the field of metal-mediated selective and easier organic reactions, the present chapter focuses on the activation of at least one main step in the cleft of a dinuclear platform, in which a 1e-1e process occurs. This contribution emphasizes on the concepts that govern the conception of the coordination sphere in order to maintain the two metal centers at the right distance and which plays a central role in the electronic and steric effects. An analysis is done on systems operating in the absence of bridging ligands, particularly for the action of alkynes. A second part is devoted to the presence of ligands, which do not play a significant redox role. A third part concerns the use of redox-active bridging ligands. Many spectrometric characterizations, crystal structures, and theoretical calculations allow focusing this search on the main features that govern the reactivity of one metal center or the

L. Maron (✉)
Laboratoire de Physique et Chimie des Nano-Objets, Institut National des Sciences Appliquées, Toulouse, France
e-mail: laurent.maron@irsamc.ups-tlse.fr

P. Kalck (✉)
Laboratoire de Chimie de Coordination du CNRS, Equipe C "Catalyse et Chimie Fine", composante de l'Ecole Nationale Supérieure des Ingénieurs en Arts Chimiques et Technologiques – INP Toulouse, Toulouse, France
e-mail: philippe.kalck@ensiacet.fr

simultaneous two metal centers in the activation, selectivity, as well as original reactivity of a reactant or an intermediate in a catalytic step.

Keywords Cooperative effect · Dinuclear complexes · Electronic and steric effects of the coordination sphere · One-electron reaction on the metal center · Oxidative addition · Redox-active ligands · Reductive elimination · Synergistic effect

1 Introduction

As the cooperative effect between two metal centers allows gaining more reactivity and higher selectivity than mononuclear complexes in the activation of reactants to perform catalyzed reactions, it is important to conceptualize the guiding principles, which underlie the building of the most adapted precursors. In the present chapter, we will concentrate on the activation of a molecule by which the two metal centers play a similar role in one or several molecular steps of the catalytic reaction. The approach of the reactant usually occurs in the cavity formed by the two metals, especially when appropriate ligands maintain them, with some flexibility, in close proximity, whatever the complex entails a homo- or a hetero-bimetallic framework. Thus, the coordination sphere plays an active and prominent role, especially here, not only to adjust the electron density along all the catalytic steps but also to maintain the appropriate steric effects to guide the approach of the reactants inside the cavity and obtain high selectivity.

In this chapter, we will focus on the concepts that we can extract from the literature to build the dinuclear complexes containing the adapted ligands in order to have activation in which the metal center operates a 1-electron reaction.

2 Mechanisms in Which Each Metal Center Is Involved in a 1e-1e Reaction

2.1 Absence of Bridging Ligands

As early as 1954, the reaction of $[Co_2(CO)_8]$ with acetylenic compounds was shown to substitute two CO ligands to give the $[Co_2(CO)_6(RC \equiv CR)]$ complexes with no loss of the dinuclear entity [1]. The X-ray crystal structure solved for the diphenylacetylene complex indicated that PhC ≡ CPh is coordinated to the two cobalt atoms in a μ-η^2:η^2 mode with their donor–acceptor components, the C–C bond being perpendicular (exactly 88°) to the Co-Co axis [2]. Thus, the two cobalt atoms are nearly in an octahedral environment and the two carbon atoms of the alkyne entity adopt a tetrahedral geometry [3].

Fig. 1 General geometry of the $[Co_2(CO)_6(PhC \equiv CPh)]$ complex

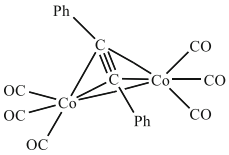

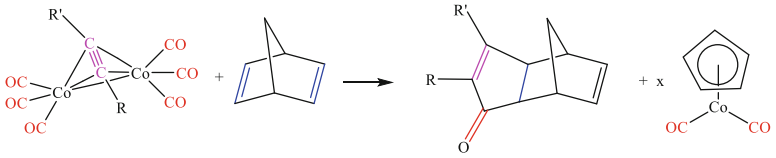

Fig. 2 Stoichiometric reaction of norbornadiene and $[Co_2(CO)_6(RC \equiv CR')]$

Fig. 3 General scope of the Pauson–Khand Reaction, catalyzed by $[Co_2(CO)_8]$

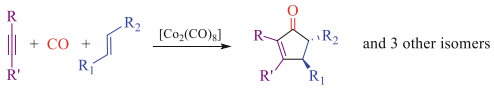

Various alkynes react with $[Co_2(CO)_8]$ to give stable $[Co_2(CO)_6(RC \equiv CR')]$ complexes that adopt the geometry shown in Fig. 1 [3–7]. Pauson and Khand discovered that such complexes stoichiometrically react with norbornadiene to provide the cyclopentenone carbonyl[2.2.1]hept-2-ene and cyclopentadienylcobaltdicarbonyl, presumably arising from the retro Diels–Alder reaction of norbornadiene (Fig. 2) [8–10].

The scope of this [2 + 2 + 1] cycloaddition of an alkyne, an alkene, and carbon monoxide, which is named Pauson–Khand Reaction (PKR) has been largely extended and performed under catalytic conditions [11, 12]. This annulation reaction involves three reactants, the alkyne, an alkene, and one equivalent of carbon monoxide to produce a cyclopentenone (Fig. 3).

Concerning the mechanism of the reaction, many studies [13–16] and DFT calculations [17, 18] have shown that the substitution of a CO ligand by the alkene occurs, followed by the C-C coupling between the two alkyne/alkene entities to produce two Co(I) centers. That means the $RC \equiv CR'$ coordinated in the μ-η^2:η^2 mode into the two cobalt(0) atoms frame and the alkene coordinated to only one cobalt atom react together to generate the Co^I-$CR = CR'$-CR_1-CR_2-Co^I chain with presumably the C=C double bond coordinated to a cobalt metal center (Fig. 4). Then, after the CO migratory insertion, occurring on the CR_2 side, a 1e-1e reductive elimination by coupling of the two CR_2 and CR carbon atoms regenerates a $[Co_2(CO)_4]$ intermediate, that under CO and in the presence of the alkyne provides $[Co_2(CO)_6(RC \equiv CR')]$ to start a new catalytic cycle.

However, even with phosphine ligands, and particularly with ThaxPhos that bridges the two cobalt metal centers (vide infra), the alkyne adopts the same μ-η^2:η^2 coordination mode. It should be noted that under photochemical activation the initial step of the Pauson–Khand reaction involves a high-spin diradical species

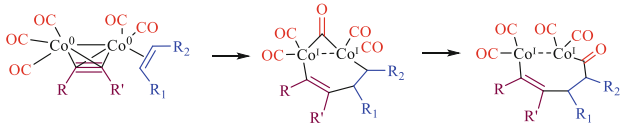

Fig. 4 Coordination of the alkene by substitution of a CO ligand of $[Co_2(CO)_6(RC \equiv CR')]$, C-C coupling, migration of a CO ligand from the $Co(CO)_3$ entity through the bridging position, and migratory CO insertion

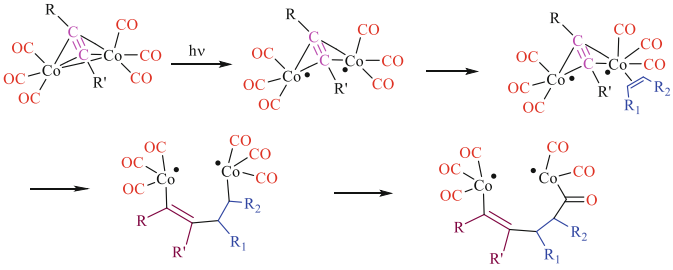

Fig. 5 Biradical species generated by irradiation of the $[Co_2(CO)_6(RC \equiv CR')]$ complex

arising from the homolytic cleavage of the Co–Co bond and not a CO loss (Fig. 5) [19]. Observations by Time-resolved Infrared Spectroscopy and theoretical calculations are in favor that the $[Co_2(CO)_6(RC \equiv CR')]$ complexes produce a triplet diradical which rapidly recombines to regenerate the parent complex [20].

The same $[Co_2(CO)_6(RC \equiv CR')]$ complex reacts with two equivalents of alkyne to provide an arene through successive coordination of one $RC \equiv CR'$ and C-C coupling to produce the cobaltacyclopentadiene $[Co_2(CO)_5(\eta^4,\eta^1\text{-}\mu\text{-}C_4R_2R'_2)]$ intermediate. This species is supposed to be a Co(0)-Co(II) species, in parallel to the [2 + 2 + 2] cycloaddition reactions using mononuclear complexes and giving rise to cyclopentadiene species [21, 22]. It further reacts with the third alkyne molecule to give the substituted benzene [23]. In fact, it has been demonstrated that an intermediate having a bis-allylic structure $[Co_2(CO)_4(\eta^{3,1},\eta^{3,1}\text{-}\mu\text{-}C_3R_3C_3R'_3)]$ is formed during the reaction of the third alkyne, giving rise to two Co(I) metal centers. Then a bent benzene $[Co_2(CO)_4(\text{cis-}(\eta^4,\eta^4\text{-}\mu\text{-}C_3R_3C_3R'_3))]$ structure is produced before the arene is liberated and the $[Co_2(CO)_x(RC \equiv CR')]$ complex is formed and starts again the catalytic cycle [24].

A review, which appeared beginning 2021, analyzes the transition-metal-catalyzed [2 + 2 + 2] cycloaddition reaction with special emphasis on the mechanistic pathway [25]. This review focuses on the addition to the two alkynes of various unsaturated substrates, i.e., alkynes, alkenes, nitriles, isocyanates, isothiocyanates, ketenes, allenes, carbodiimides, carbon dioxide, and carbon disulfide. Most of the reactions involve mononuclear complexes, and in the present part devoted to dinuclear species in the absence of bridging ligands where the reaction takes place, the trimerization of alkynes on di-cobalt complexes has a prominent place. A lot of alkynes bearing various substituents led to numerous $[Co_2(CO)_6(RC \equiv CR')]$

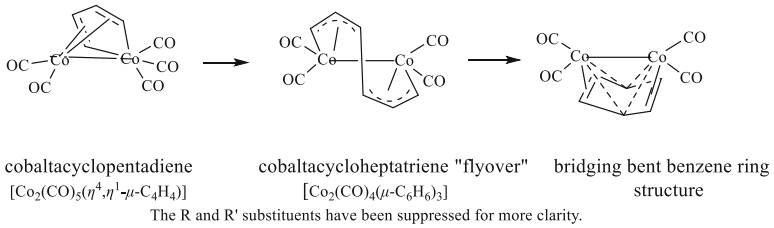

Fig. 6 Three intermediate species for the trimerization of alkynes catalyzed by $[Co_2(CO)_8]$

complexes, which were transformed into the species shown in Fig. 6 and characterized, including X-ray crystal structures. The structure of the cobaltacycloheptatriene $[Co_2(CO)_4(t\text{-}BuC(CH)_4)C\text{-}t\text{-}Bu)]$ complex has been solved as soon as 1964 and the flyover as well as the two allyl moieties proposed [26], after the discovery of the trimerization of alkynes on dicobaltoctacarbonyl, as well as on the mercury adduct $[Co(CO)_4]_2Hg$ [4, 27–32]. Addition of bromine to this di-cobalt(I) complex generates 1,2-di-t-butyl-benzene [32, 33]. The intermediate $[Co_2(CO)_5(\eta^4,\eta^1\text{-}\mu\text{-}R_2C_4R'_2)]$, which results from the reaction of cyclooctyne was characterized by an X-ray crystal structure in 1978 and shows a cyclopentadiene structure [34]. A similar geometry was revealed when N,N-dipropargylmethylamine reacts with $[Co_2(CO)_8]$ to give first at room temperature the complex in which each alkyne triple bond bridges a $Co_2(CO)_6$ entity [35]; then in refluxing toluene the bimetallic cobaltacyclopentadiene complex is formed [36]. Similarly, when the $[Co(CO)_4]^-$/CF_3COOH/$[Fe_2(CO)_9]$ mixture is reacted with phenylacetylene the $[Co_2(CO)_5(\mu^2,\eta^4\text{-}CPhCHCHCPh)]$ complex is produced [37]. Even when electronegative substituents are introduced such as CF_3 and SF_5 the two dicobalt cyclopentadiene and cycloheptatriene can be observed, the X-ray crystal structure of the $[Co_2(CO)_5(\eta^4,\eta^1\text{-}\mu\text{-}(SF_5)CCHCHC(SF_5))]$ complex being similar to that of the cyclooctyne/cyclopentadiene complex [38]. Using asymmetrically substituted alkynes such as 4-phenylbut-3-yn-2-one, the formation of the symmetrically substituted 1,3,5-triphenyltris(acetyl)benzene and the isolation of the cobaltacycloheptatriene, in addition to that of the monoalkyne complex, led to the proposal that the cobaltacyclopentadiene is a short-live intermediate on which the two alkynes have performed a head-to-tail oxidative cyclization after coordination of an alkyne to the monoalkyne complex [39, 40]. The intermediate is the flyover complex, on which the chain between the two cobalt(I) centers is –C(OMe)-PhC=C(OMe)PhC=C(OMe)PhC-, although various examples show that the regioselectivity is highly dependent on the nature of the substituents on the alkyne reagents [40]. Addition of Me_3NO for the reaction of a second alkyne equivalent to the tetrahedrane complex removing a CO equivalent allowed obtaining many cobaltacyclopentadiene complexes [41]. After oxidative coupling of one alkyne to the dicobaltatetrahedrane complex to provide the dicobaltacyclopentadiene complex, the reaction of the third alkyne transforms this intermediate into the flyover complex or, presumably by a direct Diels–Alder addition, to a bridging bent benzene

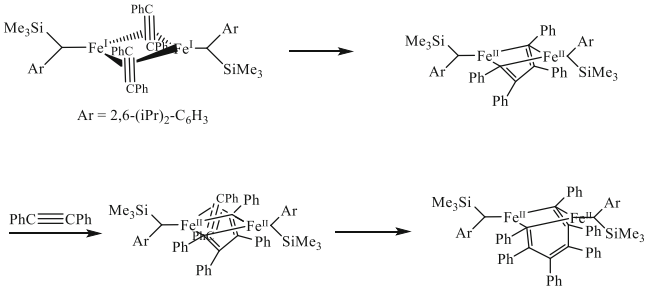

Fig. 7 Coordination of two alkynes in the bridging positions of a Fe^{I}-Fe^{I} framework, followed by their coupling, providing a Fe^{II}-Fe^{II} species, and the coordination and the coupling of a third alkyne substrate

complex [42]. DFT calculations show that for alkynes bearing bulky groups, such as CF_3 or t-Bu, the flyover complex is preferred, whereas for less sterically hindered derivatives, the cis-bent benzene structure is energetically favored [24]. Dinuclear complexes with a metal–metal interaction and bearing unsaturated alkynes, dienes and aromatic compounds have been described for their synthesis, structure, and coordination modes [43].

The bis(N-mesitylimido)pyridine ligands react with $[Co_2(CO)_8]$ to provide the formation of the $[(NNN)Co(\mu\text{-}CO)Co(CO)_4]$ and $[(NNN)Co(\mu\text{-}CO)_2Co(CO)_3]$ complexes and in acetonitrile of the $[(NNN)Co(CH_3CN)_2]^+[Co(CO)_4]^-$ ion-pair. These species catalyze the trimerization of ethyl propiolate, but with a reactivity lower than that of $[Co_2(CO)_8]$ [44].

Similarly, di-*t*-butylacetylene reacts with $[Fe_2(CO)_9]$ and provides the $[Fe_2(CO)_6(t\text{-BuC} \equiv Ct\text{-Bu})]$ complex with the alkyne being in the bridging position perpendicular to the iron–iron bond of 2.316 Å for which an Fe = Fe double bond has been proposed [7]. The $[Fe_2(CO)_4(t\text{-BuC} \equiv Ct\text{-Bu})_2]$ complex, obtained from the reaction of the alkyne with $[Fe_3(CO)_{12}]$, presents a plane containing the four acetylenic carbon atoms perpendicular to the plane formed by the two iron atoms and the four CO ligands [45].

A recent study shows that a dinuclear Fe(I) complex is formed when the [Fe(N(SiMe$_3$)Ar)carbene] complex [46], active in the cyclotrimerization of alkynes, is reacted with an alkyne, Ar being 2,6-diisopropylphenyl and the carbene ligand 1,3-bis(2,6-diisopropylphenyl)imidazolin2-ylidene [47]. The addition of one equivalent of diphenylacetylene with the mononuclear complex affords the $[Fe_2(N(SiMe_3)Ar)_2(\mu,\eta^2\text{-PhCCPh})_2]$ dimer with loss of the carbene ligand.

The X-ray crystal structure of this dinuclear Fe(I) complex revealed that the two metal centers are bridged by two alkynes as shown in Fig. 7. This complex is diamagnetic, presumably due to an antiferromagnetic coupling which could result either from the direct overlap of the metal molecular orbitals or a superexchange occurring through the two alkyne π-systems. Heating this complex to 60°C induces the coupling of the two alkyne ligands to produce the formation of the dimetallacyclopentadiene $[Fe_2(N(SiMe_3)Ar)_2(\mu,\kappa^2\text{-}C_4Ph_4)]$ complex, in which the

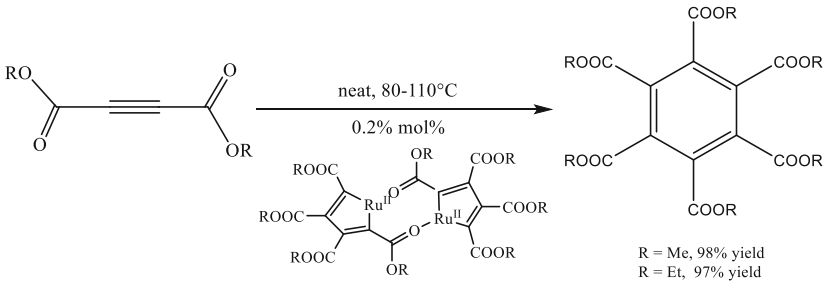

Fig. 8 Trimerization of an alkyne catalyzed by a diruthenium(II) complex

two iron atoms have been oxidized by one electron. The same reaction with diethylacetylene occurs at room temperature to provide the μ,κ^2-C_4Et_4 analogous complex; kinetics of the trimerization reaction showed that the catalysis is first order in $[Fe_2(N(SiMe_3)Ar)_2(\mu,\kappa^2\text{-}C_4Et_4)]$ and first-order dependence on [3-hexyne] in its reaction with the dinuclear complex. DFT calculations confirmed that the dinuclear species are involved in the catalyzed trimerization reaction of alkynes and a mechanism was proposed, as shown in Fig. 7, in which the third alkyne molecule coordinates to the $Fe_2(\mu,\kappa^2\text{-}C_4Et_4)$ framework, presumably after a coordination to a single iron metal center. The bridging alkyne then inserts into the diene to form the dimetallacycloheptatriene $[Fe_2(N(SiMe_3)Ar)_2(\mu,\kappa^2\text{-}C_6Me_6)]$ complex, before to give rise to a ring closure to form $[Fe_2(N(SiMe_3)Ar)_2(\mu,\eta^6\text{-}C_6Me_6)]$, which contains the C_6Me_6 arene moiety sandwiched between the two iron metal centers [47]. The arene is then displaced by the alkynes to start again the catalytic cycle. The Mössbauer data corroborate the formation of a Fe(II)-Fe(II) dimer in which each Fe is equivalent, instead of a mixed-valent Fe(I)-Fe(III) complex.

Among the catalysts that operate with ruthenium, most of them are mononuclear entities [25, 48], a few of them being dinuclear but with a reactivity reduced [49]. Figure 8 shows an example in which the trimerization of dimethyl (or diethyl)acetylene dicarboxylate involves the formation of 1.1.1.8.8.8-hexacarbonyl-3.10-dimethoxy (or diethoxy) -2,9-dioxa-1,8-diruthenatricyclo $[9.6.0.0^{4,8}]$tetradeca-2,4,6,9,11,13-hexaene-5.6.7.12.13.14-hexacarboxylic acid hexa-methyl (or ethyl) ester [49].

Particularly, when the diyne diester reacts with $[Ru_3(CO)_{12}]$ under a 5 atm CO pressure, the dinuclear ruthenacyclopentadiene is formed and its reaction with Me_3NO to produce the tetracarbonyl complex and then with dimethyl acetylene dicarboxylate, the intermediate with the alkyne in bridging position is isolated, as shown in Fig. 9 [50].

The synthesis of the $[Ni_2(\eta^5\text{-}C_5H_5)_2(\mu\text{-}\eta^2\text{:}\eta^2\text{-PhC} \equiv \text{CPh})]$ complex was performed as early as 1959 [51, 52] from $[Ni_2(\eta^5\text{-}C_5H_5)_2(CO)_2]$ [53] and the X-ray crystal structure [54] shows that the bridging diphenylacetylene ligand is almost perpendicular to the Ni^I–Ni^I bond, like in $[Co_2(CO)_6(RC \equiv CR')]$ complexes (vide supra). However, trimerization or polymerization of alkynes is performed with mononuclear Nickel complexes [25, 55]. Similarly, the reactivity of the

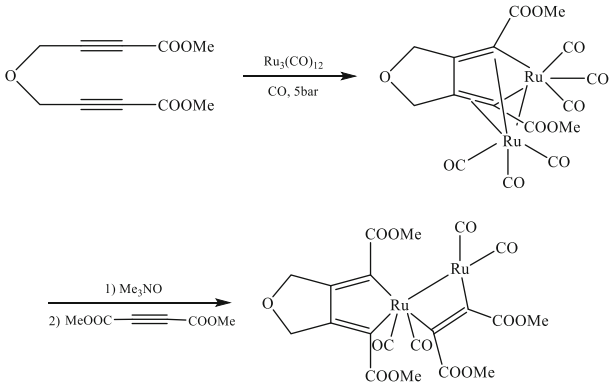

Fig. 9 Formation of a dinuclear ruthenacyclopentadiene complex by reaction of a diyne diester with $[Ru_3(CO)_{12}]$

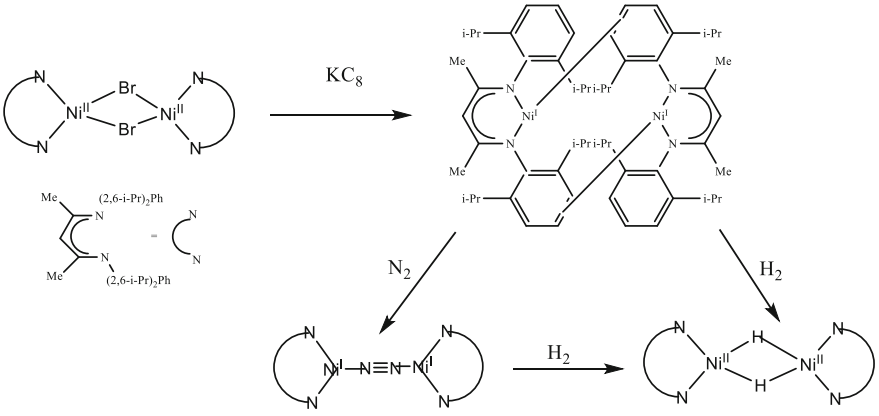

Fig. 10 Synthesis of the β-diketiminate ligand Ni(I) dimer, in which each metal atom binds to an aryl ring of the second (NN)Ni unit, which reacts with N_2 and H_2 at room temperature to produce the $[(NN)Ni^{I}(\mu\text{-}N_2)Ni^{I}(NN)]$ and $[(NN)Ni^{II}(\mu\text{-}H)_2Ni^{II}(NN)]$ complexes

$[Ni_2(\eta^4\text{-}C_8H_{12})_2(\mu\text{-}\eta^2\text{:}\eta^2\text{-PhC} \equiv \text{CPh})]$ Nickel(0) complex is modest to catalyze the cyclotrimerization of diphenylacetylene to hexaphenylbenzene, whereas hydrogenation reactions at room temperature provide cis-diphenylethylene [56].

Interestingly, the use of the bulky bidentate β-diketiminate ligand, as shown in Fig. 10, allows to prepare the dinuclear halide-bridged $[(NN)_2Ni_2(\mu\text{-}X)_2]$ (X = Cl [57], Br [58]). Reduction of this last complex by KC_8 leads to the dinuclear Ni (I) complex in which each Nickel metal center binds to the two β-diketiminato-N atoms and to the double-bond of an aryl ring of the second (NN)Ni unit in a η^2-coordination mode (Fig. 10) [58]. If t-butyl groups replace the methyl substituents on the NN ligand, the steric effect is so large that only the monomeric Ni(I) species is formed. Addition of N_2 to a hexane solution of the dinuclear Ni(I) complex results in

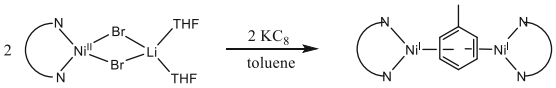

Fig. 11 Reduction of [(NN)Ni(μ-Br)$_2$Li(THF)$_2$] by KC_8 leading to the [(NN)Ni(μ-toluene)Ni(NN)] complex

the precipitation of the dinitrogen [(NN)Ni(μ-N_2)Ni(NN)] complex. Stirring at room temperature of either of these two Ni(I) complexes with one atmosphere of H_2 gives the [(NN)Ni(μ-H)$_2$Ni(NN)] complex (Fig. 10) in which the two metal centers are Ni(II).

Reduction of the [(NN)Ni(μ-Br)$_2$Li(THF)$_2$] complex by a K/Na alloy or MeMgBr in toluene [59] or potassium graphite (KC_8) generates the [(NN)Ni(μ-toluene)Ni(NN)] complex which can be considered as a dinuclear Nickel(II) species in which each metal atom is bonded to toluene in a η^3:η^3 manner reminiscent of two allyl fragments, but also as a dinuclear Nickel(I) complex, since in solution it easily gives (NN)Ni(I) species that are detected by Electron Paramagnetic Resonance (Fig. 11).

This toluene-masked Ni(I) precursor activates N_2O, O_2, to provide the [(NN)-Ni^{II}(μ-OH)$_2$$Ni^{II}$(NN)] complex presumably through [(NN)NiO] and [(NN)Ni(O_2)$^{\cdot}$] intermediate species [60]. Similarly, (μ-η^2:η^2-Se_2) and (μ-η^2:η^2-Te_2) bridges can be built, whereas the neutral P4 ligand bridges the two Ni(I) metal centers in a η^2-fashion. Recently, the dihydride bridged Ni(II) complex has been grafted onto silica, through only the substitution of one H-bridge and its capacity to hydrogenate alkenes and alkynes at room temperature demonstrated [61].

Monomer complexes of early transition metals were reacted with N_2O and CO_2 and shown to provide dimeric(μ-oxo) species involving a one-electron oxidation of the metals and release of N_2 or CO. Thus, the Ti^{II} [(η^5-C_5H_5)$_2$Ti] complex reacts at room temperature with N_2O to generate quantitatively [(η^5-C_5H_5)$_2$$Ti^{III}$($\mu$-O)$Ti^{III}$($\eta^5$-$C_5H_5$)$_2$] [62]. Similarly, [$Cp_2Ti^{III}$($\mu$-Cl)$_2$$Ti^{III}$$Cp_2$] reacts with CO_2 and gives rise to [Cp_2ClTi^{IV}(μ-O)$Ti^{IV}$$ClCp_2$] and CO, presumably through the [Cp_2ClTi^{IV}(μ-η^1,η^1-O-C(O))$Ti^{IV}$$ClCp_2$] intermediate species [63]. The Ti^{II} [$Cp_2Ti(CO)_2$] complex reacts with four equivalents of CO_2 to generate the bridged carbonate [Cp_2Ti^{III}(μ-η^1,η^2-CO_3)$Ti^{III}$$Cp_2$]$_2$ complex, whereas the zirconium [$Cp_2Zr(CO)_2$] analog produces the μ-oxo Zr^{III} [Cp_2Zr(μ-O)]$_3$ trimer.

Uranium(III) complexes have a great potential to activate small molecules and the one-electron oxidation of U(III) to U(IV) is very easy. Thus, the reactivity of CS_2 with [(η^5-MeC_5H_4)$_3$$U^{III}$(THF)] and [($\eta^5$-$Me_3SiC_5H_4$)$_3$$U^{III}$] results in the formation of the [Cp′$_3$$U^{IV}$($\mu$-$\eta^1$,$\eta^2$-$CS_2$)$U^{IV}$Cp′$_3$] dimer. This reaction is to be considered as the two-electron reduction of carbon disulfide by Uranium into CS_2^{2-} [64]. Similarly, $SPPh_3$, $SePPh_3$, and $TePPh_3$ react with [(η^5-MeC_5H_4)$_3$$U^{III}$(THF)] to form the bridging chalcogenide U^{IV} complexes [65]. In addition, the [(η^5-$Me_3SiC_5H_4$)$_3$$U^{III}$] complex reacts under normal conditions with CO_2 and N_2O to generate the μ-oxo complex [Cp′$_3$$U^{IV}$($\mu$-O)$U^{IV}$Cp′$_3$] [66]. More recently, the pre-ligand shown in Fig. 12 has been synthesized to coordinate three oxygen atoms to uranium(III) metal center and is similar to 1,4,7-tris(3,5-di-*tert*-butyl-2-hydroxybenzylate)1,4,7-

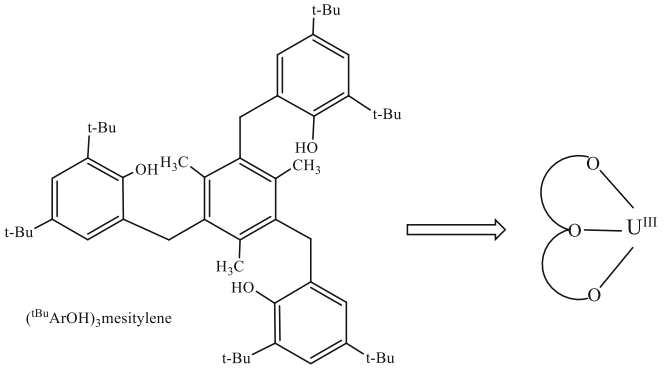

Fig. 12 (1,3,5-trimethyl-2,4,6-tris(2,4-di-*tert*-butylphenol)methyl)benzene, that generates the tripodal ligand, and representation of the corresponding U^{III} complex

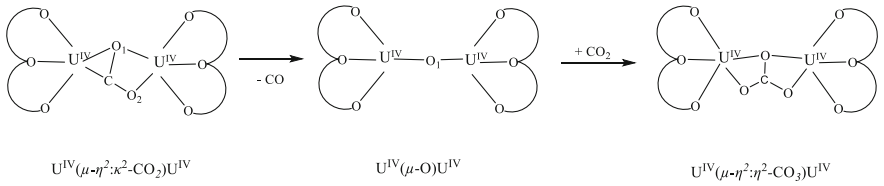

Fig. 13 Simplified pathway to show the coordination of CO_2 in the bridging position of two U^{IV} fragments, the loss of CO to produce a μ-oxo complex and then the reaction with CO_2 to form a bridging carbonate ligand

triazacyclononane which reacted with CO_2 to produce the μ-oxo bridged $[U^{IV}](\mu\text{-O})[U^{IV}]$ complex [67].

The mechanism of the CO_2 activation by U(III) complexes has been solved on the $(^{tBu}ArOH)_3$mesitylene ligand by using DFT calculations and substituting the *tert*-butyl substituents with methyl groups to simplify the calculations [68]. In a first step two U(III) species react with one equivalent of CO_2 to provide a dinuclear complex with the $U^{IV}(\mu\text{-}\eta^2\text{-}\kappa^2\text{-}CO_2)U^{IV}$ framework (Fig. 13) which can be considered as two $[(^{R}ArO)_3mes)U^{IV}]$ cationic fragments bonded to the CO_2^{2-} ligand. This complex forms a μ-oxo complex through the loss of a CO ligand and its formation is exergonic by 12.8 kcal/mol. Then, the $[U^{IV}(\mu\text{-}\eta^2\text{-}\eta^2\text{-}CO_3)U^{IV}]$ complex can be formed through a highly exergonic (−54.9 kcal/mol) irreversible pathway [68].

Similarly, Samarium(II) and Thulium(II), as Lanthanide(II) complexes can activate CO_2 in a $1e^-$ process on each metal atom of the dimer. The $[(\eta^5\text{-}C_5Me_5)_2Sm]$ complex reacts with CO_2 and DFT calculations have shown that the dinuclear Sm(II) $[Cp^*_2Sm(\mu\text{-}\eta^1\text{-}\eta^1\text{-}O{=}C{=}O)SmCp^*_2]$ adduct is produced [69]. Then a first electron transfer leads to the $[Cp^*_2Sm^{II}(\mu\text{-}\kappa^1\text{-}\eta^2\text{-}O{=}C^{\bullet} = O)Sm^{III}Cp^*_2]$ transient* species, immediately followed by the second electron transfer to provide the $[Cp^*_2Sm^{III}((\mu\text{-}\eta^2\text{-}\kappa^2\text{-}CO_2)Sm^{III}Cp^*_2)]$ complex, analogous to the $[U^{IV}(\mu\text{-}\eta^2\text{-}\kappa^2\text{-}CO_2)U^{IV}]$ complex shown on Fig. 13. This two-electron transfer reduction mechanism

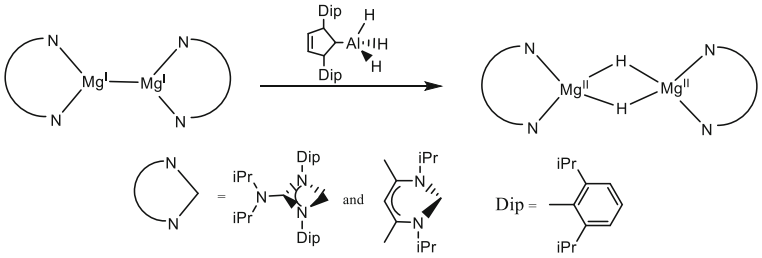

Fig. 14 Synthesis of dimagnesium(I) complexes and their reduction into di(μ-hydrido) dimagnesium(II) complexes

appears to be an easy process due to a maximum in electronic energy calculated to be 5 kcal mol^{-1}.

According to recent papers, it is interesting to mention Magnesium(I) dimers whose synthesis as stable compounds was reported in 2007, due to the introduction of bulky guanidinate and β-diketiminate L ligands (Fig. 14) [70]. Starting from [$LMg(\mu\text{-}I)_2Mg(OEt_2)L$] or [$MgI(OEt_2)L$], the reduction with an excess of potassium in toluene leads to the formation of the [$LMg^{I}\text{-}Mg^{I}L$] crystalline complexes. DFT calculations show that the Mg-Mg single covalent bond presents a high s-character and the molecule can be viewed as an anion-stabilized Mg^{2+} unit. High-resolution X-ray diffraction data on the β-diketiminate L-containing complex and theoretical calculations are consistent with a non-nuclear local maximum in the electron density, so that the Mg-Mg entity is bound by two Mg^{-} "pseudo-atom" bonds [71].

These Magnesium(I) dimers act as facile two-center/two-electron reductants toward the substrate. The [$LMg^{I}\text{-}Mg^{I}L$] complex reacts with N_2O to give the μ-oxo [$LMg^{II}\text{-}O\text{-}Mg^{II}L$] species which is reactive toward CO_2 to produce the μ-carbonato [$LMg^{II}\text{-}CO_3\text{-}Mg^{II}L$] bridging ligand [72], in a similar pathway to the Uranium and Lanthanide complexes (vide supra).

Moreover, the CyN=C=NCy carbodiimide [70], PhN=NPh azobenzene [73], cyclooctatetraene substrates, in the presence of tetrahydrofurane [73] or anthracene (not shown) [74], and AdN_3 1-adamantyl azide [75], are inserted into the Mg–Mg bond, leading to the dinuclear Mg(II) complexes shown in Fig. 15. Thus, due to the presence of bulky ligands, the dinuclear dimagnesium(I) complexes, which are thermally stable, appear as stoichiometric, selective, and safe reducing agents [76].

Using superbulky ligand by replacement of isopropyl- for 3-pentyl groups still produces the dimeric Mg(I) complex with a long Mg–Mg bond of 3.0513 (8) Å [77]. The even bulkier ligand L* $HC(C(t\text{Bu})N[2,6\text{-}(3\text{-pentyl})\text{-phenyl}])_2$ provides again a Mg(I)-Mg(I) dimer, but on one Mg(I) center the β-diketiminate ligand is bidentate, whereas on the other Mg(I) center only one Nitrogen atom is coordinated [78].

Similar complexes of calcium(I) have been prepared, but react very quickly in methyl-cyclohexane with N_2, introduced to maintain an inert atmosphere, to give a dinuclear Ca^{II} complex with a side-on bridging N_2^{2-} anion, whereas in benzene the

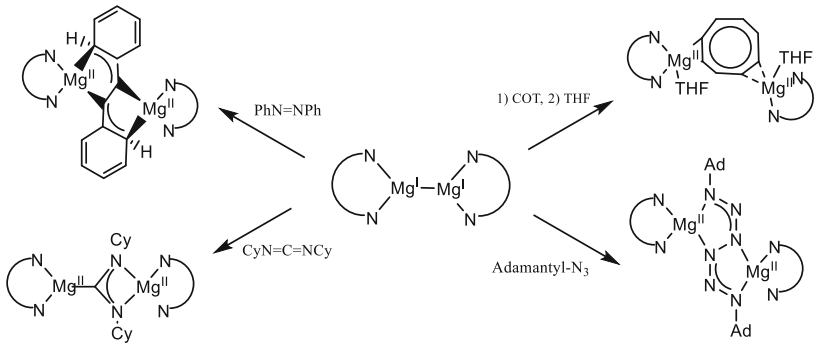

Fig. 15 Two-electron reduction of representative substrates by [LMg^{I}-$Mg^{I}L$] complexes

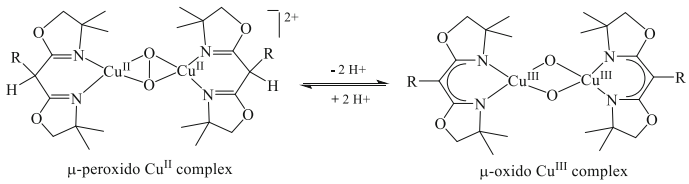

Fig. 16 Mediated interconversion between the [$Cu^{II}(\mu\text{-}\eta^2\text{-}\eta^2$-peroxido)$Cu^{II}$] and [$Cu^{III}(\mu$-oxido)$Cu^{II}$] complexes containing the bis(oxazoline) ligand (R = H, Me) and whose deprotonation gives the imino enamine tautomer

[L*Ca^{I}-Ca^{I}L*] complex produces [L*$Ca^{II}(\mu\text{-}C_6H_6)Ca^{II}$L*] containing the non-planar $C_6H_6^{2-}$ anion [79].

Recently, chiral β-diketeneiminate and amidinate have been introduced in the coordination sphere of the Mg(I)-Mg(I) framework, and first examples of enantiopure [L*Mg^{I}-Mg^{I}L*] complexes have been synthesized. Interestingly the bulky [^{t}BuC(NC_6H_2($C(H)Ph_2$)$_2$Me-2,6,4)(N-(*S*)-(−)-CHMePh)]H, L*H, ligand reacts at 60°C with $Mg^{n}Bu_2$ to provide L*Mg^{n}Bu and then, still at 60°C, with $PhSiH_3$ to generate the μ-hydrido [L*$Mg^{II}(\mu\text{-}H)_2Mg^{II}$L*] complex in 95% yield [80]. Its recrystallization from THF introduces two solvent molecules, one on each Mg^{II} center, [L*(THF)$Mg^{II}(\mu\text{-}H)_2Mg^{II}$(THF)L*], and the X-ray crystal structure reveals that the (*S*) configuration is maintained.

In the field of metalloproteins where histidine imidazole ligands are used for tuning the redox potentials and electronic structures of the metallocofactors through protonation/deprotonation, we can mention the use of bis(oxazoline) capping ligands (Fig. 16) [81]. They are proton-responsive ligands. The [(BOX)(THF)$Cu^{II}(\mu\text{-}\eta^2\text{:}\eta^2$-$O_2$)$Cu^{II}$(THF)(BOX)][$ClO_4$]$_2$ μ-peroxido complex is obtained by oxygenation of [(BOX)Cu(MeCN)][ClO_4] at 193 K in THF. The $\pi^*O_2^{2-}$ orbital is bonded to the two $Cu^{II}d_{xy}$ orbitals, and there is a strong antiferromagnetic coupling (S = 0) between the two cupric ions. Deprotonation of the complex with 1,8-diazabicyclo [5.4.0]undec-7-ene leads to the [(BOX)$Cu^{III}(\mu\text{-}O)_2Cu^{III}$(BOX)] complex containing

the $[BOX]^-$ ligand and the bis(μ-oxido) bridging atoms. Reprotonation by $[HBOX]^+$ can give the μ-peroxido complex.

2.2 *Bimetallic Complexes with Redox Innocent Bridging Ligands*

In the current synthesis environment for having a convenient access to chiral compounds in fine chemistry, many transition metal complexes bearing chiral ligands have been explored to catalyze such reactions [82]. In a first approach, the Pauson–Khand reaction involved mononuclear rhodium or iridium complexes bearing BINAP ligands to synthesize bicyclic cyclopentenones in an intramolecular mode [83–85]. The addition of (*R*)-BINAP to the $[Co_2(CO)_6(HC \equiv C\text{-t-Bu})]$ complex in refluxing THF was shown to produce the $[Co_2(CO)_6[(R)\text{-BINAP}](HC \equiv C\text{-t-Bu})]$ complex as a single diastereoisomer. The X-ray crystal structure revealed the presence of a bridged cobalt alkyne species with the two phosphorus atoms occupying basal positions, *anti* with regard to the t-Bu substituent (Fig. 17) [86]. Similar basal bridged complexes are obtained with the bis(diphenylphosphino)methane or -ethane, whereas bis(diphenylphosphino)butane, with a larger bite angle, occupies the two apical positions. The (*R*)-BINAP, dppm and dppe complexes were tested in the intermolecular [2 + 2 + 1] enantioselective cycloaddition of the 3,3-dimethylbutyne, norbornene and carbon monoxide reactants. They are not reactive in refluxing THF or toluene, even at room temperature in the presence of an excess of *N*-methylmorpholine *N*-oxide to remove one CO ligand, and open a coordination position to the alkene bond [86].

The two phosphorus atoms and the *t*-butyl group of the single diastereoisomer are in *anti*-positions so that, even by removing a CO ligand, the coordination of the C=C double bond of norbornene does not occur, due to steric hindrance.

Starting from (+)- or (−)-*cis*-1-amino-2-indanol, and introducing first the *t*-BuP and then the PR_2 phosphine ligands, leads to the ThaxPHOS ligand, represented in Fig. 18. As shown by an X-ray crystal structure for R = pyrrolyl, the dicobalt

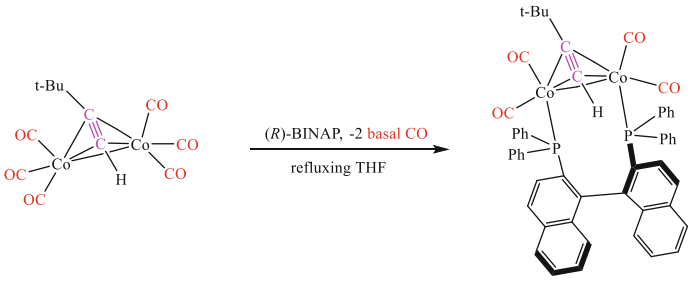

Fig. 17 Synthesis of the $[Co_2(CO)_4[(R)\text{-BINAP}](HC \equiv C\text{-t-Bu})]$ complex by the addition of the (*R*)-BINAP ligand to $[Co_2(CO)_6(HC \equiv C\text{-t-Bu})]$ at 60°C for several hours

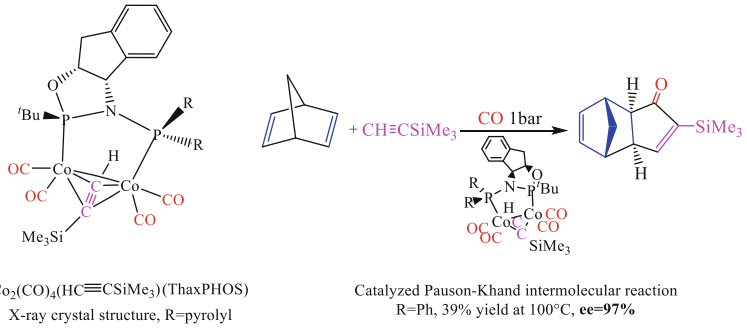

Fig. 18 Intermolecular PKR catalysis with a high enantiomeric excess using the $[Co_2(CO)_4(SiMe_3acetylene)(ThaxPHOS)]$ complex in which the diphosphine ligand is bridging the two Cobalt metal centers

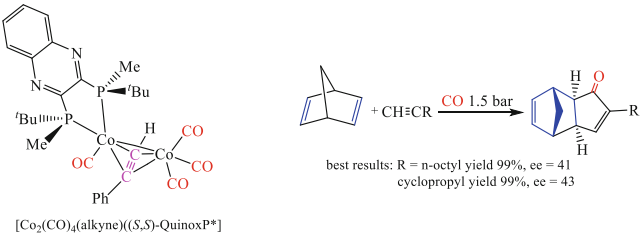

Fig. 19 Structure of the most stable stereoisomer of $[Co_2(CO)_4[(S,S)\text{-QuinoxP*}](HC \equiv CR)]$, and X-ray crystal structure of the ax-eq$_{trans}$ diastereoisomer (R = Ph)

complexes resulting from the addition of this ligand to the $[Co_2(CO)_6(alkyne)]$ precursor present the two phosphorus atoms in the apical positions, the ligand being in a bridging position [87]. The synthesis of chiral cyclopentenones via [2 + 2 + 1] enantioselective cycloaddition of an alkyne, an alkene and carbon monoxide occurs through a similar 1e-1e mechanism. The reaction can be extended to several acetylenes bearing phenyl, n-butyl groups, but with a poor diastereoselectivity; similarly, the steric hindrance induced by the two R groups should be not too high, as for R = iPr for which the yield is 10% but the ee is only 1%.

Introduction of the chiral (*S*,*S*) QuinoxP* diphosphine less basic ligand [88], with two more nearby phosphorus atoms, in the dinuclear cobalt coordination sphere (Fig. 19), results in a chelated mode on only one Cobalt center [89]. The X-ray crystal structure of the major diastereoisomer of $[Co_2(CO)_4[(S,S)\text{-QuinoxP*}](HC \equiv CPh)]$ shows that one phosphorus atom occupies the apical (or axial) position and the second one a basal (equatorial) position on the same Cobalt metal center, and that the *t*-Bu group on this second P atom is *trans* to the phenyl group of HC ≡ CPh. DFT calculations showed that this ax-eq$_{trans}$ diastereoisomer is 11.4 kcal/mol more stable than the bridged complex, and 3.2 kcal/mol than the ax-eq$_{cis}$ other

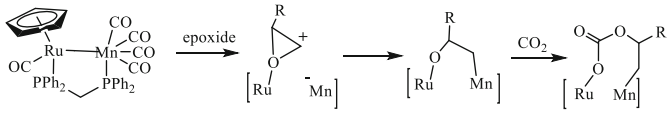

Fig. 20 Reactivity of the $[(\eta^5\text{-}C_5H_5)(CO)Ru^I(\mu\text{-}Ph_2PCH_2PPh_2)Mn^0(CO)_4]$ complex with an epoxide and CO_2 to synthesize a cyclic carbonate, main intermediates of the catalysis

diastereoisomer with which a low-energy fluxional interconversion can occur, that explains the rather modest ee observed in catalysis.

Presumably, as the BINAP ligand in the $[Co_2(CO)_6[(R)\text{-BINAP}](HC \equiv Ct\text{-}Bu)]$ complex was identified to coordinate the two Cobalt metal centers in a bridging mode and to have no reactivity in the Pauson–Khand reaction [86], the first observations of a reactivity of this chiral ligand, as well as similar ligands, with $[Co_2(CO)_6]$ to catalyze the intramolecular reaction with modest to high enantiomeric excesses [90–93], it is of interest to refer to the complete investigation showing that the coordination of BINAP results in the chelating mode leading to efficient catalysts to obtain cyclopentenones with ee as high as 88% [94].

There is still the 1e-1e process for the Pauson–Khand reaction, and according to the electronic effects and the bite angle of the bidentate ligand, as well as the nature of the substituents on the substrates, various yields and ee's are observed. Probably, in the bridging configuration, the chiral phosphorus atom exerts a significant influence on the C-C* coupling of norbornene. The enantioselective cobalt-catalyzed reactions have been reviewed, showing that this metal allows to efficiently give access to chiral compounds under relatively mild conditions [95–100].

The heterobimetallic Ruthenium–Manganese complex bridged by the bis (diphenylphosphino)methane ligand is able to open an epoxide on the two metal centers, and after migratory insertion of CO_2 into the Ru–O bond to produce, after reductive elimination from the dinuclear framework, the cyclic carbonate [101]. Theoretical calculations support the pathway in which the Ru^I-Mn^0 metal–metal bond is cleaved when the epoxide coordinates the Ru center providing a Ru^{II}-Mn^{-I} entity. The oxidative addition occurs on the two metal centers, and then the migratory CO_2 insertion happens into the Ru–O bond. Finally, the reductive elimination of the carbonate, still involving the two metal centers regenerates the active Ru^I-Mn^0 species (Fig. 20).

With such a polarization of the dinuclear entity, a Lewis acidic Ru center, which coordinates the epoxide, is associated to the nucleophilic Mn center. A similar thioether-triphenolate di-iron(III) complex, which is air-stable and easy to handle, and in which the two Iron are Lewis acidic centers, is active for the reaction of propyleneoxide with CO_2 to selectively give rise to the cyclic carbonate; however, in the absence of a co-catalyst such as tetrabutylammonium bromide, catalysis does not occur [102].

The diamagnetic Zr(III)-Ru(I) $[ZrCl(\mu\text{-}\eta^5\text{:}\eta^1\text{-}C_5H_4PEt_2)_2RuCp^*]$ complex, shown in Fig. 21, has a short interatomic distance between the two metal centers of 2.8620 (10) Å, that is in agreement with a single metal–metal bond [103]. The

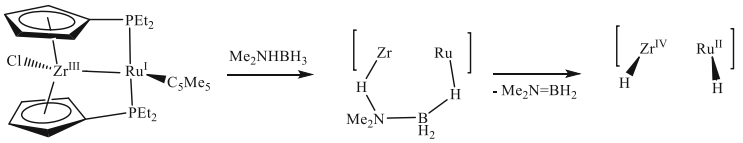

Fig. 21 Main intermediates for the catalytic dehydrogenation of $Me_2NH{\cdot}BH_3$ on the $[ZrCl(\mu\text{-}\eta^5{:}\eta^1\text{-}C_5H_4PEt_2)_2RuCp^*]$ complex

same situation prevails for Hf^{III}-Ru^I and Zr^{III}-Fe^I, all obtained by reduction ($LiBHEt_3$ or KC_8) of the $[MCl_2(\mu\text{-}\eta^5{:}\eta^1\text{-}C_5H_4PEt_2)_2M'ClCp^*]$ complexes. The catalytic dehydrogenation of dimethylamine-borane, $Me_2NH{\cdot}BH_3$, involves the simultaneous approach of the reactant through two hydrogen atoms, before producing a dihydride species (Fig. 21). Then, H_2 gas evolution occurs to come back to the active M^{III}-M'^I complex, through a bimetallic reductive elimination.

Starting from $[Cp^*ClRu^{II}(\mu_2\text{-}Me_2P\text{-}PMe_2)_2Ru^{II}ClCp^*]$ ($Cp^* = C_5Me_5$), the addition of one equivalent of silver trifluoromethane sulfonate, AgOTf, provides the monocationic monochloride-bridged complex $[Cp^*ClRu^{III}(\mu_2\text{-}Cl)(\mu_2\text{-}Me_2P\text{-}PMe_2)_2Ru^{III}Cp^*]^+OTf^-$; the addition of two equivalents of AgOTf leads to the μ-chloro dicationic complex $[Cp^*ClRu^{III}(\mu_2\text{-}Cl)(\mu_2\text{-}Me_2P\text{-}PMe_2)_2Ru^{III}Cp^*]^{2+}(\text{-}OTf^-)_2$ [104]. With the tetraphenylphosphine ligand, the synthesized complex is $[Cp^*Ru^{II}(\mu_2\text{-}Cl)_2(\mu_2\text{-}Ph_2P\text{-}PPh_2)Ru^{II}Cp^*]$, and two equivalents of AgOTf are necessary, leading to the abstraction of two electrons on the metal centers, to give $[Cp^*Ru^{II}(\mu_2\text{-}Cl)_2(\mu_2\text{-}Ph_2P\text{-}PPh_2)Ru^{II}Cp^*]^{2+}(OTf^-)_2$. No ruthenium–ruthenium bonds are observed in any of these complexes.

Using bulky ligands, such as $2,6\text{-}(C_6H_3\text{-}2,6\text{-}i\text{-}Pr_2)_2C_6H_3$, the dimeric Cr (I) complex [ArCrCrAr] has been synthesized, and the interaction between the two d^5 metal centers, represented as a quintuple metal–metal bond, results in a very short 1.8351 (4) Å Cr-Cr distance [105]. Similarly, the dimeric Mo-Mo $[Mo_2(\mu\text{-}\eta^2\text{-}RC(N\text{-}2,6\text{-}iPr_2C_6H_3)_2]_2$ complexes, containing d^5 Mo(I) centers, can be prepared using the amidinato ligands (R = H or Ph). The 1σ, 2π and 2δ interactions between the two Molybdenum centers result in the very short 2.02 Å distance [106].

The complex shown in Fig. 22 contains two aminopyridinato ligands with bulky substituents that maintain the dinuclear structure in which the two Chromium metal centers share a quintuple metal–metal bond [107, 108]. The addition of a terminal alkyne (one equivalent or even an excess) leads to the dimetallacyclobutene, in which there is formally a quadruple Cr–Cr bond and a C=C double bond resulting from the [2 + 2] cycloaddition of the terminal alkyne [109, 110].

Starting from the $[Cr(\mu\text{-}HC(N\text{-}2,6\text{-}iPr_2C_6H_3)_2]_2$ complex, the addition of three equivalents of trimethylsilyl alkyne allowed to synthesize the dichromium complex with a $1,3,5\text{-}(SiMe_3)_3C_6H_3$ aromatic bridging molecule in a η^6,η^6 mode (Fig. 22) [111]. DFT calculations show clearly that three unpaired spins on each chromium center are coupled in a ferromagnetic mode, and that each Cr atom has a +1.52 charge and the benzene bridging ligand −1.03, presumably due to the presence of the three $SiMe_3$ substituents. Further addition of trimethylsilyl alkyne regenerates

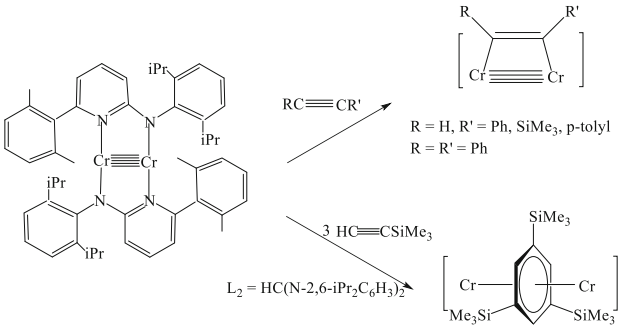

Fig. 22 [2 + 2] and [2 + 2 + 2] cycloadditions of alkynes to di(μ-amidinato)Cr_2 complexes

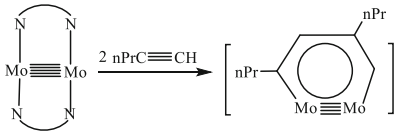

Fig. 23 Isolation of the quadruply bonded Mo^{II}-Mo^{II} complex resulting from the [2 + 2 + 2] cycloaddition of 2 mol of pentyne to the $[Mo^{I}_2(\mu\text{-}\kappa^2\text{-RC(N-2,6-iPr}_2C_6H_3)_2)_2]$ amidinate (R = H, Ph) complex

the initial Cr_2 complex with its quintuple metal–metal bond and liberates the 1,3,5-$(SiMe_3)_3C_6H_3$ benzene compound. Interestingly, the quintuply Molybdenum-Molydenum complex bearing bridging amidinates ligands, reacts with two equivalents of the pentyne reactant, leading to a [2 + 2 + 2] cycloaddition, and the formation of a quadruply Mo-Mo complex, $[Mo_2(\mu\text{-}\kappa^1\text{:}\kappa^1\text{-1,3-nPrC}_4H_2)\text{-}(\mu\text{-}\kappa^2\text{-RC(N-2,6-iPr}_2C_6H_3)_2)_2]$ with two Mo-C σ bonds (Fig. 23) [112].

These isolated complexes for which the X-Ray crystal structure has been determined, show the steps of the trimerization of alkynes to synthesize tri-substituted compounds, even if the second addition has been supposed to involve a cyclobutadiene intermediate.

The Zr-Rh and Zr-Ir complexes $[(CH_3)Zr(\mu\text{-}C_5H_4PR_2)_2Rh(CO)(PPh_3)]$ [113, 114] and $[(CH_3)Zr(\mu\text{-}C_5H_4PR_2)_2Ir(CO)(PPh_3)]$ [115] have been prepared and associate a Zr(III) metal center with a Rh(0) or a Ir(0) entity. Reaction of isopropylalcohol at 0°C occurs through an oxidative addition providing an i-PrO substituent on Zr and a hydrido ligand on Rh, with the formation of a Zr^{IV}-Rh^{I} complex with no more metal–metal bond. Heating to room temperature induces the reductive elimination of methane and restores a Zr^{III}-Rh^{0} complex in which the $O^{i}Pr$ ligand has substituted the CH_3 ligand of the initial complex (Fig. 24).

In CH_2Cl_2 the starting complex is not stable (R = *i*-Pr, Cy) and loses the PPh_3 ligand, so that the methyl group comes in the bridging position before reacting with the CO ligand in a migratory insertion step to form an acetyl group σ-bonded to Rhodium and π-bonded to Zirconium. This intermediate species reacts with CH_2Cl_2

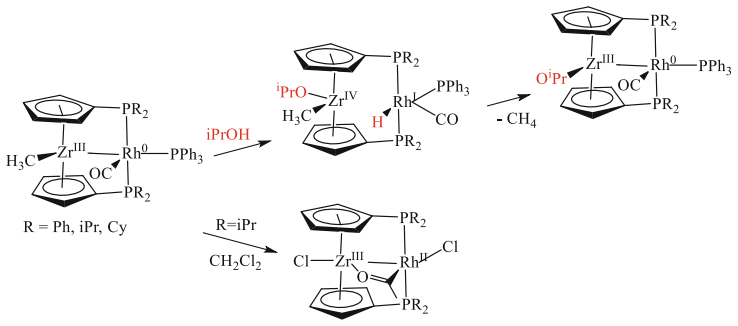

Fig. 24 Oxidative addition of iso-propanol on the two Zr^{III} and Rh^0 metal centers of the complex, followed by a two metal centers reductive elimination of CH_4 from the Zr^{IV}-Rh^I intermediate to produce $[(O^iPr)Zr(\mu\text{-}C_5H_4PR_2)_2Rh(CO)(PPh_3)]$

to form the dichloro complex shown in Fig. 24, which associates the Zr^{III}-Rh^{II} entities [114, 116].

2.3 *Redox Active Bridging Ligands*

In addition to the modification of the metal coordination sphere from both an electronic and steric effect, and the cooperativity between the two metal centers, the use of redox-active ligands allows to maintain the oxidation states of the metals through changes in the electronic configuration, which occurs on them. Thus, reversible transfers of 1–3 electrons with the metal can allow to elaborate highly active catalysts, especially using metals from the first line, particularly Iron, Cobalt, or Nickel [117].

For instance, the use of the dinucleating ligand containing two iminopyridine units maintained with a xanthene linker keeps the two Nickel metal centers at 2.451 Å when a diphenylacetylene substrate is bridging them, and a Ni^I–Ni^I bond is present; DFT calculations suggest they are antiferromagnetically coupled (Fig. 25) [118]. The addition of one equivalent of ethylprop-2-ynoate substitutes diphenylacetylene and the resulting complex adopts the same structure. Provided non-coordinative solvents are used the first complex catalyzes the cyclotrimerisation of phenylacetylene, ethylprop-2-ynoate, but due to some flexibility of the ligand the distance between the two metal centers can increase, resulting in the cyclotetramerization.

The naphthyridine diimine ligand is rigid and its extended π-system allows to build the $[Ni_2(\mu\text{-}\eta^2\text{:}\eta^2\text{-}C_6H_6)(^{iPr}NDI)]$ complex in which the two Ni^I metal atoms are coordinated by the four Nitrogen atoms of the 1,1′-(1,8-naphthyridine-2,7-diyl)bis(*N*-2,6-diisopropylphenyl)ethan-1-imine platform bearing the two terminal $(i\text{-}Pr)_2$-phenyl bulky substituents (Fig. 26) [119]. As shown by the X-ray crystal structure

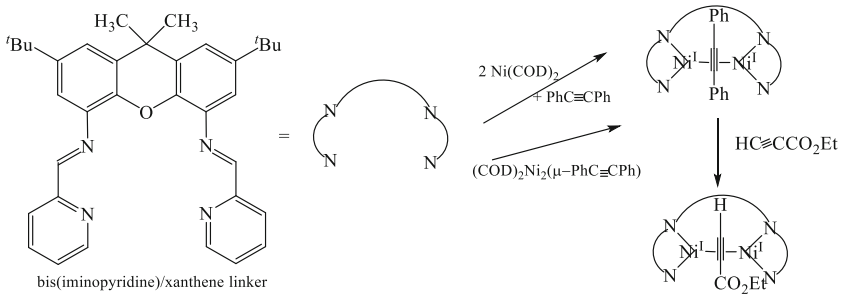

Fig. 25 Synthesis of dinuclear xanthene-bridged bis(iminopyridine) di-Nickel complexes bridged by diphenylacetylene or ethylprop-2-ynoate

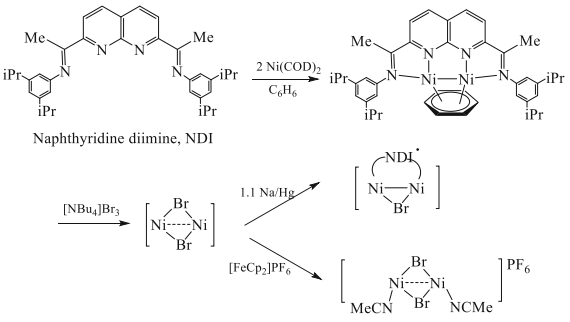

Fig. 26 Oxidation of the $[Ni_2(\mu\text{-}\eta^2\text{:}\eta^2\text{-}C_6H_6)(^{iPr}NDI)]$ complex

the Ni-Ni distance is 2.496 (1) Å, and DFT calculations are consistent with Ni^I metal centers and a $(^{iPr}NDI)^{2-}$ oxidation state for the ligand.

The S = 0 $[Ni_2(\mu\text{-}\eta^2\text{:}\eta^2\text{-}C_6H_6)(^{iPr}NDI)]$ complex can be oxidized by $[NBu_4]Br_3$ to give the S = 1 $[Ni_2(\mu\text{-}Br)_2(^{iPr}NDI)]$ species that reacts with 1.1 equivalent of sodium amalgam to produce the S = 1/2 $[Ni_2(\mu\text{-}Br)(^{iPr}NDI^{\cdot})]$ complex in which the NDI ligand has a significant radical character. The dibromo complex can be oxidized in acetonitrile with $[FeCp_2][PF_6]$ to give the S = 3/2 $[Ni_2(\mu\text{-}Br)_2(^{iPr}NDI)(CH_3CN)_2]^+$ cationic species. The initial complex can be reduced in THF by KC_8 to generate the S = 1/2 anionic $[Ni_2(\mu\text{-}\eta^2\text{:}\eta^2\text{-}C_6H_6)(K^+(THF)_3)(^{iPr}NDI)]^{1-}$ entity. The two metal centers are in close contact and move from 2.496 Å in the starting complex, to 2.5316 and 2.5399 Å (2 molecules in the asymmetric unit) for the $(\mu\text{-}Br)_2$ complex, 2.378 Å in the $(\mu\text{-}Br)$ radical species, so that the two Ni metal atoms are close to be Ni(I). For the most reduced complex, the Ni-Ni platform gains one electron, whereas in the most oxidized situation, it loses one electron. Thus, these examples are clearly indicative of the redox role of the ^{iPr}NDI ligand [119].

The Ph_2SiH_2 and Et_2SiH_2 silanes present a dinuclear mode of activation on the $[Ni_2(\mu\text{-}\eta^2\text{:}\eta^2\text{-}C_6H_6)(^{iPr}NDI)]$ complex to provide a symmetric coordination adduct with μ-H atoms nearly equidistant between the Ni and Si atoms (Fig. 27). This situation is not yet the $\mu\text{-}SiR_2$ silylene dihydride which would result from the double oxidative addition on the Ni-Ni template, and DFT calculations are consistent with a

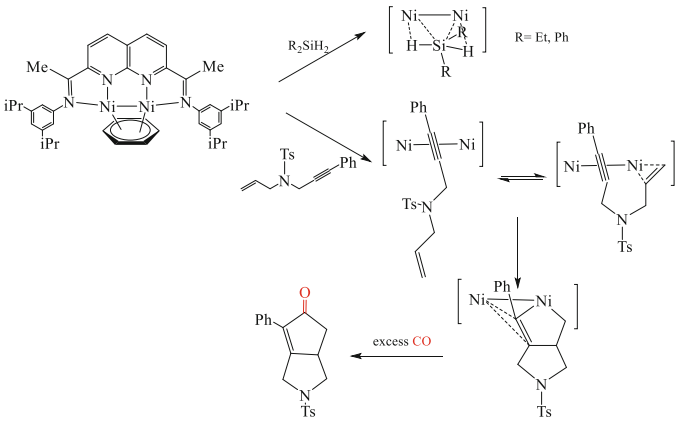

Fig. 27 Silane adduct with the [$Ni_2(\mu\text{-}\eta^2\text{:}\eta^2\text{-}C_6H_6)(^{iPr}NDI)$] complex. Metallacycle intermediate with a stabilizing Ni-π interaction of the C=C bond

$[NDI]^{2-}$ situation [120]. The starting complex catalyzes the hydrosilylation of alkenes, alkynes, and various C=O double bonds.

The [$Ni_2(\mu\text{-}\eta^2\text{:}\eta^2\text{-}C_6H_6)(^{iPr}NDI)$] complex reacting with the enyne shown in Fig. 27 leads to a mixture of transient adducts, one with the alkyne moiety coordinated in the bridging position and the second one with the alkyne and alkene moieties coordinated, both species being in equilibrium. They convert at room temperature to the nickellacyclopentene complex in which the C=C bond presents an η^2-interaction with the second Ni atom, as shown by the X-ray crystal structure and DFT calculations, so that this step can be formulated as a redox-neutral migratory insertion [121]. Introducing a CO atmosphere on this complex leads to the terminal cyclopentenone product of the [2 + 2 + 1] Pauson–Khand reaction.

The same precursor [$Ni_2(\mu\text{-}\eta^2\text{:}\eta^2\text{-}C_6H_6)(^{iPr}NDI)$] can be used to perform the highly selective [4 + 1]-cycloaddition of vinylidenes, generated from 1,1-dichloroalkenes, to dienes providing cyclopentenes [122]. The reaction needs Zn as a stoichiometric reductant, and in fact, the active species is the [$Ni_2(\mu\text{-Cl})(^{iPr}NDI^{\cdot})$] complex (Fig. 28). The mechanism involves oxidative addition, coordination of the diene, migratory insertion, and reductive elimination on the Ni-Ni core in which the two metals stabilize the π-systems of both the vinylidene and diene components.

Similarly, the same [$Ni_2(\mu\text{-}\eta^2\text{:}\eta^2\text{-}C_6H_6)(^{iPr}NDI)$], [$Ni_2(\mu\text{-Cl})(^{iPr}NDI^{\cdot})$] or [$Ni_2(\mu\text{-Cl})_2(^{iPr}NDI)$] complexes are selective catalysts to perform the reductive cyclopropanation of alkenes with CH_2Cl_2 as the methylene source in the presence of Zn (Fig. 29) [123]. Extension of this catalysis to the [2 + 1]-cycloaddition of vinylidenes, obtained from 1,1-dichloroalkenes, to alkenes allows to selectively prepare methylenecyclopropanes [124].

Moreover, organic azides (ArN_3) react with [$Ni_2(\mu\text{-}\eta^2\text{:}\eta^2\text{-}C_6H_6)(^{iPr}NDI)$] to quickly generate the azide [$Ni_2(\mu\text{-NAr})(^{iPr}NDI)$] with loss of N_2. An X-ray crystal structure of the complex for the (2,6-diphenyl)phenyl azide shows that the μ-NAr

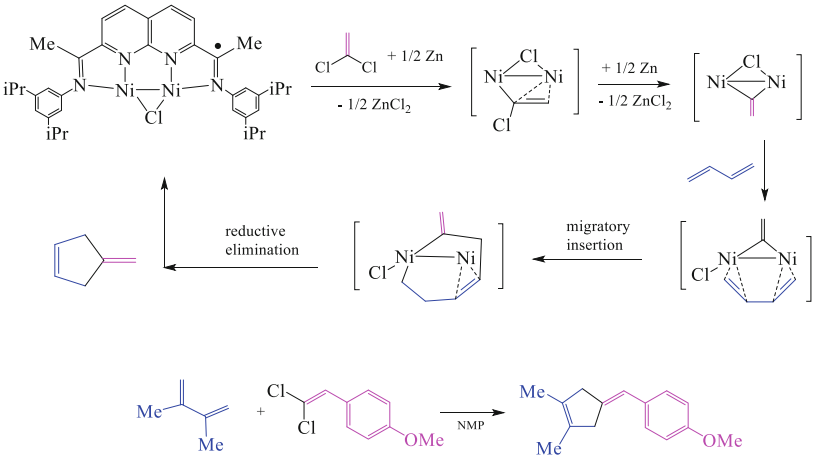

Fig. 28 [$Ni_2(\mu$-Cl)(^{iPr}NDI$^{\cdot}$)]-catalyzed reductive [4 + 1]-cycloaddition of a 1,1-dichloroalkene and a diene

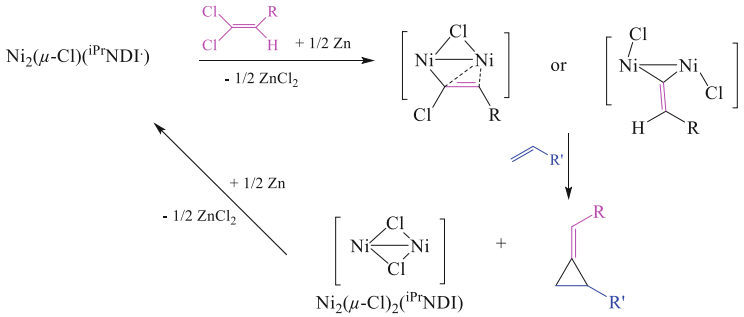

Fig. 29 Mechanism of the [$Ni_2(\mu$-Cl)(^{iPr}NDI$^{\cdot}$)]-catalyzed methylenecyclopropanation

ligand symmetrically bridges the two Nickel metal centers. This complex is paramagnetic and the LUMO is a Ni_2-NAr *anti*-bonding combination; the HOMO has a Ni-Ni(π^*) character and is delocalized into the NDI ligand and its π system [125]. This $Ni_2(\mu$-NAr) complex can be oxidized in THF by $[FeCp_2]PF_6$ into the cationic [$Ni_2(\mu$-NAr)(^{iPr}NDI)(THF)][PF_6] complex and results in an extension of the Ni-Ni distance from 2.3415 (9) Å to 2.515 (1) Å, as well as the Ni-N distances, consistently with a disruption in the three-center/two-electron π-bond [126]. DFT calculations show that the most probable pathway involves the C-H 1,2-addition to generate a Ni–C bond in *ortho* position of the phenyl substituent leading to a metallacycle and a N–H bond. The last step is a C-N reductive elimination providing the amine, and restores the Ni–Ni bond (Fig. 30).

Whereas norbornadiene usually coordinates metals through highly stable π-bonds between the C=C double bond and the metal center, the [$Ni_2(\mu$-η^2:η^2-C_6H_6)(^{iPr}NDI)]

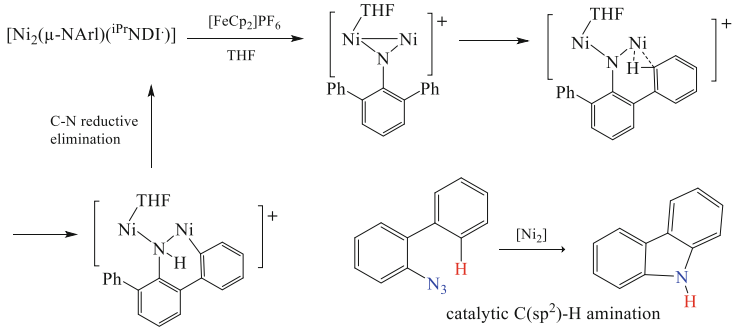

Fig. 30 Most probable mechanism for the C-H activation by the cationic $[Ni_2(\mu\text{-NAr})(^{iPr}NDI)(THF)][PF_6]$ complex through a 1,2-addition pathway

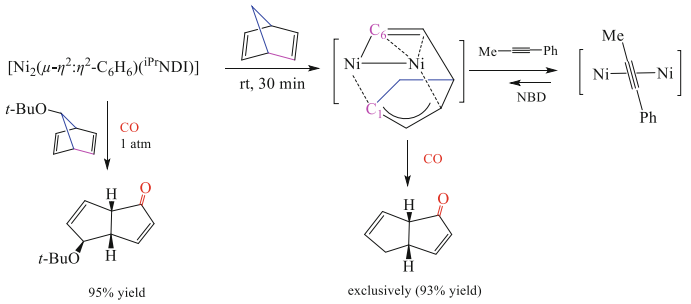

Fig. 31 $C(sp^3)$–$C(sp^2)$ bond oxidative addition of norbornadiene on the $[Ni_2(\mu\text{-}\eta^2\text{:}\eta^2\text{-}C_6H_6)(^{iPr}NDI)]$ complex and reaction with carbon monoxide

complex induces the oxidative addition of the C–C bond [127]. It is one $C(sp^3)$–$C(sp^2)$ bond that is cleaved and the C_1 and C_6 atoms are now separated by 2.876 Å; the activation barrier is 10.6 kcal/mol. Reaction under mild conditions of CO gives quickly the bicylo[3.3.0] ketone and not the bicyclo[2.3.1] that would result from the direct CO insertion into the bond having been activated. For this migratory insertion step, the allylic moiety has been transposed and the reductive elimination is fully regioselective (Fig. 31).

Moreover, introducing a substituent on C_7, such as *t*-BuO, results in the synthesis of a single diastereoisomer in the ketone and is due to the steric preference of the *t*-BuO group to be positioned away from the ^{iPr}NDI ligand [127].

Introducing the chiral NDI ligand (NDI*) in the coordination sphere of the di-nickel framework allows performing the enantioselective cyclopropanation reaction through alkylidene transfer from a 1,1-dichloroalkene to an alkene (Fig. 32). Catalysis occurs at 23°C in diethyether/*N*,*N*-dimethylacetamide in the presence of Zinc and yields as high as 99% and enantioselectivities of 96/4 are obtained, particularly with the Ar substituent 3,5-F_2-C_6H_3 [128]. Presumably, the mechanism

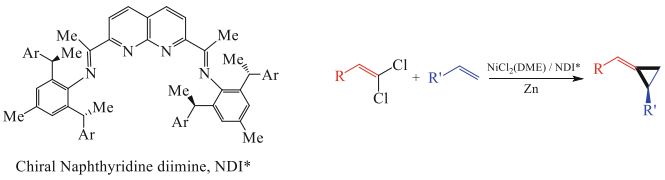

Fig. 32 Enantioselective cyclopropanation reaction catalyzed by [Ni_2(NDI*)] generated in situ from $NiCl_2$(DME)

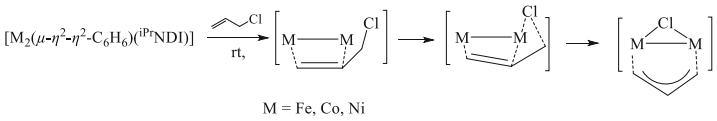

Fig. 33 Mechanism of the oxidative addition of allyl chloride to the [$M_2(\mu\text{-}\eta^2\text{:}\eta^2\text{-}C_6H_6)$(^{iPr}NDI)] complexes (M = Fe, Co, Ni)

is similar to that shown in Fig. 28 with an oxidative addition of a C–Cl bond on the two Ni^I centers.

Thus, the NDI binucleating ligand has the capacity to maintain the two Ni metal centers in a close vicinity and has this particular feature to allow to perform two-electron redox-reactions through electron transfer from its reduced form to the Ni^I–Ni^I bond [129, 130].

This peculiar feature has been extended to dicobalt and diiron complexes bearing the ^{iPr}NDI ligand [131]. The reaction of Na_2[^{iPr}NDI], obtained from ^{iPr}NDI and Na/Hg amalgam, with $CoCl_2$ and $FeCl_2$ in THF leads to the [$M^{II}{}_2(\mu\text{-Cl})Cl_2$(^{iPr}NDI)(THF)] species; their reduction with KC_8 in benzene results in the high yield synthesis of the [$M_2(\mu\text{-}\eta^2\text{:}\eta^2\text{-}C_6H_6)$(^{iPr}NDI)] complexes. As for Nickel, the Cobalt complex is diamagnetic, and the Iron dimer paramagnetic (S = 2) with the unpaired electrons localized on the two Iron metal centers, in an electronic configuration close to [^{iPr}NDI]$^{2-}$[Fe_2]$^{2+}$, whereas for the Co_2 complex, a significant anionic charge is carried by the NBI ligand. The two-electron oxidative addition of allyl chloride occurs on these three complexes to provide the isostructural [$M^I{}_2(\mu\text{-Cl})(\mu\text{-}C_3H_5)$(^{iPr}NDI)] complexes, in which the redox active NDI ligand maintains the +1 oxidation state to each of the metals, contrary to what it could be considered that a M^{II}-M^{II} dinuclear complex has been produced. Indeed, Natural Bond Orbital (NBO) population analysis shows that the metals maintain approximately the +1 oxidation state by delocalization of a significant fraction (−0.68 for Ni, −0.69 for Co, and −0.93 for Fe) of the redox equivalents into the π-system of the NDI ligand [131].

The mechanism, shown in Fig. 33, considers the substitution of benzene by the allyl chloride, with coordination of the alkene functionality in parallel to the M–M bond. Then, in the transition structure, the C-Cl cleavage occurs on one metal center and the C=C bond interacts with the second metal center. The activation barrier is relatively low, 0.4-4.1 kcal mol^{-1}, with regard to the alkene-coordinated complex. In the final complexes, for which the relative energy is −35.9 kcal mol^{-1}/Ni, −29.2/Co

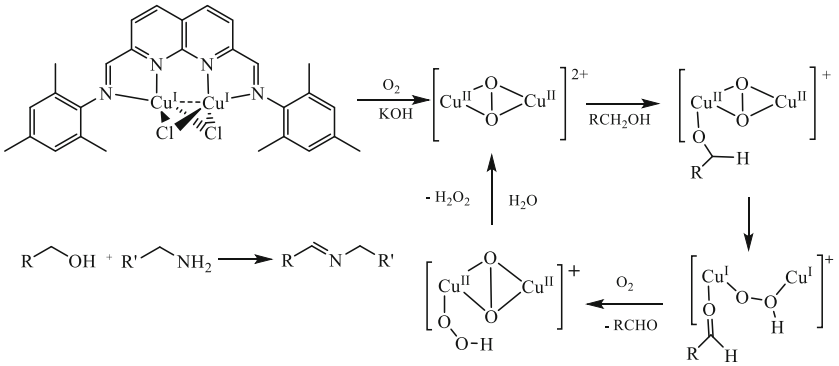

Fig. 34 Structure of the bimetallic Cu^I precursor and the various catalytic steps for the oxidation of the alcohol into an aldehyde

and −46.5/Fe, the M–M bond is maintained, and the chloro and allyl ligands symmetrically bridge the two metals [131].

A similar diimine-1,8-naphthyridine expanded pincer ligand with two bulky mesityl substituents, the 2,7-bis(N-mesitylmethylimino)-1,8-naphthyridine ligand (^{mes}NDI), binds two copper(I) metal centers, bridged by two chloro atoms, with a Cu-Cu distance of 2.6432 (11) Å (Fig. 34) [132]. This complex reacts with dioxygen and KOH at 60 °C in toluene to generate the (μ-η^2:η^2-peroxo)dicopper(II) active species, that coordinates the alcohol and catalyzes the formation of an aldehyde which reacts with primary amines to prepare imines.

The dinuclear ruthenium(II) complex [Ru_2(μ-OAc)$_3$(^{mes}NDI)]Cl, bridged by the (^{mes}NDI) ligand, has three more bridging acetate ligands, one being *trans* to the naphthyridine core, and the Ru-Ru distance is 2.2953 (8) Å [133]. It catalyzes at 70° C in toluene and in the presence of KOH (10 mol%) the acceptorless dehydrogenation of benzyl alcohol into benzaldehyde with 89% yield and near-quantitative elimination of dihydrogen. The substrate scope is large, even if secondary and aliphatic alcohols reach modest yields (38–45%). The mechanism suggested in Fig. 35 involves the decoordination of the acetate ligand *trans* to the (^{mes}NDI) ligand and proceeds on the equatorial platform. The approach of the alcohol occurs on the two metal atoms and the next step is a β-hydride elimination, followed by the departure of the aldehyde, and then the coordination of a new alcohol molecule with its dehydrogenation to produce an alkoxy group and a dihydrogen molecule.

The 1,8-naphthyridine ligand functionalized at the 2- and 7- positions with dipyridyl substituents has been explored to synthesize dinuclear complexes with 6 coordination nitrogen-containing sites [134]. The ligand with R = Me maintains the two Cu^I centers at ~2.5 Å and its synthesis starting from [Cu(NCCH$_3$)$_4$][PF$_6$] results in the coordination of 1 mol of acetonitrile σ-bridging symmetrically the two metal centers (Fig. 36). The binucleating ligand with R = F (dipyridylfluoronaphthyridine, DPFN) is more interesting, particularly due to its solubility and its resistance to oxidizing conditions. Its reaction with Co

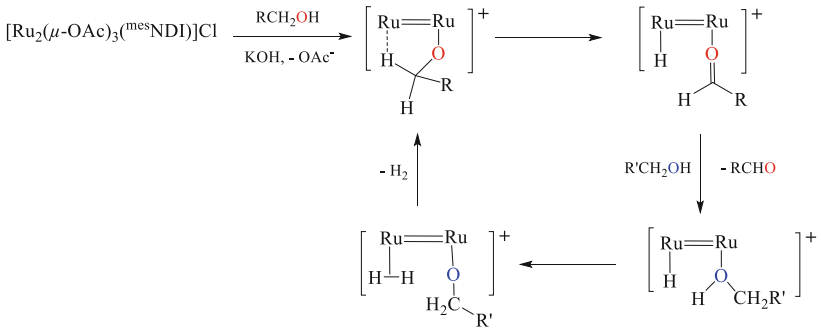

Fig. 35 Mechanism of the dehydrogenation of a RCH_2OH alcohol into the RCHO aldehyde and H_2 on a diruthenium platform

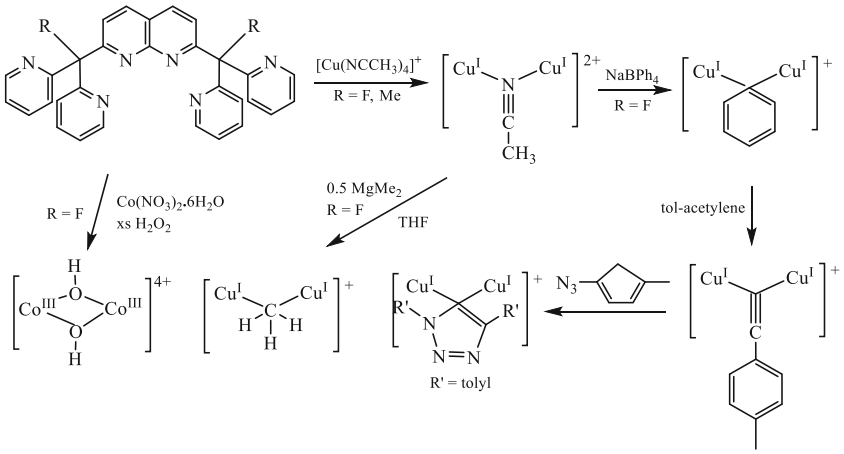

Fig. 36 Use of the 2,7-bis(fluoro-di(2-pyridyl)methyl)1,8-naphthyridine ligand to form Cu_2 complexes with bridging 3c,2e ligands and the $Co_2(\mu\text{-}OH)_2$ species

$(NO_3)_2.6H_2O$ in ethanol, and then addition of an excess of H_2O_2 results in the formation of $[Co_2(\mu\text{-}OH)_2(OH_2)_2(DPFN)]^{4+}[NO_3]_4$ [135]. The $[Co^{III}{}_2(OH_2)_2]$ core can be oxidized into the $[(OH_2)Co^{III}\text{-}Co^{III}(OH)]$ and $[(OH)Co^{III}\text{-}Co^{III}(OH)]$ species; proton-coupled electron transfers produce, respectively, $[(OH_2)Co^{III}\text{-}Co^{IV}(O)]$ and $[(OH)Co^{III}\text{-}Co^{IV}(O)]$. By further proton-coupled electron transfer of the first $Co^{III}\text{-}Co^{IV}$ species or the one-electron oxidation of the second one, the $[Co^{III}(\mu\text{-}OOH)Co^{III}]$ core is generated and reminds the mechanism of photosystem II [135]. Extension of this reactivity to the $[Co_2(\mu\text{-}OH)_2(OH_2)_2(DPEN)]^{2+}$ complex with the bridging (dipyridylethanenaphtyridine) ligand shows that the two-electron reduction and then the protonation allow to remove 1 mol of water and to generate a $Co^{II}\text{-}Co^{II}$ core which presents an open binding site [136].

In the $[Cu_2(\mu\text{-}\eta^1\text{:}\eta^1\text{-}NCCH_3)(DPFN)]$ complex the acetonitrile ligand is in a symmetrically bridging position between the two Cu^I centers in a $\mu\text{-}\eta^1\text{:}\eta^1$-fashion,

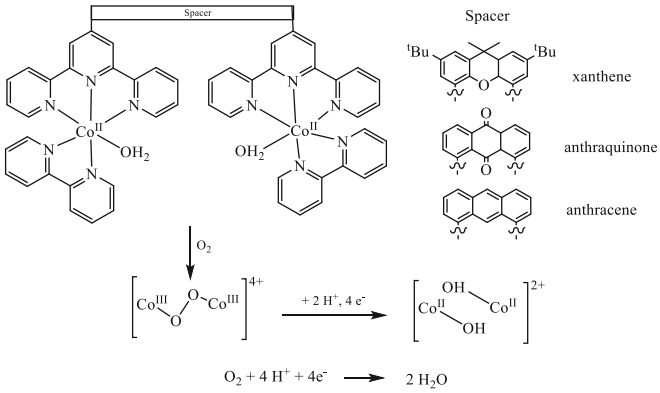

Fig. 37 Structure of the dicobalt complex bridged by the 1,8-bis (2,2:6,2-terpyrid-4-yl)spacer ligand, its reaction with oxygen to produce the μ-peroxo dicobalt(III) species

and the two empty orbitals of the two copper centers interact with the donor orbital of the N-atom to form a 3-center,2-electron (3c,2e) bond [134]. This complex reacts with $NaBPh_4$ to form a bridging phenyl ligand in the place of acetonitrile ($d_{Cu\text{-}Cu}$ = 2.3927 Å) [137], or with dimethylmagnesium to form a methyl group in the bridging position (Cu-Cu distance: 2.3549 (3) Å) [138]. These syntheses have been extended to C_6F_5, 3,5-$(CF_3)_2C_6H_3$ aryl groups [137], and CH_2CH_3, $CH_2C(CH_3)_3$ alkyl substrates [138]. In addition, the μ-phenyl complex reacts with *p*-tolylacetylene to afford the bridging *p*-tolylacetylide complex [139]; its further reaction with an excess of *p*-tolylazide leads to the bridging μ-η^1:η^1-(1,4-bis(4-tolyl)-1,2,3-triazolide complex (Fig. 36). The bridging organic reactants have the N- or C-atoms, which hold the two copper(I) centers that are in a close vicinity in (3c-2e) bond [140, 141].

The dinuclear cobalt complex bridged by the 1,8-bis (2,2:6,2-terpyrid-4-yl)xanthene, anthraquinone, or antracene ligand, with the two coordination cobalt spheres completed with 2,2′-bipyridine, is able to perform with high selectivity the biomimetic four-electron oxygen reduction reaction (Fig. 37) [142]. These complexes react slowly with air in ethanol/water solution at reflux to provide the μ-peroxo $[Co_2(\mu\text{-}O_2)(bipy)_2(L)]$ and for the spacer xanthene, the X-ray crystal structure reveals a Co-Co distance of 4.441 Å. These species react with $HClO_4$ to generate H_2O in electrochemical experiments through a $[Co_2(OH)_2]^{2+}$ intermediate.

With the bridging bis(2-pyridyl)-3,5-pyrazolate ligand and a 2,2′;6′,2″--terpyridine ligand on each metal center, 10 Nitrogen coordinating atoms are present on this di-cobalt framework (Fig. 38). As the previous complex, it can perform the four-electron oxygen reduction reaction. The water oxidation reaction has been particularly studied to give all the intermediates species [143, 144]. Particularly, the addition of dioxygen to the initial Co^{II}-Co^{II} complex involves a 1e-1e oxidative addition to lead to the peroxide-bridged $Co^{III}(\mu\text{-}O_2)Co^{III}$ species. Reaction with 1 equivalent of Ce^{IV} at pH 1 generates the superoxido-bridged $Co^{III}(\mu\text{-}O{\cdot}O)Co^{III}$ species, which coordinates one molecule of H_2O to provide the $(H_2O)Co^{III}Co^{III}(O{\cdot}O)$ intermediate; its deprotonation gives the $(HO{\cdot})Co^{III}Co^{III}(O{\cdot}O)$

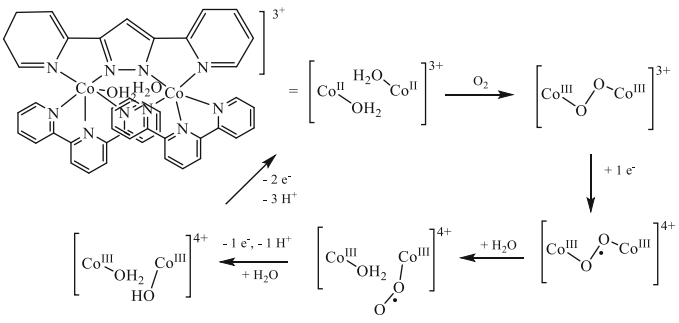

Fig. 38 Cobalt(III) dimer bridged by the bis(2-pyridyl)-3,5-pyrazolate ligand and having two ter-pyridine ligands. Main intermediates in the catalyzed-water oxidation reaction

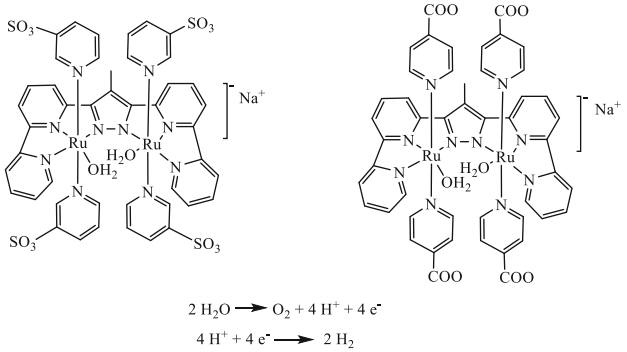

Fig. 39 4-Methylbis(bipyridyl)pyrazolate bridging scaffold maintaining the two ruthenium metal centers in close proximity, with pyridine-3-sulfonate or 4-carboxylate axial ligands

biradical species, which coordinates a molecule of H_2O and loses O_2, generating the $(H_2O)Co^{III}Co^{III}(OH)$ intermediate. The redox process only involves the oxygen atoms and the Co^{III} centers play the role of scaffolds that support the oxygen radical species.

The 4-methylbis(bipyridyl)pyrazolate ligand has been designed to bridge two ruthenium metal centers and maintain them in close proximity as with the previous bis(2-pyridyl)-3,5-pyrazolate ligand. Moreover, sulfonatopyridine ligands provide a significant solubility in water (Fig. 39) [145].

Instead of the pyrazolate scaffold (Figs. 38 and 39), the pyridazine cycle allows to synthesize the neutral dinucleating L ligand shown in Fig. 40, also containing 10 Nitrogen atoms able to coordinate the two Cobalt metal centers [146]. Reaction of L with two equivalents of $Co(OTf)_2$ in CH_3CN at 60°C leads to the $[LCo^{II}{}_2(OTf)_2](OTf)_2$ complex. Addition of $[NH_4][PF_6]$ allows to obtain crystals of the $[LCo^{II}{}_2(CH_3CN)_3][PF_6]_4$ complex whose X-ray structure shows that one acetonitrile ligand has substituted one Nitrogen atom of the pyridazine scaffold, the two Cobalt(II) atoms being hexacoordinated. Oxidation of $[LCo^{II}{}_2(OTf)_2](OTf)_2$

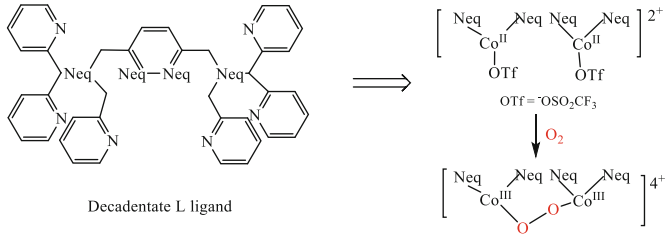

Fig. 40 Synthesis of the *N*,*N*′-(pyridazine-3,6-diylbis(methylene)bis(1,1-di(pyridine-2-yl)-*N*-(pyridine-2-ylmethyl)methyl)methanamine) L ligand

under aerobic conditions gives quantitatively the $[LCo^{III}{}_2(\mu\text{-}1,2\text{-}O_2)](OTf)_4$ complex, the two Co(III) centers being octahedral, and the Neq Nitrogen atoms being in the equatorial plane. However, using octamethylferrocene as electron donor in the presence of trifluorooacetic acid for the reduction of O_2, which gives H_2O with the Cobalt(III) dimer bridged by the bis(2-pyridyl)-3,5-pyrazolate ligand and coordinated by two ter-pyridine ligands ($O_2 + 4\ H^+ + 4\ Fe(Me_4Cp)_2 \rightarrow H_2O + 4\ [Fe(Me_4Cp)_2]^+$), the present $[LCo^{III}{}_2(\mu\text{-}1,2\text{-}O_2)](OTf)_4$ complex catalyzes the two-electron reduction into hydrogen peroxide:

$$O_2 + 2\ H^+ + 2\ Fe(Me_4Cp)_2 \rightarrow H_2O_2 + 2\ \left[Fe(Me_4Cp)_2\right]^+$$

Thus, subtle variations in the ligand result in few differences in the coordination sphere, particularly in the electron donation, inducing a different reactivity, under similar reaction conditions.

The (3.1.3.1)porphyrin, in which the inner ring has been somewhat extended by four carbon atoms [147], denoted H_2EP in Fig. 41, has been synthesized to have a planar and cyclic ligand able to coordinate two Mg^{2+} ions [148]. It is an electride, i.e., it belongs to a class of ionic compounds that have trapped electrons as anions. Activation of H_2, CO_2, N_2O, CH_4, and C_6H_6 results in the dissociation of the H–H, C–O, N–O, and C–H bonds leading to bridged Mg(II) dimers. DFT calculations show the presence of a non-nuclear attractor, located close to the middle of the two Mg^I atoms. The reactants are shown to approach one Mg^I center, and then an interaction with the second Mg^I center takes place. In the transition state between Mg_2EP and H_2, CH_4 and C_6H_6 the interaction occurs between the Mg–Mg bond σ-bond orbital and the σ*-orbital of the reactants leading to an elongated H–H or C–H bond length. An oxygen bridge between the two Mg^{II} centers results from the reaction of CO_2 or N_2O and further reaction with CO_2 gives the carbonato-bridged complex. The Mg_2EP precursor reacts with methane to cleave one C–H bond and produce the $Mg^{II}(CH_3)$-$(H)Mg^{II}$ complex.

A pyrazolate core with two β-diketiminate binding pockets, containing bulky (2,6-diisopropyl)phenyl groups, affords a hexadentate ligand (L) which maintains the two Nickel atoms at 3.8066 (5) Å, so that a μ-H hydride bridging ligand as well as a metal–metal bond are unlikely [149]. Reaction of the diamagnetic $[LNi(\mu\text{-Br})$

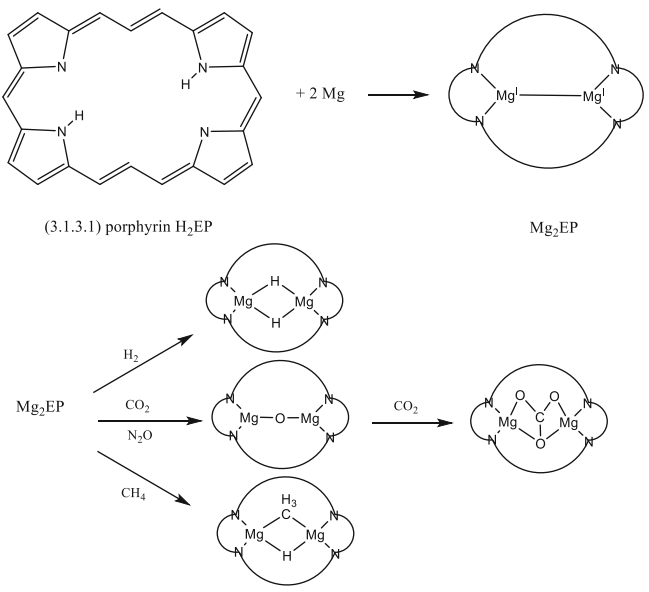

Fig. 41 Synthesis of the $[Mg^{I}{}_2((3.1.3.1)porphyrin)]$ and its reaction with H_2, N_2O or CO_2 and CH_4 to give Mg^{II} dimers

Ni] precursor (Fig. 42) with 2.5 eq. of $KBHEt_3$ in THF at room temperature leads to the $[KLNi(H)_2Ni]$ complex with two hydride ligands located in the bimetallic pocket, and interacting with the K^+ cation which also interacts with two aryl rings of the (2,6-diisopropyl)phenyl substituents. This complex reacts with dibenzo (18-crown-6) to produce the anionic $[LNi^{II}(H)_2Ni^{II}]^-$ species with the [K (DB18C6] cation in which the two terminal Nickel–hydride bonds are directed toward the bimetallic cleft. At room temperature, under vacuum, it loses H_2 to form the dinickel(I) complex [K(DB18C6] $[LNi^{I}{}_2]$, and is considered as easily formed when various small molecules react with $[LNi^{II}(H)_2Ni^{II}]^-$ which is described as a masked dinickel(I) synthon [150]. The use of strong reducing agents such as KC_8 leads to $K[Ni^{I}{}_2]$ Ni at +1 oxidation state with the K^+ cation tetrasolvated by THF located above the pyrazolate (the same situation prevails for $[Na(THF)_2]^+$ resulting from the treatment with sodium naphtalenide). Moreover protonation of $[LNi^{II}(H)_2Ni^{II}]^-$ with $[H(OEt_2)_2]BAr^{F}{}_4$ generates the cationic dinickel(I) complex $[L^{H2}Ni^{I}{}_2]$ associated to the $[BAr^{F}{}_4]^-$ anion where the Ni-Ni distance is 4.1032 (5) Å and the double protonation produces two γ-CH_2 units in the two β-diimine subunits. Thus, there is an access to three types of di-nickel(I) complexes, anionic, neutral, and cationic species.

Either the $[KLNi(H)_2Ni]$ or $[K(DB18C6]^+[LNi^{II}(H)_2Ni^{II}]^-$ complexes react with one equivalent of O_2 to give the μ-1,2-peroxo dinickel(II) $[KLNi(\mu\text{-}O_2)Ni]$ or [K $(DB18C6]^+[LNi^{II}(\mu\text{-}O_2)Ni^{II}]^-$ complexes. The first one further reacts with more O_2 under ambient conditions to produce with loss of KO_2 the μ-superoxo neutral

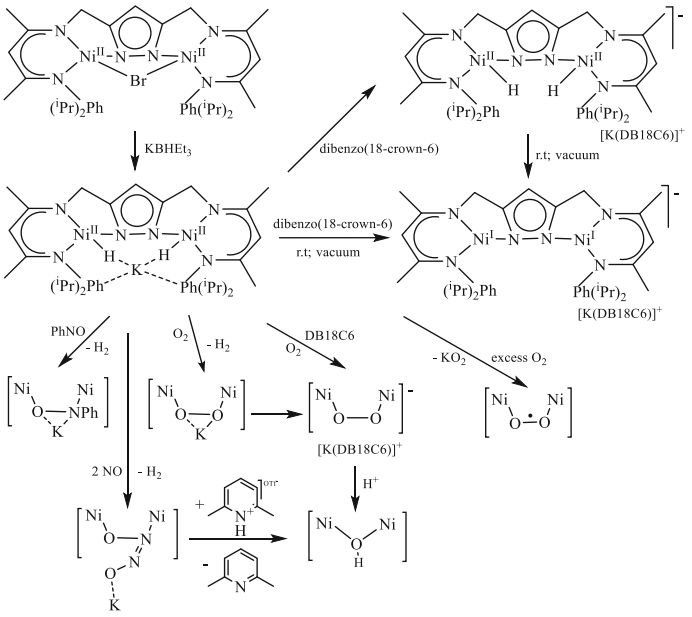

Fig. 42 Synthesis of the $[KLNi^{II}(H)_2Ni^{II}]^-$ complex, which is a masked dinickel(I) synthon reacting with various reactants to give bridged dinickel(II) complexes

complex $[LNi^{II}\text{-}O^{\cdot}O\text{-}Ni^{II}]$, whereas protonation of the second one gives access to the μ-hydroxo dinickel(II) $[LNi^{II}(\mu\text{-}OH)Ni^{II}]$ complex [151].

The PhNO reactant removes the H_2 molecule from the $K[LNi(H)_2Ni]$ complex and binds facially the dinickel(II) framework, in a μ-κ(O),κ(N) mode, as the $(PhNO)^{2-}$ entity through its HOMO, which is the π^*_{NO} orbital perpendicular to the Ph-N-O plane [152]. This diamagnetic $[LNi^{II}(\mu\text{-}PhNO)Ni^{II}]^-$ complex is oxidized by $[Fe(Cp^{Me5})_2]PF_6$ into the $[LNi^{II}(\mu\text{-}PhN^{\cdot}O)Ni^{II}]$ which contains the bridging $(PhNO)^{\cdot-}$ entity. The π^*_{NO} orbital becomes the Singly Occupied Molecular Orbital (SOMO), and Mulliken population analysis shows that the unpaired spin density is 69% located on the bound PhNO, mainly on the N atom (32%), and 10% on the Nickel center bound to the O atom, and 17% on the other Nickel center. Protonation with a Brönsted acid, such as 2,6-lutidinium triflate, of the $[LNi^{II}(\mu\text{-}PhNO)Ni^{II}]^-$ complex occurs on the Nitrogen atom of the bridging nitrosobenzene unit and provides the diamagnetic $[LNi^{II}(\mu\text{-}Ph(H)NO)Ni^{II}]$ complex, with a μ-κ(O),κ(N)-ONHPh O-deprotonated phenylhydroxylamine bridge.

The masked dinickel(I) complex arising from the dihydride species reacts at room temperature with RNO_2 nitro substrates to perform a cooperative $2e^-$ reduction into $[RNO_2]^{2-}$ and a μ-κ(O),κ(O′)-binding mode, the K^+ (or Na^+) cation being closely associated with the bound reduced reactant. The reaction further provides a μ-κ(O),κ(N)-formaldoximato ligand O-N=CH_2, when R = CH_3, or a μ-κ(O),κ(N)-deprotonated hydroxylamine ligand O-N(H)Ph, when R = Ph, with the simultaneous formation in each case of the $[LNi^{II}(\mu\text{-}OH)Ni^{II}]$ complex (Fig. 42) [153].

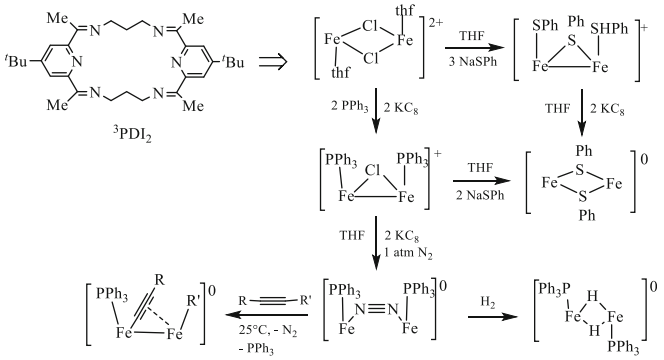

Fig. 43 Macrocyclic, pyridyldiimine-based scaffold, ligand with two propyl linkers and two bulky *t*-butyl substituents, $^{3}PDI_2$. Reactivity of the $[(^{3}PDI_2)Fe_2(\mu\text{-}Cl)_2(thf)_2]^{2+}$ complex in some illustrative reactions in which the two Iron atoms remain Fe^{II}

Another strategy has been developed to maintain some geometrical flexibility in the ligand to have various situations where the cooperativity between the two metal centers allows performing more extended activation reactions. The ligand in which two pyridyldiimines components are linked by two propyl chains, and with two *t*-Bu bulky groups, $^{3}PDI_2$ (Fig. 43) enables to synthesize the isostructural series of dinuclear iron, cobalt, and nickel complexes [154]. The reactant is $[Sr(^{3}PDI_2)](OTf)_2$. Addition of $FeCl_2$ in THF at room temperature leads to the complex $[(^{3}PDI_2)Fe_2(\mu\text{-}Cl)_2(thf)_2](OTf)_2$ and the triflate anion can be substituted with the $[B(3,5\text{-}(CF_3)_2C_6H_3)_4]^-$ anion to obtain higher solubility [155]. In the 36 e^- $[(^{3}PDI_2)Fe_2(\mu\text{-}Cl)_2(thf)_2]^{2+}$ species, the two Iron metal centers are Fe(II), in an octahedral coordination environment, with the three Nitrogen atoms of each PDI fragment providing 6 e^-. There is no bonding interaction (3.3262 Å) between the two high spin (S = 2) ferromagnetically coupled Fe(II) atoms. Reduction of this complex by 2 eq. of KC_8 in the presence of two phosphine ligands, affords the 34 e^- $[(^{3}PDI_2)Fe_2(\mu\text{-}Cl)(PPh_3)_2]^{+}$ complex with a folded geometry, a Fe-Fe distance of 2.710 Å and a diamagnetism, consistent with a weak metal–metal bond. The $^{3}PDI_2$ ligand has 1 electron on each PDI part ($PDI^{\cdot-}$), and the complex has two Fe(II) metal centers. This reduction reaction is thus a 2 e^- process occurring in close vicinity of the two metals on the ligand, each Fe(II) center having a antiferromagnetic coupling to a ligand-based spin and the other metal center ($S_{Fe} = 1$). Reaction of 3 eq. of NaSPh to $[(^{3}PDI_2)Fe_2(\mu\text{-}Cl)_2(thf)_2](OTf)_2$ in THF leads to the $[(^{3}PDI_2)Fe_2(\mu\text{-}SPh)(SPh)_2](OTf)$ complex, which associates a $(^{3}PDI_2)^0$ ligand with two Fe(II) metal atoms in a high spin ($S_{Fe} = 2$) configuration as in the starting $(\mu\text{-}Cl)_2$ complex. Moreover, the addition of NaSPh to the μ-chloro $[(^{3}PDI_2)Fe_2(\mu\text{-}Cl)(PPh_3)_2]^{+}$ complex or reduction with 2 eq. of KC_8 of $[(^{3}PDI_2)Fe_2(\mu\text{-}SPh)(SPh)_2]^{+}$ produces the 34 e^- di(μ-thiolato) complex $[(^{3}PDI_2)Fe_2(\mu\text{-}SPh)_2]^0$ in which the PDI fragments each contains 1 e^- associated to a Fe(II)-Fe(II) central framework, their distance being 2.7321 Å (Fig. 42).

Similarly reduction of the $[(^3PDI_2)Fe_2(\mu\text{-}Cl)(PPh_3)_2]^+$ complex under one atmosphere of N_2 by 2 eq. of KC_8 induces the formation of the $[(^3PDI_2)Fe_2(\mu\text{-}N_2)(PPh_3)_2]$ complex, in which the ligand is $(^3PDI_2)^{4-}$ associated to Fe^{II} ions in a low-spin configuration [156]. The N_2 molecule is in a $\mu\text{-}N_2\text{-}\kappa^1(N),\kappa^1(N')$ configuration between the two metal centers. This bridging dinitrogen complex reacts at room temperature with an alkyne substrate through an oxidative addition process, which involves a C(sp)–C(sp^2) bond cleavage (generally a C-Ph) except if the R group is an alkyl too bulky substituent, so that a C(sp)-C(sp^3) cleavage occurs. This reaction is non-assisted and can be done in the dark. DFT calculations allow to propose a $[(^3PDI_2)Fe_2(\mu\text{-}RCCR')(PPh_3)]$ monoalkyne adduct as intermediate, the alkynyl unit bridging symmetrically the two metal centers. Both the metals and the redox-active $^3PDI_2$ ligand are involved in the C–C bond cleavage. The resulting $[(^3PDI_2)Fe_2(CCR)(R')(PPh_3)]^0$ complex involves the $(^3PDI_2)^{3-}$ ligand; its hydrogenation or hydroboration leads to hydrofunctionalization leading to $[(^3PDI_2)Fe_2(\mu\text{-}N_2)(PPh_3)_2]^0$ or $[(^3PDI_2)Fe_2(\mu\text{-}H)_2(PPh_3)_2]^0$ [157]. Reaction at room temperature of the $(\mu\text{-}N_2)$ complex with dihydrogen (1 atm) leads to the bridged dihydride $[(^3PDI_2)Fe_2(\mu\text{-}H)_2(PPh_3)_2]^0$ species which involves the $(^3PDI_2)^{4-}$ ligand.

The analogous $[(^3PDI_2)Fe_2(\mu\text{-}Cl)(PMe_3)_2]^+$ folded complex can be reacted with NaN_3 to give the linear diiron nitride unfolded $[(^3PDI_2)Fe_2(\mu\text{-}N)(PMe_3)_2]^+$ complex, which is diamagnetic and associates the $(^3PDI_2)^{3-}$ ligand retaining a three electron's worth of electron density with two Fe^{II} ions [158].

The reaction of the RCH_2OH alcohol provides the coordination on one Cu^{II} center of the OCH_2R moiety, with the simultaneous formation of a monocationic species. This complex evolves toward a $Cu^I(\mu\text{-}\eta^1\text{:}\ \eta^1)$ hydroperoxide entity where the O=CHR aldehyde is coordinated to one Cu^I metal center. The aldehyde is released and reacts with the amine, and the reaction of dioxygen regenerates the peroxo bridge, with the coordination of the hydroperoxide on a single Cu^{II} center.

3 Mechanisms in Which Only One Metal Center Is Involved in a 1e Reaction

In the very broad context of metalloproteins and metalloenzymes which contain metal–sulfur bonds, metallodithiolate ligands play a peculiar role in bio-inspired catalysis [159, 160]. Interestingly, to mimic the [FeFe]- and [NiFe]-hydrogenases that catalytically produce or split dihydrogen in nature, two similar dithiolato-bridged dinuclear complexes are analyzed [161]. The heterobimetallic $[NiFeS_2]$ active site of the [NiFe]-hydrogenase is associated to 3 Iron-sulfur clusters, which ensure the electron transfer between a redox protein and the catalytic center, present a catalytic cycle involving two steps of 1 e^- reduction (E) and two steps of protonation (chemical reaction C) for the ECEC hydrogen evolution reaction [162].

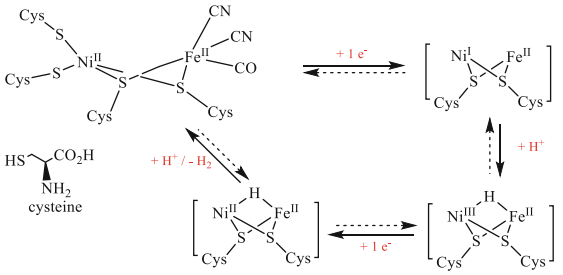

Fig. 44 Catalytic cycle on the active site of [NiFe]-hydrogenase, involving the succession of 1 e^- reduction (E), 1 protonation (C), E and C steps for the hydrogen evolution reaction (ECEC)

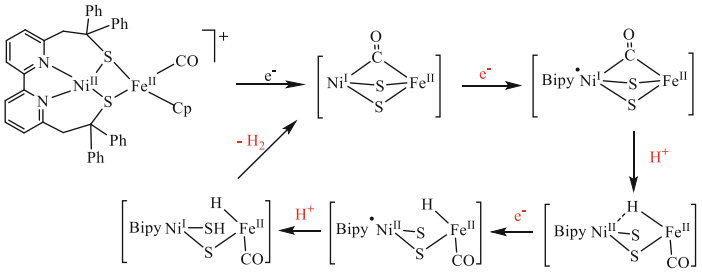

Fig. 45 Proton reduction into dihydrogen catalyzed by the Ni^{I}-Fe^{II} complex produced by one electron reduction of the dithiolato bridged Ni^{II}-Fe^{II} complex in the [NiFe]-hydrogenase mimic

$$2\,H^+ + 2\,e^- \rightarrow H_2$$

Catalysis apparently occurs on the Nickel metal center whose oxidation state evolves from +I to +III oxidation state, but the Iron metal center, which remains Fe^{II}, is significantly synergistic, not only to stabilize and activate the bridging hydride, but also to give some electronic flexibility to the coordination sphere of the dinuclear entity, through the thiolate bridges, and thanks to the CO and CN^- ligands (Fig. 44).

The bridging ligand 2,2′-(2,2′-bipyridine-6,6′-diyl)bis(1,1-diphenylethane-thiol) is fully deprotonated to produce the Ni^{II}-Fe^{II} complex shown in Fig. 45. After a first reduction leading to the active Ni^{I}-Fe^{II} species a succession of electron transfers and chemical reactions with H^+ (ECEC) is similar to that one operating in the [NiFe]-hydrogenase. The redox chemistry occurs on the Ni metal center but involves the bipyridine ligand, whereas the two protonation steps concern the formation of a hydrido–iron bond semi-bridging the nickel, and then a SH bond on the decoordinated sulfur atom as a proton relay. Similarly, a $Fe^{II}Fe^{II}$ complex, in which the two metal centers are bridged by the same ligand and a CO ligand, is active in electrocatalytic hydrogen production [161].

Recently, the similar Co^{II}-Fe^{II} cationic complex has been synthesized, and two sulfur atoms and the CO ligand are in bridging positions [163]. The single unpaired electron of this S = ½ complex (d^7 Co^{II} – d^6 Fe^{II}) is localized on the Co center associated to the Lewis acidic Fe center. The first one-electron reduction process is easier to perform than those on the Ni^{I}-Fe^{II} and Fe^{II}-Fe^{II} complexes and provides the

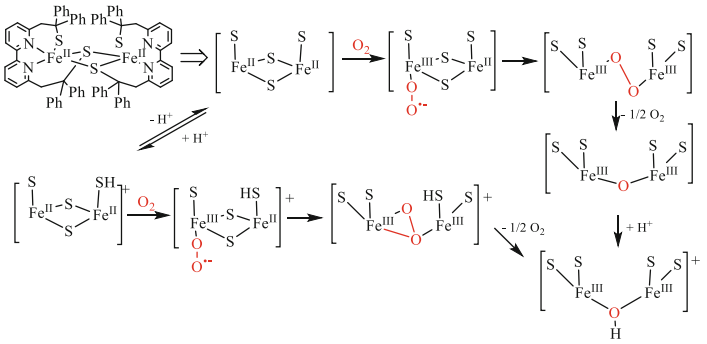

Fig. 46 Two first steps of the O_2 activation predicted by DFT calculations on the dinuclear Fe^{II} complex containing the bridging 2,2′-(2,2′-bipyridine-6,6′-diyl)bis(1,1-diphenylethane-thiol) ligands

diamagnetic Co^{I}-Fe^{II} complex, which has been isolated. As for the two previous complexes, the second reduction occurs on the redox-non-innocent bipyridine-dithiolato ligand. However, on the contrary of the two complexes associating Ni^{I} and Fe^{II} to Fe^{II}, this complex that is easy to reduce, is not active to perform the electrocatalytic transformation of H^+ into H_2.

The 2,2′-(2,2′-bipyridine-6,6′-diyl)bis(1,1-diphenylethane-thiol) provides the LS^{2-} ligand which reacts with $Fe(BF_4)_2.6H_2O$ to give the $[(LS)Fe^{II}Fe^{II}(LSH)](BF_4)$ complex having two disulfide bridging sulfur atoms and one thiolate and one thiol ligands (Fig. 46) [164, 165]. In the presence of NaH in acetonitrile, deprotonation is done, and the $[(LS)Fe^{II}Fe^{II}(LS)]$ is obtained. As shown by DFT calculations both complexes coordinate O_2 to one metal site to afford a Fe^{II}-Fe^{III} superoxo intermediate. The $[(LS)Fe^{III}(O_2^{\cdot})Fe^{II}(LS)]$ species evolves toward the $[(LS)Fe^{III}(\mu\text{-}1,2\text{-}O_2)Fe^{III}(LS)]$ complex, in which only the peroxo ligand bridges the two Fe^{III} metal atoms. Similarly the $[(LS)Fe^{III}(O_2^{\cdot})Fe^{II}(LSH)]$ intermediate gives rise to the $[(LS)Fe^{III}(\mu\text{-}\eta^1\text{:}\eta^2\text{-}O_2)Fe^{III}(LSH)]$ complex containing the rare $\mu\text{-}\eta^1\text{:}\eta^2$-peroxo coordination of the bridging O_2 ligand (Fig. 46).

Presumably by the way of a dismutation process, two μ-peroxo complexes afford two μ-oxo $[(LS)Fe^{III}(\mu\text{-}O)Fe^{III}(LS)]$ species and one molecule of O_2. In the case of the thiol-containing complex, a similar dismutation occurs between two protonated peroxo intermediates to generate the μ-OH $[(LS)Fe^{III}(\mu\text{-}OH)Fe^{III}(LS)]$ hydroxo complex, which can be obtained by protonation of the μ-oxo species (Fig. 46).

An electrogenerated Pd^{III}-Pd^{III} dimer containing six HSO_4^- ligands is able to activate methane under relatively mild conditions in sulfuric acid to provide the $^{\cdot}CH_3$ radical, a Pd^{II}-Pd^{III}, which give rise to methyl bisulfate CH_3OSO_3H with a turnover frequency as high as 2,000 h^{-1} [166]. The introduction of O_2 or the $[Pd^{III}$-$Pd^{II}]$ complex suppresses the formation of CH_3SO_3H indicating that the reaction obeys a radical chain sequence. The $[Pd^{III}$-Pd^{III}-$CH_3]$ intermediate produces methyl bisulfate by reductive elimination and, as the reaction proceeds in the presence of large quantities of sulfuric acid, regenerates the $[Pd^{III}$-$Pd^{III}]$ complex with its six HSO_4^-

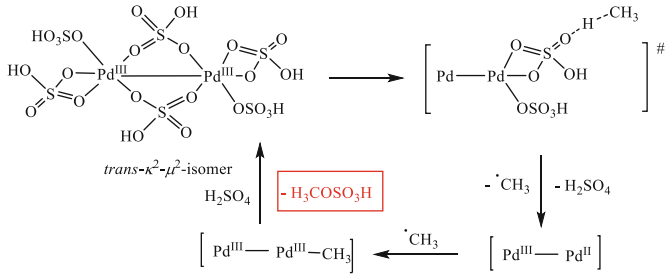

Fig. 47 Formation of a ·CH3 radical on a Pd^{III}-Pd^{III} complex in acidic medium

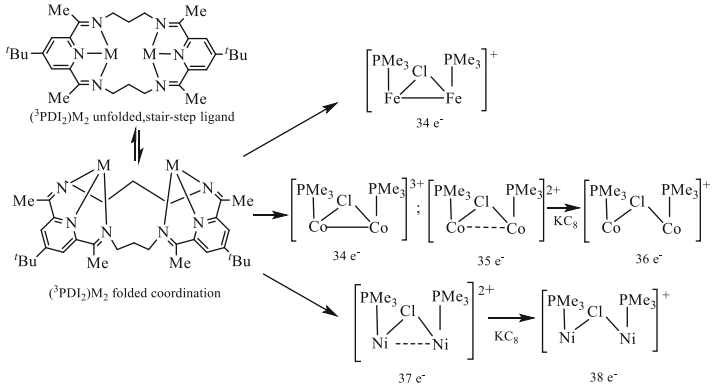

Fig. 48 The redox-active $^3PDI_2$ ligand in Iron, Cobalt, and Nickel dinuclear complexes

ligands (Fig. 47). DFT calculations support this unconventional H atom abstraction pathway in which an oxygen atom is directly affording the electrophilic C-H activation through the influence of the two palladium metal atoms.

In this part, it is of interest to consider the dinuclear Iron, Cobalt, and Nickel complexes that are coordinated by the redox-active $^3PDI_2$ ligand in the isostructural series, in which each metal is coordinated to a PMe_3 ligand and a μ-chloro ligand is in a bridging position [154]. The 34 e^- $[(^3PDI_2)Fe_2(\mu\text{-}Cl)(PPh_3)_2]^+$ complex has already been presented in the previous paragraph. The $[(^3PDI_2)Fe_2(\mu\text{-}Cl)(PMe_3)_2]^+$ complex adopts the same geometry and the $[(^3PDI_2)Co_2(\mu\text{-}Cl)(PMe_3)_2]^{3+}$ complex is isoelectronic. The reduction of this complex with AgOTf gives rise to the 35 e^- $[(^3PDI_2)Co_2(\mu\text{-}Cl)(PMe_3)_2]^{2+}$ entity and further reduction with KC_8 to the 36 e^- $[(^3PDI_2)Co_2(\mu\text{-}Cl)(PMe_3)_2]^+$ species. The two dinickel complexes $[(^3PDI_2)Ni_2(\mu\text{-}Cl)(PMe_3)_2]^{2+}$ and $[(^3PDI_2)Ni_2(\mu\text{-}Cl)(PMe_3)_2]^+$ have a 37 and 38e^- configuration, respectively. These six isostructural complexes, shown in Fig. 48, have been characterized by cyclic voltammetry, SQUID magnetometry, UV-visible-Infrared spectroscopies, NMR, and X-ray crystallography. DFT calculations have been done to determine the electronic flexibility of the $^3PDI_2$ ligand and the dinuclear platform. It

is interesting to analyze how the addition of one electron to the coordination sphere operates on one metal center or on the full ligand-M_2 system.

Each PDI component of the $^3PDI_2$ ligand contains two unoccupied redox-active valence orbitals: a_2-PDI_{π^*} and b_1-PDI_{π^*}. Their combination to produce $^3PDI_2$ results in valence orbitals a_1 and b_2 through bonding and antibonding combinations of the b_1-PDI_{π^*} fragments; similarly b_1 and a_2 result from the bonding and antibonding combinations of a_2-PDI_{π^*}. With the two metals placed on the z-axis the sets of the M_2 orbitals present σ-symmetry (σ-M_2 and σ*-M_2, d_z^2-based), π-symmetry (π_1-M_2 and π_1*-M_2 as well as π_2-M_2 and π_2*-M_2, d_{xz} and d_{yz}), and δ-symmetry δ_1-M_2 and δ_1*-M_2 as well as δ_2-M_2 and δ_2*-M_2, d_{xy} and $d_{x^2-y^2}$-based). Binding the two M_2 and $^3PDI_2$ orbitals provides seven fully occupied δ_1, δ_1*, π_1, π_1*, π_2, π_2*, and σ orbitals, whereas the other three σ*, δ_2, and δ_2* orbitals present variable occupation across the series.

For the diamagnetic $[(^3PDI_2)Fe_2(\mu\text{-Cl})(PMe_3)_2]^+$ and $[(^3PDI_2)Co_2(\mu\text{-Cl})(PMe_3)_2]^{3+}$ complexes, the electronic configuration is $(\delta_1)^2$, $(\delta_1^*)^2$, $(\pi_1)^2$, $(\pi_1^*)^2$, $(\pi_2)^2$, $(\pi_2^*)^2$, $(\sigma)^2$ and $(\sigma^*)^0$ with a metal–metal bond, $d_{Fe\text{-}Fe} = 2.6511$ (9) Å and $d_{Co\text{-}Co} = 2.6334(4)$Å. From the complete investigation, the $(^3PDI_2)^{3-}$ ligand is associated to a $(Fe_2)^{+5}$ dinuclear platform, with a d^{11} electron-count for the two metals in the $[(^3PDI_2)Fe_2(\mu\text{-Cl})(PMe_3)_2]^+$ complex and $(^3PDI_2)^-/(Co_2)^{+5}/d^{13}$ represent the assignments for $[(^3PDI_2)Co_2(\mu\text{-Cl})(PMe_3)_2]^{3+}$.

Formal one-electron reduction of the previous complex can be obtained by addition in THF of 2 $CoCl_2$, then 2 PMe_3 and 1 KC_8 to $[Sr(^3PDI_2)(OTf)_2]$ to provide $[(^3PDI_2)Co_2(\mu\text{-Cl})(PMe_3)_2]^{2+}$. The Co-Co distance increases somewhat to 2.7930 (8) Å and is considered as a half-order M–M bond; it is associated to a ligand-based oxidation state between $(^3PDI_2)^{2-}/(Co_2)^{+5}/d^{13}$ and $(^3PDI_2)^-/(Co_2)^{+4}/d^{14}$. Thus, the chemical reduction, with a $(\sigma)^2$ and $(\sigma^*)^1$ situation, partially cleaves the metal–metal bond and the added electron is shared between the Co_2 platform and the ligand-based π* system, which can be written $(^3PDI_2)^{1.5-}$. The orbital populations can be considered as a strong antiferromagnetic coupling between $S_{Co2} = 1$ and $S_L = -½$ ($J = -2{,}943\ cm^{-1}$). The second two-electron reduction leading by reaction of 2 KC_8 to the 36 e^- monocationic diamagnetic $[(^3PDI_2)Co_2(\mu\text{-Cl})(PMe_3)_2]^+$ complex, with a $(\sigma)^2/(\sigma^*)^2$ configuration, results in the absence of metal–metal bond. Here we are in the combination $(^3PDI_2)^{3-}/(Co_2)^{5+}/d^{13}$ and the two electron reduction of the tricationic complex adds electron density to the $^3PDI_2$ π* system.

For the 37 e^- $[(^3PDI_2)Ni_2(\mu\text{-Cl})(PMe_3)_2]^{2+}$ complex, the 2.7140 (4) Å distance between the Ni atoms is consistent with a half-order bond as for $[(^3PDI_2)Co_2(\mu\text{-Cl})(PMe_3)_2]^{2+}$. The electron configuration is $(\delta_1)^2$, $(\delta_1^*)^2$, $(\pi_1)^2$, $(\pi_1^*)^2$, $(\pi_2)^2$, $(\pi_2^*)^2$, $(\sigma)^2$, $(\sigma^*)^1$, $(\delta_2)^1$, $(\delta_2^*)^1$, and due to the bonding of δ_2 and antibonding of δ_2* characters that cancel each other out, the Ni-Ni system presents a net σ-bond with a formal order of 0.5. The configuration is considered as $(^3PDI_2)^0/(Ni_2)^{3+}/d^{17}$ even it neglects the small amount of electron density transfer into the $^3PDI_2$ π* system. The one-electron reduction into the 38 e^- $[(^3PDI_2)Ni_2(\mu\text{-Cl})(PMe_3)_2]^+$ complex results in a doubly occupied σ* orbital so that the configuration is now $(\delta_1)^2$, $(\delta_1^*)^2$, $(\pi_1)^2$, $(\pi_1^*)^2$, $(\pi_2)^2$, $(\pi_2^*)^2$, $(\sigma)^2$, $(\sigma^*)^2$. The δ_2 and δ_2* orbitals remain singly occupied, so that this species is paramagnetic ($S = 1$) and the two Nickel atoms are distant of

3.2104 (4) Å. The electron transfer occurred mainly on the ligand, which becomes $(^3PDI_2)^-$ and is associated to $(Ni_2)^{3+}$ and a d^{17} electron count [154].

This analysis shows that adding one electron to a dinuclear framework in which the two metal centers are maintained in close contact by a redox-active ligand in which two pyridyldiimines components are linked by two propyl chains, which give some geometrical flexibility, results in an electronic repartition on the complex. This reaction is not a specific addition of one electron on the ^{3}PDI part of the ligand, nor on the bimetallic platform.

Concerning the four-electron reduction of O_2 in H_2O catalyzed by the (μ-1,2-peroxo) dicobalt(III) complex shown in Fig. 38, $[Co^{III}$(terpy)(μ-bis(pyridyl)-pyrazolate)(μ-1,2-O_2)(terpy)$Co^{III}]^{3+}$ is obtained by reaction of O_2 under ambient conditions in methanol with the $[Co^{II}(\mu\text{-Cl})Co^{II}]^{2+}$ complex having the same N-containing ligands [167]. This μ-1,2-peroxo complex catalyzes the four-electron reduction of O_2 to water using octamethylferrocene, $Fe(CpMe_4)_2$ or more efficiently $Fe(CpMe_5)_2$ with trifluoroacetic acid as H^+ source:

$$4\ Fe(CpMe_4)_2 + \left[Co^{III}(\mu - O_2)Co^{III}\right]^{3+} + 4\ H^+ \rightarrow 4\ Fe(CpMe_4)_2{}^+ + \left[Co^{II} - Co^{II}\right]^{3+} + 2\ H_2O$$

The catalytic cycle (Fig. 49) shows that the reaction proceeds through an electron transfer of 1 e^- to reduce the intermediate species, and by protonation; the proton-coupled electron transfer (PCET) which transforms the $[Co^{III}(\mu\text{-}O_2)Co^{III}]^{3+}$ species into the $[Co^{III}(OH)(O^{\cdot})Co^{III}]^{4+}$ intermediate is the rate-determining step, and involves the $[Co^{II}(\mu\text{-}O_2)Co^{III}]^{3+}$ intermediate. A further PCET reaction results in the formation of $[Co^{III}(OH_2)(H_2O)Co^{III}]^{3+}$ species, which needs two 1-e^- steps to give $[Co^{II}(OH_2)(H_2O)Co^{III}]^{3+}$ and then the dicobalt(II) $[Co^{II}(OH_2)(H_2O)Co^{II}]^{3+}$ complex which regenerates the μ-1,2-peroxo complex.

The $[Co^{II}(\mu\text{-Cl})Co^{II}]^{2+}$ complex can be oxidized by 2 equivalent of Ce^{IV} in MeCN to provide the $[Co^{III}$(terpy)(μ-bis(pyridyl)pyrazolate)$(H_2O)(OH)$(terpy)-$Co^{III}]^{4+}$ complex in which the aqua and hydroxo ligands are coordinated to the two Co^{III} metal centers sharing a proton [167]. This compound catalyzes the 4e^- reduction of O_2 by octa- or decamethylferrocene into water in the presence of trifluoroacetic acid, as efficiently as the $[Co^{III}(\mu\text{-}O_2)Co^{III}]^{3+}$ species. It undergoes a three-e^- reduction by 3 equivalent of $Co(Cp)_2$ to give the $[Co^{II}(H_2O)(OH)Co^{I}]^+$ intermediate, which is protonated, in an equilibrium step, into the hydrido $[Co^{II}(OH_2)(OH)(H)Co^{III}]^{2+}$ species [168]. Further reaction with a proton produces H_2 by heterolytic cleavage and the $[Co^{II}(OH_2)(OH)Co^{III}]^{3+}$ complex in the rate-determining step of the catalytic production of hydrogen. In the final step, this later species reacts with $[Co^{II}(OH_2)(H_2O)Co^{I}]^+$ to give two equivalents of the $[Co^{II}(H_2O)(OH)Co^{II}]^{2+}$.

The $[LCo^{II}{}_2(OTf)_2](OTf)_2$ complex presents two consecutive one-electron reductions $Co^{II}Co^{II}$ to $Co^{II}Co^{I}$ and $Co^{II}Co^{I}$ to $Co^{I}Co^{I}$ processes, consistent with a weak

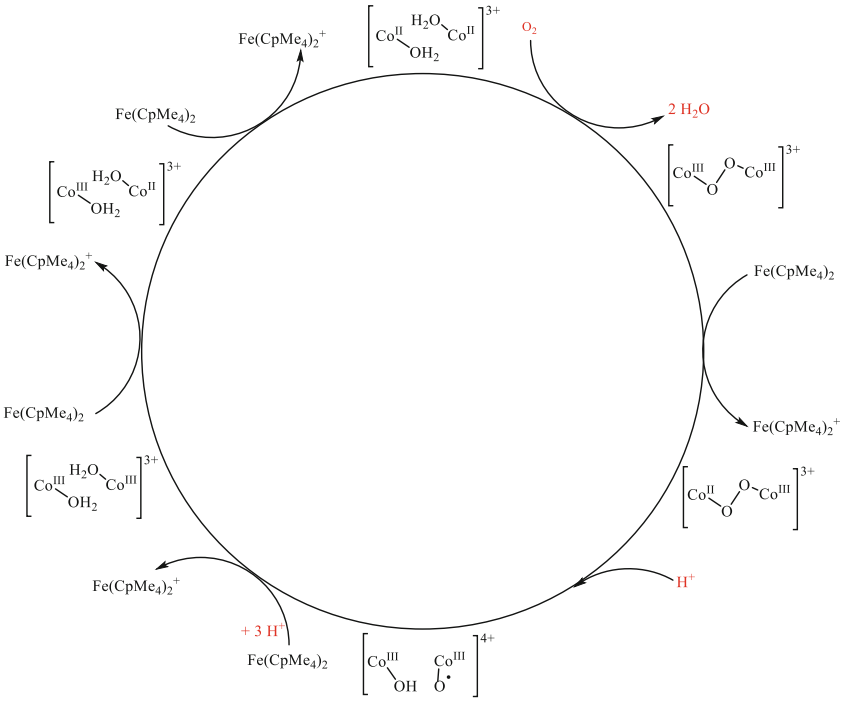

Fig. 49 Catalytic cycle for the $4e^-$ reduction of O_2 by $Fe(CpMe_4)_2$ into water in the presence of CF_3COOH, catalyzed by the dinuclear Co^{III} peroxo complex $[Co^{III}(terpy)(\mu\text{-bis(pyridyl)pyrazolate})(\mu\text{-}1,2\text{-}O_2)(terpy)Co^{III}]^{3+}$

electronic communication between the two Cobalt metal centers through the pyridazine bridge [146].

Epoxidation of an alkene can be catalyzed by the $[(Bipy)(H_2O)Ru^{II}(\mu\text{-bimp})Ru^{II}(H_2O)(Bipy)]^{3+}$ complex, obtained by dissolution of the $[(Bipy)Ru^{II}(\mu\text{-Cl})Ru^{II}(Bipy)]^{2+}$ complex in a CF_3SO_3H aqueous solution at pH 1. As summarized in Fig. 50, a dinuclear ruthenium catalyst containing the bis-facial $bimp^-$ bridging ligand is used to perform the epoxidation of alkenes [169]. The *trans* isomer, in which the two bipyridine ligands are located on opposite sides of the distorted plane formed by the pyrazolate framework, is more stable than the *cis* isomer. The bis-aqua complex is active in the epoxidation of *cis*-β-methylstyrene, in the presence of the PhIO oxidant with an epoxide selectivity of 88% for a complete conversion and an initial turnover frequency of 73 min^{-1} and a turnover number of 1760. The active species is the *trans*-$O = Ru^{IV}\text{-}Ru^{IV}{=}O$ intermediate for which one Ru = O group transfers its oxygen atom, whereas the second one interacts with H atom(s) of the substrate. A series of $1e^-/1\ H^+$ steps are necessary to transform the $[(Bipy)(H_2O)Ru^{II}(\mu\text{-bimp})Ru^{II}(H_2O)(Bipy)]^{3+}$ complex into the $O = Ru^{IV}\text{-}Ru^{IV}{=}O$ active species (Fig. 50).

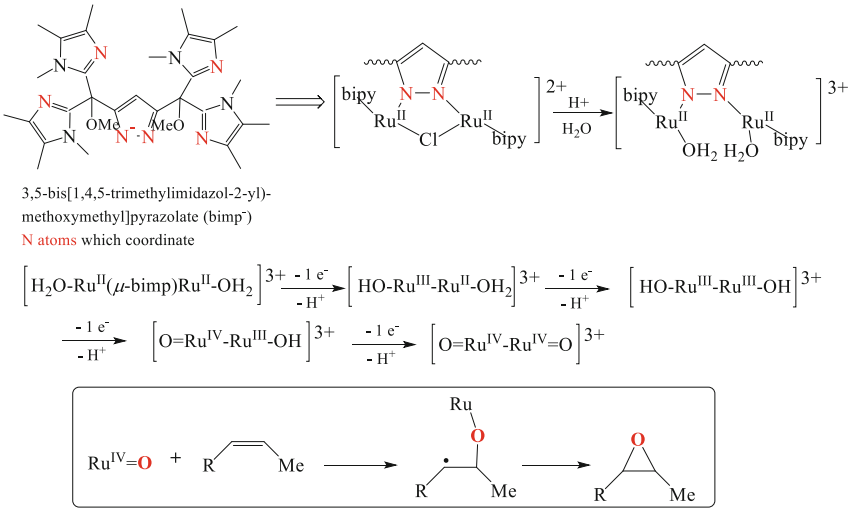

Fig. 50 $1e^-/1\ H^+$ steps involved in the catalytic cycle of the epoxidation of an alkene

The same epoxidation reaction can be carried out with water as source of oxygen in combination with sunlight [170]. A dye-sensitized photoelectrosynthesis cell allows coproducing dihydrogen. At the photoanode the $[(H_2O)Ru^{II}\text{-}Ru^{II}(H_2O]$ complex, in which the bridging ligand is pyrazolate-3,5-dicarboxylate and each metal center coordinates the tridentate 2,2′:6,2″-terpyridine ligand, the water-soluble 4-styrene sulfonic acid is transformed into the epoxide, that in acidic medium is hydrolyzed to the diol:

At the anode: $(HSO_3S)PhCH{=}CH_2 + H_2O \rightarrow (HSO_3S)PhCHOCH_2 + 2\ H^+ + 2\ e^-$ giving $(HSO_3S)PhCH(OH)\text{-}CH_2OH$ in acidic water.

At the cathode: $2\ H^+ + 2\ e^- \rightarrow H_2$

The active species is $[O = Ru^{IV}\text{-}Ru^{IV}{=}O]$ and the epoxidation transforms it into $[(HO)\text{-}Ru^{II}\text{-}Ru^{II}\text{-}(OH)]$, which requires two steps to regenerate it via $[(HO)Ru^{III}\text{-}Ru^{IV}{=}O]$. Protons diffusing through a H^+ exchange membrane to a Pt cathode are transformed into H_2.

Thus, it is important to underline that a bridging dinucleating ligand has a main role in the delocalization of the electron density over the two metals, particularly when they present a mixed valence.

4 Conclusions

In the absence of a bridging ligand, the two metal $2e^-$ reduction of a substrate ($1e^-$ on each metal) implies first its coordination in between the two metal centers. This coordination implies either no oxidation of the metal (Co) or the oxidation of the two metals (U, Ln, Mg, Ca), as well as the possible presence of two binding sites on the

reactant. The reaction of a substrate like CO_2, CO needs their reduction and this is why oxidants like Ti(III), U(III), Ln(II), or Mg(I) are very efficient. The Mg (I) reactivity appears to be very similar to that observed for the f-elements so that, in the present case, Mg(I) is "transition metal"-like.

Bridging ligands, which maintain the two metal centers in close vicinity, but have no significant role as redox systems, play an important role due to the transmission of electronic effects between the two centers and for the approach of the reactant, to which the steric effects can add a determining influence. Not only the chirality of a bidentate ligand can be exerted on the complex where the substrate comes in coordination between the two metal centers, but the presence of a Lewis acid metal center in a close vicinity of a basic metal center can determine the approach of the substrate, as well its orientation to perform a $1e^{-}$-$1e^{-}$ oxidative addition, and/or the $1e^{-}$-$1e^{-}$ reductive elimination. Thus, suitable ligands need to be synthesized for holding two metals in close proximity, with or without a metal–metal bond, and for accommodating electronic effects and structural changes along the catalytic steps.

Sophisticated ligands, having multi-coordination sites, can be synthesized to maintain the right distance between the two metal centers, with sometimes some structural flexibility, so that they present somewhat the same oxidation state, whereas along the various catalytic activation steps the redox characteristics of these ligands play a pro-active role. Most of the time these ligands contain Nitrogen coordination centers and unsaturated systems, and their reactivity is more deeply understood, due to mechanistic and DFT theoretical studies.

In the last part, which is focused on the $1e^{-}$ reactions occurring on one metal center, we take into account the bimetallic systems where a succession of reactions occurs, and are often called biomimetic, or bioinspired catalysts. Recent mechanistic and theoretical studies have shown that a reaction, which is $1e^{-}$-$1e^{-}$ in the balance sheet, is in fact the succession of $1e^{-}$ and chemical reactions, such as protonation, so that it is better to extract the concepts that guide toward the right coordination sphere of the bimetallic complexes. Interestingly, as for the redox-active ligands, these systems allow obtaining active catalytic systems involving metals from the first line, particularly Nickel, Iron, and Cobalt.

References

1. Sternberg HW, Greenfield H, Friedel RA, Wotiz J, Markby R, Wender I (1954) Metallo-organic complex derived from dicobalt octacarbonyl and acetylenes. J Am Chem Soc 76: 1457–1458
2. Sly WG (1959) The molecular configuration of dicobalt hexacarbonyl diphenylacetylene. J Am Chem Soc 81:18–20
3. Dickson RS, Fraser PJ (1974) Compounds derived from alkynes and carbonyl complexes of cobalt. Adv Organometal Chem 12:323–377
4. Dickson RS, Yawney DBW (1967) Transition metal complexes of substituted alkynes. I. 3,3,3-Trifluoropropyne complexes of iron and cobalt. Aust J Chem 20:77–84

5. Dickson RS, Yawney DBW (1968) Transition metal complexes of substituted alkynes. II Pentafluorophenylacetylene complexes of iron and cobalt. Aust J Chem 21:97–102
6. Dickson RS, Yawney DBW (1968) Transition metal complexes of substituted alkynes. III. A dicyanoacetylene cobalt carbonyl complex. Aust J Chem 21:1077–1080
7. Cotton FA, Jamerson JD, Stultz BR (1976) Metal-metal multiple bonds in organometallic compounds. I. (di-*tert*-butylacetylene)hexacarbonyldiiron and -dicobalt. J Am Chem Soc 98: 1774–1779
8. Khand IU, Knox GR, Pauson PL, Watts WE (1973) Organocobalt complexes. I. Arene complexes derived from dodecacarbonyltetracobalt. J Chem Soc Perkin Trans 1:975–977
9. Pauson PL, Khand IU, Knox GR, Watts WE (1971) Cobalt-induced cleavage reaction and a new series of arenecobalt carbonyl complexes. J Chem Soc D Chem Comm 36
10. Khand IU, Knox GR, Pauson PL, Watts WE, Foreman MI, Organocobalt complexes. II. (1973) Reaction of acetylenehexacarbonyl dicobalt complexes, $(RC2R_1)Co_2(CO)_6$, with norbornene and its derivatives. J Chem Soc Perkin Trans 1:977–981
11. Pauson PL (1985) The Khand reaction. A convenient and general route to a wide range of cyclopentenone derivatives. Tetrahedron 41:5855–5860
12. Rautenstrauch V, Megard P, Conesa J, Kuester W (1990) 2-pentyl-2-cyclopenten-1-one from catalytic Pauson-Khand reactions. Angew Chem Int Ed 29:1413–1416
13. Magnus P, Principe LM (1985) Origins of 1,2- and 1,3-stereoselectivity in dicobaltoctacarbonyl alkene-alkyne cyclizations for the synthesis of substituted bicyclo [3.3.0]octenones. Tetrahedron Lett 26:4851–4854
14. La Belle BE, Knudsen MJ, Olmstead MM, Hope H, Yanuck MD, Schore NE (1985) Synthesis of 11-oxatricyclo[5.3.1.$0^{2,6}$]undecane derivatives via organometallic cyclizations. J Org Chem 50:5215–5222
15. Li G, Li Q-S, Xie Y, King RB, Schaefer HFI (2009) (Acetylene)dicobalt carbonyl derivatives: decarbonylation of the $H_2C_2Co_2(CO)_6$ tetrahedrane. Organometallics 28:3390–3394
16. Moulton BE (2010) The Pauson-Khand reaction. Organometal Chem 36:93–120
17. Yamanaka M, Nakamura E (2001) Density functional studies on the Pauson-Khand reaction. J Am Chem Soc 123:1703–1708
18. Lesage D, Milet A, Memboeuf A, Blu J, Greene AE, Tabet J-C, Gimbert Y (2014) The Pauson-Khand revisited: origin of CO in the final product. Angew Chem Int Ed 53:1939–1942
19. Manton JC, Cerpentier FJR, Harvey EC, Clark IP, Greetham GM, Long C, Pryce MT (2019) Photochemical or electrochemical bond breaking – exploring the chemistry of (μ_2-alkyne) $Co_2(CO)_6$ complexes using time-resolved infrared spectroscopy, spectro-electrochemical and density functional methods. Dalton Trans 48:14642–14652
20. Boyle NM, Coleman AC, Long C, Ronayne KL, Browne WR, Feringa BL, Pryce MT (2010) Evidence for cobalt-cobalt bond homolysis and wavelength-dependent CO loss in (μ_2-alkyne) $Co_2(CO)_6$ complexes. Inorg Chem 49:10214–10216
21. Dominguez G, Perez-Castells J (2011) Recent advances in [2+2+2] cycloaddition reactions. Chem Soc Rev 40:3430–3444
22. Agenet N, Gandon V, Vollhardt KPC, Malacria M, Aubert C (2007) Cobalt-catalyzed cyclotrimerization of alkynes: the answer to the puzzle of parallel reaction pathways. J Am Chem Soc 129:8860–8871
23. Yamamoto K, Nagae H, Tsurugi H, Mashima K (2016) Mechanistic understanding of alkyne cyclotrimerization on mononuclear and dinuclear scaffolds: [4 + 2] cycloaddition of the third alkyne onto metallacyclopentadienes and dimetallacyclopentadienes. Dalton Trans 45:17072–17081
24. Wu P, Zeng Y, Fan Q, Feng H, Xie Y, King RB, Schaefer HFI (2014) Flyover compounds and bridging bent benzene derivatives as intermediates in the cobalt carbonyl cyclotrimerization of alkynes. Organometallics 33:2352–2357
25. Roglans A, Pla-Quintana A, Sola M (2021) Mechanistic studies of transition-metal-catalyzed [2 + 2 + 2] cycloaddition reactions. Chem Rev 121:1894–1979

26. Mills OS, Robinson G (1964) The structure of an organocobalt intermediary in the synthesis of ortho-substituted t-butylbenzenes. Proc Chem Soc 187
27. Dickson RS, Yawney DBW (1969) Transition metal complexes of substituted alkynes. IV. Some bridging alkyne-cobalt complexes. Aust J Chem 22:533–541
28. Dickson RS, Fraser PJ (1970) Transition metal complexes of substituted alkynes. VI. Substituent arrangement in some bridging tris(alkyne)-cobalt complexes. Aust J Chem 23:475–480
29. Dickson RS, Fraser PJ, Gatehouse BM (1972) Crystal and molecular structure of a racemic complex: μ-[1-3,6-η: 1,4-6-η-1,3,6-tris(trifluoromethyl)-1,3,5-hexatriene-1,6-diyl]bis (dicarbonylcobalt)(Co-Co). J Chem Soc Dalton Trans 20:2278–2282
30. Hübel W, Braye EH, Clauss A, Weiss E, Krüerke U, Brown DA, King GSD, Hoogzand C (1959) Organometallic complexes. I. Reaction of metal carbonyls with acetylenic compounds. J Inorg Nucl Chem 9:204–210
31. Hübel W, Hoogzand C (1960) Die cyclisierende Trimerisierung von Alkinen mit Hilfe von Metallcarbonyl-Verbindungen. Chem Ber 93:103–115
32. Krüerke U, Hübel W (1961) Über Organometall-Komplexe. VIII. Reaktionen von Kobaltcarbonyl-Verbindungen mit Alkinen. Chem Ber 94:2829–2856
33. Krüerke U, Hoogzand C, Hübel W, Vanhee G (1961) Über Organometall-Komplexe. VI. 1,2,4-tri-tert-butylbenzol. Chem Ber 94:2817–2820
34. Bennett MA, Donaldson PB (1978) Isolation of intermediates in the dicobalt octacarbonyl-catalyzed cyclotrimerization of cyclooctyne. Crystal and molecular structure of a cobaltacyclopentadiene complex. Inorg Chem 17:1995–2000
35. Battaglia LP, Delledonne D, Nardelli M, Predieri G, Chiusoli GP, Costa M, Pelizzi C (1989) Activation of unsaturated substrates by cobalt complexes. Crystal structure and reactivity of a complex of dicobalt octacarbonyl with N-methylbis(α,α-dimethylpropargyl)amine. J Organomet Chem 363:209–222
36. Predieri G, Tiripicchio A, Tiripicchio Camellini M, Costa M, Sappa E (1992) Formation of metallacycles from terminal diynes with geminal methyl groups α to the triple bonds. Synthesis and crystal structure of $Co_2(CO)_5[(HC{\equiv}CCMe_2)_2NMe]$, an intermediate in cobalt-catalyzed organic syntheses. J Organomet Chem 423:129–139
37. Moldes I, Papworth T, Ros J, Alvarez-Larena A, Piniella JF (1995) The structure of $[Co_2(CO)_5(\mu^2,\eta^4\text{-CPhCHCHCPh})]$ a cobalt analog of the 'ferroles'. J Organomet Chem 489: C65–C67
38. Henkel T, Klauck A, Seppelt K (1995) Pentafluoro-λ^6-sulfanylacetylene complexes of cobalt. J Organomet Chem 501:1–6
39. Gervasio G, Sappa E, Marko L (1993) Synthesis and crystal structure of $[Co_2(CO)_4(PhCCC(O)CH_3)_3]$. Its role in the cyclotrimerization of 1-phenylbut-1-yn-3-one to 1,3,5-triphenyltris (carboxymethyl)benzene. J Organomet Chem 444:203–209
40. Giordano R, Sappa E, Predieri G (1995) Reactions of $Co_2(CO)_8$ with RC_2R' alkynes. Part II . Synthesis of $Co_2(CO)_6(RC_2R')$ complexes; oligomerization or cyclotrimerization reactions of substituted acetylenes. Inorg Chim Acta 228:139–146
41. Baxter RJ, Knox GR, Pauson PL, Spicer MD (1999) Synthesis of dicarbonyl(η^4-tricarbonylcobaltacyclopentadiene)cobalt complexes from $Co_2(CO)_8$. A general route to intermediates in cobalt carbonyl mediated alkyne trimerization. Organometallics 18:197–205
42. Baxter RJ, Knox GR, Moir JH, Pauson PL, Spicer MD (1999) Formation of arenes and of tetracarbonyl(hexatrienediyl)dicobalt ("Flyover") complexes from $Co_2(CO)_8$. Organometallics 18:206–214
43. Tsurugi H, Laskar P, Yamamoto K, Mashima K (2018) Bonding and structural features of metal-metal bonded homo- and hetero-dinuclear complexes supported by unsaturated hydrocarbon ligands. J Organomet Chem 869:251–263
44. Hollingsworth RL, Beattie JW, Grass A, Martin PD, Groysman S, Lord RL (2018) Reactions of dicobalt octacarbonyl with dinucleating and mononucleating bis(imino)pyridine ligands. Dalton Trans 47:15353–15363

45. Nicholas K, Bray LS, Davis RE, Pettit R (1971) Tetracarbonyldi-μ-2,2,5,5-tetramethylhex-3-yne-di-iron. A novel complex containing an iron-iron double bond. Chem Commun 12:608
46. Lipschutz MI, Chantarojsiri T, Dong Y, Tilley TD (2015) Synthesis, characterization, and alkyne trimerization catalysis of a heteroleptic two-coordinate FeI complex. J Am Chem Soc 137:6366–6372
47. Witzke RJ, Hait D, Chakarawet K, Head-Gordon M, Don Tilley T (2020) Bimetallic mechanism for alkyne cyclotrimerization with a two-coordinate Fe precatalyst. ACS Catal 10:7800–7807
48. Doerksen RS, Hodik T, Hu G, Huynh NO, Shuler WG, Krische MJ (2021) Ruthenium-catalyzed cycloadditions to form 5-, 6- and 7-membered rings. Chem Rev 121:4045–4083
49. Lindner E, Jansen RM, Mayer HA, Hiller W, Fawzi R (1989) Preparation, properties, and reactions of metal-containing heterocycles. 65. The behavior of tetracarbonyl(η^2-ethene)ruthenium toward activated alkenes and alkynes. Organometallics 8:2355–2360
50. Yamamoto Y, Miyabe Y, Itoh K (2004) Synthesis of a dinuclear ruthenabicyclic complex and its ligand-substitution reactions. Eur J Inorg Chem:3651–3661
51. Tilney-Bassett JF, Mills OS (1959) Cyclopentadienylnickel-acetylene complexes. J Am Chem Soc 81:4757–4758
52. Tilney-Bassett JF (1961) Cyclopentadienylnickel-acetylene complexes. J Chem Soc:577–581
53. Fischer EO, Palm C (1958) Aromatic complexes of metals. XVII. Cyclopentadienyt-metal carbonyls of nickel. Chem Ber 91:1725–1731
54. Mills OS, Shaw BW (1968) Carbon compounds of the transition metals. XI. The structure of (diphenylacetylene)bis(cyclopentadienylnickel). J Organomet Chem 11:595–600
55. Lin C-Y, Power PP (2017) Complexes of Ni(I): a "rare" oxidation state of growing importance. Chem Soc Rev 46:5347–5399
56. Day VW, Abdel-Meguid SS, Dabestani S, Thomas MG, Pretzer WR, Muetterties EL (1976) Metal clusters in catalysis. 7. Molecular structure and chemical properties of a novel metal-metal bonded nickel complex. J Am Chem Soc 98:8289–8291
57. Eckert NA, Bones EM, Lachicotte RJ, Holland PL (2003) Nickel complexes of a bulky β-diketiminate ligand. Inorg Chem 42:1720–1725
58. Pfirrmann S, Yao S, Ziemer B, Stosser R, Driess M, Limberg C (2009) β-Diketiminato nickel (I) complexes with very weak ligation allowing for H_2 and N_2 activation. Organometallics 28: 6855–6860
59. Bai G, Wei P, Stephan DW (2005) A β-diketiminato-nickel(II) synthon for nickel (I) complexes. Organometallics 24:5901–5908
60. Yao S, Driess M (2012) Lessons from isolable nickel(I) precursor complexes for small molecule activation. Acc Chem Res 45:276–287
61. Czerny F, Searles K, Sot P, Teichert JF, Menezes PW, Copéret C, Driess M (2021) Well-defined, silica-supported homobimetallic nickel hydride hydrogenation catalyst. Inorg Chem 60:5483–5487
62. Bottomley F, Brintzinger HH (1978) Reactions of nitrogen oxides with di(cyclopentadienyl)-titanium complexes. JCS Chem Comm:234–235
63. Fachinetti G, Floriani C, Chiesi-Villa A, Guastini C (1979) Carbon dioxide activation. Deoxygenation and disproportionation of carbon dioxide promoted by bis(cyclopentadienyl)-titanium and -zirconium derivatives. A novel bonding mode of the carbonato and a trimer of the zirconyl unit. J Am Chem Soc 101:1767–1775
64. Brennan JG, Andersen RA, Zalkin A (1986) Chemistry of trivalent uranium metallocenes: electron-transfer reactions with carbon disulfide. Formation of $[(RC_5H_4)_3U]_2[\mu\text{-}\eta^1\text{-}\eta^2\text{-}CS_2]$. Inorg Chem 25:1756–1760
65. Brennan JG, Andersen RA, Zalkin A (1986) Chemistry of trivalent uranium metallocenes: electron-transfer reactions. Synthesis and characterization of $[(MeC_5H_4)_3U]_2E$ (E = S, Se, Te) and the crystal structures of hexakis(methylcyclopentadienyl)sulfidodiuranium and tris (methylcyclopentadienyl)(triphenylphosphine oxide)uranium. Inorg Chem 25:1761–1765

66. Berthet J-C, Le Maréchal J-F, Nierlich M, Lance M, Vigner J, Ephritikhine M (1991) Synthesis and crystal structure of the oxo-bridged bimetallic organouranium complex $[(Me_3SiC_5H_4)_3U]_2[\mu\text{-}O]$. J Organomet Chem 408:335–341
67. Castro-Rodriguez I, Meyer K (2005) Carbon dioxide reduction and carbon monoxide activation employing a reactive uranium(III) complex. J Am Chem Soc 127:11242–11243
68. Castro L, Lam OP, Bart SC, Meyer K, Maron L (2010) Carbonate formation from CO_2 via oxo versus oxalate pathway: theoretical investigations into the mechanism of uranium-mediated carbonate formation. Organometallics 29:5504–5510
69. Labouille S, Nief F, Maron L (2011) Theoretical treatment of redox processes involving lanthanide(II) compounds: reactivity of organosamarium(II) and organothulium (II) complexes with CO_2 and pyridine. J Phys Chem A 115:8295–8301
70. Green SP, Jones C, Stasch A (2007) Stable magnesium(I) compounds with Mg-Mg bonds. Science 318:1754–1757
71. Platts JA, Overgaard J, Jones C, Iversen BB, Stasch A (2011) First experimental characterization of a non-nuclear attractor in a dimeric magnesium(I) compound. J Phys Chem A 115: 194–200
72. Kefalidis CE, Stasch A, Jones C, Maron L (2014) On the mechanism of the reaction of a magnesium(I) complex with CO_2: a concerted type of pathway. Chem Commun 50:12318–12321
73. Bonyhady SJ, Green SP, Jones C, Nembenna S, Stasch A (2009) A dimeric magnesium (I) compound as a facile two-center/two-electron reductant. Angew Chem Int Ed 48:2973–2977
74. Jones C, McDyre L, Murphy DM, Stasch A (2010) Magnesium(I) reduction of benzophenone and anthracene: first structural characterisation of a magnesium ketyl. Chem Commun 46: 1511–1513
75. Bonyhady SJ, Jones C, Nembenna S, Stasch A, Edwards AJ, McIntyre GJ (2010) β-Diketiminate-stabilized magnesium(I) dimers and magnesium(II) hydride complexes: synthesis, characterization, adduct formation, and reactivity studies. Chem A Eur J 16:938–955
76. Stasch A, Jones C (2011) Stable dimeric magnesium(I) compounds: from chemical landmarks to versatile reagents. Dalton Trans 40:5659–5672
77. Gentner TX, Rösch B, Ballmann G, Langer J, Elsen H, Harder S (2019) Low valent magnesium chemistry with a super bulky β-diketiminate ligand. Angew Chem Int Ed 58:607–611
78. Rösch B, Gentner TX, Eyselein J, Friedrich A, Langer J, Harder S (2020) Mg-Mg bond polarization induced by a superbulky β-diketiminate ligand. Chem Commun 56:11402–11405
79. Rösch B, Gentner TX, Langer J, Färber C, Eyselein J, Zhao L, Ding C, Frenking G, Harder S (2021) Dinitrogen complexation and reduction at low-valent calcium. Science 371:1125–1128
80. de Bruin-Dickason CN, Rosengarten CA, Deacon GB, Jones C (2021) Enantiopure dimagnesium(I) and magnesium(II) hydride complexes incorporating chiral amidinate or β-diketiminate ligands. Chem Commun 57:1599–1602
81. Goswami VE, Walli A, Förster M, Dechert S, Demeshko S, Holthausen MC, Meyer F (2017) Acid/base triggered interconversion of $\mu\text{-}\eta^2\text{:}\eta^2$-peroxido and bis(μ-oxido) dicopper intermediates capped by proton-responsive ligands. Chem Sci 8:3031–3037
82. Sigman MS, Harper KC, Bess EN, Milo A (2016) The development of multidimensional analysis tools for asymmetric catalysis and beyond. Acc Chem Res 49:1292–1301
83. Jeong N, Sung BK, Kim JS, Park SB, Seo SD, Shin JY, In KY, Choi YK (2002) Pauson-Khand-type reaction mediated by Rh(I) catalysts. Pure Appl Chem 74:85–91
84. Shibata T, Takagi K (2000) Iridium-chiral diphosphine complex catalyzed highly enantioselective Pauson-Khand-type reaction. J Am Chem Soc 122:9852–9853
85. Shibata T, Kobayashi Y, Maekawa S, Toshida N, Takagi K (2005) Iridium-catalyzed enantioselective cycloisomerization of nitrogen-bridged 1,6-enynes to 3-azabicylo[4.1.0] heptenes. Tetrahedron 61:9018–9024
86. Derdau V, Laschat S, Dix I, Jones PG (1999) Cobalt-alkyne complexes with diphosphine ligands as mechanistic probes for the Pauson-Khand reaction. Organometallics 18:3859–3864

87. Orgué S, Leon T, Riera A, Verdaguer X (2015) Asymmetric intermolecular cobalt-catalyzed Pauson-Khand reaction using a P-stereogenic bis-phosphane. Org Lett 17:250–253
88. Imamoto T, Sugita K, Yoshida K (2005) An air-stable P-chiral phosphine ligand for highly enantioselective transition-metal-catalyzed reactions. J Am Chem Soc 127:11934–11935
89. Garçon M, Cabre A, Verdaguer X, Riera A (2017) Synthesis, coordination study, and catalytic Pauson-Khand reactions of QuinoxP*$(CO)_4$-μ-alkyne dicobalt complexes. Organometallics 36:1056–1065
90. Hiroi K, Watanabe T, Kawagishi R, Abe I (2000) Asymmetric catalytic Pauson-Khand reactions with chiral phosphine ligands: dramatic effects of substituents in 1,6-enyne systems. Tetrahedron Lett 41:891–895
91. Hiroi K, Watanabe T, Kawagishi R, Abe I (2000) Catalytic use of chiral phosphine ligands in asymmetric Pauson-Khand reactions. Tetrahedron Asymm 11:797–808
92. Sturla S, Buchwald SL (2002) Cobalt-phosphite-catalyzed asymmetric Pauson-Khand reaction. J Org Chem 67:3398–3403
93. Schmid TM, Consiglio G (2004) Asymmetric cyclocarbonylation of 1,6-enynes with cobalt catalysts. Tetrahedron Asym 15:2205–2208
94. Gibson SE, Kaufmann KAC, Loch JA, Steed JW, White AJP (2005) A study of [Co_2(alkyne)(binap)$(CO)_4$] complexes (BINAP=(1,1′-binaphtalene)-2,2′-diylbis(diphenylphosphine)). Chem A Eur J 11:2566–2576
95. Pellissier H, Clavier H (2014) Enantioselective cobalt-catalyzed transformations. Chem Rev 114:2775–2823
96. Simeonov SP, Nunes JPM, Guerra K, Kurteva VB, Afonso CAM (2016) Synthesis of chiral cyclopentenones. Chem Rev 116:5744–5893
97. Pellissier H (2018) Recent developments in enantioselective cobalt-catalyzed transformations. Coord Chem Rev 360:122–168
98. Pellissier H (2020) Enantioselective cobalt-catalysed transformations. In: Hapke M, Hilt G (eds) Cobalt catalysis in organic synthesis. Wiley Online Library, pp 337–416
99. Yoshikai N (2019) Recent advances in enantioselective C-C bond formation via organocobalt species. Synthesis 51:135–145
100. Cabré A, Riera A, Verdaguer X (2020) P-Stereogenic amino-phosphines as chiral ligands: from privileged intermediates to asymmetric catalysis. Acc Chem Res 53:676–689
101. Man ML, Lam KC, Sit WN, Ng SM, Zhou Z, Lin Z, Lau CP (2006) Synthesis of heterobimetallic Ru-Mn complexes and the coupling reactions of epoxides with carbon dioxide catalyzed by these complexes. Chem A Eur J 12:1004–1015
102. Buonerba A, De Nisi A, Grassi A, Milione S, Capacchione C, Vagin S, Rieger B (2015) Novel iron(III) catalyst for the efficient and selective coupling of carbon dioxide and epoxides to form cyclic carbonates. Cat Sci Technol 5:118–123
103. Miyazaki T, Tanabe Y, Yuki M, Miyake Y, Nishibayashi Y (2011) Synthesis of group IV (Zr, Hf)-group VIII (Fe, Ru) heterobimetallic complexes bearing metallocenyl diphosphine moieties and their application to catalytic dehydrogenation of amine-boranes. Organometallics 30:2394–2404
104. Miyake Y, Nomaguchi Y, Yuki M, Nishibayashi Y (2007) Synthesis and reactivity of diphosphine-bridged diruthenium complexes. Organometallics 26:3611–3613
105. Nguyen T, Sutton AD, Brynda M, Fettinger JC, Long GJ, Power PP (2005) Synthesis of a sable compound with fivefold bonding between two chromium(I) centers. Science 310:844–847
106. Tsai Y-C, Chen H-Z, Chang C-C, Yu J-SK, Lee G-H, Wang Y, Kuo T-S (2009) Journey from Mo-Mo quadruple bonds to quintuple bonds. J Am Chem Soc 131:12534–12535
107. Brynda M, Gagliardi L, Widmark P-O, Power PP, Roos BO (2006) A quantum chemical study of the quintuple bond between two chromium centers in [PhCrCrPh]: *trans*-bent versus linear geometry. Angew Chem Int Ed 45:3804–3807

108. La Macchia G, Li Manni G, Todorova TK, Brynda M, Aquilante F, Roos BO, Gagliardi L (2010) On the analysis of the Cr-Cr multiple bond in several classes of dichromium compounds. Inorg Chem 49:5216–5222
109. Noor A, Tamne ES, Qayyum S, Bauer T, Kempe R (2011) Cycloaddition reactions of a chromium-chromium quintuple bond. Chem A Eur J 17:6900–6903
110. Shen J, Yap GPA, Werner J-P, Theopold KH (2011) Reactions of a quintuply bonded chromium dimer with alkynes. Chem Commun 47:12191–12193
111. Huang Y-S, Huang G-T, Liu Y-L, Yu J-SK, Tsai Y-C (2017) Reversible cleavage/formation of the chromium-chromium quintuple bond in the highly regioselective alkyne cyclotrimerization. Angew Chem Int Ed 56:15427–15431
112. Chen H-Z, Liu S-C, Yen C-H, Yu J-SK, Shieh Y-J, Kuo T-S, Tsai Y-C (2012) Reactions of metal-metal quintuple bonds with alkynes: [2+2+2] and [2+2] cycloadditions. Angew Chem Int Ed 51:10342–10346
113. Bosch BE, Bruemmer I, Kunz K, Erker G, Froehlich R, Kotila S (2000) Structural characterization of heterodimetallic Zr/Pd and Zr/Rh catalyst precursors containing the $C_5H_4PPh_2$ ligand. Organometallics 19:1255–1261
114. Cornelissen C, Erker G, Kehr G, Froehlich R (2005) Chemistry of metal-metal-bonded early-late heterobimetallics: cooperative reactions of functional groups at a persistent organometallic Zr-Rh framework. Organometallics 24:214–225
115. Cornelissen C, Erker G, Kehr G, Froehlich R (2004) Formation and reactions of metal-metal bonded heterobimetallic ($C_5H_4PR_2$)-bridged (Zr-Ir) and (Zr-Rh) complexes: evidence for the participation of metal hydride intermediates. Dalton Trans:4059–4063
116. Erker G, Kehr G, Froehlich R (2006) Group 4 bent metallocenes and functional groups — finding convenient pathways in a difficult terrain. Coord Chem Rev 250:36–46
117. Chirik PJ, Wieghardt K (2010) Radical ligands confer nobility on base-metal catalysts. Science 327:794–795
118. Hollingsworth RL, Bheemaraju A, Lenca N, Lord RL, Groysman S (2017) Divergent reactivity of a new dinuclear xanthene-bridged bis(iminopyridine) di-nickel complex with alkynes. Dalton Trans 46:5605–5616
119. Zhou Y-Y, Hartline DR, Steiman TJ, Fanwick PE, Uyeda C (2014) Dinuclear nickel complexes in five states of oxidation using a redox-active ligand. Inorg Chem 53:11770–11777
120. Steiman TJ, Uyeda C (2015) Reversible substrate activation and catalysis at an intact metal–metal bond using a redox-active supporting ligand. J Am Chem Soc 137:6104–6110
121. Hartline DR, Zeller M, Uyeda C (2016) Well-defined models for the elusive dinuclear intermediates of the Pauson-Khand reaction. Angew Chem Int Ed 55:6084–6087
122. Zhou Y-Y, Uyeda C (2019) Catalytic reductive [4+1]-cycloadditions of vinylidenes and dienes. Science 363:857–862
123. Zhou Y-Y, Uyeda C (2016) Reductive cyclopropanations catalyzed by dinuclear nickel complexes. Angew Chem Int Ed 55:3171–3175
124. Pal S, Zhou Y-Y, Uyeda C (2017) Catalytic reductive vinylidene transfer reactions. J Am Chem Soc 139:11686–11689
125. Powers IG, Kiattisewee C, Mullane KC, Schelter EJ, Uyeda C (2017) A 1,2-addition pathway for C(sp^2)-H activation at a dinickel imide. Chem A Eur J 23:7694–7697
126. Powers IG, Andjaba JM, Zeller M, Uyeda C (2020) Catalytic C(sp^2)-H amination reactions using dinickel imides. Organometallics 39:3794–3801
127. Hartline DR, Zeller M, Uyeda C (2017) Catalytic carbonylative rearrangement of norbornadiene via dinuclear carbon-carbon oxidative addition. J Am Chem Soc 139:13672–13675
128. Braconi E, Cramer NA (2020) A chiral naphthyridine diimine ligand enables nickel-catalyzed asymmetric alkylidenecyclopropanations. Angew Chem Int Ed 59:16425–16429
129. Farley CM, Uyeda C (2019) Organic reactions enabled by catalytically active metal-metal bonds. Trends Chem 1:497–509

130. Uyeda C, Farley CM (2021) Dinickel active sites supported by redox-active ligands. Acc Chem Res 54:3710–3719
131. Behlen MJ, Zhou Y-Y, Steiman TJ, Pal S, Hartline DR, Zeller M, Uyeda C (2017) Dinuclear oxidative addition reactions using an isostructural series of Ni_2, Co_2, and Fe_2 complexes. Dalton Trans 46:5493–5497
132. Dutta I, De S, Yadav S, Mondol R, Bera JK (2017) Aerobic oxidative coupling of alcohols and amines towards imine formation by a dicopper(I,I) catalyst. J Organomet Chem 849–850:117–124
133. Dutta I, Sarbajna A, Pandey P, Rahaman SMW, Singh K, Bera JK (2016) Acceptorless dehydrogenation of alcohols on a diruthenium(II,II) platform. Organometallics 35:1505–1513
134. Davenport TC, Tilley TD (2011) Dinucleating naphthyridine-based ligand for assembly bridged dicopper(I) centers: three-center two electron bonding involving an acetonitrile donor. Angew Chem Int Ed 50:12205–12208
135. Davenport TC, Ahn HS, Ziegler MS, Tilley TD (2014) A molecular structural analog of proposed dinuclear active sites in cobalt-based water oxidation catalysts. Chem Commun 50: 6326–6329
136. Brodsky CN, Passard G, Ullman AM, Jaramillo DE, Bloch ED, Huynh M, Gygi D, Costentin C, Nocera DG (2018) Oxygen activation at a dicobalt centre of a dipyridylethane naphthyridine complex. Dalton Trans 47:11903–11908
137. Ziegler MS, Levine DS, Lakshmi KV, Tilley TD (2016) Aryl group transfer from tetraarylborato anions to an electrophilic dicopper(I) center and mixed-valence μ-aryl dicopper(I,II) complexes. J Am Chem Soc 138:6484–6491
138. Ziegler MS, Torquato NA, Levine DS, Nicolay A, Celik H, Tilley TD (2018) Dicopper alkyl complexes: synthesis, structure, and unexpected persistence. Organometallics 37:2807–2823
139. Ziegler MS, Lakshmi KV, Tilley TD (2017) Dicopper Cu(I)Cu(I) and Cu(I)Cu(II) complexes in copper-catalyzed azide−alkyne cycloaddition. J Am Chem Soc 139(15):5378–5386
140. Desnoyer AN, Nicolay A, Rios P, Ziegler MS, Tilley TD (2020) Bimetallics in a nutshell: complexes supported by chelating naphthyridine-based ligands. Acc Chem Res 53:1944–1956
141. Wang Q, Brooks SH, Liu T, Tomson NC (2021) Tuning metal–metal interactions for cooperative small molecule activation. Chem Commun 57:2839–2853
142. Arima H, Wada M, Nakazono T, Wada T (2021) Tuning oxygen reduction catalysis of dinuclear cobalt polypyridyl complexes by the bridging structure. Inorg Chem
143. Gimbert-Suriñach C, Moonshiram D, Francàs L, Planas N, Bernales V, Bozoglian F, Guda A, Mognon L, López I, Hoque MA, Gagliardi L, Cramer CJ, Llobet A (2016) Structural and spectroscopic characterization of reaction intermediates involved in a dinuclear Co−hbpp water oxidation catalyst. J Am Chem Soc 138:15291–15294
144. Vogiatzis KD, Polynski MV, Kirkland JK, Townsend J, Hashemi A, Liu C, Pidko EA (2019) Computational approach to molecular catalysis by 3d transition metals: challenges and opportunities. Chem Rev 119:2453–2523
145. Neudeck S, Maji S, Lopez I, Meyer S, Meyer F, Llobet A (2014) New powerful and oxidatively rugged dinuclear Ru water oxidation catalyst: control of mechanistic pathways by tailored ligand design. J Am Chem Soc 136:24–27
146. Di Giovanni C, Gimbert-Surinach C, Nippe M, Benet-Buchholz J, Long JR, Sala X, Llobet A (2016) Dinuclear cobalt complexes with a decadentate ligand scaffold: hydrogen evolution and oxygen reduction catalysis. Chem A Eur J 22:361–369
147. König H, Eickmeier C, Möller M, Rodewald U, Franck B (1990) Synthesis of a bisvinylogous octaethylporphyrin. Angew Chem Int Ed 29:1393–1395
148. Saha R, Chattaraj PK (2018) Acivation of small molecules (H_2, CO_2, N_2O, CH_4, and C_6H_6) by a porphyrinoid-based dimagnesium(I) complex, an electride. ACS Omega 3:17199–17211
149. Manz D-H, Duan P-C, Dechert S, Demeshko S, Oswald R, John M, Mata RA, Meyer F (2017) Pairwise H_2/D_2 exchange and H_2 substitution at a bimetallic dinickel(II) complex featuring two terminal hydrides. J Am Chem Soc 139:16720–16731

150. Duan P-C, Schulz RA, Römer A, Van Kuiken BE, Dechert S, Demeshko S, Cutsail III GE, De Boer S, Mata RA, Meyer F (2021) Ligand protonation triggers H_2 release from a dinickel dihydride complex to give a doubly "T"-shaped dinickel(I) metallodiradical. Angew Chem Int Ed 60:1891–1896
151. Duan P-C, Manz D-H, Dechert S, Demeshko S, Meyer F (2018) Reductive O_2 binding at a dihydride complex leading to redox interconvertible μ-1,2-peroxo and μ-1,2-superoxo dinickel (II) intermediates. J Am Chem Soc 140:4929–4939
152. Ferretti E, Dechert S, Meyer F (2019) Reductive binding and ligand-based redox transformations of nitrosobenzene at a dinickel(II) core. Inorg Chem 58:5154–5162
153. Kothe T, U-Uyun K, Dechert S, Meyer F (2020) Reductive binding of nitro substrates at a masked dinickel(I) complex and proton-coupled conversion to reduced nitroso ligands. Inorg Chem 59:14207–14217
154. Wang Q, Zhang S, Cui P, Weberg AB, Thierer LM, Manor BC, Gau MR, Carroll PJ, Tomson NC (2020) Interdependent metal-metal bonding and ligand redox-activity in a series of dinuclear macrocyclic complexes of iron, cobalt, and nickel. Inorg Chem 59:4200–4214
155. Zhang S, Wang Q, Thierer LM, Weberg AB, Gau MR, Carroll PJ, Tomson NC (2019) Tuning metal−metal interactions through reversible ligand folding in a series of dinuclear iron complexes. Inorg Chem 58:12234–12244
156. Liu T, Gau MR, Tomson NC (2020) Mimicking the constrained geometry of a nitrogen-fixation intermediate. J Am Chem Soc 142:8142–8146
157. Liu T, Murphy RP, Carroll PJ, Gau MR, Tomson NC (2022) C−C σ-bond oxidative addition and hydrofunctionalization by a macrocycle-supported diiron complex. J Am Chem Soc 144: 14037–14041
158. Zhang S, Cui P, Liu T, Wang Q, Longo TJ, Thierer LM, Manor BC, Gau MR, Carroll PJ, Papaefthymiou GC, Tomson NC (2020) N-H bond formation at a diiron bridging nitride. Angew Chem Int Ed 59:15215–15219
159. Denny JA, Darensbourg MY (2015) Metallodithiolates as ligands in coordination, bioinorganic, and organometallic chemistry. Chem Rev 115:5248–5273
160. Gennari M, Duboc C (2020) Bio-inspired, multifunctional metal−thiolate motif: from electron transfer to sulfur reactivity and small-molecule activation. Acc Chem Res 53:2753–2761
161. Wang L, Gennari M, Barrozo A, Fize J, Philouze C, Demeshko S, Meyer F, Orio M, Artero V, Duboc C (2020) Role of the metal ion in bio-inspired hydrogenase models: investigation of a homodinuclear FeFe complex vs its heterodinuclear NiFe analogue. ACS Catal 10:177–186
162. Ghosh AC, Duboc C, Gennari M (2021) Synergy between metals for small molecule activation: enzymes and bio-inspired complexes. Coord Chem Rev 428:213606
163. Sun L, Adam SM, Mokdad W, David R, Milet A, Artero V, Duboc C (2022) A bio-inspired heterodinuclear hydrogenase CoFe complex. Faraday Discuss 234:34–41
164. Wang L, Gennari M, Cantú Reinhard FG, Guttierrez J, Morozan A, Philouze C, Demeshko S, Artero V, Meyer F, de Visser SP, Duboc C (2019) A non-heme diiron complex for (electro)-catalytic reduction of dioxygen: tuning the selectivity through electron delivery. J Am Chem Soc 141:8244–8253
165. Wang L, Gennari M, Cantú Reinhard FG, Padamati SK, Philouze C, Flot D, Demeshko S, Browne R, Browne WR, Meyer F, de Visser SP, Duboc C (2020) O_2 activation by non-heme thiolate-based dinuclear Fe complexes. Inorg Chem 59:3249–3259
166. Kim RS, Nazemi A, Cundari TR, Surendranath Y (2020) A Pd^{III} sulfate dimer initiates rapid methane monofunctionalization by H atom abstraction. ACS Catal 10:14782–14792

167. Fukuzumi S, Mandal S, Mase K, Ohkubo K, Park H, Benet-Buchholz J, Nam W, Llobet A (2012) Catalytic four-electron reduction of O_2 via rate-determining proton-coupled electron transfer to a dinuclear cobalt-μ-1,2-peroxo complex. J Am Chem Soc 134:9906–9909
168. Mandal S, Shikano S, Yamada Y, Lee Y-M, Nam W, Llobet A, Fukuzumi S (2013) Protonation equilibrium and hydrogen production by a dinuclear cobalt-hydride complex reduced by cobaltocene with trifluoroacetic acid. J Am Chem Soc 135:15294–15297
169. Aguiló J, Francàs L, Bofill R, Gil-Sepulcre M, García-Antón J, Poater A, Llobet A, Escriche L, Meyer F, Sala X (2015) Powerful bis-facially pyrazolate-bridged dinuclear ruthenium epoxidation catalyst. Inorg Chem 54:6782–6791
170. Farras P, Di Giovanni C, Clifford JN, Garrido-Barros P, Palomares E, Llobet A (2016) Light driven styrene epoxidation and hydrogen generation using H_2O as an oxygen source in a photoelectrosynthesis cell. Green Chem 18:255–260

Top Organomet Chem (2023) 70: 207–234
https://doi.org/10.1007/3418_2022_78

Published online: 5 January 2023

Magnetism in Binuclear Compounds: Theoretical Insights

Rémi Maurice, Talal Mallah, and Nathalie Guihéry

Contents

Abstract This chapter is devoted to theoretical calculations aimed at determining the electronic structure of binuclear complexes, including isotropic and anisotropic interactions in both the strong and in the weak-exchange coupling limits. The theory of effective Hamiltonians is used to extract magnetic anisotropy terms in various regimes and in particular those for which the giant-spin approximation holds. While only a second-rank symmetric tensor is necessary to describe the zero-field splitting

R. Maurice (✉)
Univ Rennes, CNRS, ISCR (Institut des Sciences Chimiques de Rennes) – UMR 6226, Rennes, France

SUBATECH, UMR CNRS 6457, IN2P3/IMT Atlantique/Université de Nantes, Nantes, France
e-mail: remi.maurice@univ-rennes1.fr

T. Mallah
Institut de Chimie Moléculaire et des Matériaux d'Orsay (ICMMO), UMR CNRS 8182 – Bât. Henri Moissan, 17, avenue des Sciences, Université Paris-Saclay, Orsay, France
e-mail: talal.mallah@universite-paris-saclay.fr

N. Guihéry (✉)
Laboratoire de Chimie et Physique Quantiques, UMR 5626, Université de Toulouse 3, Paul Sabatier, Toulouse, France
e-mail: nathalie.guihery@irsamc.ups-tlse.fr

in centrosymmetric compounds with a single electron on each metal ion, a 4-rank tensor must also be introduced to describe the anisotropic exchange in the case of two unpaired electrons per metal ion. The magnitude of these additional interactions was found to be larger than those of the well admitted 2-rank tensor. Even though, the magnetic anisotropy of binuclear complexes can often be predicted from the knowledge of the local anisotropy of its mononuclear constituents, the large magnitude of the 4-rank tensor makes theoretical calculations important if not mandatory to rationalize experimental results on firm grounds in systems where anisotropic binuclear interactions are important.

Keywords Ab initio calculations · Binuclear compounds · Dzyaloshinskii–Moriya interaction · Effective Hamiltonian theory · Isotropic and anisotropic exchange · Magnetic anisotropy · Model Hamiltonians · Spin–orbit coupling · Zero-field splitting

1 Introduction

Remarkable properties of matter such as magnetism [1], magnetoresistive effects [2], molecular bistability [3], superconductivity [4], or multiferroicity [5] offer interesting prospects for technological applications in various fields. One may quote, for instance, magnetic levitation trains, energy storage with zero loss, information storage and even quantum computing [6]. As they result from the quantum behavior of the matter, they have also been the subject of fundamental research in quantum mechanics (quantum tunneling, quantum interferences, coherence/de-coherence phenomena, etc.), solid-state physics, and chemistry. Systems that house such properties have unpaired electrons and exhibit magnetic properties. They can be of different sizes ranging from mononuclear complexes (zero dimension, 0D) to nanoparticles and correlated materials (1D, 2D, and 3D). Intense efforts have been devoted to the understanding of the microscopic origin of magnetic properties. This requires analyzing both the weak interactions due to relativistic effects, responsible for the single-molecule magnet (SMM) behavior, for instance [7], and the interactions between magnetic centers.

From the theoretical point of view, binuclear complexes are the smallest systems where the effect of exchange coupling on magnetic anisotropy can be thoroughly studied. This allows getting insight into the physical properties of large nuclearity species and high dimesional materials. Experimental results on the determination of anisotropy parameters in binuclear complexes are scarce because of the difficulty to extract and evaluate the relative magnitude of the different parameters from spectroscopic data [8–12]. Theory allows one to understand why it is so difficult to experimentally characterize such systems and was successfully used in several key cases [13–17].

Beyond, the understanding of the mechanism of anisotropic exchange, binuclear species were used to successfully slow down the magnetic relaxation of molecular magnets [18–23]. In addition, binuclear complexes based on lanthanides were proposed in the field of molecular quantum information as models for quantum gates due to the magnetic anisotropy of metal ions and the presence of weak antiferromagnetic exchange coupling [24, 25]. Models of potential quantum gates based on binuclear transition metal ions were also proposed [26–28].

This book chapter focuses on the theoretical determination of the low-energy spectra and wave functions of mononuclear and binuclear compounds from which all significant interactions can be obtained. Part of our ambition is to provide rationalization of complex properties from the understanding of what governs the magnitude and nature of microscopic interactions.[1]

2 Model Hamiltonians and Their Extraction from Theoretical Calculations

2.1 Why Model Hamiltonians Are Mandatory for the Description of Magnetic Systems?

The lowest-energy wave functions of highly correlated materials cannot be described using a single electronic configuration (e.g., with a single Slater determinant). The zeroth order description of a magnetic system having N unpaired electrons (spins) in N orbitals must deal with all distributions of the spins in all the orbitals. As a consequence, for an infinite size system, an infinite space has to be considered. Moreover, as the low-energy spectrum of a magnetic system is quasi-degenerate, a high precision is required. To reach the suitable accuracy, theoretical descriptions should also account for the interaction among all the other electrons (core electrons of the magnetic centers and ligand electrons) and with the magnetic electrons, i.e. appropriate descriptions must treat dynamic electron correlation. Finally, as one is interested in anisotropic magnetic interactions, relativistic effects must be accounted for. For these reasons, both experimentalists in charge of the characterization of the magnetic properties and solid-state physicists who model the collective properties of magnetic materials consider Hamiltonians that are simpler than the exact electronic one. These Hamiltonians are called model Hamiltonians. The model space on which they are spanned only considers the most important electronic configurations and the interactions between these configurations are called model interactions. It is important to note that model interactions are effective interactions

[1] Parts of this chapter concerning magnetism are reused from the Habilitation to direct research of Rémi Maurice: Maurice, R (2018) On the role of relativistic effects on the structural, physical and chemical properties of molecules and materials. Habilitation to direct research, Université de Nantes (UNAM), https://hal.archives-ouvertes.fr/tel-02308305.

which, even if they appear as being simple interactions (such as hopping integrals or exchange integrals) result from much more complicated electronic mechanisms in terms of the reference non-relativistic or relativistic molecular Hamiltonian.

2.2 *Theoretical Tools for the Extraction of Model Interactions*

2.2.1 Theoretical Calculations

The first calculations performed on magnetic systems concerned the coupling between magnetic centers. As it will be shown later, the coupling is considered as effective interaction of the Heisenberg Dirac van Vleck (HDVV) model [29–31]. Once known, they permit one to reproduce the low-energy spectrum, i.e. the energy of all the spin states belonging to a given electronic configuration. Both density functional theory (DFT) and wave function theory (WFT) methods can be used to determine the magnetic coupling. As it will be rationalized later in this chapter, the best available method up to date is the "difference dedicated configuration interaction" (DDCI) method [32]. The values reported here have been computed using this method implemented in either the ORCA [33] or CASDI [34] codes.

At low temperature, a lift of degeneracy is observed between the various M_S components of the spin states in the absence of magnetic fields. This zero-field splitting (ZFS) is due to relativistic effects [35]. Various methods have been developed in the last decades to compute or extract ZFS parameters from the outcomes of quantum mechanical calculations. Following the pioneering work of McWeeny and Mizuno on the so-called spin–spin coupling [36], various perturbative and linear response approaches have been designed to compute the ZFS parameters within DFT or WFT frameworks that do include spin–spin coupling and/or spin–orbit coupling terms [37–43]. One should note that the perturbative and linear response theory based DFT approaches do not lead to values in agreement with experimental results in the case of nickel(II) complexes [44], although satisfactory accuracy can be obtained in the case of other d^n configurations, e.g. in the case of manganese(II) or manganese(III) complexes (with d^5 and d^4 configurations, respectively) [45, 46]. Therefore, WFT based approaches are recommended because they usually lead to accurate values in the case of any d^n configuration [15, 45–53]. Although one can use second-order perturbation theory to compute ZFS parameters [40], a more popular approach nowadays consists in performing spin–orbit configuration interaction (SOCI) calculations. Within the contracted scheme, the electronic energy plus spin–orbit coupling matrix is diagonalized in a second step [54, 55]. In order to obtain more accurate excitation energies on the diagonal of this matrix [56, 57], additional electron correlation is introduced after the multi-configurational self-consistent field (MCSCF) step, typically at a multireference perturbation theory (MRPT) level or multireference configuration interaction (MRCI) level. Note that more recently, an alternative multiconfiguration and multistate pair-density

functional theory (MC-PDFT) has been proposed with the objective of combining stakes of both WFT and DFT [58]. In any case, after the SOCI step, the ZFS parameters and the magnetic anisotropy axes can be determined with the effective Hamiltonian theory [47], or with the pseudospin approach of Chibotaru and Ungur [59]. Values reported here have been computed using the SOCI method implemented in both the ORCA and MOLCAS codes and extracted using the effective Hamiltonian theory [33, 60].

2.2.2 The Effective Hamiltonian Theory

This section briefly presents the effective Hamiltonian theory applied to the extraction of magnetic interactions. From the energies and wave functions computed with sophisticated quantum chemistry methods, it is possible to extract in a rational way all the interactions of a model Hamiltonian using this theory. As we will not enter into details, we encourage the interested reader to refer to more specialized books or articles [61–63].

The basic idea consists in looking for an effective Hamiltonian that is spanned in a model space constituted of only the most important electron distributions and keeping only the most important interactions. This Hamiltonian is simpler than the exact electronic Hamiltonian but must perfectly reproduce the spectrum of low energy of the studied compounds [64]. In the des Cloizeaux formalism [65], it satisfies:

$$\widehat{H}^{\text{eff}}\widetilde{\Psi}_i = E_i\widetilde{\Psi}_i \tag{1}$$

where E_i and $\widetilde{\Psi}_i$ are, respectively, the energies and orthogonalized projections onto the model space of the wavefunctions of the exact electronic Hamiltonian. As the energies and wavefunctions of the exact electronic Hamiltonian are computed ab initio all matrix elements of this effective Hamiltonian can be calculated numerically using the following expression:

$$\widehat{H}^{\text{eff}}_{\text{kl}} = \langle k|\sum_i E_i|\widetilde{\Psi}_i\Big\rangle\Big\langle\widetilde{\Psi}_i||l\rangle \tag{2}$$

The model Hamiltonian is then assimilated to the effective Hamiltonian. To perform the extraction, one writes down the analytical expression of all matrix elements of the model Hamiltonian as functions of the model interactions. From a one-to-one correspondence between each of the numerical and analytical matrix elements and by resolution of the then generated system of equations, a value can eventually be attributed to all model interactions.

It is worthwhile to note that the projections of the wavefunctions onto the model space are calculated. The validity of the model space can therefore be checked and the model can be improved by introducing additional electron distributions in the

model space when required. As all matrix elements are numerically computed, additional operators (and therefore interactions) can be introduced if necessary. Such a method enables one to question the validity of any model Hamiltonian to extract in a rational way appropriate interactions and to refine existing models (and even help in proposing new and adequate models).

3 Mononuclear Compounds

In mononuclear systems, such as mononuclear transition metal complexes, the M_S components of an orbitally non-degenerate state may split and mix in the absence of any external perturbation. This effect, referred to as ZFS, can only occur for states with $S > 1/2$. It is well known that it can be observed in the presence of an anisotropic ligand field around the paramagnetic center of interest, and relates to relativistic effects (essentially spin–orbit coupling). Derivations of ZFS parameters with simple ligand–field and spin–orbit coupling Hamiltonians can be found in textbooks such as Griffith [66], and Abragam and Bleaney [67]. A typical configuration to illustrate these types of derivations is the d^8 one, nickel(II) complexes, for instance. Within an octahedral ligand field, it can be easily shown that the spin components of the ground $^3A_{2g}$ remain degenerate. If one considers an axially distorted field, the M_S components of this ground state (labeled $^3B_{1g}$ in the D_{4h} symmetry point group) are no longer three-fold degenerate. If one considers an appropriate coordinate frame (for which the quantization axis is oriented along the axial distortion), it can be easily shown that:

$$E(M_S = 0) = -\frac{2\varsigma^2}{\Delta_2} \tag{3}$$

and

$$E(M_S = -1) = E(M_S = 1) = -\frac{\varsigma^2}{\Delta_1} - \frac{\varsigma^2}{\Delta_2} \tag{4}$$

where ς is the (effective) monoelectronic spin–orbit coupling constant of nickel(II), Δ_1 is the "in-plane" electronic excitation energy (corresponding to a $x^2-y^2 \rightarrow xy$ orbital excitation), and Δ_2 is the "out-of-plane" electronic excitation energy (corresponding to an appropriate combination of $x^2-y^2 \rightarrow xz$ and $z^2 \rightarrow xz$ excitations and/or to a combination of $x^2-y^2 \rightarrow yz$ and $z^2 \rightarrow yz$ excitations). The splitting between the $M_S = 0$ and the $|M_S| = 1$ components can be effectively described by the following model Hamiltonian:

$$\widehat{H}_1 = D\left(\widehat{S}_Z^2 - \frac{1}{3}\widehat{S}^2\right) \tag{5}$$

where D is the "axial" ZFS parameter. Thus, one can express this parameter in terms of both the electronic excitation energies and the ς constant:

$$D = -\frac{\varsigma^2}{\Delta_1} + \frac{\varsigma^2}{\Delta_2} \tag{6}$$

If the symmetry of the field is further lowered, the $|M_S| = 1$ components of the ground orbital state split; appropriate linear combinations of these components are formed. As previously, one can recast the problem in terms of a simple model Hamiltonian:

$$\widehat{H}_2 = D\left(\widehat{S}_Z^2 - \frac{1}{3}\widehat{S}^2\right) + E\left(\widehat{S}_X^2 - \widehat{S}_Y^2\right) = D\left(\widehat{S}_Z^2 - \frac{1}{3}\widehat{S}^2\right) + \frac{E}{2}\left(\widehat{S}_+^2 - \widehat{S}_-^2\right) \tag{7}$$

where E is the "rhombic" ZFS parameter. Naturally, the D and E parameters can also be derived from a ligand-field theory perspective (equations not shown here for the sake of simplicity) [15, 68]. In the general case (i.e., in the absence of specific symmetry elements), the "natural" quantization axis is not known, and one needs to consider a symmetric second-rank ZFS tensor:

$$\widehat{H}_3 = \widehat{S}\overline{\overline{D}}\widehat{S} \tag{8}$$

After having determined the $\overline{\overline{D}}$ tensor components in an arbitrary axes frame, diagonalization of this tensor gives access to its principal axes. The axial and rhombic ZFS parameters can be easily determined from the diagonal elements of this tensor in this frame (i.e., its eigenvalues). By convention, the axial ZFS parameter is chosen to be at least three times larger than the rhombic one in absolute value (such that $|\frac{E}{D}| \leq \frac{1}{3}$). This convention fixes the Z anisotropy axis, while another convention must discriminate the X and Y ones (note that two different conventions are commonly used in the literature, $E \geq 0$ or $\frac{E}{D} \geq 0$). If D is negative, Z is the "easy" axis of magnetization, while it is the "hard" one if D is positive. This model Hamiltonian, $\widehat{S}\overline{\overline{D}}\widehat{S}$, also describes the ZFS in $S = \frac{3}{2}$ systems with orbitally non-degenerate ground states, such as nearly tetrahedral cobalt(II) complexes (d^7 configuration). Values of the ZFS parameters for the Ni(II) and Co(II) complexes (represented in Fig. 1) are compared to experimental ones in Table 1. These values have been computed using the SOCI method [54, 55], implemented in the MOLCAS code [60], and extracted using the effective Hamiltonian method [47].

For larger spin quantum numbers ($S \geq 2$), additional terms may have to be introduced in the model Hamiltonian to describe properly the energy levels and to ensure a good correspondence between the model vectors and the "true" wave functions:

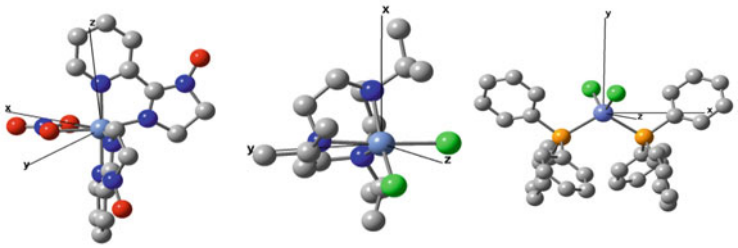

Fig. 1 The $[Ni(HIM2\text{-}py)_2NO_3]^+$, $[Ni(iPrtacn)Cl_2]$, $[CoCl_2(PPh_3)_2]$ compounds, respectively, referred to as compounds **1**, **2,** and **3** in Table 1. The magnetic anisotropy axes are indicated [47]

Table 1 Computed and experimental (electron paramagnetic resonance) values of the ZFS parameters for the Ni(II) and Co(II) complexes represented in Fig. 1 [47]

Compound number	ZFS (cm^{-1})	Calculated values	Exp. values
1	*D*	−10.60	−10.15[a]
	E	0.76	0.10[a]
2	*D*	+16.45	+15.70[b]
	E	3.82	3.40[b]
3	*D*	−14.84	−14.76[c]
	E	0.54	1.14[c]

[a] Values from Rogez et al. [69]
[b] Values from Krzystek et al. [70]
[c] Values from Rebilly et al. [71]

$$\widehat{H}_4 = \widehat{\vec{S}}\overline{\overline{D}}\widehat{S} + \sum_{q=-k}^{k}\sum_{k=4}^{2S} B_k^q \widehat{O}_k^q \tag{9}$$

where k is the rank of the involved spherical tensor and is even, q may be odd, and $\widehat{O}_k^q$ are extended Stevens operators [67, 72–74]. The interested reader can have an example of the extraction of these additional interactions with the effective Hamiltonian approach in an article of Maurice et al. [75]

4 Binuclear Compounds

In polynuclear compounds two different approaches can be used. In the first one, referred to as the giant-spin approximation, only the lift of degeneracy of the M_S components of the ground spin states is described. Nevertheless, a more generalized definition will be presented here which allows one to deal with various spin states. It is expected to be appropriate when the ground spin state is well separated energetically from the first excited spin state, i.e. for strongly coupled spins. This model will be presented in the first following subsection. The second approach designated as the

multispin approximation describes all the states resulting from the coupling of the local ground states of all the paramagnetic ions. In this model both isotropic and anisotropic interactions between the magnetic centers are at work. In a second subsection, firstly the isotropic spin model will be introduced and the physical content of its leading interactions will be recalled. We will then concentrate on the various anisotropic interactions of this more refined model.

4.1 Giant-Spin Approximation and Its Generalization to a Block-Spin Approach

Anisotropic interactions can modify substantially low-energy spectra by splitting and mixing the M_S components of each spin state that arise from the previously described isotropic interactions, as well as by mixing components or linear combinations of components that belong to different spin "states." The mixing of components belonging to different spin states is usually referred to as "spin mixing" or "*S* mixing" [76, 77]. This spin mixing arises from spin–orbit coupling. One should note that symmetry rules apply, and that some types of spin mixings can be symmetry forbidden. Two main types of coupling between different spin-state components can occur, couplings between (1) M_S components belonging to *S* and *S* + 1 states, and (2) M_S components belonging to S and S + 2 states. In the former case, this coupling is dominated by the "direct," i.e. first-order, spin–orbit coupling between these components [14, 78]. If the system of interest possesses a symmetry center, these terms vanish by symmetry. In the latter case, the interaction is "indirect," i.e. at second order of perturbation, that is, involves spin components of states that do not belong to a model space spanned by the M_S components of all the spin states generated by the isotropic interactions (e.g., the M_S components of the lowest quintet, triplet, and singlet states of a nickel(II)-nickel(II) binuclear complex) [14, 75]. Note that these two types of couplings will be later attributed to different types of effective interactions in terms of the multispin model (see Sect. 4.2.2). If these coupling matrix elements are negligible with respect to the isotropic interaction (s), i.e. in the "strong-exchange limit," one can consider a block-diagonal model matrix [79, 80], which can be referred to as the "block-spin model" [49, 62]. In this case, the different spin blocks can be dealt with independently, and each spin block effectively described as if it were belonging to a mononuclear system, i.e. using $\widehat{H}_4$ if an arbitrary coordinate frame is considered, or as follows if the magnetic anisotropy axes frame of the spin block of interest is considered:

$$\widehat{H}_5 = D\left(\widehat{S}_Z^2 - \frac{1}{3}\widehat{S}^2\right) + \frac{E}{2}\left(\widehat{S}_+^2 - \widehat{S}_-^2\right) + \sum_{n=0}^{k}\sum_{k=4}^{2S} B_k^n \widehat{O}_k^n \qquad (10)$$

where *n* is the rank of the involved spherical tensor and is even, and $\widehat{O}_k^n$ are standard Stevens operators. Note that when only a large *S* ground spin block is considered, it

is usually referred to as the "giant-spin approximation" in the literature. If spin mixing is only a perturbation of the block spin picture, which can be seen as an "intermediate-exchange regime," one can add additional operators that are distinct from the extended/standard Stevens operators to effectively account for its effect on the energy levels of the block of interest. This task was achieved for describing the $S = 2$ block of centrosymmetric nickel(II)-nickel(II) binuclear complexes by Maurice et al. [75], which in principle also gives access to the effective stabilization or destabilization of the $S = 0$ level that is due to the mixing with spin components of the $S = 2$ block (in the case of antiferromagnetic or ferromagnetic coupling, respectively) [49]. If the spin mixing and the standard block-spin terms are of the same order of magnitude, as is the case in the "weak-exchange limit," one should stress that the use of giant-spin or block-spin approximations is problematic, and that no systematic studies have been performed to discuss the consequences of these approximations on the parameter values that are extracted from experiments.

Concerning the computation of giant-spin or block-spin parameter values, a wide range of examples, including the "classical" Mn_{12} SMM [38], has been reported in the literature based on DFT and perturbation theory. These works usually lead to D parameter values in good agreement with experimental ones [38, 81–87]. However, since, as mentioned previously, current DFT implementations to compute ZFS parameters seem to be largely off for the local anisotropy of nickel(II) paramagnetic centers [44], it would be interesting to see which values would be computed for nickel based SMMs such as Ni_4 ones [88]. Concerning WFT, only few studies have been reported that concern the $[Ni_2(en)_4Cl_2]^{2+}$ (en = ethylenediamine) complex [14, 75], and also model nickel(II)-nickel(II) binuclear complexes [89]. Concerning the $[Ni_2(en)_4Cl_2]^{2+}$ complex, the comparison of reliable computational data and experimental data is problematic since no rhombic parameters were introduced in the latest experimental parameter determination [90], while calculations showed significant rhombic parameter values for the $S = 2$ and $S = 1$ blocks. For the $S = 2$ block, the computed D value, $-3.0\ cm^{-1}$, is a bit larger in absolute value than the experimental one, $-1.8\ cm^{-1}$, although still in reasonable agreement with it. Therefore, it can be seen as a successful application of WFT to the giant-spin problem. Note that similar quality results have been obtained on the previously quoted Ni_4 complex [91], with consistent estimates ranging from 1/2 to 3/4 of the experimental value. Concerning the study of the model systems and the D and E parameters and the $S = 2$ and $S = 1$ blocks, it appeared that the corresponding D parameters tend to have opposite signs, although no strong correlation between these two parameters was found [89]. Moreover, the D parameter of the $S = 1$ block seems to be always larger in absolute value than the one of the $S = 2$ block by a factor that ranges from 2 to 5 [89].

4.2 The Multispin Approximation

In the multispin approximation, the model space is constituted of all the products of the atomic ground states M_S components. As a consequence, the diagonalization of this model gives access to all M_S components of the states of the configuration, and not only to those of a single spin state as it was the case for the giant-spin model. For instance, considering a complex constituted of two Ni(II) ions ($S = 1$) ions, the coupling between the local triplets will generates 9 states issued from the quintet, triplet, and singlet spin states. In the next paragraphs, both isotropic and anisotropic interactions will be introduced following increasing complexity reasoning.

4.2.1 Isotropic Exchange

The HDVV model is an isotropic spin Hamiltonian [29–31]. It is relevant for the description of magnetic systems for which a large gap exists between the electronic ground state of the magnetic centers and their locally excited or ionized states. In such cases, the space which spans the model Hamiltonian can be restricted to products of local ground spin states and the only degrees of freedom are the M_S components of the spins of the magnetic centers. One should note that the spatial configurations can be omitted since these are assumed to be essentially the same for all the states and therefore the working basis is only constituted of pure spin functions. This spin Hamiltonian has the following expression for a binuclear system constituted of two magnetic centers A and B:

$$\begin{aligned}\widehat{H}_6^{HDvV} &= J\widehat{S}_A.\widehat{S}_B = J\left(\widehat{S}_{Z_A}.\widehat{S}_{Z_B} + \widehat{S}_{X_A}.\widehat{S}_{X_B} + \widehat{S}_{Y_A}.\widehat{S}_{Y_B}\right) \\ &= J\left(\widehat{S}_{Z_A}.\widehat{S}_{Z_B} + \frac{1}{2}\left(\widehat{S}_{-_A}.\widehat{S}_{+_B} + \widehat{S}_{+_A}.\widehat{S}_{-_B}\right)\right) \end{aligned} \tag{11}$$

where J is the isotropic exchange effective integral often called the magnetic coupling. Depending on the J sign, this coupling can be ferromagnetic ($J < 0$) meaning that the ground state is the highest possible spin state, or antiferromagnetic ($J > 0$) when the ground state has the lowest possible spin quantum number. Let us recall that the system is said to be ferrimagnetic when the coupled spins are of different values and the coupling is antiferromagnetic, i.e. the ground state has the lowest spin but is non-zero.

For a binuclear system having only one unpaired electron per center, the spin operators couple the spin distributions $|\uparrow\downarrow\rangle$ and $|\downarrow\uparrow\rangle$, i.e. exchanges the spin M_S components of the two electrons and the sign of J determines whether the singlet or the triplet will be the ground state as the energy difference between these two states $\Delta E_{ST} = E(\text{Triplet}) – E(\text{Singlet}) = J$. This exchange goes through ionic intermediate electronic configurations in which one electron has jumped on the other center, as explained by the Anderson mechanism (represented in Fig. 2) [92, 93]. To

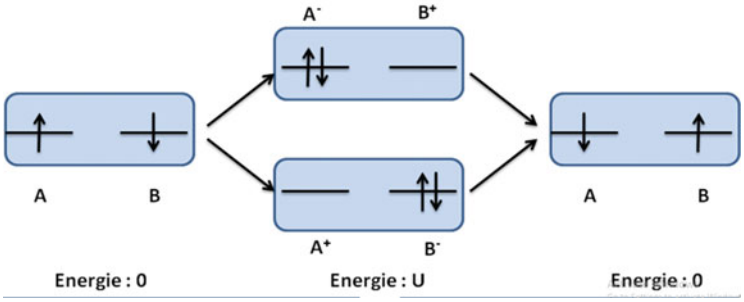

Fig. 2 Neutral and ionic forms involved in the Anderson mechanism responsible for the kinetic contribution to the magnetic exchange

rationalize the nature (sign) of this coupling, one may derive this Hamiltonian from the more sophisticated generalized Hubbard model which introduces both the neutral and ionic configurations [94]. The representative matrix of this Hamiltonian is:

$$\left(\widehat{H}_7^{\,Hubbard}\right) = \begin{matrix} \left\langle a\,\vec{b}\right| \\ \langle b\bar{a}| \\ \langle a\bar{a}| \\ \left\langle b\,\vec{b}\right| \end{matrix} \begin{pmatrix} 0 & K & t & t \\ K & 0 & t & t \\ t & t & U & K \\ t & t & K & U \end{pmatrix} \tag{12}$$

where K is the always positive exchange integral of the exact electronic Hamiltonian, t is the hopping integral (the same as the β integral of the Hückel Hamiltonian), and U the difference of Coulomb repulsion between the ionic distribution in which the two electrons occupy the same orbital and the neutral one in which the two electrons occupy a different orbital ($U = J_{aa} - J_{ab}$, where J_{aa} and J_{ab} are the Coulomb repulsion integrals of the exact electronic Hamiltonian). Diagonalizing the neutral and ionic blocs separately leads to:

$$\left(\widehat{H}_7^{\,Hubbard}\right) = \begin{matrix} \left\langle \left(|a\,\vec{b}| - |b\bar{a}|\right)/\sqrt{2}\right| \\ \left\langle \left(|a\,\vec{b}| + |b\bar{a}|\right)/\sqrt{2}\right| \\ \left\langle \left(|a\,\vec{b}| - |b\bar{a}|\right)/\sqrt{2}\right| \\ \left\langle \left(|a\,\vec{b}| + |b\bar{a}|\right)/\sqrt{2}\right| \end{matrix} \begin{pmatrix} -K & 0 & 0 & 0 \\ 0 & +K & 0 & 2t \\ 0 & 0 & U-K & 0 \\ 0 & 2t & 0 & U+K \end{pmatrix} \tag{13}$$

At the second order of perturbation the energy of the singlet and triplet states are:

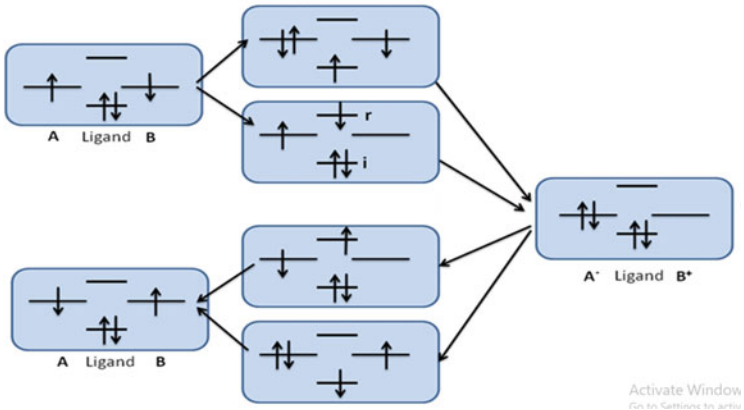

Fig. 3 Example of the generalized Anderson mechanisms responsible for the kinetic contribution to the magnetic exchange in presence of a bridging ligand. The central orbitals belong to the ligand (s)

$$\begin{aligned} E(\text{Singlet}) &= +K - \frac{4t^2}{U} \\ E(\text{Triplet}) &= -K \end{aligned} \tag{14}$$

from which the magnetic coupling J can be deduced:

$$J = \Delta E_{ST} = E(Triplet) - E(\text{Sing}let) = -2K + \frac{4t^2}{U} \tag{15}$$

When the magnetic centers are connected through a bridging ligand, the generalized Anderson mechanism is responsible for the magnetic coupling (see Fig. 3) [95]. The electrons and the orbitals of the ligand mediate this coupling and metal to ligand charge transfer (MLCT) and ligand to metal charge transfer (LMCT) configurations are involved in the process, leading to a more sophisticated expression of the magnetic coupling. It is however still possible to express the J integral as in Eq. 15 but K, t, and U become effective interactions which, respectively, incorporate spin polarization effects, MLCT and LMCT contributions and screening due to electron correlation.

This Hamiltonian is applicable to systems having more than one unpaired electron per center. The model space is still constituted of the products of the ground spin state of each magnetic center (highest spin state according to the Hund's rule). As shown in various papers, the physical content of the magnetic coupling at the second order of perturbation is still given by the direct exchange and the kinetic exchange [96–98]. One should however note that deviations to the Heisenberg spectrum may be observed. They are due to local excited states which may play a non-negligible role [99]. These effects, which are accounted for at the fourth order of perturbations, are described with additional interactions in the model Hamiltonian, such as the

Table 2 Magnetic couplings (in cm^{-1}) of Cu(II) systems calculated using the DDCI method and compared to the experimental value [63]

	$[Cu(tmeen)(OH)]_2Br_2$[a]	$[Cu(bipy)(OH)]_2(NO_3)_2$[b]	$Sr_2CuO_2Cl_2$	La_2CuO_4
DDCI	−500	157	−952	−1,077
Expt.	−507[c]	172[d]	−1,008[e]	[−1,030,-1,096][f]

[a] Meen = *N,N,N′,N′*-tetramethylethylenediamine
[b] Bipy = 2,2′-bipyridine
[c] Value from Mitchel et al. [102]
[d] Value from Majeste and Meyers [103]
[e] Value from Greven et al. [104]
[f] Values from Sulewski et al. [105] Aeppli et al. [106] and Singh et al. [107]

biquadratic interaction and the three-body operator for polymetallic ($N > 2$) compounds [100]. Note that N-body operators must sometimes be used for N-metallic compounds.

From a theoretical chemistry point of view, an accurate calculation of the magnetic coupling requires accounting for various effects such as charge and spin polarization effects and a correct evaluation of the energy of the LMCT and MLCT intermediate configurations of the generalized Anderson mechanism. As it accounts for all these effects, the DDCI method provides very precise values of magnetic couplings in transition metal complexes [63]. To reach the same accuracy in organic compounds, it is often required to determine accurate magnetic orbitals upstream, as the spins can be spread over several centers and an adequate description of their delocalization is crucial for the obtaining of precise magnetic couplings [101]. Computed values of magnetic couplings at the DDCI level are compared to experimental ones in Table 2.

4.2.2 Anisotropic Exchange Interactions

(a) Anisotropy of exchange between centers having a single unpaired electron: the symmetric tensor. When the binuclear system is centrosymmetric and consists of magnetic centers having a single unpaired electron, the only anisotropic interaction that is spin and symmetry allowed is the symmetric anisotropic exchange [108]. As an interesting example of such anisotropic system, one may quote the paramagnetic copper acetate molecule (see Fig. 4), which has raised a series of fundamental questions. At first, copper acetate was assumed to be mononuclear, i.e. containing just one Cu(II) ion per molecule. However, the unexpected decrease of the magnetic susceptibility at low temperature, first measured by Guha in 1951 [109], attracted the attention of Bleaney and Bowers who performed an electron paramagnetic resonance (EPR) study in 1952 [110]. As they observed a small zero-field splitting in the first excited triplet state, they suggested the existence of interacting pairs of cupric ions. Several debates followed these studies concerning both the nature of the magnetic interactions (either metal–metal or through ligand) and the sign of the zero-field splitting. A

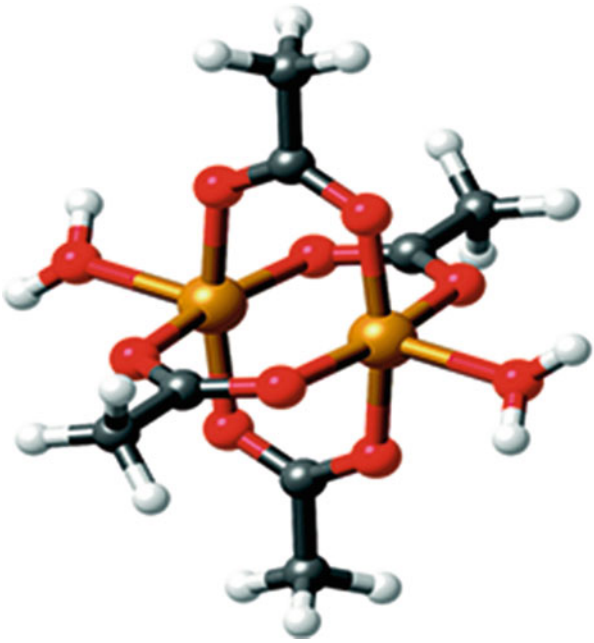

Fig. 4 Schematic representation of the copper acetate molecule

new EPR study performed in 2008 [111] finally showed that the axial anisotropy parameter is negative and a theoretical rationalization has been proposed in 2011 [15]. For such a simple binuclear system having one unpaired electron per center, the Hamiltonian writes:

$$\widehat{\mathbf{H}}_8^{\mathrm{MS}} = J\widehat{\mathbf{S}}_a.\widehat{\mathbf{S}}_b + \widehat{\mathbf{S}}_a.\overline{\overline{\mathbf{D}}}_{ab}.\widehat{\mathbf{S}}_b \tag{16}$$

where $\overline{\overline{\mathbf{D}}}_{ab}$ is the symmetric anisotropic exchange tensor. One should note that as the system is centrosymmetric the Dzyaloshinskii–Moriya term is strictly zero [108, 112, 113]. In such a simple case, analytical derivation of the ZFS D and E parameters can be performed. At the second order of perturbations their expression is[15]:

$$\begin{aligned} D &= 2\frac{\varsigma^2 J_{X^2-Y^2,XY}}{\Delta E^2_{X^2-Y^2,XY}} - \frac{1}{4}\frac{\varsigma^2 J_{X^2-Y^2,XZ}}{\Delta E^2_{X^2-Y^2,XZ}} - \frac{1}{4}\frac{\varsigma^2 J_{X^2-Y^2,YZ}}{\Delta E^2_{X^2-Y^2,YZ}} \\ E &= \frac{1}{4}\frac{\varsigma^2 J_{X^2-Y^2,YZ}}{\Delta E^2_{X^2-Y^2,YZ}} - \frac{1}{4}\frac{\varsigma^2 J_{X^2-Y^2,XZ}}{\Delta E^2_{X^2-Y^2,XZ}} \end{aligned} \tag{17}$$

where

Table 3 D and E value in cm^{-1} of the lowest triplet state of the copper acetate molecule [15]. SSC and SOC, respectively, stand for spin–spin coupling and spin–orbit coupling

	D_{SSC}	D_{SOC}	$D_{SSC+SOC}$	E_{SSC}	E_{SOC}	$E_{SSC+SOC}$
DDCI+SOCI	−0.118	−0.200	−0.319	0.000	0.006	0.006
Expt.[a]	–	–	−0.335	–	–	0.01

[a] Value from Ozarowski et al. [111]

$$\begin{aligned} \Delta E^2_{X^2-Y^2,N} &= \sqrt{\Delta_{\Phi^T_N}.\Delta_{\Phi^S_N}} \\ J_{X^2-Y^2,N} &= E_{\Phi^T_N} - E_{\Phi^S_N} \end{aligned} \tag{18}$$

are, respectively, geometric mean of the excitation energies $\Delta_{\Phi^S_N}$ and $\Delta_{\Phi^T_N}$ corresponding to the same spatial single-excitation and the energy differences between the singlet Φ^S_N and triplet Φ^T_N excited state. Provided that the spin–orbit free low-energy spectrum is computed using the DDCI method, the ZFS parameters of the lowest triplet states [15] (given in Table 3) compare very well with experiment [111].

(b) Anisotropy of exchange between centers having a single unpaired electron: the antisymmetric components. In the absence of some symmetry elements, such as, for instance, a symmetry center, a mixing between the $S = 0$ and $S = 1$ spin components occurs. It can be described via antisymmetric components of a second-rank exchange tensor, which can mathematically be reduced to pseudo-vector components, and added to the previous model Hamiltonian:

$$\widehat{H}_9 = J\widehat{S}_A.\widehat{S}_B + \widehat{S}_A\overline{\overline{\mathbf{D}}}_{ab}\widehat{S}_B + \overline{d}\widehat{S}_A \times \widehat{S}_B \tag{19}$$

where $\overline{d}$ corresponds to the antisymmetric exchange, usually referred to as the Dzyaloshinskii–Moriya (DM) pseudo-vector [112, 113]. While the isotropic coupling term J acts in a same way on the diagonal elements of the three $S = 1$ components, the D tensor components are related to the splitting and mixing of these components, and the $\overline{d}$ pseudo-vector mixes these components with the $S = 0$ one (spin mixing between S and $S + 1$ blocks). Concerning the mechanisms, Moskvin carefully discussed them in 2007 in the case of copper oxides, highlighting potential contributions from the bridging ligands [114]. Note that in the general case, too many effective parameters are introduced to allow simple extractions from experiment. Indeed, many techniques are essentially sensitive to energy levels, and not to spin mixing. Moreover, it is crucial to determine the angles of the symmetric tensor principle axes and the pseudo-vector to get a full multispin picture. Therefore, it is hard to get any reliable data from experiments concerning the DM pseudo-vector, unless the symmetric exchange components can be considered as negligible compared to the antisymmetric ones, which would allow one to get the pseudo-vector norm even from powder samples.

From a computational perspective, it is straightforward to distinguish the symmetric and antisymmetric exchange terms as soon as an (effective) interaction matrix between the $S = 1$ and $S = 0$ blocks is determined. Since most of the perturbative approaches to compute ZFS have been originally designed only to describe a spin block, they do not allow one to determine the DM pseudo-vector. One way of tackling the problem consists in using the effective Hamiltonian theory on top of SOCI calculations that consider both $S = 1$ and $S = 0$ spin components. Such approach was first followed by Maurice et al. in a study of model copper(II)-copper (II) dinuclear complexes [15], which notably confirmed the hypothesis of Moskvin that bridging ligands also play a role in the antisymmetric exchange. This approach has then been applied to ionic solids within the embedded cluster approach [78, 115, 116]. One should also mention that Atanasov et al. reported a study of "real" copper (II)-copper(II) complexes based on a ligand-field theory based analysis [117].

From a methodological point of view, since the DM components are essentially governed by the direct spin–orbit coupling between the S and $S + 1$ sets of blocks of interest, we initially thought that it was not necessary to compute local or delocalized ligand-field excited states to obtain good semi-quantitative estimates of them (contrary to the symmetric exchange components or single-ion anisotropies) [78, 118]. In fact, the situation is somehow more complex and depends on both the regime (i.e., far from the single-site first-order SOC vs. close to it) and also on the way to optimize the state-average orbitals in the CASSCF step. Because those discussions are actually quite technical, we will only summarize here the main outcomes and encourage the interested reader to consult the original papers [16, 119]. First of all, the orbital wave function differentiation of the singlet and triplet wave functions is key to generate non-zero DM components. This is why it is easier to obtain accurate results if the singlet and triplet active orbitals are optimized separately (in a state-specific framework or with a state-averaging scheme per spin block). Second, far from the single-site first-order regime, the "direct" SOC largely dominates (recall that accuracy is contingent to fulfilling the previous orbital differentiation condition). In terms of orbital contributions, it is easy to show that only the excitations that preserve the $|m_l|$ values contribute to the Z DM component (also denoted d_Z). Being associated with the $l_z s_z$ product of operators, the coupling is proportional to $|m_l|$, meaning that the $XY \leftrightarrow X^2–Y^2$ channel is on the paper twice more efficient than the $XZ \leftrightarrow YZ$ one (of course, analysis of the actual nature of the magnetic orbitals may counterbalance this).

Concerning situations close to the single-site first-order regime, we have shown that it is crucial to use "decontracted" CASSCF wave functions to get accurate DM components, which can be extracted either with the effective Hamiltonian theory or the intermediate Hamiltonian theory. The closer to this situation, the more important the "decontraction" is expected to be. Naturally, for larger systems (in terms of nuclearity or even of molecular size), the use of DDCI to generate such revised CASSCF wave functions is prohibited because of the computational cost. This is why in our first attempt to compute $|d_Z|$ in a real trinuclear copper(II) complex out of "decontracted" CASSCF states was based on NEVPT2 (quasi-degenerate

formulation) [120]. By doing so, we ended up having a $|d_Z|$ value of ca. 20 cm^{-1}, in fair agreement with experiment (36 cm^{-1}) [121].

(c) Anisotropy of exchange between centers having several unpaired electrons: the fourth-rank tensor. When two unpaired electrons are present on a paramagnetic center, its single-ion anisotropy must also be introduced in the model Hamiltonian. Therefore, when the two magnetic centers trigger two unpaired electrons, it appeared natural from a phenomenological point of view to simply add their single-ion anisotropies to the model Hamiltonian [79, 80], such as:

$$\widehat{H}_{10} = J\widehat{S}_A.\widehat{S}_B + \widehat{S}_A\overline{\overline{\mathbf{D}}}_A\widehat{S}_A + \widehat{S}_B\overline{\overline{\mathbf{D}}}_B\widehat{S}_B + \widehat{S}_A\overline{\overline{\mathbf{D}}}_{AB}\widehat{S}_B + \overline{d}\widehat{S}_A \times \widehat{S}_B \tag{20}$$

where $\overline{\overline{D}}_A$ and $\overline{\overline{D}}_B$ are the local anisotropy tensors of the A and B centers, respectively, while the other terms keep their previously mentioned meanings. This model Hamiltonian is often considered in the literature, e.g., in experimental studies of the $[Ni_2(en)_4Cl_2]^{2+}$ complex [111, 122–124].

From a computational perspective, it is common to compute the single-ion anisotropy tensors. For this, while not treating the full complexity associated with the low-energy levels, one can (1) mimic the effect one of the paramagnetic ions by a zero-electron ab initio model potential, (2) replace one of the paramagnetic ions by a diamagnetic one with a similar effective charge and a similar ionic radius [14, 116, 125], (3) consider one of the ions in its lowest-energy closed-shell excited configuration [89], or (4) consider the ground and excited configurations of the ion of interest while keeping the other paramagnetic center in its high-spin configuration [126]. Although one may expect to obtain similar values with all these approaches, the fourth one is meant to be more reliable. However, one should note that, even if the determination of the local anisotropy tensors can provide useful information to interpret magnetic data, it is not sufficient to describe properly the energy levels and to have model vectors in good correspondence with the actual ones after diagonalization of a model Hamiltonian that only contains isotropic interactions and local anisotropic ones. Computing ab initio the energy levels of binuclear systems is particularly challenging when the two ions of interest bear at least two unpaired electrons. So far, only the $[Ni_2(en)_4Cl_2]^{2+}$ and model Ni(II)-Ni(II) complexes have been studied with such approaches [14, 89]. Several important conclusions arose from these works. First, it was shown that $\widehat{H}_7$ is not a good model Hamiltonian for centrosymmetric Ni(II)-Ni(II) complexes, since fourth-rank tensor components need to be introduced in the model to have a good matching between the model interaction matrix and the effective one [14]. Therefore, the following model Hamiltonian was proposed:

$$\widehat{H}_{11} = J\widehat{S}_A.\widehat{S}_B + \widehat{S}_A\overline{\overline{\mathbf{D}}}_A\widehat{S}_A + \widehat{S}_B\overline{\overline{\mathbf{D}}}_B\widehat{S}_B + \widehat{S}_A\overline{\overline{\mathbf{D}}}_{AB}\widehat{S}_B + \widehat{S}_A \otimes \widehat{S}_A\overline{\overline{\overline{\overline{\mathbf{D}}}}}_{AB}\widehat{S}_B \otimes \widehat{S}_B + \overrightarrow{d}\widehat{S}_A \times \widehat{S}_B \quad (21)$$

where $\overline{\overline{\overline{\overline{\mathbf{D}}}}}_{AB}$ is a fourth-rank tensor. When all these terms are introduced in the model Hamiltonian, their direct extraction with the effective Hamiltonian theory is practically impossible if one does not consider relations between fourth-rank tensor components [14]. When relations are assumed, the extraction of the other parameters belonging to $\widehat{H}_{11}$ becomes possible [89]. In this way, no bias is introduced in the determination of the second-rank anisotropy tensors, in particular the local ones. Two important conclusions were formulated in the study of model Ni(II)-Ni(II) complexes [89]: (1) the local ZFS parameters D and E obtained from a full treatment are found in good agreement with those computed from simple schemes that aims only at computing local terms, and (2) the fourth-rank tensor components have a stronger impact on the effective Hamiltonian matrix than the second-rank symmetric exchange ones. Concerning the former conclusion, it validates the approaches that only aim at computing local parameters. Concerning the second one, it implies that experimental determinations of the multispin Hamiltonian parameters are not reliable since $\widehat{H}_{11}$ is not practically applicable to experimental problems. Also, note that all the phenomenological interactions introduced in Eq. 21 (single-ion anisotropies and symmetric exchange tensors) are involved in the S and $S + 2$ mixing [75]. As a perspective, other electronic configurations should be studied to see if $\widehat{H}_{11}$ also applies to cases with more than three electrons per magnetic site, or if higher-rank tensors should also be involved in the model Hamiltonian.

(d) Extraction of all anisotropic interactions in model complexes: interferences between local anisotropies. In the general case, the multispin Hamiltonian contains all previously presented operators. As a consequence, the extraction of all the parameters may turn to a real nightmare. Indeed, as all tensors may have different principal axes, non-zero components can be found everywhere and the number of equations necessary to extract them can be larger than the number of matrix elements computed in the effective Hamiltonian theory. A method that allows the extraction in many different cases has been proposed [89]. It consists in reducing the number of parameters by introducing rotation of the various tensors (using the Euler's angles) such that one directly deals with diagonal 2-rank tensors (2 parameters) and a maximally reduced 4-rank tensor (6–9 parameters only).

Using model compounds of Ni(II) (see Fig. 5) it was possible to generate various local anisotropies in order to understand how these local anisotropies combine and what the resulting anisotropy of the binuclear compound is [89]. It is interesting to note that despite the complexity of the model, very intuitive molecular anisotropies are obtained. By imposing specific distortions around each magnetic ion in model complexes, the synergy and interferences of local anisotropies can be studied in the following cases: (1) both local anisotropies are axial and the relative positions of the

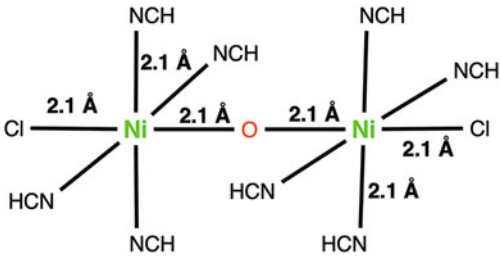

Fig. 5 Distorted model binuclear Ni(II) complex [89]. The bridging ligand is O^{2-} while the external (green) ligands are either CN^- (complex M1) or Cl^- (complex M2). The other ligands are HCN

principal axes is varied (collinear, perpendicular, or twisted), (2) both local anisotropies are planar and the relative orientations of the planes are varied, (3) one local anisotropy is axial while the other one is planar and both the relative positions of the plane and the axis are varied. The following conclusions could be drawn:

- Destructive interferences occur in most of the cases, leading to a weaker magnetic anisotropy of the whole complex in comparison to that of the single ions.
- When the local anisotropies are axial and the axes are not orthogonal, an axial anisotropy could be maintained and the axis of the molecular compound bisects the local axes.
- The following cases illustrated in Fig. 6 however happened to be synergistic:

(i) The local anisotropies are axial and the two axes are collinear. The negative D value of the binuclear complex is larger than that of the single ions. Interestingly if the rhombicity parameters of the single ions are zero, the whole complex does not exhibit any rhombicity as well.
(ii) The local anisotropies are both planar and rhombic and the two easy axes of magnetization are collinear. The resulting anisotropy is axial. If the two hard axes are perpendicular, it is even possible to get a complex that does not exhibit any rhombicity.
(iii) One single ion has an axial anisotropy while the other one has a planar anisotropy, and the easy axis of the first ion is in the easy plane of the other ion. The resulting anisotropy of the complex is axial.

5 Concluding Remarks

This chapter was devoted to the study of magnetic interactions in binuclear complexes. While High-Field High-Frequency Electron Paramagnetic Resonance (HFHF-EPR) has provided experimental information regarding the zero-field splitting of mononuclear species [127–129], the complexity of the models describing binuclear compounds prevents one from having such insights in the physics governing their electronic spectra. Theoretical calculations may constitute a good alternative to elucidate their properties. Through various examples of increasing complexity, and as far as binuclear complexes are concerned, it was shown that:

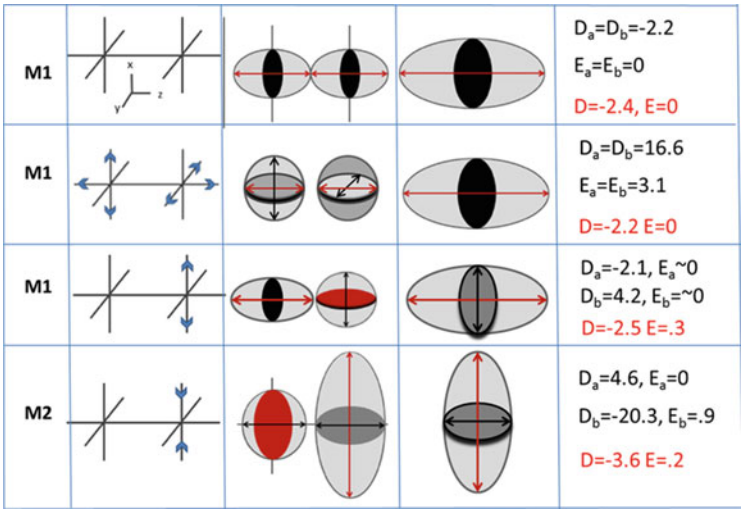

Fig. 6 First column: model compounds: in M1 the external ligand (green) is CN^- while in M2, it is Cl^-; Second column: distortion imposed to the Ni(II) ions; Third column: ellipsoids representing the local anisotropy tensors; Fourth column: ellipsoid representing the resulting molecular anisotropy tensor of the binuclear complex quintuplet state. Black (red) double arrows indicate easy (hard) axes of magnetization; black (red) ovals indicate easy (hard) planes of magnetization. A prolate ellipsoid indicates an axial anisotropy ($D < 0$) while an oblate ellipsoid indicates a planar anisotropy ($D > 0$). Fifth column: values of the local (a and b) ZFS parameters and value of the ZFS parameters obtained for the binuclear complex in its essentially quintuplet spin state (in cm^{-1}) [89]

(i) The giant-spin approximation is appropriate in the strong and intermediate coupling regime.
(ii) The multispin model involving only a 2-rank tensor is reliable for centrosymmetric compounds having a single unpaired electron. In such a simple case analytical formula of both the D and E parameters can be derived providing a rationalization of the magnitude and sign of the ZFS parameters.
(iii) The Dzyaloshinskii–Moriya operator correctly describes the antisymmetric contribution to the ZFS.
(iv) For systems containing two unpaired electrons per magnetic center a 4-rank tensor must be introduced to accurately describe the anisotropy of the interaction. Its elements are by far larger than those of the 2-rank tensor. It is worthwhile noticing that operators involving six spins would appear in systems having three unpaired electrons per center.
(v) Despite the complexity of these operators, the anisotropy of a binuclear compound may be relatively easily anticipated from chemical and physical intuition from the local anisotropies of the paramagnetic ions. The anisotropy of the complex may in some well-defined cases (i.e., geometries) result from synergistic combinations of the local anisotropies.

Extension of this approach to complexes of higher spins and/or nuclearities is of course one of the obvious perspectives of this chapter. Although we have recently shown that we are capable of treating tri- and tetranuclear complexes (Cu_3 and Ni_4) with satisfying theoretical approximations (far beyond what could have been possible to do a decade ago) [91, 120], a more detailed methodological study will soon have to be performed in order to test alternatives to the CASSCF step bottleneck on these systems prior to applying the retained approximations to larger systems.

References

1. Kahn O (1993) Molecular magnetism, New York
2. Pippard AB (1989) Magnetoresistance in metals, Cambridge
3. A. Hauser, Light-induced spin crossover and the high-spin -> low-spin relaxation. Spin crossover in transition metal compounds II 2004, 234, 155–198
4. Bardeen J, Cooper LN, Schrieffer JR (1957) Phys Rev 108:1175–1204
5. Ederer C, Spaldin NA (2004) Magnetoelectrics – a new route to magnetic ferroelectrics. Nat Mater 3:849–851
6. Leuenberger MN, Loss D (2001) Quantum computing in molecular magnets. Nature 410:789–793
7. Gatteschi D, Sessoli R (2003) Quantum tunneling of magnetization and related phenomena in molecular materials. Angew Chem Int Ed 42:268–297
8. Coffman RE, Buettner GR (1979) General magnetic dipolar interaction of spin-spin coupled molecular dimers. Application to an EPR spectrum of xanthine oxidase. J Phys Chem 83: 2392–2400
9. Bencini A, Gatteschi D (1985) The effect of the local zero field splitting of the nickel(II) ion on the E.P.R. spectra of exchange coupled copper(II) ($S = 1/2$)-nickel(II) ($S = 1$) pairs. Mol Phys 54:969–977
10. Hulliger J (1987) Large isotropic exchange interactions from E.P.R. on doublet-triplet organometallic molecular pairs in diamagnetic host-lattices. Mol Phys 60:97–111
11. Retegan M, Collomb M-N, Neese F, Duboc C (2013) A combined high-field EPR and quantum chemical study on a weakly ferromagnetically coupled dinuclear Mn(iii) complex. A complete analysis of the EPR spectrum beyond the strong coupling limit. Phys Chem Chem Phys 15:223–234
12. Morsing TJ, Weihe H, Bendix J (2016) Probing effective Hamiltonian operators by single-crystal EPR: a case study using dinuclear Cr(III) complexes. Inorg Chem 55:1453–1460
13. Maurice R, de Graaf C, Guihéry N (2010) Magnetic anisotropy in binuclear complexes in the weak-exchange limit: from the multispin to the giant-spin Hamiltonian. Phys Rev B 81: 214427
14. Maurice R, Guihery N, Bastardis R, de Graaf C (2010) Rigorous extraction of the anisotropic multispin Hamiltonian in bimetallic complexes from the exact electronic Hamiltonian. J Chem Theory Comput 6:55–65
15. Maurice R, Sivalingam K, Ganyushin D, Guihery N, de Graaf C, Neese F (2011) Theoretical determination of the zero-field splitting in copper acetate monohydrate. Inorg Chem 50:6229–6236
16. Bouammali M-A, Suaud N, Martins C, Maurice R, Guihéry N (2021) How to create giant Dzyaloshinskii–Moriya interactions? Analytical derivation and ab initio calculations on model dicopper(II) complexes. J Chem Phys 154:134301
17. Ruamps R, Maurice R, de Graaf C, Guihéry N (2014) Interplay between local anisotropies in binuclear complexes. Inorg Chem 53:4508–4516

18. Demir S, Zadrozny JM, Nippe M, Long JR (2012) Exchange coupling and magnetic blocking in Bipyrimidyl radical-bridged dilanthanide complexes. J Am Chem Soc 134:18546–18549
19. Chow CY, Bolvin H, Campbell VE, Guillot R, Kampf JW, Wernsdorfer W, Gendron F, Autschbach J, Pecoraro VL, Mallah T (2015) Assessing the exchange coupling in binuclear lanthanide(III) complexes and the slow relaxation of the magnetization in the antiferromagnetically coupled Dy-2 derivative. Chem Sci 6:4148–4159
20. Zhang J, Zhang H, Chen Y, Zhang X, Li Y, Liu W, Dong Y (2016) A series of dinuclear lanthanide complexes with slow magnetic relaxation for Dy2 and Ho2. Dalton Trans 45: 16463–16470
21. Viciano-Chumillas M, Koprowiak F, Mutikainen I, Wernsdorfer W, Mallah T, Bolvin H (2017) Hysteresis in a bimetallic holmium complex: a synergy between electronic and nuclear magnetic interactions. Phys Rev B 96
22. Liu X-W, Wu Z, Chen J-T, Li L, Chen P, Sun W-B (2020) Regulating the single-molecule magnetic properties of phenol oxygen-bridged binuclear lanthanide complexes through the electronic and spatial effect of the substituents. Inorg Chem Front 7:1229–1238
23. Dey S, Rajaraman G (2021) Attaining record-high magnetic exchange, magnetic anisotropy and blocking barriers in dilanthanofullerenes. Chem Sci 12:14207–14216
24. Aguilà D, Barrios LA, Velasco V, Roubeau O, Repollés A, Alonso PJ, Sesé J, Teat SJ, Luis F, Aromí G (2014) Heterodimetallic [LnLn′] lanthanide complexes: toward a chemical design of two-qubit molecular spin quantum gates. J Am Chem Soc 136:14215–14222
25. Luis F, Alonso PJ, Roubeau O, Velasco V, Zueco D, Aguilà D, Martínez JI, Barrios LA, Aromí G (2020) A dissymmetric [Gd2] coordination molecular dimer hosting six addressable spin qubits. Commun Chem 3:176
26. El-Khatib F, Cahier B, Lopez-Jorda M, Guillot R, Riviere E, Hafez H, Saad Z, Girerd JJ, Guihery N, Mallah T (2017) Design of a binuclear Ni(II) complex with large Ising-type anisotropy and weak anti-ferromagnetic coupling. Inorg Chem 56:10655–10663
27. El-Khatib F, Cahier B, Lopez-Jorda M, Guillot R, Riviere E, Hafez H, Saad Z, Guihery N, Mallah T (2018) A bis-binuclear Ni-II complex with easy and hard axes of magnetization: complementary experimental and theoretical insights. Eur J Inorg Chem:469–476
28. Kharwar AK, Mondal A, Sarkar A, Rajaraman G, Konar S (2021) Modulation of magnetic anisotropy and exchange interaction in phenoxide-bridged dinuclear co(II) complexes. Inorg Chem 60:11948–11956
29. Dirac PAM (1929) Proc R Soc London Ser A 123:714–733
30. Heisenberg W (1928) Z Phys 49:619–636
31. van Vleck JH (1945) Rev Mod Phys:1727–1747
32. Miralles J, Castell O, Caballol R, Malrieu JP (1993) Specific Ci calculation of energy differences – transition energies and bond-energies. Chem Phys 172:33–43
33. Neese F. ORCA, an ab initio, density functional and semiempirical program package, max-Planck-Institut für Bioanorganische Chemie, Mülheim an der Ruhr, Germany
34. Maynau D, Ben Armor N CASDI suite of programs. Université Paul Sabatier, Toulouse
35. McWeeny R (1965) J Chem Phys 42:1717–1725
36. McWeeny R, Mizuno Y (1961) Proc R Soc London Ser A 259:554–577
37. Neese F, Solomon EI (1998) Calculation of zero-field splittings, g-values, and the relativistic nephelauxetic effect in transition metal complexes. Application to high-spin ferric complexes. Inorg Chem 37:6568–6582
38. Pederson MR, Khanna SN (1999) Magnetic anisotropy barrier for spin tunneling in Mn12O12 molecules. Phys Rev B 60:9566–9572
39. Aquino F, Rodriguez JH (2005) First-principle computation of zero-field splittings: application to a high valent Fe(IV)-oxo model of nonheme iron proteins. J Chem Phys 123
40. Ganyushin D, Neese F (2006) First-principles calculations of zero-field splitting parameters. J Chem Phys 125
41. Neese F (2006) Importance of direct spin-spin coupling and spin-flip excitations for the zero-field splittings of transition metal complexes: a case study. J Am Chem Soc 128:10213–10222

42. Neese F (2007) Calculation of the zero-field splitting tensor on the basis of hybrid density functional and Hartree-Fock theory. J Chem Phys 127
43. Schmitt S, Jost P, van Wullen C (2011) Zero-field splittings from density functional calculations: analysis and improvement of known methods. J Chem Phys 134
44. Kubica A, Kowalewski J, Kruk D, Odelius M (2013) Zero-field splitting in nickel (II) complexes: a comparison of DFT and multi-configurational wavefunction calculations. J Chem Phys 138
45. Zein S, Neese F (2008) Ab initio and coupled-perturbed density functional theory estimation of zero-field splittings in Mn-II transition metal complexes. J Phys Chem A 112:7976–7983
46. Duboc C, Ganyushin D, Sivalingam K, Collomb MN, Neese F (2010) Systematic theoretical study of the zero-field splitting in coordination complexes of Mn(III). Density functional theory versus multireference wave function approaches. J Phys Chem A 114:10750–10758
47. Maurice R, Bastardis R, de Graaf C, Suaud N, Mallah T, Guihery N (2009) Universal theoretical approach to extract anisotropic spin Hamiltonians. J Chem Theory Comput 5: 2977–2984
48. Atanasov M, Ganyushin D, Pantazis DA, Sivalingam K, Neese F (2011) Detailed ab initio first-principles study of the magnetic anisotropy in a family of trigonal pyramidal iron (II) pyrrolide complexes. Inorg Chem 50:7460–7477
49. Maurice R (2011) PhD thesis, zero-field anisotropic spin Hamiltonians in first-row transition metal complexes: theory, models and applications (http://thesesups.ups-tlse.fr/1430), Toulouse (University of Toulouse)
50. Costes JP, Maurice R, Vendier L (2012) Pentacoordinate NiII complexes: preparation, magnetic measurements, and ab initio calculations of the magnetic anisotropy terms. Chem A Eur J 18:4031–4040
51. Gomez-Coca S, Cremades E, Aliaga-Alcalde N, Ruiz E (2013) Mononuclear single-molecule magnets: tailoring the magnetic anisotropy of first-row transition-metal complexes. J Am Chem Soc 135:7010–7018
52. Ruamps R, Batchelor LJ, Maurice R, Gogoi N, Jimenez-Lozano P, Guihery N, de Graaf C, Barra AL, Sutter JP, Mallah T (2013) Origin of the magnetic anisotropy in Heptacoordinate Ni-II and Co-II complexes. Chem A Eur J 19:950–956
53. Ruamps R, Maurice R, Batchelor L, Boggio-Pasqua M, Guillot R, Barra AL, Liu JJ, Bendeif E, Pillet S, Hill S, Mallah T, Guihery N (2013) Giant Ising-type magnetic anisotropy in trigonal bipyramidal Ni(II) complexes: experiment and theory. J Am Chem Soc 135:3017–3026
54. Malmqvist PA, Roos BO, Schimmelpfennig B (2002) The restricted active space (RAS) state interaction approach with spin-orbit coupling. Chem Phys Lett 357:230–240
55. Roos BO, Malmqvist PA (2004) Relativistic quantum chemistry: the multiconfigurational approach. Phys Chem Chem Phys 6:2919–2927
56. Teichtel C, Pélissier M, Spiegelman F (1983) Chem Phys 81:273–282
57. Llusar R, Casarrubios M, Barandiaran Z, Seijo L (1996) Ab initio model potential calculations on the electronic spectrum of Ni2+−doped MgO including correlation, spin-orbit and embedding effects. J Chem Phys 105:5321–5330
58. Wu D, Zhou C, Bao JJ, Gagliardi L, Truhlar DG (2022) Zero-field splitting calculations by multiconfiguration pair-density functional theory. J Chem Theory Comput 18:2199–2207
59. Chibotaru LF, Ungur L (2012) Ab initio calculation of anisotropic magnetic properties of complexes. I. Unique definition of pseudospin Hamiltonians and their derivation. J Chem Phys:137
60. Aquilante F, De Vico L, Ferre N, Ghigo G, Malmqvist PA, Neogrady P, Pedersen TB, Pitonak M, Reiher M, Roos BO, Serrano-Andres L, Urban M, Veryazov V, Lindh R (2010) Software news and update MOLCAS 7: the next generation. J Comput Chem 31:224–247
61. Moreira IPR, Illas F (2006) A unified view of the theoretical description of magnetic coupling in molecular chemistry and solid state physics. Phys Chem Chem Phys 8:1645–1659

62. Maurice R, de Graaf C, Guihery N (2013) Theoretical determination of spin Hamiltonians with isotropic and anisotropic magnetic interactions in transition metal and lanthanide complexes. Phys Chem Chem Phys 15:18784–18804
63. Malrieu JP, Caballol R, Calzado CJ, de Graaf C, Guihery N (2014) Magnetic interactions in molecules and highly correlated materials: physical content, analytical derivation, and rigorous extraction of magnetic Hamiltonians. Chem Rev 114:429–492
64. Bloch C (1958) Nucl Phys 6:329–347
65. des Cloizeaux J (1960) Nucl Phys 20:321–346
66. Griffith JS (1961) The theory of transition metal ions. Cambridge University Press, Cambridge
67. Abragam A, Bleaney B (1986) Electron paramagnetic resonance of transition ions. , New York
68. Maurice R, Vendier L, Costes JP (2011) Magnetic anisotropy in Ni-II-Y-III binuclear complexes: on the importance of both the first coordination sphere of the Ni-II ion and the Y-III ion belonging to the second coordination sphere. Inorg Chem 50:11075–11081
69. Rogez G, Rebilly JN, Barra AL, Sorace L, Blondin G, Kirchner N, Duran M, van Slageren J, Parsons S, Ricard L, Marvilliers A, Mallah T (2005) Very large ising-type magnetic anisotropy in a mononuclear Ni-II complex. Angew Chem Int Ed 44:1876–1879
70. Krzystek J, Zvyagin SA, Ozarowski A, Fiedler AT, Brunold TC, Telser J (2004) Definitive spectroscopic determination of zero-field splitting in high-spin cobalt(II). J Am Chem Soc 126: 2148–2155
71. Rebilly JN, Charron G, Riviere E, Guillot R, Barra AL, Serrano MD, van Slageren J, Mallah T (2008) Large magnetic anisotropy in pentacoordinate Ni-II complexes. Chem A Eur J 14: 1169–1177
72. Stevens KWH (1952) Proc R Soc London Ser A 65:209–215
73. Altshuler SA, Kozyrev BM (1974) Electron paramagnetic resonance in compounds of transition elements. , New York
74. Rudowicz C, Chung CY (2004) The generalization of the extended Stevens operators to higher ranks and spins, and a systematic review of the tables of the tensor operators and their matrix elements. J Phys-Condens Mat 16:5825–5847
75. Maurice R, de Graaf C, Guihery N (2010) Magnetic anisotropy in binuclear complexes in the weak-exchange limit: from the multispin to the giant-spin Hamiltonian. Phys Rev B 81
76. Liviotti E, Carretta S, Amoretti G (2002) S-mixing contributions to the high-order anisotropy terms in the effective spin Hamiltonian for magnetic clusters. J Chem Phys 117:3361–3368
77. Carretta S, Liviotti E, Magnani N, Santini P, Amoretti G (2004) S mixing and quantum tunneling of the magnetization in molecular nanomagnets. Phys Rev Lett 92
78. Pradipto AM, Maurice R, Guihery N, de Graaf C, Broer R (2012) First-principles study of magnetic interactions in cupric oxide. Phys Rev B 85
79. Boca R (1999) Theoretical foundations of molecular magnetism. , Amsterdam
80. Boca R (2004) Zero-field splitting in metal complexes. Coord Chem Rev 248:757–815
81. Kortus J, Baruah T, Bernstein N, Pederson MR (2002) Magnetic ordering, electronic structure, and magnetic anisotropy energy in the high-spin Mn-10 single molecule magnet. Phys Rev B 66
82. Baruah T, Pederson MR (2003) Density functional study of the conformers of CO4-based single-molecule magnet. Int J Quant Chem 93:324–331
83. Kortus J, Pederson MR, Baruah T, Bernstein N, Hellberg CS (2003) Density functional studies of single molecule magnets. Polyhedron 22:1871–1876
84. Park K, Pederson MR, Richardson SL, Aliaga-Alcalde N, Christou G (2003) Density-functional theory calculation of the intermolecular exchange interaction in the magnetic Mn-4 dimer. Phys Rev B 68
85. Ribas-Arino J, Baruah T, Pederson MR (2005) Density-functional study of two Fe-4-based single-molecule magnets. J Chem Phys 123
86. Ribas-Arino J, Baruah T, Pederson MR (2006) Toward the control of the magnetic anisotropy of Fe-II cubes: a DFT study. J Am Chem Soc 128:9497–9505

87. Ruiz E, Cirera J, Cano J, Alvarez S, Loose C, Kortus J (2008) Can large magnetic anisotropy and high spin really coexist? Chem Commun:52–54
88. Moragues-Canovas M, Helliwell M, Ricard L, Riviere E, Wernsdorfer W, Brechin E, Mallah T (2004) An Ni-4 single-molecule magnet: synthesis, structure and low-temperature magnetic behavior. Eur J Inorg Chem:2219–2222
89. Ruamps R, Maurice R, de Graaf C, Guihery N (2014) Interplay between local anisotropies in binuclear complexes. Inorg Chem 53:4508–4516
90. Herchel R, Boca R, Krzystek J, Ozarowski A, Dura M, van Slageren J (2007) Definitive determination of zero-field splitting and exchange interactions in a Ni(II) dimer: investigation of [Ni-2(en)(4)Cl-2]Cl-2 using magnetization and tunable-frequency high-field electron paramagnetic resonance. J Am Chem Soc 129:10306–10307
91. Maurice R (2021) Magnetic anisotropy in a Cubane-like Ni4 complex: an ab initio perspective. Inorg Chem 60:6306–6318
92. Anderson PW (1950) Phys Rev 79:350–356
93. Anderson PW (1959) Phys Rev 115:2–13
94. Ovchinnikov AA (1993) Mod Phys Lett B 7:1397–1405
95. Anderson PW (1963) Solid State Phys 14:99–214
96. Calzado CJ, Cabrero J, Malrieu JP, Caballol R (2002) Analysis of the magnetic coupling in binuclear complexes. II. Derivation of valence effective Hamiltonians from ab initio CI and DFT calculations. J Chem Phys 116:3985–4000
97. Calzado CJ, Cabrero J, Malrieu JP, Caballol R (2002) Analysis of the magnetic coupling in binuclear complexes. I. Physics of the coupling. J Chem Phys 116:2728–2747
98. Calzado CJ, Angeli C, Taratiel D, Caballol R, Malrieu JP (2009) Analysis of the magnetic coupling in binuclear systems. III. The role of the ligand to metal charge transfer excitations revisited. J Chem Phys:131
99. Bastardis R, Guihery N, de Graaf C (2008) Isotropic non-Heisenberg terms in the magnetic coupling of transition metal complexes. J Chem Phys 129
100. Bastardis R, Guihery N, de Graaf C (2007) Microscopic origin of isotropic non-Heisenberg behavior in S=1 magnetic systems. Phys Rev B 76
101. Suaud N, Ruamps R, Guihery N, Malrieu JP (2012) A strategy to determine appropriate active orbitals and accurate magnetic couplings in organic magnetic systems. J Chem Theory Comput 8:4127–4137
102. Mitchell TP, Bernard WH, Wasson JR (1970) Acta Crystallogr Sect B:26
103. Majeste RJ, Meyers EA (1970) J Phys Chem 74:3497–3500
104. Greven M, Birgeneau RJ, Endoh Y, Kastner MA, Matsuda M, Shirane G (1995) Neutron-scattering study of the 2-dimensional spin S=1/2 square-lattice Heisenberg-antiferromagnet Sr2cuo2cl2. Zeitschrift Fur Physik B-Condensed Matter 96:465–477
105. Sulewski PE, Fleury PA, Lyons KB, Cheong SW, Fisk Z (1990) Light-scattering from quantum spin fluctuations in La2cuo4, Nd2cuo4, Sm2cuo4. Phys Rev B 41:225–230
106. Aeppli G, Hayden SM, Mook HA, Fisk Z, Cheong SW, Rytz D, Remeika JP, Espinosa GP, Cooper AS (1989) Magnetic dynamics of La2cuo4 and La2-Xbaxcuo4. Phys Rev Lett 62: 2052–2055
107. Singh RRP, Fleury PA, Lyons KB, Sulewski PE (1989) Quantitative-determination of quantum fluctuations in the Spin-1/2 planar antiferromagnet. Phys Rev Lett 62:2736–2739
108. Buckingham AD, Pyykko P, Robert JB, Wiesenfeld L (1982) Mol Phys 46:177–182
109. Guha BC (1951) Proc R Soc London Ser A 206:353–373
110. Bleaney B, Bowers KD (1952) Proc R Soc London Ser A 214:451–465
111. Ozarowski A (2008) The zero-field-splitting parameter D in binuclear copper(II) carboxylates is negative. Inorg Chem 47:9760–9762
112. Dzyaloshinskii I (1958) J Phys Chem Solid 4:241–255
113. Moriya T (1960) Phys Rev 120:91–98
114. Moskvin AS (2007) Dzyaloshinsky-Moriya antisymmetric exchange coupling in cuprates: oxygen effects. J Exp Theory Phys 104:913–927

115. Maurice R, Pradipto AM, de Graaf C, Broer R (2012) Magnetic interactions in LiCu2O2: single-chain versus double-chain models. Phys Rev B 86
116. Bogdanov NA, Maurice R, Rousochatzakis I, van den Brink J, Hozoi L (2013) Magnetic state of pyrochlore Cd2Os2O7 emerging from strong competition of ligand distortions and longer-range crystalline anisotropy. Phys Rev Lett 110
117. Atanasov M, Comba P, Hanson GR, Hausberg S, Helmle S, Wadepohl H (2011) Cyano-bridged homodinuclear copper(II) complexes. Inorg Chem 50:6890–6901
118. Maurice R, Pradipto AM, Guihery N, Broer R, de Graaf C (2010) Antisymmetric magnetic interactions in oxo-bridged copper(II) bimetallic systems. J Chem Theory Comput 6:3092–3101
119. Bouammali M-A, Suaud N, Maurice R, Guihéry N (2021) Extraction of giant Dzyaloshinskii–Moriya interaction from ab initio calculations: first-order spin–orbit coupling model and methodological study. J Chem Phys 155:164305
120. Bouammali M-A, Suaud N, Guihéry N, Maurice R (2022) Antisymmetric exchange in a real copper triangular complex. Inorg Chem 61:12138–12148
121. Yoon J, Mirica LM, Stack TDP, Solomon EI (2004) Spectroscopic demonstration of a large antisymmetric exchange contribution to the spin-frustrated ground state of a D3 symmetric hydroxy-bridged trinuclear Cu(II) complex: ground-to-excited state superexchange pathways. J Am Chem Soc 126:12586–12595
122. Ginsberg AP, Brookes RW, Martin RL, Sherwood RC (1972) Inorg Chem 11:2884–2889
123. Journaux Y, Kahn O, Chevalier B, Eourneau J, Claude R, Dworkin A (1978) Chem Phys Lett 55:140–143
124. Joung KO, O'Connor CJ, Sinn E, Carlin RL (1979) Inorg Chem 18:804–808
125. Maurice R, Verma P, Zadrozny JM, Luo SJ, Borycz J, Long JR, Truhlar DG, Gagliardi L (2013) Single-ion magnetic anisotropy and isotropic magnetic couplings in the metal-organic framework Fe-2(dobdc). Inorg Chem 52:9379–9389
126. Retegan M, Cox N, Pantazis DA, Neese F (2014) A first-principles approach to the calculation of the on-site zero-field splitting in polynuclear transition metal complexes. Inorg Chem 53: 11785–11793
127. Krzystek J, Ozarowski A, Telser J (2006) Multi-frequency, high-field EPR as a powerful tool to accurately determine zero-field splitting in high-spin transition metal coordination complexes. Coord Chem Rev 250:2308–2324
128. Krzystek J, Telser J (2016) Measuring giant anisotropy in paramagnetic transition metal complexes with relevance to single-ion magnetism. Dalton Trans 45:16751–16763
129. Suaud N, Rogez G, Rebilly JN, Bouammali MA, Guihery N, Barra AL, Mallah T (2020) Playing with magnetic anisotropy in hexacoordinated mononuclear Ni(II) complexes, an interplay between symmetry and geometry. Appl Mag Res 51:1215–1231